



HAL
open science

Multifield approach and interface locating method for two-phase flows in nuclear power plant

Solène Fleau

► **To cite this version:**

Solène Fleau. Multifield approach and interface locating method for two-phase flows in nuclear power plant. Physics [physics]. Université Paris-Est, 2017. English. NNT : 2017PESC1081 . tel-01621735

HAL Id: tel-01621735

<https://theses.hal.science/tel-01621735>

Submitted on 23 Oct 2017

HAL is a multi-disciplinary open access archive for the deposit and dissemination of scientific research documents, whether they are published or not. The documents may come from teaching and research institutions in France or abroad, or from public or private research centers.

L'archive ouverte pluridisciplinaire **HAL**, est destinée au dépôt et à la diffusion de documents scientifiques de niveau recherche, publiés ou non, émanant des établissements d'enseignement et de recherche français ou étrangers, des laboratoires publics ou privés.



UNIVERSITÉ — — PARIS-EST

ÉCOLE DOCTORALE 531: Sciences, Ingénierie & Environnement

Dissertation

submitted to Université Paris-Est Marne-la-Vallée for the degree of Doctor in Fluid Mechanics

by

Solène FLEAU

Multifield approach and interface locating method for two-phase flows in nuclear power plant

presented on June 21st, 2017

Committee in charge :

Mr. Jacques MAGNAUDET	Director of Research at the CNRS	IMFT - Toulouse	Jury chairman
Mr. Marc MASSOT	Professor	CMAP - Saclay	Reviewer
Mr. Dominique LEGENDRE	Professor	IMFT - Toulouse	Reviewer
Mr. Eric CHENIER	Doctor - HDR	MSME - Marne-la-Vallée	Examiner
Mr. Stéphane VINCENT	Professor	MSME - Marne-la-Vallée	Research Director
Mr. Stéphane MIMOUNI	Expert Research Engineer	EDF R&D - Chatou	Industrial Supervisor

Remerciements

Je voudrais commencer par remercier mes rapporteurs Marc Massot et Dominique Legendre pour leur lecture attentive de mon manuscrit de thèse ainsi que Jacques Magnaudet et Eric Chénier pour avoir accepté de faire partie de mon jury.

Je remercie également mon encadrant à EDF R&D Stéphane Mimouni et mon directeur de thèse du laboratoire MSME Stéphane Vincent. Nous avons formé un trinôme très efficace durant ces trois années grâce à votre capacité d'écoute et de conseils.

Plus généralement, je remercie le département MFEE d'EDF R&D et en particulier l'équipe NEPTUNE, l'ex-groupe I81 et le groupe I8B pour leur aide et leur soutien. De la même manière, je remercie l'équipe TCM du laboratoire MSME.

J'adresse un remerciement particulier à tous les doctorants que j'ai cotoyé durant ma thèse que ce soit à l'université ou à EDF qu'ils aient ou non fini leur thèse à ce jour. Je n'oublie pas Daria, ma collègue de bureau pendant 2 ans et demi.

Je remercie également les filles (et gars) de la gym pour les discussions en pleine séance de torture ainsi que Nelly pour ses conseils et son "spécial" qui m'ont maintenu en forme durant ces trois années.

Enfin, je remercie ma famille au sens large et mes amis pour leur aide tout au long de ma thèse et pour avoir supporté les 45°C de ma salle de soutenance sans broncher. Une petite dédicace pour finir à la vieille titi qui n'a pas pu être là et au chat.

Contents

1	Introduction	9
1.1	Industrial Context	9
1.1.1	Nuclear power plants with water reactors	9
1.1.2	Safety issues	10
1.2	Framework of the thesis work	13
1.3	Content of this thesis	14
I	Large interface modeling within the multifield approach in laminar isothermal flows	15
2	Modeling approaches for the simulation of two-phase flows	19
2.1	Résumé du chapitre	19
2.2	Flow regimes	19
2.3	Single-phase flow equations	20
2.4	From single-phase flows to two-phase flows	21
2.4.1	Direct Numerical Simulation (DNS)	21
2.4.2	Fixed grid approaches	22
2.4.3	Single-fluid model	24
2.4.4	Interface tracking methods	25
2.4.5	Two-fluid model	28
2.4.6	Numerical scheme	29
3	Multifield approach	33
3.1	Résumé du chapitre	33
3.2	Concept and motivations	34
3.3	Model for the dispersed field	36
3.3.1	Drag force	36
3.3.2	Lift force	36
3.3.3	Added mass force	37
3.3.4	Turbulent dispersion force	37
3.3.5	Interfacial area transport equation	38
3.4	Model for the large interfaces: Large Bubble Model (LBMo)	38
3.4.1	Drag force	38
3.4.2	Surface tension	39

3.4.3	Interface sharpening	41
3.5	Model for the badly resolved structures	42
3.5.1	Detection	42
3.5.2	Treatment	43
3.6	Transfer between the dispersed and the continuous gas fields	43
4	Conservative implementation of the interface sharpening equation	45
4.1	Résumé du chapitre	45
4.2	Formulation of the interface sharpening equation	46
4.3	Conservative implementation	46
4.3.1	Numerical scheme	46
4.3.2	Effect of the conservative implementation on simulation results	49
4.4	Recompression threshold	52
4.4.1	Implementation of the criterion	52
4.4.2	Optimization of the threshold β	53
4.5	Identification of diffused interfaces	56
4.5.1	Interface smearing criterion	56
4.5.2	Illustration with Thorpe's experiment	57
4.6	Conclusion	63
5	Evaluation of the spurious velocities induced by the surface tension model	65
5.1	Résumé du chapitre	65
5.2	Air bubble in still water at 298.15 K	65
5.2.1	Theory	66
5.2.2	Simulation	67
5.3	Steam bubble in still water at 378.15 K	69
5.4	Conclusion	70
6	Implementation and validation of a new drag force model	73
6.1	Résumé du chapitre	73
6.2	Standard drag force model	74
6.3	New drag force expression	74
6.4	Validation of the new drag force expression	77
6.4.1	Bhaga and Weber's rising bubbles	77
6.4.2	Kelvin-Helmholtz instability	78
6.5	Conclusion	82
7	Comparison between the Large Bubble Model (LBMo) and dedicated large interface tracking methods	83
7.1	Résumé du chapitre	83
7.2	Comparison with a one-fluid approach	84
7.3	Comparison with other codes on the Rayleigh-Taylor instability test case	85

7.3.1	Theory	85
7.3.2	Simulation	86
7.4	Comparison with LIM	87
7.5	Conclusion	89
8	Conclusion	91
II	Computation of heat and mass transfers	93
9	Simulation of large interfaces with phase change	97
9.1	Résumé du chapitre	97
9.2	Adjustment of the numerical scheme	97
9.3	Adjustment of the Large Bubble Model	98
9.4	Implementation of a new heat and mass transfer source term	99
9.4.1	Relation between mass transfer terms and heat fluxes	99
9.4.2	Available models in the literature	100
9.4.3	New heat transfer term	101
9.5	Validation of the new heat transfer model	102
9.5.1	Sucking problem	102
9.5.2	Stefan problem	108
9.6	Conclusion	112
10	Simulation of multifield flows with coexistence of large interfaces and a dispersed gas field	115
10.1	Résumé du chapitre	115
10.2	Test case description	116
10.3	Effect of the interface sharpening equation on three field simulations	117
10.4	Transition between the continuous gas field and the dispersed gas field	119
10.4.1	Transition from the dispersed gas field to the continuous gas field	119
10.4.2	Effect of the mesh refinement	120
10.4.3	Effect of the time step	123
10.4.4	Effect of the characteristic time step of the transition	123
10.5	Conclusion	124
11	Prediction of flow regimes: improvement of the isothermal mass transfer terms	125
11.1	Résumé du chapitre	125
11.2	METERO test case	126
11.3	Prediction of flow regimes	129
11.4	Improvement of the isothermal mass transfer term	130
11.4.1	Improved coalescence term	133
11.4.2	Validation	133
11.4.3	Interfacial area conservation	134

11.5	Conclusion	136
12	Conclusion	137
III	Investigation of Large Eddy Simulation for turbulent flows	139
13	Properties of turbulent flows and modeling strategies	143
13.1	Résumé du chapitre	143
13.2	Properties of homogeneous isotropic turbulence: single-phase flows . .	143
13.2.1	Main characteristics	143
13.2.2	A multitude of scales	144
13.2.3	Kolmogorov's energy cascade	145
13.3	Properties of turbulent two-phase flows	147
13.4	Simulation of turbulent flows	148
13.4.1	Direct Numerical Simulation (DNS)	149
13.4.2	Reynolds Average Navier-Stokes (RANS) / Unsteady Reynolds Average Navier-Stokes (URANS)	149
13.4.3	Large Eddy Simulation	151
14	Large Eddy Simulation of turbulent two-phase flows	153
14.1	Résumé du chapitre	153
14.2	LES filtering of the single-fluid model equations	154
14.2.1	Simple filtering	155
14.2.2	Favre's averaging	157
14.2.3	Discussion	159
14.3	Models for the subgrid terms	160
14.3.1	Functional models	160
14.3.2	Structural models	162
14.3.3	Mixed scale models	165
14.3.4	Boundary conditions in LES	166
14.4	Monotonically Integrated Large Eddy Simulation (MILES)	166
14.5	Filter notion	167
14.6	Interactions between turbulence and interfaces	168
14.7	Interactions between turbulence and dispersed fields	169
14.7.1	LES filtering of the two-fluid model equations	169
14.7.2	Effect on the subgrid models	171
15	Feasibility study of LES on a single-phase flow	173
15.1	Résumé du chapitre	173
15.2	Description of the test case	174
15.2.1	Notations	174
15.2.2	Characteristics of the flow	174
15.3	Simulation parameters	175

15.3.1	Flow parameters	175
15.3.2	Mesh	176
15.3.3	Numerical parameters	178
15.4	Results	178
15.4.1	Averaging effects	178
15.4.2	Turbulence model comparison	178
15.4.3	Sensibility to the mesh refinement in the span-wise direction	181
15.4.4	Sensibility to the mesh refinement in the stream-wise direction	183
15.4.5	Sensibility to the time scheme order	185
15.5	Conclusion	187
16	<i>A priori</i> LES study on two-phase flows with the two-fluid model	189
16.1	Résumé du chapitre	189
16.2	Simulation of the phase inversion benchmark	190
16.2.1	Presentation of the test case	190
16.2.2	Validation of the macroscopic behavior	191
16.3	Filtering of the two-fluid model equations	195
16.3.1	Simple filtering	195
16.3.2	Favre's averaging	197
16.4	Comparison of the order of magnitude of the different subgrid-scale terms	200
16.5	Comparison of the turbulence models	203
16.5.1	Modeling errors for all the subgrid terms	203
16.5.2	Turbulent viscosity predicted by the turbulence models	205
16.5.3	Focus on the drag subgrid term τ_{drag}	206
16.5.4	Focus on the pressure subgrid term $\tau_{pressure}$	208
16.5.5	Focus on the ADM order	210
16.5.6	Effect of the filter	211
16.6	Conclusion	213
17	True LES: implementation of the Approximate Deconvolution Model (ADM)	215
17.1	Résumé du chapitre	215
17.2	Validation of the implementation on a single-phase flow	216
17.3	To two-phase flow simulations with LES	219
17.4	ADM implementation for two-phase flows	221
17.5	Conclusion	224
18	Conclusion	227
IV	Industrial application	229
19	ULPU-V experiment	233
19.1	Résumé du chapitre	233

19.2	Description of the experiment	234
19.3	Simulation set up	235
19.4	First step: multifield simulation with standard phase change models	236
19.5	Second step: multifield simulation with new phase change model for continuous fields	240
19.6	Third step: Full multifield simulation	241
19.7	Conclusion	244
V	Conclusion	245
VI	Perspectives	251
A	To the need of the Large Bubble Model	255
A.1	Deactivation of the interface sharpening	255
A.2	Deactivation of the surface tension model	255
A.3	Deactivation of the drag force	256
A.4	Conclusion	257
B	Conservative implementation of the interface sharpening equation, further validations	259
B.1	Square bubble test case	259
B.2	Simulation of a stationary bubble	262
B.2.1	Effect of a non conservative implementation	262
B.2.2	Optimization of the threshold value β	262
B.3	Simulation of an oscillating bubble	266
B.4	Simulation of Thorpe's experiment	268
B.4.1	Optimization of the threshold value β	268
B.4.2	Activation of the interface smearing criterion	269
B.5	Conclusion	270
C	Validation of the Large Bubble Model on unstructured grids	273
C.1	Reconstruction	274
C.2	Efficiency of the interface sharpening equation	275
C.3	Evaluation of the spurious velocities	275
C.4	Conclusion	276
D	Calculation of convergence orders using the Richardson's extrapolation	279
E	Further validations of the new drag force expression for the LBM	281
E.1	Interfacial liquid/liquid test case: Rayleigh-Taylor instability	281
E.2	Bubble test case: Oscillating bubble	283
E.3	Conclusion	283

F	Few words about the Large Interface Model (LIM)	285
F.1	Interface tracking method	285
F.2	Interfacial momentum source terms	286
F.3	Phase change model with the LIM	286
G	Further comparisons between the LBMo and dedicated large interface tracking methods	289
G.1	Comparison between the LBMo and one-fluid models	289
G.1.1	Rayleigh-Taylor instability	289
G.1.2	Kelvin-Helmholtz instability	291
G.2	Comparison between the LBMo and the LIM	296
G.2.1	Bhaga and Weber’s rising bubble test case	296
G.2.2	Rayleigh-Taylor instability	297
G.3	Conclusion	297
H	Theory of the sucking problem	299
H.1	Notations	299
H.2	Energy balance equations and other relations	299
H.3	Temperature profile	300
H.4	Interface position	301
I	Further validations of the mass transfer term for large interfaces with phase change	303
I.1	Sucking problem at $1.013 \cdot 10^7 Pa$	303
I.2	Growing steam bubble	305
I.3	Inversed sucking problem	308
I.4	Conclusion	309
J	Effect of the turbulence modeling on the Hänsch’s bubble column	311
J.1	Simulation	311
J.2	Conclusion	311
K	Castillejos’ test case	313
K.1	Test case description	313
K.2	Simulation results	314
K.3	Conclusion	316
L	Relations between LES results and experimental data	317
L.1	Notations	317
L.2	Average relations	318
M	Extra validations of the standard LES models on a single-phase flow	319
M.1	Sensibility to the mesh refinement in the span-wise direction	319
M.2	Sensibility to the mesh refinement in the stream-wise direction	321

N	<i>A priori</i> LES study with the phase inversion benchmark, case 2	323
N.1	Presentation of the test case	323
N.2	Validation of the macroscopic behavior	324
N.3	Comparison of the order of magnitude of the different subgrid-scale terms	327
N.4	Comparison of the turbulence models	328
N.5	Conclusion	328

Nomenclature

Roman characters

A_i	m^2	Interfacial area
C_A	-	Coefficient of the added mass force
C_D	-	Coefficient of the drag force
C_L	-	Coefficient of the lift force
C_p	$J.m^{-1}.K^{-1}$	Specific heat capacity
d	m	Diameter
D^T	$m^2.s^{-1}$	Turbulent mass diffusivity
D_{diff}	$m^2.s^{-1}$	Diffusion coefficient
g	$m.s^{-2}$	Gravity acceleration
H	$J.kg^{-1}$	Enthalpy
I	$kg.m^{-2}.s^{-2}$	Interfacial momentum transfer
$\underline{\underline{I_d}}$	-	Identity matrix
k	m^{-1}	Wavenumber
K	$m^2.s^{-2}$	Turbulent kinetic energy
L	$J.kg^{-1}$	Latent heat
\mathbf{n}	-	Unit normal vector
P	Pa	Pressure
q	$W.m^{-2}$	Interfacial heat flux
\mathbf{Q}	$W.m^{-2}$	Conductive thermal flux
R	m	Radius
$\underline{\underline{S}}$	s^{-1}	Viscous stress tensor

$\underline{\underline{S}}e$	$kg.m^{-2}.s^{-2}$	External momentum source term
$\underline{\underline{S}}^T$	$kg.m^{-1}.s^{-2}$	Turbulent stress tensor
T	K	Temperature
\mathbf{t}	-	Unit tangent vector
\mathbf{u}	$m.s^{-1}$	Velocity
u_τ	$m.s^{-1}$	Shear velocity

Dimensionless numbers

At	$\frac{\rho_1 - \rho_2}{\rho_1 + \rho_2}$	Atwood number
Ca	$\frac{\mu u}{\sigma}$	Capillary number
Eo	$\frac{d^2 \Delta \rho g}{\sigma}$	Eötvös number
m	$\frac{u \Delta t}{\Delta x}$	Courant–Friedrichs–Lewy (CFL) number
F_0	$\frac{\chi_v \Delta t}{\Delta x^2}$	Fourier number
Oh	$\frac{\mu_2}{\sqrt{\sigma \rho_2 H}}$	Ohnesorge number
Re	$\frac{dU}{\nu}$	Reynolds number
S_C^T	$\frac{\mu^T}{D^T}$	Turbulent Schmidt number
We	$\frac{\rho L u^2}{\sigma}$	Weber number

Greek characters

α	-	Volume fraction
χ	$m^2.s^{-1}$	Thermal diffusivity
ϵ	$m^2.s^{-3}$	Dissipation rate of turbulent kinetic energy
η	m	Kolmogorov's length
Γ	$kg.m^{-3}.s^{-1}$	Interfacial mass transfer rate
κ	m^{-1}	Curvature
λ	$W.m^{-1}.K^{-1}$	Thermal conductivity
μ	$kg.m^{-1}.s^{-1}$	Dynamic viscosity
μ^T	$kg.m^{-1}.s^{-1}$	Dynamic eddy viscosity
ν	$m^2.s^{-1}$	Cinematic viscosity
ν^T	$m^2.s^{-1}$	Cinematic eddy viscosity
ω	s^{-1}	Pulsation
Ω	m^3	Cell volume
ρ	$kg.m^{-3}$	Density
σ	$N.m^{-1}$	Surface tension coefficient
τ	s	Non physical time
τ_w	$kg.m^{-1}.s^{-2}$	Wall shear stress
θ, γ	-	Angular coordinates
Δt	s	Numerical time step
Δx	m	Cube root of the cell volume

Operators

∇	Nabla operator: $\left(\frac{\partial}{\partial x}, \frac{\partial}{\partial y}, \frac{\partial}{\partial z}\right)$
∇^{Int}	Surface derivative operator along the interface
δ_{ij}	Dirac function
$\ \cdot\ $	Norm for a vector
$\underline{\underline{\cdot}}$	Tensor notation
\otimes	Tensor product
$*$	Convolution operator
$\bar{\cdot}$	Filtered quantity
$\tilde{\cdot}$	Favre's averaging
$\hat{\cdot}$	Test filter
\sum_k	Sum over the fields
\sum_{ncel}	Sum over all the cells of the computational domain
\sum_I	Sum over one cell faces
$tr(\cdot)$	Trace of a matrix
$\langle \cdot \rangle$	Average
$ \cdot $	Absolute value of a number
$[\cdot]$	Jump operator

Subscripts and superscripts

i, j	Space directions
Int	Interface
I	Cell index
k, p	Fluid index
$ncel$	Total cell number
s	Stratified cell (LI3C)
n	Current time step
$n + 1$	Next time step
l	Liquid phase
v	Vapor phase
cl	Continuous liquid field
cg	Continuous gas field
dg	Dispersed gas field
$*$	Intermediate values
$+$	Dimensionless wall distance

Acronyms

ADM	Approximate Deconvolution Model
AMR	Adaptive Mesh Refinement
CMFD	Computational Multi-Fluid Dynamics
CHF	Critical Heat Flux
CPU	Central Processing Unit
CSF	Continuum Surface Force
CLSVOF	Coupled Level-Set Volume Of Fluid
ECC	Emergency Core Cooling
DNB	Departure from Nuclear Boiling
DNS	Direct Numerical Simulation
FT	Front-Tracking
IRC	Inertial Range Consistent
IVR	In-Vessel Retention
LBMo	Large Bubble Model
LES	Large Eddy Simulation
LIM	Large Interface Model
LS	Level-Set
LI3C	Large Interface represented with 3 Cells thick layers
NE	Numerical Errors
PLIC	Piecewise Linear Interface Construction
PTS	Pressurized Thermal Shock
MILES	Monotonically Integrated Large Eddy Simulation
RANS	Reynolds Average Navier-Stokes
RSFS	Resolvable SubFilter-Scale
RSTM	Reynolds Stress Transport Models
SGS	SubGrid Scale

SIMPLE	Semi-Implicit Method for Pressure-Linked Equations
THINC	Tangent of Hyperbola INterface Capturing method
URANS	Unsteady Reynolds Average Navier-Stokes
USFS	Unresolvable SubFilter-Scale
VOF	Volume Of Fluid
WALE	Wall-Adapting Local Eddy-Viscosity

Chapter 1

Introduction

1.1 Industrial Context

Turbulent two-phase flows with phase change heat transfer are an object of research in many industrial fields. Indeed, wave surges are responsible for a large range of coastal phenomena and has led to intensive work programs in oceanography. At the same time, researchers are challenged by the simulation of evaporation and condensation to improve cooling systems and to deal with large heat fluxes in electronics and power engineering. In pipelines also, the understanding of complex flows containing oil, gas and water is of the highest importance to extract hydrocarbons efficiently and reduce costs. Comprehension of such turbulent two-phase flows with phase change constitutes a huge opportunity in the aeronautics, automotive, engine, biology, meteorology and many other applications.

In nuclear power plants, these flows are present at normal conditions in condensers and steam generators. They also may appear during various hypothetical accidents such as boiling crisis, which can threaten the integrity of the reactor pressure vessel and conduct to a contamination of the environment with radioactive nuclei. Therefore, important investigations are carried out to understand these complex flows and so to ensure safety of the nuclear reactors and the thermal power systems.

This section proposes a short presentation of nuclear power plants with water reactors to understand how electricity is produced and where turbulent two-phase flows occur in operating conditions. Then, different safety issues involving such flows are detailed to highlight their complexity and the challenges that have to be taken up to achieve accurate simulations of the phenomena.

1.1.1 Nuclear power plants with water reactors

In nuclear power plants with a pressurized water reactor or a boiling water reactor, electricity is produced by a turbine which is driven by steam water. To obtain this vapor phase, cool water is heated up in the reactor pressure vessel by the exothermic fissions of uranium nuclei. This hot primary water enters the steam

generator in which cold secondary water is flowing through U-shape pipes (see Figure 1). Thus, the secondary water evaporates. The obtained steam is dried before entering the turbine. Finally, the recondensation of the secondary water is ensured by a third water loop which is eventually cooled in a cooling tower before reinjection in a water course.

In terms of thermodynamic conditions, water flowing in the nuclear reactor vessel is on average at 579 K with a pressure of $1.55 \cdot 10^7\text{ Pa}$ (155 bars). The inner diameter of the vessel is around equal to 4 m depending on the nuclear power plant and the height around equal to 13 m .

To prevent radiological exposures, the primary water loop and the reactor building which contains the steam generator are confined. Nevertheless, in case of safety issues, water flows play a crucial role to maintain the pressure and temperature conditions in the reactor vessel and so to avoid the release of radioactive products in the environment.

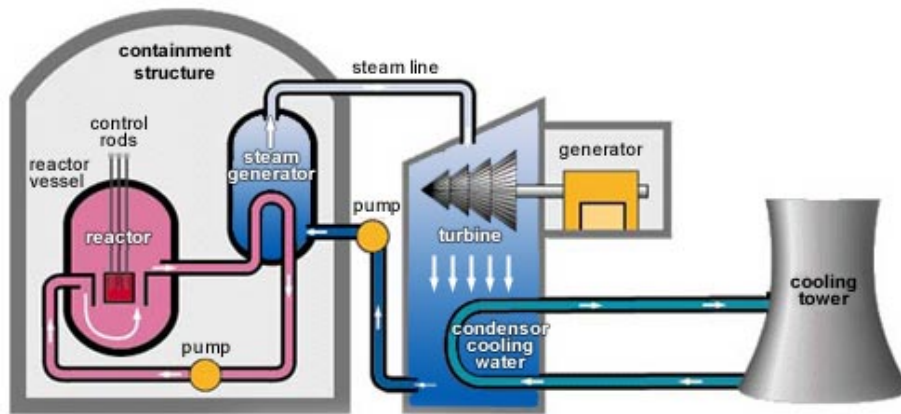


Figure 1: Schematic view of a nuclear power plant with a water pressurized reactor, the primary water loop is in pink and the secondary water loop in dark blue [1].

1.1.2 Safety issues

EDF gives a strong attention to nuclear safety issues. Thus, many studies and research works are conducted on these topics. In this section, some examples of subjects investigated by EDF R&D are proposed.

1.1.2.1 Steam generators

In nuclear power plants with a pressurized water reactor or a boiling water reactor, the creation of steam, necessary to drive the turbine, takes place in the steam generator which is located in the reactor building. Hot water is heated up by the fission reactions in the reactor vessel, enters the steam generator and heats up the water from the secondary circuit. In the secondary water flow, the pressure is fixed

at 7.10^6 Pa (70 bars), corresponding to a boiling temperature of 560 K smaller than for the primary water flow. The steam generator is generally 20 m high with a diameter of 3 m . For a 900 Megawatts electric nuclear power plant, the inner diameter of the U-shape pipes, in which the secondary water flows, is equal to 22 mm .

This steam generator is one of the weak points of the nuclear power plant because it contains both contaminated water from the primary circuit and secondary water that is in contact with the environment. In case of a pipe breakup, fission products can be released in water courses and groundwater.

Therefore, to prevent a tube breaking due to tube vibrations in steam generators and to improve their lifetime, investigations have been carried out to predict the properties of the flow in terms of flow types and bubble sizes. Nevertheless, as we can see in Figure 2, the variety of flow regimes (annular flow, dispersed bubbles and droplets, large and deformable bubbles) existing in vertical superheated tubes makes the simulations challenging.

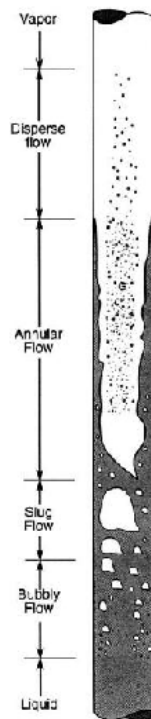


Figure 2: Steam/water flow in a vertical superheated tube (Brennen [22]).

1.1.2.2 Loss of Coolant

To prevent core heat up and damage, an Emergency Core Cooling (ECC) is installed in nuclear power plants. This system injects subcooled water through the cold leg in the reactor pressure vessel. The thermal load of cold water on the hot structure under pressurized conditions, called the Pressurized Thermal Shock (PTS)

can threaten the integrity of the vessel which is one of the three barriers against the fission product release in the environment and can not be replaced.

The thermal hydraulics problem is to evaluate the heat up of water between the ECC injection and the vessel. The fluid in the primary circuit can be either in single-phase or two-phase conditions depending on the leak size, its location and the operating conditions of the nuclear power plant. When the loss of coolant occurs in a two-phase flow, the injection of subcooled water induces the presence of a stratified flow in a part of the cold leg. Close to the ECC injection and in the downcomer region below the junction with the cold leg, the flow is more complex with a dispersed phase and turbulent phenomena. Thus, different flow regimes can be observed from the ECC injection to the cold leg: a free liquid ECC jet which plunges into a free surface, a dispersed flow with bubbles in a stratified flow configuration and finally a wavy free surface (see Figure 3).

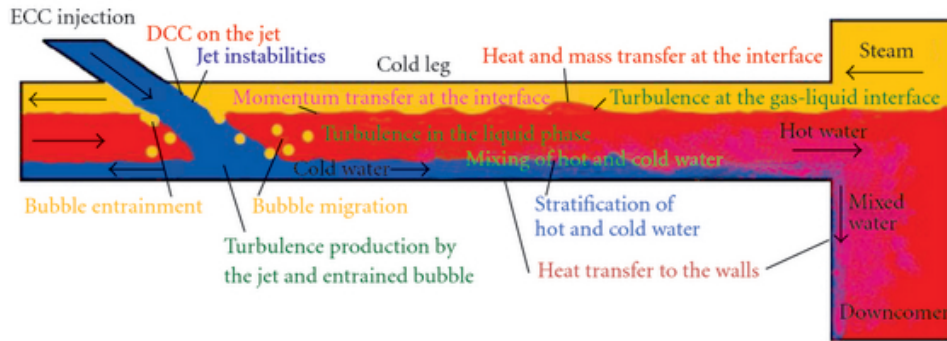


Figure 3: Schematic view of the flow regimes and phenomena occurring during a PTS situation with partially filled cold leg [82].

1.1.2.3 Departure from Nuclear Boiling (DNB)

The understanding of the Departure from Nuclear Boiling (DNB) is crucial in nuclear power plants. Indeed, in the reactor vessel, if the liquid water heat flux becomes higher than the Critical Heat Flux (CHF) of the system, the fluid begins to boil (see the Nukiyama curve in Figure 4). Then, small bubbles are nucleated along the tube surface and form large deformable bubbles by coalescence. These large bubbles can finally form a vapor film at the hot surface which is then insulated from the liquid. Since the surface is not cooled anymore by liquid water, the heat flux exchange decreases and the temperature of the tube increases dramatically. This situation can be particularly dangerous if it occurs at the fuel rod surface since the cooling is not ensured anymore.

Due to their sizes, the large deformable bubbles cannot be modeled with a dispersed approach. Therefore, a multifield approach which considers separately the

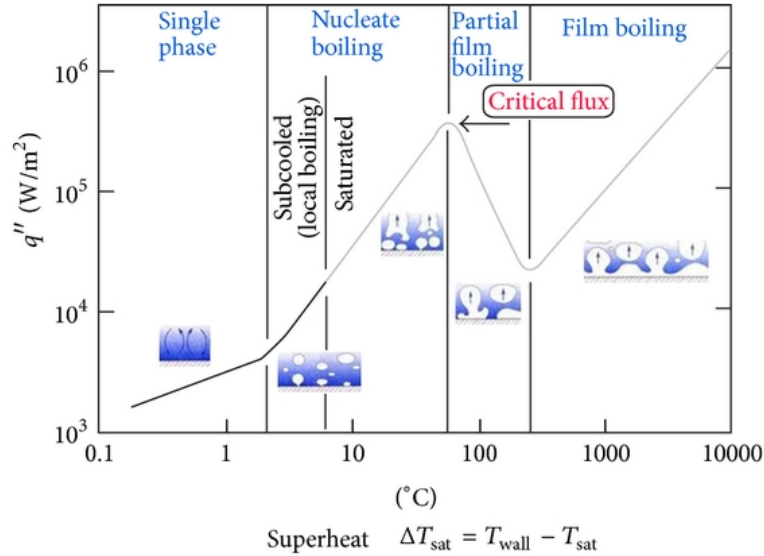


Figure 4: Typical pool boiling curve for water under atmospheric pressure called the Nukiyama curve [8], q'' corresponds to the heat flux.

bulk fluid, the dispersed bubbles and the large bubbles seems to better suit the simulation of the DNB. Thus, the main goal of the present work and which also makes its originality is the development of this multifield approach.

1.2 Framework of the thesis work

The first section gave some examples of the type of flows occurring in nuclear power plants. Nevertheless, in operating conditions or during safety issues, many phenomena are still not understood. This can be explained by two main factors. The first explanation is the complexity of the geometries, especially in steam generator within the U-shape pipes. The second and maybe most important point is the lack of experimental studies. Indeed, the flow conditions are not easy to reproduce and measurements are difficult to perform on operating nuclear power plants.

One attractive way that have been explored for few decades now is the development of Computational Multi-Fluid Dynamics (CMFD) codes to improve our knowledge in physical phenomena occurring in nuclear power plants. For this purpose, EDF R&D have invested in its own CMFD tools for single-phase flows simulation with *Code_Saturne* [7] and multiphase flows through the code NEPTUNE_CFD [60]. This thesis work, whose subject is the multifield approach and interface locating method for two-phase flows in nuclear power plants, is a part of the MULTIPATH project. This project is financially supported by CEA (Commissariat l'Énergie Atomique et aux Energies Alternatives), EDF (Électricité de France), IRSN (Institut de Radioprotection et de Sûreté Nucléaire) and AREVA NP.

1.3 Content of this thesis

In nuclear power plants, turbulent boiling flows are involved in many safety issues presented in section 1.1.2. Different flow regimes have to be taken into account. Moreover, thermal exchange can have crucial effects on the flow establishment. Therefore, approaches have to be developed to take into account all these phenomena. This thesis work presents a multifield approach coupled with turbulent and heat and mass transfer models devoted to the simulation of such complex flows.

This report is composed of four main parts dealing with three different properties of these flows. In the first part, the multifield approach developed to deal with small spherical inclusions and large and deformable ones at the same time is detailed. A specific treatment called the Large Bubble Model (LBMo) used to simulate accurately the second type of structures is presented and improved. Only laminar and isothermal flows are considered in this part. Then, in the second part, heat and mass transfer terms are explored. The first chapter is devoted to the implementation and validation of a heat and mass transfer term for the simulation of large interfaces with phase change using the LBMo. Then, a second type of mass transfers is studied to consider the coalescence of the small spherical bubbles forming larger ones and the breakup of the large ones into small inclusions. In the third part, turbulence is investigated. For this purpose, the state of the art concerning turbulence modeling in two-phase flows is detailed. Then, Large Eddy Simulation (LES) is explored using DNS results first. According to the results obtained in the *a priori* study, LES models are implemented in NEPTUNE_CFD. Their ability to predict various flow regimes is assessed. Finally, in the last part, an industrial application is proposed involving a turbulent non isothermal flow in an industrial geometry.

Part I

Large interface modeling within the
multifield approach in laminar
isothermal flows

The first challenge that has to be taken up consists in the treatment of flows containing inclusions of different sizes and shapes. Thus, the first chapter is devoted to the description of the different models and associated numerical methods available for the simulation of interfaces in two-phase flows. However, these approaches have been developed for only one type of interfacial structures either small and spherical or large and deformable. In the second chapter, a multifield approach is presented to simulate accurately the two types of inclusions evolving at the same time and in a couple way in a two-phase flow.

In this multifield approach, one phase can be split into two fields if this phase is present in the flow in the form of small spherical inclusions and large deformable structures at the same time. In this case, the first category of inclusions is modeled using a dispersed approach. The second category is treated as an interface between two continuous fields. An accurate simulation of complex flows requires suitable models for both fields. The dispersed fields have been widely studied in the last few decades [132] and are currently at the state of the art (see section 3.3). Thus, the next three chapters are devoted to the improvement of the Large Bubble Model (see section 3.4), developed for the simulation of large interfaces within the two-fluid model. Finally, the last chapter compares the ability of the LBMo to simulate with the same accuracy large and deformable interfaces than dedicated methods in order to validate the work.

In this part, only isothermal, laminar and incompressible flows will be considered. The simulations will always involve two continuous fields (liquid or gas). No dispersed fields will be defined since the LBMo concerns only the simulation of large interfaces. The validation of the improved LBMo on turbulent flows with phase change will be proposed in the next parts of this thesis report.

Chapter 2

Modeling approaches for the simulation of two-phase flows

In this chapter, the main regimes than can be observed in two-phase flows are detailed. Then, different modeling strategies for the simulation of these flows are presented.

2.1 Résumé du chapitre

Ce chapitre présente l'état de l'art des modèles utilisés pour la simulation d'écoulements diphasiques. Dans le premier paragraphe, les principaux régimes d'écoulements sont définis. On s'intéresse ensuite à leur modélisation. Pour ce faire, les équations de Navier-Stokes appliquées aux écoulements monophasiques constituent le point de départ. Les écoulements diphasiques peuvent alors être considérés comme deux écoulements monophasiques délimités par une interface. C'est le parti pris par les approches dites de simulation numérique directe. Mais elles nécessitent des maillages qui suivent les interfaces ce qui peut s'avérer très coûteux voire impossible dans le cas d'interfaces très perturbées. Par conséquent, un second type d'approche est présenté, basé cette fois sur des maillages fixes. Dans cette catégorie, on trouve d'une part les modèles 1-fluide ou méthodes de suivi d'interfaces et d'autre part les modèles bi-fluide initialement dédiés à la simulation de petites structures sphériques. Pour les applications nucléaires, c'est ce modèle bi-fluide qui a été choisi et qui est implémenté dans le code NEPTUNE_CFD utilisé dans cette thèse. Par conséquent, le schéma numérique du code est décrit dans ce chapitre.

2.2 Flow regimes

The term “two-phase flow” is used to define flows in which at least two immiscible phases are present and formed interfaces. Different types of flows can be distinguished depending on the interface geometry [45], as illustrated in Figures 2.1:

- Separated phases such as annular or stratified flows,

- Transition flows with large deformable bubbles,
- Dispersed phases with small bubbles, droplets or particles.

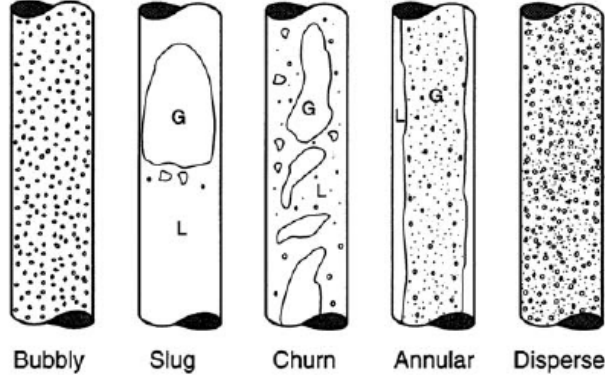


Figure 2.1: Schematic view of different types of two-phase flows in a vertical tube (Brennen [22]).

These different flow regimes coexist sometimes in the same flow. The simulations of such flows are therefore very challenging. The CMFD tools used to predict the flow behavior have to be able to deal with a large range of flow structures, regime transitions, turbulence and phase change effects.

2.3 Single-phase flow equations

To simulate multiphase flows, conservation equations are solved to predict the fluid position, velocity, pressure and temperature. To obtain these equations for two-phase flows, let us consider first a single-phase flow.

For single-phase flows, the Navier-Stokes' equations are solved to describe the fluid motion. The three conservation equations can be written as follows:

- The mass balance equation:

$$\frac{\partial \rho}{\partial t} + \nabla \cdot (\rho \mathbf{u}) = 0 \quad (2.1)$$

with ρ the density and \mathbf{u} the velocity field.

- The momentum balance equation:

$$\frac{\partial}{\partial t} (\rho \mathbf{u}) + \nabla \cdot (\rho \mathbf{u} \otimes \mathbf{u}) = -\nabla P + \nabla \cdot (\mu \underline{\underline{S}}) + \rho \mathbf{g} \quad (2.2)$$

with $\nabla \cdot (\rho \mathbf{u} \otimes \mathbf{u}) = (\rho \mathbf{u} \cdot \nabla) \mathbf{u}$ for incompressible flows, P the pressure, μ the viscosity, $\underline{\underline{S}}_{ij} = \frac{\partial u_i}{\partial x_j} + \frac{\partial u_j}{\partial x_i} - \frac{2}{3} \frac{\partial u_i}{\partial x_i} \delta_{ij}$ the viscous stress tensor and \mathbf{g} the gravity acceleration.

- The energy balance equation:

$$\frac{\partial}{\partial t} (\rho H) + \nabla \cdot (\rho H \mathbf{u}) = -\nabla \mathbf{Q} + \nabla \cdot (\underline{\underline{\mu}} \underline{\underline{S}} \cdot \mathbf{u}) + \rho \mathbf{g} \cdot \mathbf{u} + \frac{\partial P}{\partial t} \quad (2.3)$$

with $H = e + \frac{1}{2} \mathbf{u}^2 + \frac{P}{\rho}$ the total enthalpy, $\mathbf{Q} = -\lambda \nabla T$ the conductive thermal flux, λ the thermal conductivity and T the temperature.

These equations are usually used to predict the behavior of single-phase flows.

2.4 From single-phase flows to two-phase flows

2.4.1 Direct Numerical Simulation (DNS)

Two-phase flows with separated interfaces can be considered in a first approach as two single-phase flows respectively located in two subdomains Ω_1 and Ω_2 , as illustrated in Figure 2.2. These two subdomains are separated by an interface Γ_{12} . With this representation of a two-phase flow, the more natural solution for the simulation seems to consider an unstructured grid following the interface contour to simulate separately the two fluids in each subdomain Ω_1 and Ω_2 . The classical Navier-Stokes' equations are then solved in each subdomain considering the properties of the fluid present in the subdomain [37]. The only difference with the single-phase model is the presence of the interface Γ_{12} , which requires the definition of jump conditions:

$$[\mathbf{u}] \cdot \mathbf{n}^{\text{Int}} = [\mathbf{u}] \cdot \mathbf{t}^{\text{Int}} = 0 \quad (2.4)$$

with $[\mathbf{u}] = \mathbf{u}_{\Omega_2} - \mathbf{u}_{\Omega_1}$ the jump operator, \mathbf{n}^{Int} the unit normal vector to the interface Γ_{12} and \mathbf{t}^{Int} the unit tangent vector to the interface Γ_{12} .

$$[-P \underline{\underline{I}}_d + (\underline{\underline{\mu}} \underline{\underline{S}})] \cdot \mathbf{n}^{\text{Int}} = \sigma \kappa \mathbf{n}^{\text{Int}} \quad (2.5)$$

with $\underline{\underline{I}}_d$ the identity matrix, σ the surface tension coefficient and κ the interface curvature.

The main advantage of the Direct Numerical Simulation is that it uses directly the Navier-Stokes' equation to predict the fluid motion. Nevertheless, this approach requires unstructured grids which follow the interface during the whole calculation. Building automatically such grids is not easy to manage especially with complex interfaces [122]. Moreover, the remeshing process at each calculation step is time consuming and sometimes impossible to realize automatically in 3D due to the shape of local mesh cell that degenerates.

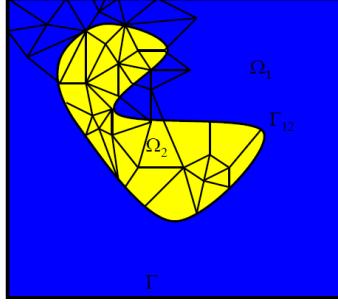


Figure 2.2: Schematic view of a two-phase flow, the flow behavior is predicted using a Direct Numerical Simulation with an adaptive unstructured grid [206].

2.4.2 Fixed grid approaches

Due to the different issues of the Direct Numerical Simulation, another approach based on fixed grids has been considered, as illustrated in Figure 2.3.

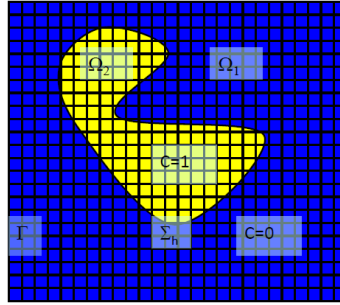


Figure 2.3: Schematic view of a two-phase flow, the flow behavior is predicted using fixed grid approaches [206], C in the figure corresponds to the phase indicator function referred as χ_k in this section.

In this case, a phase indicator function is introduced to locate each phase in the domain and then to obtain the conservation equations for the two-phase flows. This function is equal to 1 in phase k and to 0 otherwise:

$$\chi_k(\mathbf{x}, t) = \begin{cases} 1 & \text{for } \mathbf{x} \in \Omega_k(t) \\ 0 & \text{otherwise} \end{cases} \quad (2.6)$$

with $\Omega_k(t)$ the volume occupied by phase k . The phase indicator function has the following properties:

$$\sum_k \chi_k = 1 \quad (2.7)$$

$$\chi_m \chi_n = \delta_{nm} \chi_m \quad (2.8)$$

$$\nabla \chi_k = -\mathbf{n}_k^{Int} \delta^{Int} \quad (2.9)$$

$$\frac{\partial \chi_k}{\partial t} = \mathbf{u}^{Int} \mathbf{n}_k^{Int} \delta^{Int} \quad (2.10)$$

with δ^{Int} the Dirac function centered at the interface and \mathbf{u}^{Int} the interface velocity.

Therefore, each local quantity Φ (density, viscosity, velocity, pressure, temperature, enthalpy) becomes in the two-phase formulation $\Phi_k \chi_k$. Moreover, since the phase indicator function is discontinuous at the interface, its derivation induces the apparition of interfacial source terms in the three balance equations. Thus, the conservation equations can now be written [88]:

- The mass balance equation:

$$\frac{\partial}{\partial t} (\chi_k \rho_k) + \nabla \cdot (\chi_k \rho_k \mathbf{u}_k) = \chi_k \rho_k (\mathbf{u}^{Int} - \mathbf{u}_k) \cdot \mathbf{n}_k^{Int} \delta^{Int} \quad (2.11)$$

- The momentum balance equation:

$$\begin{aligned} \frac{\partial}{\partial t} (\chi_k \rho_k \mathbf{u}_k) + \nabla \cdot \left(\chi_k \left(\rho_k \mathbf{u}_k \otimes \mathbf{u}_k + P_k \underline{\underline{I}}_d - \mu_k \underline{\underline{S}}_k \right) \right) - \chi_k \rho_k \mathbf{g} \\ = \left(\rho_k \mathbf{u}_k \otimes (\mathbf{u}^{Int} - \mathbf{u}_k) - P_k \underline{\underline{I}}_d + \mu_k \underline{\underline{S}}_k \right) \cdot \mathbf{n}_k^{Int} \delta^{Int} \end{aligned} \quad (2.12)$$

- The energy balance equation:

$$\begin{aligned} \frac{\partial}{\partial t} (\chi_k \rho_k H_k) + \nabla \cdot \left(\chi_k \left(\rho_k H_k \mathbf{u}_k - \mu_k \underline{\underline{S}}_k \cdot \mathbf{u}_k - P_k \mathbf{u}_k + \mathbf{Q}_k \right) \right) - \frac{\partial}{\partial t} (\chi_k P_k) - \chi_k \rho_k \mathbf{g} \cdot \mathbf{u}_k \\ = (\rho_k H_k + P_k) (\mathbf{u}^{Int} - \mathbf{u}_k) \cdot \mathbf{n}_k^{Int} \delta^{Int} \\ + \left(\mu_k \underline{\underline{S}}_k - \mathbf{Q}_k \right) \cdot \mathbf{n}_k^{Int} \delta^{Int} \end{aligned} \quad (2.13)$$

Moreover, this set of equations is accompanied by two jump conditions at the interface:

- Mass jump condition:

The mass transfer Γ_k of phase k at the interface is defined:

$$\Gamma_k = \rho_k (\mathbf{u}^{Int} - \mathbf{u}_k) \cdot \mathbf{n}_k^{Int} \delta^{Int} \quad (2.14)$$

One can note that:

$$\sum_k \Gamma_k = \sum_k \rho_k (\mathbf{u}^{Int} - \mathbf{u}_k) \cdot \mathbf{n}_k^{Int} \delta^{Int} = 0 \quad (2.15)$$

- Momentum jump condition:

$$\sum_k \left(\mathbf{u}_k \Gamma_k - \left(-P_k \underline{\underline{I}}_d + \mu_k \underline{\underline{S}}_k \right) \right) \mathbf{n}_k^{Int} = \sigma \mathbf{n}_k^{Int} \nabla^{Int} \cdot \mathbf{n}_k^{Int} - \nabla^{Int} \sigma \quad (2.16)$$

with ∇^{Int} the surface derivative operator along the interface. The term $\nabla^{Int} \sigma$ is considered equal to 0 in all this thesis since we are not dealing with Marangoni effects.

Since this method does not require adaptive unstructured grid, it has been chosen in this thesis for the simulation of two-phase flows. Different models are available to solve these equations. The most common are the single-fluid model and the two-fluid model (used in the NEPTUNE_CFD code). In the next sections, the conservation equations obtained within the scope of each model will be presented.

2.4.3 Single-fluid model

In the single-fluid model, it is assumed that the two phases reach the mechanical balance and have the same local average velocity. Therefore, mixture quantities are defined for the density, viscosity, velocity, pressure, enthalpy and temperature (referred as Φ) using the following expression:

$$\Phi = \chi_1 \Phi_1 + \chi_2 \Phi_2 \quad (2.17)$$

With Φ_k the quantity evaluated in phase k.

Therefore, with the jump conditions at the interface, the conservation equations described above become for an incompressible flow:

- The mass balance equation:

$$\nabla \cdot \mathbf{u} = 0 \quad (2.18)$$

- The momentum balance equation:

$$\frac{\partial}{\partial t} (\rho \mathbf{u}) + \nabla \cdot (\rho \mathbf{u} \otimes \mathbf{u}) = -\nabla P + \nabla \cdot (\mu \underline{\underline{S}}) + \rho \mathbf{g} + \nabla^{Int} \cdot \mathbf{n}^{Int} \sigma \mathbf{n}^{Int} \delta^{Int} \quad (2.19)$$

with $\underline{\underline{S}}_{ij} = \frac{\partial u_i}{\partial x_j} + \frac{\partial u_j}{\partial x_i}$. The term $-\frac{2}{3} \frac{\partial u_i}{\partial x_i} \delta_{ij}$ in the viscous stress tensor disappear since the flow is considered incompressible.

- The energy balance equation:

$$\begin{aligned} \frac{\partial}{\partial t} (\rho H) + \nabla \cdot (\rho H \mathbf{u}) = & -\nabla \cdot \mathbf{Q} + \nabla \cdot (\mu \underline{\underline{S}} \cdot \mathbf{u}) + \rho \mathbf{g} \cdot \mathbf{u} \\ & + \frac{\partial P}{\partial t} + E^{Int} \end{aligned} \quad (2.20)$$

with E^{Int} the energy transfer at the interface.

With the one-fluid model, an extra equation is required to evaluate the volume average of the phase indicator function (*ie* the volume of fluid) which is necessary to define the mixture density and viscosity. This is the role played by the interface tracking methods presented in the next section.

2.4.4 Interface tracking methods

When the flow contains two continuous fields, an adding issue to the resolution of the Navier-Stokes' equations is the location of the interface. Choosing the method to track the interface relies on two parameters. First, the interface must be as thin as possible to be close to the physical situation. Secondly, the numerical solver has to stay stable, which encourages the work on smeared interfaces. In this section, the most widespread methods for interface tracking are described.

A first approach, called Front-Tracking (FT), has been developed by Unverdi and Tryggvason [203]. Computational points are connected together to form a one dimensional front (for two dimensional simulations) which represents the interface. Due to the interface deformation, some points are regularly added or deleted to ensure a constant distance between each point. Interface disconnections or reconnections are allowed when the distance of the two interfaces are on the order of a cell size. Then, in order to match the Eulerian fix grid with the moving Lagrangian interface, the interface presence is projected on the Eulerian grid. An advantage of this method is the control of numerical diffusion since the thickness of the interface is imposed by the discrete delta function which is not directly advected. Nevertheless, this method suffers from implementation difficulties, in particular in 3D, when connections and rupture of interfacial structures have to be managed. In addition, these methods are *a priori* not volume conservative as they rely on a linear element approximation of the real interface shape. An illustration of this method is proposed in Figure 2.4.

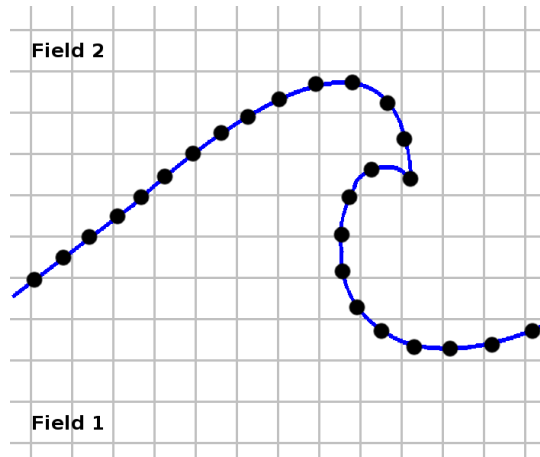


Figure 2.4: Schematic view of a Front-Tracking method on a moving interface.

For incompressible two-phase flows, the Volume Of Fluid (VOF) method has been

widely used. In this method, the interface presence is located by a color function C which corresponds to the volume fraction in each cell [71]. The function is in the range 0 and 1 depending on the field present in the cell and 0.5 at the interface. The mixture density is then defined as:

$$\rho = C\rho_1 + (1 - C)\rho_2 \quad (2.21)$$

The same expression is used for the definition of the other mixture quantities. Figure 2.5 gives a schematic representation of this method. To update C , the following advection equation is solved at each time step:

$$\frac{\partial C}{\partial t} + \mathbf{u} \cdot \nabla C = 0 \quad (2.22)$$

The interface is then reconstructed from this function. Different schemes are available. The Piecewise Linear Interface Construction (PLIC) proposed by Youngs [220] approximates the interface with segments (see Figure 2.5). This method was used by Larocque [95] to simulate turbulent two-phase flows with large interfaces. Welch and Wilson [212] also chose this method for the simulation of flows with phase change. The main advantage of the VOF method is mass conservation. Nevertheless, since the color function is sharp, it does not allow an accurate numerical evaluation of local normals and curvatures of interfaces, that are in fact gradients and Laplacians of the VOF function C . Specific additional functions that depend on C are required, such as height functions [152] or smooth VOF [61], to accurately calculate normal and interface curvatures.

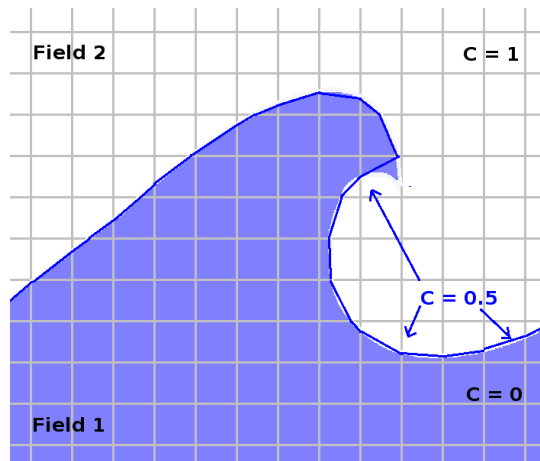


Figure 2.5: Schematic view of a moving interface followed with a VOF-PLIC method.

Lately, the Level-Set (LS) method has become popular. To locate the interface, a Level-Set function Φ is defined and corresponds to a signed distance function [190]. The zero contour is used to track the interface. The mixture density is then defined as:

$$\rho = \Phi\rho_1 + (1 - \Phi)\rho_2 \quad (2.23)$$

The same expression is used for the definition of the other mixture quantities. An illustration is given in Figure 2.6. An advection equation is solved to update the Level-Set function:

$$\frac{\partial \Phi}{\partial t} + \mathbf{u} \cdot \nabla \Phi = 0 \quad (2.24)$$

Contrary to the VOF method, the Level-Set approach does not ensure mass conservation. Nevertheless, high order of accuracy are difficult to reach due to the hyperbolic character of the Level-Set and the distance property that is lost as soon as the advection equation on the Level-Set is discretized and solved. Thus, Olsson and Kreiss [146] proposed to add an artificial compression of the interface to improve mass conservation (see section 3.4.3 for details). However, the disadvantages of mass conservation procedures is that they destroy the signed distance properties of Φ . Redistance algorithms also exist to fix this drawback.

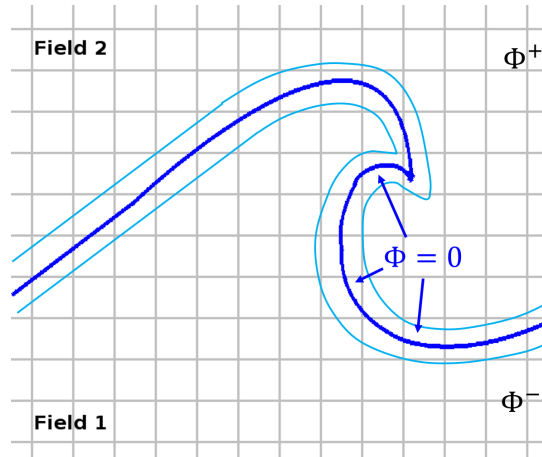


Figure 2.6: Schematic view of a Level-Set method on a moving interface, in green two isocontours of the Level-Set function Φ^+ and Φ^- are represented on each side of the interface.

To take advantage of the mass conservation property of the VOF method and the high order of accuracy of the Level-Set approach to calculate normals and curvatures of the interface, a coupled LS and VOF (CLSVOF) method has been developed. This has been done for example in [171].

To spare CPU when the flow contains interfaces, some Adaptive Mesh Refinement (AMR) methods can also be used [226]. Close to the interface, the mesh is more refined to gain in accuracy. But far from it, only a coarse grid is necessary to obtain a suitable result. This approach is particularly interesting when few interfaces are present in the flow and when the flow is laminar. It was for example used by Can and Prosperetti [25] to simulate a vapor bubble.

2.4.5 Two-fluid model

Bubbly flows occurring in nuclear power plants are often modeled with an Eulerian dispersed description within the two-fluid model of Ishii extended to n-phase [75]. This two-fluid model is implemented in the code NEPTUNE_CFD which is based on a finite volume approach.

2.4.5.1 Volumetric averaging

In the code NEPTUNE_CFD, volumetric averaging is used:

$$\langle \Phi \rangle_k = \frac{1}{\Omega_k} \int_{\Omega_k} \Phi d\Omega = \frac{1}{\Omega_k} \int_{\Omega} \chi_k \Phi d\Omega \quad (2.25)$$

and

$$\langle \chi_k \Phi \rangle = \frac{1}{\Omega} \int_{\Omega} \chi_k \Phi d\Omega \quad (2.26)$$

with Ω_k the volume occupied by the phase k and Ω the cell volume. The volume fraction of each phase α_k has the following expression:

$$\alpha_k = \langle \chi_k \rangle = \frac{1}{\Omega} \int_{\Omega} \chi_k d\Omega = \frac{\Omega_k}{\Omega} \quad (2.27)$$

Therefore, the volumetric average of Φ is given by:

$$\langle \chi_k \Phi \rangle = \alpha_k \langle \Phi \rangle_k \quad (2.28)$$

2.4.5.2 Conservation laws

After applying the volumetric averaging to the equations detailed in section 2.4.2, three balance equations, solved for each phase k are obtained (the brackets are implicit):

- The mass balance equation:

$$\frac{\partial}{\partial t} (\alpha_k \rho_k) + \nabla \cdot (\alpha_k \rho_k \mathbf{u}_k) = \sum_{p \neq k} \Gamma_{p \rightarrow k} \quad (2.29)$$

with α_k the volume fraction of phase k , ρ_k its density, \mathbf{u}_k its velocity field, $\Gamma_{p \rightarrow k}$ the interfacial mass transfer.

- The momentum balance equation:

$$\begin{aligned} \frac{\partial}{\partial t} (\alpha_k \rho_k \mathbf{u}_k) + \nabla \cdot (\alpha_k \rho_k \mathbf{u}_k \otimes \mathbf{u}_k) = & -\alpha_k \nabla P_k + \nabla \cdot \left(\alpha_k \left(\mu_k \underline{\underline{S}}_k + \underline{\underline{S}}_k^T \right) \right) \\ & + \sum_{p \neq k} I_{p \rightarrow k} + \alpha_k \rho_k \mathbf{g} + \alpha_k \underline{\underline{S}} e_k \end{aligned} \quad (2.30)$$

with $\nabla \cdot (\alpha_k \rho_k \mathbf{u}_k \otimes \mathbf{u}_k) = (\alpha_k \rho_k \mathbf{u}_k \cdot \nabla) \mathbf{u}_k$, $\underline{\underline{S}}_{ij,k} = \frac{\partial u_{i,k}}{\partial x_{j,k}} + \frac{\partial u_{j,k}}{\partial x_{i,k}} - \frac{2}{3} \frac{\partial u_{i,k}}{\partial x_i} \delta_{ij}$ the viscous stress tensor, $\underline{\underline{S}}_{ij,k}^T = -\rho_k \langle u'_i u'_j \rangle_k$ the turbulent stress tensor, $I_{p \rightarrow k}$ the interfacial momentum transfer and $\underline{\underline{S}}e_k$ external source terms.

- The energy balance equation:

$$\begin{aligned} \frac{\partial}{\partial t} (\alpha_k \rho_k H_k) + \nabla \cdot (\alpha_k \rho_k H_k \mathbf{u}_k) = & -\nabla \cdot (\alpha_k \mathbf{Q}_k) + \nabla \cdot (\alpha_k \mu_k \underline{\underline{S}}_k \cdot \mathbf{u}_k) \\ & + \alpha_k \frac{\partial P_k}{\partial t} + \alpha_k \rho_k \mathbf{g} \cdot \mathbf{u}_k \\ & + E_{p \rightarrow k}^{Int} + E'_{p \rightarrow k} \end{aligned} \quad (2.31)$$

with $H_k = e_k + \frac{1}{2} \mathbf{u}_k^2 + \frac{P_k}{\rho_k}$ the total enthalpy, $\mathbf{Q}_k = -\lambda_k \nabla T_k$ the conductive thermal flux, λ_k the thermal conductivity and T_k the temperature, $E_{p \rightarrow k}^{Int}$ the bulk interfacial heat transfer and $E'_{p \rightarrow k}$ other energy transfers.

Thus, contrary to the one-fluid model, the viscosity μ_k , the density ρ_k , the local velocity \mathbf{u}_k , the enthalpy H_k and the temperature T_k are defined for each phase in each cell of the whole domain.

Conservation of volume, mass, momentum and energy lead to four others equations:

$$\sum_k \alpha_k = 1 \quad (2.32)$$

$$\Gamma_{p \rightarrow k} + \Gamma_{k \rightarrow p} = 0 \quad (2.33)$$

$$I_{p \rightarrow k} + I_{k \rightarrow p} = \frac{1}{\Omega} \int_{Int} (\sigma \kappa^{Int} \mathbf{n}^{Int}) dS \quad (2.34)$$

$$E_{p \rightarrow k}^{Int} + E_{k \rightarrow p}^{Int} = 0 \quad (2.35)$$

The assumption of a common pressure for all phases is made: $\forall k, P_k = P$.

The different transfer terms for mass, momentum and energy which allow closing the system will be presented in the next chapter.

2.4.6 Numerical scheme

A Semi-Implicit Method for Pressure-Linked Equations (SIMPLE) solver is implemented in the code NEPTUNE_CFD [149]. A schematic view of this algorithm is proposed in Figure 2.7 for isothermal and incompressible test cases. Thus, no energy balance equation is solved. The equivalent scheme for non isothermal flows will be presented in Chapter 9.

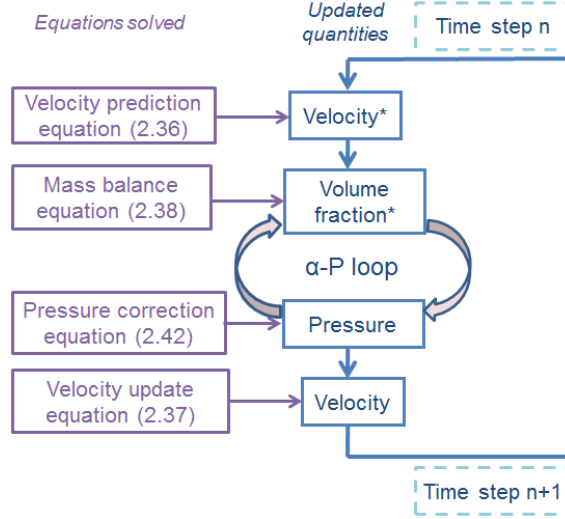


Figure 2.7: Schematic view of the numerical scheme in the code `NEPTUNE_CFD`, * denotes the intermediate values, the volume fractions and the pressure fields are obtained by solving the so called α -P loop.

When the simulation starts, the boundary conditions are set. Then, an intermediate value of the velocity field is evaluated by solving the momentum balance equation (Equation (2.30)) and neglecting the volume fractions and pressure variations ($\delta\alpha = \alpha_k^{n+1} - \alpha_k^n \rightarrow 0$ and $\delta P = P^{n+1} - P^n \rightarrow 0$):

$$\begin{aligned} \rho_k \frac{u_{i,k}^* - u_{i,k}^n}{\Delta t} + \frac{1}{\alpha_k^n} \left(\nabla \cdot (\alpha_k^n \rho_k u_{i,k}^n (u_{i,k}^* - u_{i,k}^n)) - (u_{j,k}^* - u_{j,k}^n) \nabla \cdot (\alpha_k^n \rho_k u_{i,k}^n) \right) = \\ -\nabla P^n + \frac{1}{\alpha_k^n} \nabla \cdot \left(\alpha_k^n (\mu_k + \mu_k^T) \left(\underline{\underline{S}}_k^* - \underline{\underline{S}}_k^n \right) \right) \\ + \rho_k g_i + \frac{1}{\alpha_k^n} I_{i,k} \end{aligned} \quad (2.36)$$

With $u_{i,k}^n$ the velocity field of phase k at time step n , $u_{i,k}^*$ the intermediate velocity field, $\underline{\underline{S}}_k^*$ the viscous stress tensor obtained with the intermediate velocity $u_{i,k}^*$ and μ_k^T the dynamic eddy viscosity (see Chapter 13).

Using this intermediate velocity field, the volume fractions and the pressure fields are both iteratively determined within the so-called α -P loop briefly described below to ensure mass conservation. At the beginning of the loop, the iteration number q is equal to 0 and $\alpha_k^{(0)} = \alpha_k^n$, $P^{(0)} = P^n$. Then, for each iteration q , the modified mass balance equation (2.38) is solved. To obtain this equation, the velocity field appearing in the mass balance equation (2.29) is replaced using the momentum balance equation (2.30) and neglecting the convective and diffusive terms (see Equation (2.37)).

$$\rho_k \frac{u_{i,k}^{n+1} - u_{i,k}^*}{\Delta t} = -C_k \nabla (\delta P) - \frac{D_k}{\alpha_k^n} \nabla (\delta \alpha_k) \quad (2.37)$$

With C_k a positive coefficient which obeys $\sum_k \alpha_k^n C_k = 1$ and D_k a positive coefficient non zero only when we are dealing with dispersed fields [60, 123]. If we are only taking into account the drag force, the coefficient C_k can be written: $C_k = \frac{\rho_1 \rho_2 + C_D \rho_k \Delta t}{\rho_1 \rho_2 + C_D (\alpha_1 \rho_1 + \alpha_2 \rho_2) \Delta t}$, with C_D the drag force coefficient. This way, we obtain the mass correction equation:

$$\rho_k \frac{\alpha_k^{(q)} - \alpha_k^n}{\Delta t} + \nabla \cdot \left(\alpha_k^{(q)} (\rho_k u_{i,k,conv}^* - \Delta t C_k \partial_{x_j} (\delta P^{(q-1)})) - \Delta t D_k \nabla \alpha_k^{(q)} \right) = \Gamma_k^{(q-1)} \quad (2.38)$$

With α_k^n the volume fraction of phase k at time step n, $\alpha_k^{(q)}$ the volume fraction at iteration q of the α -P loop, $u_{i,k,conv}^* = u_{i,k}^* + \delta t \frac{D_k}{\rho_k \alpha_k^n} \nabla \alpha_k^n$ the convection velocity, $\delta P^{(q-1)} = P^{(q-1)} - P^n$ the pressure increment.

Then, to update the pressure field, a correction equation (2.42) is solved. To obtain this equation, Equations (2.38) and (2.39) are subtracted. Then, the obtained equation is sum up over all the phases k. Finally, two approximations (2.40) and (2.41) are considered.

$$\rho_k \frac{\alpha_k^{n+1} - \alpha_k^n}{\Delta t} + \nabla \cdot (\alpha_k^{n+1} (\rho_k u_{i,k,conv}^* - \Delta t C_k \nabla (\delta P)) - \Delta t D_k \nabla \alpha_k^{n+1}) = \Gamma_k \quad (2.39)$$

$$\rho_k (\alpha_k^{n+1} - \alpha_k^{(q)}) \simeq \frac{\alpha_k^{(q)}}{c_k^2} (\delta P - \delta P^{(q-1)}) + \rho_k (\alpha_k^{n+1} - \alpha_k^{(q)}) \quad (2.40)$$

with c_k^2 a positive variable homogeneous to a velocity.

$$\Gamma_k^{n+1} - \Gamma_k^{(q-1)} \simeq \partial_P \Gamma_k (\delta P - \delta P^{(q-1)}) \quad (2.41)$$

$$\sum_k \left(\frac{\alpha_k^{(q)}}{\rho_k c_k^2 \Delta t} - \frac{1}{\rho_k} \partial_P \Gamma_k \right) \delta W + \sum_k \left(\frac{1}{\rho_k} \nabla \cdot (-\Delta t \alpha_k^{(q)} C_k \nabla (\delta W)) \right) = \frac{1}{\Delta t} \left(\sum_k \alpha_k^{(q)} - 1 \right) \quad (2.42)$$

With $\delta W = \delta P - \delta P^{(q-1)}$.

At the end, the velocity field is updated with respect to the pressure correction δP and the volume fraction increment $\delta \alpha_k$ (only for the dispersed fields) using Equation (2.37). More details about the numerical scheme of the code NEPTUNE_CFD can be found in [60, 123].

The data structure is face-based to allow simulations on arbitrary-shaped cells including non-conforming meshes. The simulations are performed on fixed grids with collocated variables.

Chapter 3

Multifield approach

After explaining the motivation to consider a multifield approach, this chapter presents the interfacial momentum transfers for the dispersed fields and the continuous fields. The treatment of the mass transfers between the continuous and the dispersed field of the same phase are also explained.

3.1 Résumé du chapitre

Les approches de type 1-fluide permettent de simuler avec précision les interfaces larges. Pour simuler des écoulements contenant des inclusions de taille très variées avec ces approches, il est nécessaire de raffiner le maillage au vu de la plus petite inclusion présente dans l'écoulement. Cependant, dans le cas d'applications industrielles, les maillages générés seraient beaucoup trop coûteux en temps de calcul voire impossible à faire tourner. De leur côté, les modèles bi-fluide ont pour objectif la simulation d'écoulements bouillants contenant des petites bulles dispersées dans une phase porteuse. Néanmoins, les modèles dispersés peuvent générer d'importants niveaux d'erreur dès que l'écoulement contient de grandes poches déformables. Les deux approches présentent donc de nombreux avantages mais ne peuvent pas simuler avec précision et un temps de calcul raisonnable des écoulements contenant des inclusions avec une grande variété de tailles et de formes. Pour répondre à cette problématique, ce chapitre présente un modèle multi-champ qui sera utilisé dans la thèse. Ce modèle est basé sur une approche bi-fluide pour la simulation des petites bulles sphériques, considérées comme un champ dispersé. Les grandes poches déformables sont, elles, considérées comme des interfaces entre deux champs continus. De ce fait, un écoulement diphasique eau/vapeur est scindé en trois champs: un champ continu liquide, un champ dispersé gaz contenant les petites bulles sphériques et un champ continu gaz présent dans les grosses poches déformables. Les différentes forces qui s'appliquent à ces structures sont détaillées. Les transferts isothermes entre le champ continu gaz et le champ dispersé gaz dus au fractionnement et à la coalescence des bulles sont également traités.

3.2 Concept and motivations

There are several approaches for two-phase flow modeling, describing the interfaces either with a dispersed or a located point of view. Bubbly flows are often modeled with an Eulerian dispersed approach within the two-fluid model of Ishii [75]. An ensemble average description of the inclusions is done with a given volume fraction of gas and an average diameter in each grid cell. The average momentum balance equation is in this case closed with a set of interfacial forces, based on empirical or statistical correlations. Nevertheless, this approach is limited to bubbles in the spherical or slightly ellipsoidal assumption. One can remark that Lagrangian tracking of point particle bubbles or droplets also exist. However, these approaches are not used for industrial applications as they induce a too large numerical cost. These techniques are restricted to academic configurations of dispersed two-phase flows.

On the other hand, large interfaces are located using interface tracking methods within the one-fluid model. Interfacial transfers in the momentum balance equation are modeled thanks to local quantities such as the curvature and the unit normal vector to the interface.

Some research groups have been working on the transition regimes between bubbly and separated flows. The necessity of a multifield approach has been highlighted in different works [5, 15, 41]. In the four fields and two-fluid model, each phase is split into a dispersed and a continuous field. A spatial cutting length is defined to distinguish the modeled structures and the simulated ones.

This concept allows the simulations of a wide range of two-phase flows regimes with both a good accuracy on the behavior of the most distorted interfacial structures and less CPU consumption than the direct simulation of all the two-phase scales.

In this thesis, the multifield approach implemented in the code `NEPTUNE_CFD` and based on the two-fluid model is used [38]. With this model, a complex two-phase flow containing small spherical and large deformable bubbles in a liquid bulk is split into three fields: continuous liquid, dispersed gas and continuous gas. The small spherical bubbles are defined as a dispersed field whereas the large deformable bubbles are considered as interfaces between a continuous liquid field and a continuous gas field. An illustration is proposed in Figure 3.1. In the two-fluid model, the k index appearing in the conservation equations (2.29), (2.30) and (2.31) does not refer anymore to the phase but to the field. In the three field approach, these equations are solved three times: one time for each field.

By using the code `NEPTUNE_CFD` and the two-fluid model, the choice has been made to use an Eulerian description for the small spherical bubbles, as also done in [42, 64, 98, 204]. Nevertheless, some research groups have chosen to use a Lagrangian description of the dispersed fields composed of small spherical droplets within the multifield approach for the simulation of atomization spray [17, 227]. Finally, some researcher have developed a multifield approach based on one-fluid models with a Lagrangian description of the small spherical inclusions. We can cite

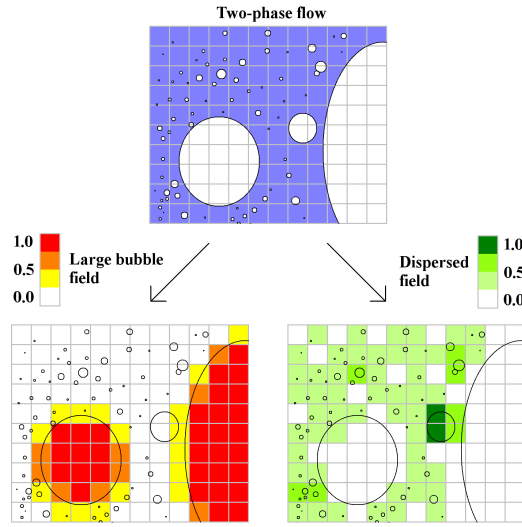


Figure 3.1: Schematic view of the three field model applied to a two-phase flow containing a continuous liquid phase with bubbles of different diameters, the continuous gas field corresponds to the red scale on the left and the dispersed gas field to the green scale on the right, [38].

the works of Capecelatro *et al.* [26], Herrmann [69] and Zuzio and Estivaleres [226] with the Level-Set method and Tomar *et al.* [195] and Ling *et al.* [108] with the VOF method.

Since we are dealing with three different fields, the interfacial momentum transfer terms required for each field have to be examined. The models for the dispersed fields with the two-fluid model have been widely studied and validated in the code NEPTUNE_CFD [40, 127, 132] and are currently at the state of the art. The modeling effort is then focused on the large interfaces formed by two continuous fields. An approach, called the Large Interface Model (LIM), is already available in the CMFD tool to simulate large interfaces within the two-fluid model. A short description of the model is proposed in Appendix F. Nevertheless, at the beginning of the thesis work, this model was not coupled to the dispersed fields. Therefore, a specific model, called the Large Bubble Model (LBMo), has been developed for the simulation of large interfaces within the multifield approach. The LIM will only be used as a comparison model to validate the LBMo on large interface simulations since the LIM is a model devoted to such simulations. In all this work, the LIM simulations are performed using the interface sharpening equation detailed in this thesis work since the model does not include a recompression step. Finally, it has to be noted that a multifield approach has been recently proposed by M erigoux *et al.* in [124] based on the LIM.

3.3 Model for the dispersed field

Four forces are taken into account for the interfacial momentum transfers applied to the dispersed field. These closure laws have been validated in the NEPTUNE_CFD code on industrial test cases [40, 127, 132] and are currently at the state of the art.

3.3.1 Drag force

This force corresponds to the force exerted by the fluid on an obstacle in the direction of the flow. The expression proposed by Ishii [76] is used for bubbles with small deformations:

$$\mathbf{F}_{Drag,cl \rightarrow dg} = -\frac{1}{8} A_i \rho_{cl} C_D \|\mathbf{u}_{dg} - \mathbf{u}_{cl}\| (\mathbf{u}_{dg} - \mathbf{u}_{cl}) \quad (3.1)$$

The subscript cl refers to the continuous liquid field and dg to the dispersed gas field. A_i corresponds to the interfacial area. The drag coefficient C_D is given by:

$$C_D = \frac{2}{3} d_{dg} \sqrt{\frac{g|\rho_{dg} - \rho_{cl}|}{\sigma}} \left(\frac{1 + 17.67(1 - \alpha_{dg})^{9/7}}{18.67(1 - \alpha_{dg})^{3/2}} \right) \quad (3.2)$$

with d_{dg} the bubble diameter.

3.3.2 Lift force

The lift force corresponds to the fluid force component that is perpendicular to the flow. Its expression is given below:

$$\mathbf{F}_{Lift,cl \rightarrow dg} = -C_L \alpha_{dg} \rho_{cl} (\mathbf{u}_{dg} - \mathbf{u}_{cl}) \otimes (\nabla \otimes \mathbf{u}_{cl}) \quad (3.3)$$

For spherical bubbles, the coefficient C_L is taken equal to 0.5. For deformed bubbles, the value of the coefficient depends on a modified Eötvös number proposed by Tomiyama [196]:

$$E_{oH} = \frac{g(\rho_{dg} - \rho_{cl}) d_H^2}{\sigma} \quad (3.4)$$

with $d_H = d_{dg} \sqrt[3]{1 + 0.163 E_o^{0.757}}$, d_{dg} the maximum vertical dimension of the bubbles and $E_o = \frac{d_{dg}^2 \Delta \rho g}{\sigma}$ the Eötvös number [213].

Then, if $E_{oH} < 4$:

$$C_L = \min(0.288 \tanh(0.121 Re), 0.00105 E_{oH}^3 - 0.0159 E_{oH}^2 - 0.0204 E_{oH} + 0.474) \quad (3.5)$$

if $4 < E_{oH} < 10$:

$$C_L = 0.00105 E_{oH}^3 - 0.0159 E_{oH}^2 - 0.0204 E_{oH} + 0.474 \quad (3.6)$$

if $E_{oH} > 10$:

$$C_L = -0.27 \quad (3.7)$$

The larger the modified Eötvös number is, the more ellipsoidal the dispersed bubbles are.

3.3.3 Added mass force

The added mass force refers to the acceleration of the dispersed field which introduces a force on the fluid in motion. Its expression is given by [225]:

$$\mathbf{F}_{Mass,cl \rightarrow dg} = -C_A \frac{1 + 2\alpha_{dg}}{1 - \alpha_{dg}} \alpha_{dg} \rho_l \frac{du_r^{dg,l}}{dt} \quad (3.8)$$

where:

$$\frac{du_r^{dg,l}}{dt} = \left(\frac{\partial \mathbf{u}_{dg}}{\partial t} + \mathbf{u}_{dg} \cdot \nabla \mathbf{u}_{dg} \right) - \left(\frac{\partial \mathbf{u}_{cl}}{\partial t} + \mathbf{u}_{cl} \cdot \nabla \mathbf{u}_{cl} \right) \quad (3.9)$$

The value of the coefficient C_A is fixed at 0.5 corresponding to its value for spherical bubbles.

3.3.4 Turbulent dispersion force

This force corresponds to the interaction between turbulence and bubbles. For example, in a dispersed multiphase flow, turbulence in the continuous field causes particles in the dispersed field to be transported from regions of high concentration to regions of low concentration. The applied turbulent dispersion force is expressed as:

$$\mathbf{F}_{Turb,cl \rightarrow dg} = -\mathbf{F}_{Turb,dg \rightarrow cl} = -GTD \rho_{cl} k_{cl} \nabla \alpha_{dg} \quad (3.10)$$

with k_{cl} the turbulent kinetic energy of the continuous liquid field.

Most of the time, GTD is an adjustable parameter in the literature. Following Haynes [68], Lavieville *et al.* [97] have recently proposed the following formula:

$$GTD = (F_D \tau_{lg}^t - 1) \frac{b + \eta_r}{1 + \eta_r} + C_A \frac{b^2 + \eta_r}{1 + \eta_r} \quad (3.11)$$

with $F_D = -\frac{1}{8} A_i \frac{1}{\alpha_{dg}} C_D \|\mathbf{u}_{dg} - \mathbf{u}_{cl}\|$.

τ_{lg}^t is the Lagrangian time scale of the fluid turbulence along particle trajectories defined by:

$$\tau_{lg}^t = \frac{3}{2} C_\mu \frac{k_{cl}}{\epsilon_{cl}} \left(1 + \beta \frac{(\mathbf{u}_{dg} - \mathbf{u}_{cl})^2}{k_{cl}} \right)^{-\frac{1}{2}} \quad (3.12)$$

with β a constant value equal to 2.7.

η_r is defined by $\eta_r = \frac{\tau_{lg}^t}{\tau_{lg}^F}$ with:

$$\tau_{lg}^F = \frac{1}{F_D} \left(\frac{\rho_{dg}}{\rho_{cl}} + C_A \right) \quad (3.13)$$

$$b = \frac{\rho_{cl} + \rho_{cl}C_A}{\rho_{dg} + \rho_{cl}C_A} \quad (3.14)$$

3.3.5 Interfacial area transport equation

When mentioned in the text, an interfacial area transport equation is solved to evaluate an average diameter of the dispersed field in each cell. Different approaches are available to model coalescence and breakup in the dispersed approach. Among others, we can cite the works of Ruyer and Seiler [178] and Liao *et al.* [105]. A critical review of several coalescence / breakup models for isothermal test cases can be found in [137]. In this thesis, the Ruyer-Seiler model [178] is chosen since it allows obtaining a more accurate prediction in boiling flows when condensation and evaporation of the dispersed field occur.

3.4 Model for the large interfaces: Large Bubble Model (LBMo)

The presence of large interfaces in a flow requires special treatments such as the interface location and the application of local closure laws.

3.4.1 Drag force

In the two-fluid model, the drag force is crucial (see Appendix A). Contrary to the single-fluid approach, with this model, two different velocities are defined, one for each phase. Therefore, at the interface, these two velocities have to be coupled. The drag force corresponds to the coupling term between these velocities at the interface. In the first instance, the expression used in the code NEPTUNE_CFD is [38]:

$$\mathbf{F}_{Drag,cl \rightarrow cg} = \frac{\alpha_{cl}\alpha_{cg}(\mathbf{u}_{cl} - \mathbf{u}_{cg})(\alpha_{cl}\rho_{cl} + \alpha_{cg}\rho_{cg})}{\tau} \quad (3.15)$$

with $\tau = \frac{\Delta t}{100}$ and Δt the time step. Nevertheless, with this expression, the drag force depends on the time step. Therefore, if the simulation is performed with a variable time step, the intensity of the drag force will vary during the simulation. A first modification was made by using a constant value for τ equal to 1.10^{-7} s. This value corresponds to the lowest value used for τ in its previous definition.

A simulation of the experiment of Raymond and Rosant [155] has been performed in [38] with this drag force. The rise of an air bubble in liquids with different viscosities has been studied in terms of bubble final velocities and bubble aspect ratios (ratio between the maximum vertical dimension h and maximum horizontal

3.4. MODEL FOR THE LARGE INTERFACES: LARGE BUBBLE MODEL (LBMO)

dimension w). The name and properties of the fluids for each simulation are reported in Table 3.1. The results are compared with the experimental data in Figures 3.2 and 3.3.

Simulation	Viscosity ($Pa \cdot s$)	Density ($kg.m^{-3}$)	Surface tension ($N.m^{-1}$)
S1	0.687	1250	0.063
S3	0.242	1230	0.063
S5	0.0733	1205	0.064
S6	0.0422	1190	0.064

Table 3.1: Properties of the fluids used in the experiments of Raymond and Rosant [155].

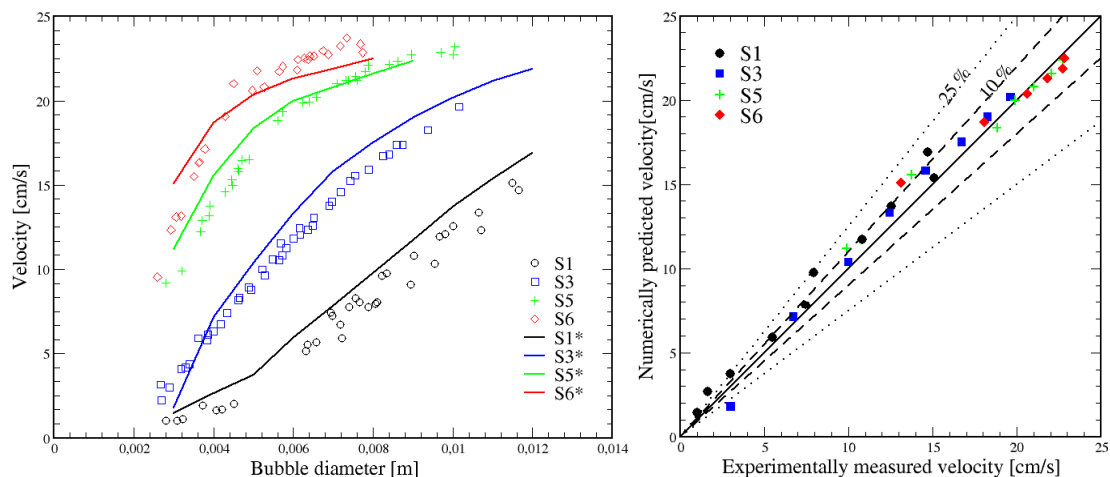


Figure 3.2: Comparison between the experimental data of Raymond and Rosant [155] (symbols) and the simulation results obtained with $\tau = \frac{\Delta t}{100}$ [38] (continuous lines) for the four simulations S1, S3, S5 et S6.

These figures show that higher relative errors are obtained especially for the prediction of the bubble shape for the simulations S5 and S6. The drag force has more difficulties to predict the correct bubble shape when the liquid has smaller viscosities. This corresponds to bubbles with a small aspect ratio, that is to say with an ellipsoidal shape. Therefore, in Chapter 6, a new expression for this drag force will be developed in order to take into account the fluid viscosities.

3.4.2 Surface tension

Another requirement for large interface simulations is the surface tension force [32] (see Appendix A). Because the interface has a finite thickness, the choice was

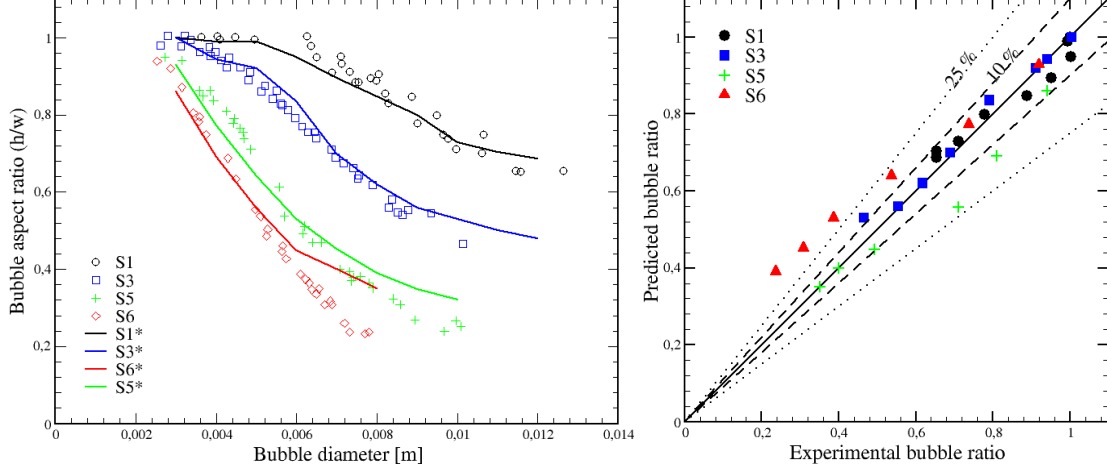


Figure 3.3: Comparison between the experimental data of Raymond and Rosant [155] (symbols) and the simulation results obtained with $\tau = \frac{\Delta t}{100}$ [38] (continuous lines) for the four simulations S1, S3, S5 et S6.

made to use the Continuum Surface Force (CSF) model proposed by Brackbill *et al.* [21]:

$$\mathbf{F}_{sta} = \sigma \kappa \nabla \alpha_k \quad (3.16)$$

with:

$$\kappa = -\nabla \cdot \left(\frac{\nabla \alpha_k}{\|\nabla \alpha_k\|} \right) \quad (3.17)$$

To calculate more precisely the curvature κ , the volume fractions are artificially smeared [38].

Since the momentum balance equation is solved for the two continuous fields in the two-fluid model, the force is split between these two fields. Therefore, the expression of the volumetric force becomes [13]:

$$F_{ST,k} = \beta_k \sigma \kappa \nabla \alpha_k \quad (3.18)$$

with $\sum \beta_k = 1$.

Bartosiewicz *et al.* [13] propose two different expressions for β_k , a mass and a volume formulation:

$$\beta_k = \frac{\alpha_k \rho_k}{\sum \alpha_i \rho_i} \quad (3.19)$$

or

$$\beta_k = \alpha_k \quad (3.20)$$

In [13], the two formulations have been compared with the simulation of the Kelvin-Helmholtz instability in the Thorpe's experiment [193]. The authors obtained

the same results in terms of wave aspect and wave numbers but gave restrictions for simulations with higher density ratios. Štrubelj [188] compared also the two formulations by simulating a pressure jump over a droplet interface. In this test case, the density ratio is large and the surface tension plays a dominant role. He showed that the differences between the two models were minimal but the volume averaging gave better results. Therefore, in this thesis, only the volume formulation will be considered.

3.4.3 Interface sharpening

The numerical spreading of the interface induced by the two-fluid model does not allow a sharp interface location (see Appendix A). Thus, different methods have been developed to limit the interface smearing. A first idea has been proposed by Xiao *et al.* [216] and is based on a hyperbolic tangent interpolation of the volume fraction at each time step. The Tangent of Hyperbola INterface Capturing (THINC) method has been applied to simulations within a VOF method and showed significant improvements of the interface location [74, 216, 217]. This method has been adapted to the two-fluid model [145] for the simulation of compressible flows. More recently, another interface sharpening technique has been developed based on the resolution of an anti-diffusion equation. Good results have also been obtained with a two-fluid modeling [183]. Hänsch *et al.* [64] proposed to add a clustering force in the momentum balance equation. This method avoids solving an extra equation and has been validated for the simulation of three field two-fluid test cases. Finally, Tiwari *et al.* [194] presented an extra equation for the volume fractions able to simulate accurately highly compressible flows and strong shock waves.

In the code NEPTUNE_CFD, a third interface sharpening method has been implemented. This technique, initially proposed by Harten [67] and then developed by Olsson and Kreiss [146] for the Level-Set method, is based on the resolution of a compression equation.

Harten [67] first introduced the following equation for the interface compression:

$$\frac{\partial \alpha_k}{\partial \tau} + \nabla \cdot g(\alpha_k) = \varepsilon \nabla \cdot (\nabla \alpha_k) \quad (3.21)$$

with τ an artificial time and $g(\alpha_k)$ the compression flux which has to be positive at the interface and zero everywhere else. The diffusion term $\varepsilon \nabla \cdot (\nabla \alpha_k)$ is added to prevent discontinuities at the interface.

Olsson and Kreiss [146] proposed the following expression for the compression flux:

$$g(\alpha_k) = \alpha_k (1 - \alpha_k) \mathbf{n} \quad (3.22)$$

The value of the coefficients τ and ε was proposed by Štrubelj [188]:

$$\varepsilon = \frac{\Delta x_{min}}{2} \quad \text{and} \quad \Delta \tau = \frac{\Delta x_{min}}{32} \quad (3.23)$$

$\Delta x_{min} = \min(\Omega^{\frac{1}{3}})$, Ω being the cell volume and the minimum value calculated over the computational domain. With these parameters, the final interface width is always equal to 5 cells whatever the initial interface diffusion.

Nevertheless, with this interface sharpening equation, Olsson and Kreiss [146] observed a slow mesh convergence with the rising air bubble test case. Therefore, they proposed to apply only the diffusion term in the normal direction of the interface since it could be balanced by the compressive term [147]. On a mathematical point of view, the term $\nabla \cdot (\nabla \alpha_k)$ was replaced by $\nabla \cdot (\nabla \alpha_k \cdot \vec{n}) \vec{n}$. However, Sato and Ničeno [170] showed that the method proposed by Olsson *et al.* induced interface deformations even after the correction proposed in [147]. Therefore, they modified the equation as follows:

$$\frac{\partial \alpha_k}{\partial \tau} + \beta \nabla \cdot (\alpha_k (1 - \alpha_k) \vec{n}) = \beta \epsilon \Delta \alpha_k \quad (3.24)$$

$$\text{with } \beta = \begin{cases} \beta_{min} & \text{for } \alpha_k \leq 0 \\ \frac{1 - \beta_{min}}{\alpha_{sat}} \alpha_k + \beta_{min} & \text{for } 0 < \alpha_k < \alpha_{sat} \\ 1 & \text{for } \alpha_k \geq \alpha_{sat} \end{cases}$$

Different validation test cases were used to validate this approach and to tune the value of the two parameters β_{min} and α_{sat} which were found equal to 0.01 and 2 respectively.

A simulation of a rising air bubble in [38] with the equation proposed by Sato and Ničeno, highlighted non physical bubble fragmentations which were not observed with the Olsson and Kreiss' equation. Therefore, the Olsson and Kreiss' equation (3.21) adapted to the two-fluid formulation has been implemented in the code NEPTUNE_CFD [38]. However, mass conservation issues have been observed. To solve this problem, a conservative implementation of the equation will be presented in Chapter 4.

3.5 Model for the badly resolved structures

In a real flow, the distinction between a large interface and a dispersed field can be difficult and requires a smooth transition. Therefore, a special treatment has been developed in the code NEPTUNE_CFD to deal with these so called badly resolved structures.

3.5.1 Detection

The detection of these structures is based on the criterion proposed by Maeda *et al.* [115] and applied by Pigny and Coste [150] to identify the resolved interfaces. This criterion is fixed at $8\Delta x$ and corresponds to the limit diameter of a spherical bubble to obtain an accurate curvature calculation with a collocated variables definition. Indeed, as shown in Figure 3.4, if a gradient of a scalar quantity such as the

phase function is estimated over an extended cell neighborhood on each part of the bubble, $8\Delta x$ is the limit diameter so that the compact support of the gradient calculation does not overlap. The criterion is thus based on numerical considerations.

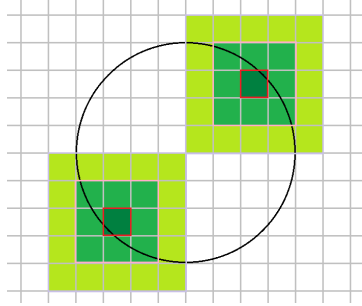


Figure 3.4: Schematic view in 2D of a bubble at the limit diameter of $8\Delta x$, the interface curvature is calculated in the two red highlighted cells, the gradient estimation is made over an extended cell neighborhood represented in green.

Therefore, the curvature of a bubble at the limit resolution is $\frac{1}{4\Delta x}$. Since the interface thickness after interface sharpening is equal to 5 cells, the second criterion for badly resolved structures is for cubic meshes:

$$\kappa \|\nabla \alpha_k\|_{\Omega} = \frac{1}{4\Delta x} \frac{1}{5\Delta x} \Delta x^3 = \frac{\Delta x}{20} \quad (3.25)$$

3.5.2 Treatment

Since these structures are not well resolved, they cannot be precisely located. Thus, the interface sharpening equation is not solved in cells containing badly resolved structures [38]. Moreover, the surface tension force is deactivated in these cells.

3.6 Transfer between the dispersed and the continuous gas fields

Two types of isothermal transfers have been studied: breakup and coalescence. In the first case, dispersed bubbles are created from the continuous field. The following expression for the corresponding mass transfer has been proposed by Denèfle in [38]:

$$\Gamma_{cg \rightarrow dg} = \alpha_{cg} \frac{\rho_g}{\Delta t} C_{cg \rightarrow dg} H \left(\kappa \|\nabla \alpha_{cg}\|_{\Omega} - \frac{\Delta x}{20} \right) \quad (3.26)$$

with H the Heaviside function and $C_{cg \rightarrow dg}$ a relaxation time modeling the fragmentation time scale. The transfer occur when the large inclusions can be considered badly resolved.

In case of coalescence, a part of the dispersed field is added to the continuous field. The criterion to consider this phenomenon is based on the volume fraction of the dispersed field. The critical volume fraction is fixed at 0.3 according to experimental observations of bubbly flows [57, 139, 191]. Thus, the following mass transfer term has been used by Denèfle in [38] et Hänsch *et al.* in [64]:

$$\Gamma_{dg \rightarrow cg} = \alpha_{dg} \frac{\rho_g}{\Delta t} C_{dg \rightarrow cg} H(\alpha_{dg} - 0.3) \quad (3.27)$$

with $C_{dg \rightarrow cg}$ a relaxation time modeling the coalescence time scale.

To take into account the possibility of having three fields (continuous liquid, continuous gas and dispersed gas) at the same time, the total mass transfer $\Gamma_{dg \rightarrow cg}^{Tot}$ appearing in the mass balance equation (2.29) is defined:

$$\Gamma_{dg \rightarrow cg}^{Tot} = \Gamma_{dg \rightarrow cg} - \Gamma_{cg \rightarrow dg} \quad (3.28)$$

with $\Gamma_{dg \rightarrow cg}^{Tot} + \Gamma_{cg \rightarrow dg}^{Tot} = 0$ (without phase change).

The model proposed here is a first approach to consider mass transfer between two fields coming from the same phase. Thus, it can be criticized at different levels. First, the criterion for the coalescence process is very empirical. An idea to improve this point could be to evaluate the sphericity of the dispersed inclusions using the Eötvös number (3.4). When the dispersed structures tends to deform, they are transferred in the continuous field. Moreover, still during the coalescence process, the diameter of the dispersed field is not taken into account. However, this information is significant especially if we want to ensure a conservation of the interfacial area or the volume. Concerning the fragmentation process, once more, no information are extracted from the resolved interface to predict the dispersed structures diameter. This could be done by considering the local curvature of the resolved interface.

Figure 3.5 summarizes the different criteria used to deal with mass transfer between the dispersed and the continuous gas fields.

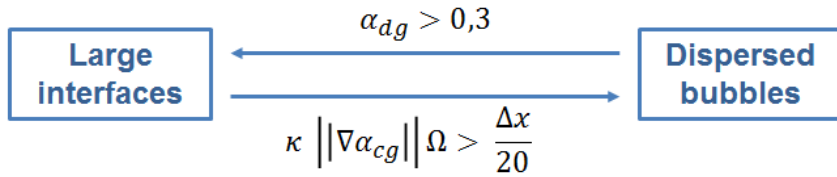


Figure 3.5: Summary of the criteria used to activate mass transfers between the continuous gas field and the dispersed gas field.

Thus, Chapter 10 and 11 are devoted to the study of these transfer terms and their improvement.

Chapter 4

Conservative implementation of the interface sharpening equation

The interface smearing induced by the two-fluid model decreases the accuracy of the large interfaces location. On the contrary, a sharp interface does not allow an accurate evaluation of the curvature. [38]. Therefore, an interface sharpening equation has to be implemented in the code to control the interface thickness (see section 3.4.3). However, special care has to be taken in the implementation of this interface sharpening equation to ensure mass conservation. This is currently one on the main drawback of most of the CMFD tools for which the recompression process induces mass losses. Thus, in this chapter, the different steps required to implement the interface sharpening equation in a conservative way are detailed. This conservative implementation has been validated with a large range of test cases from bubbly flows to interfacial liquid/liquid test cases. For clarity reasons, only one validation will be presented for each section. Readers are encouraged to go to Appendix B for complementary validations. All the laminar and isothermal flows considered in this chapter are simulated with continuous fields. No dispersed fields are considered since the interface sharpening equation is used for the simulation of large interfaces between two continuous fields.

This chapter has been presented at the 9th International Conference on Multiphase Flow (ICMF 2016, 22-27 May 2016) [49].

4.1 Résumé du chapitre

Le chapitre précédent présentait le Modèle Large Bulle (Large Bubble Model, LBMo en anglais) utilisé pour la simulation de grandes interfaces déformables. Ce modèle comprend trois éléments que sont la recompression d'interface, la force de tension de surface et une loi de traînée. Ce chapitre s'intéresse au premier élément, nécessaire pour contrôler l'épaisseur de l'interface. Cependant, dans sa forme originelle, l'implémentation de l'équation de recompression n'était pas conservative en masse. Par conséquent, une implémentation conservative est détaillée. Puis, différents critères sont introduits pour limiter l'ajout de vitesses parasites. Toutes

ces étapes sont validées avec des cas tests contenant de grandes interfaces dans des écoulements laminaires et isothermes. Aucun champ dispersé n'est considéré. Les champs sont tous continus. Cette configuration est également utilisée dans les trois chapitres suivants.

4.2 Formulation of the interface sharpening equation

To locate precisely interfaces within the two-fluid model, the interface sharpening equation, adapted from Olsson and Kreiss [146], is solved:

$$\frac{\partial \alpha_k}{\partial \tau} + \nabla \cdot \alpha_k (1 - \alpha_k) \mathbf{n} = \varepsilon \nabla \cdot (\nabla \alpha_k) \quad (4.1)$$

The interface sharpening equation is iteratively solved to ensure convergence of the prescribed interface thickness. The value of the coefficients τ and ε is chosen, as recommended in [188], to ensure an interface thickness equal to 5 cells:

$$\varepsilon = \frac{\Delta x_{min}}{2} \quad \text{and} \quad \Delta \tau = \frac{\Delta x_{min}}{32} \quad (4.2)$$

To illustrate the convergence of the equation and its ability to always obtain interfaces with 5 cells thickness, a bubble, with a diameter of 2 *cm*, is simulated in a still liquid with a square uniform Cartesian mesh of 5 *cm* side length. The interface is spread using the following diffusion equation, which is iterated either 10, 20 or 50 times before being sharpened with the interface sharpening equation (4.1):

$$\frac{\partial \alpha_k}{\partial \tau_1} = D_{diff} \nabla \cdot (\nabla \alpha_k) \quad (4.3)$$

with $\Delta \tau_1 D_{diff} = \frac{\Delta x_{min}^2}{4}$. With these parameters, the interface is spread over the same number of cells whatever the grid. In terms of distance, the interface is diffused on a smaller distance when the mesh is refined.

Thus, Figure 4.1 shows that, whatever the mesh refinement and the initial interface diffusion, the final interface has always a thickness of 5 cells. Only the iteration number of the interface sharpening equation varies according to the initial diffusion state. The extra iterations do not affect this thickness. The mesh refinement does not increase the iteration number required to reach the final interface thickness.

4.3 Conservative implementation

4.3.1 Numerical scheme

A conservative implementation of the interface sharpening step is crucial to ensure mass conservation in the simulations. Nevertheless, to ensure mass conservation, the numerical scheme has to be adapted. As we can see in Figure 4.2, the

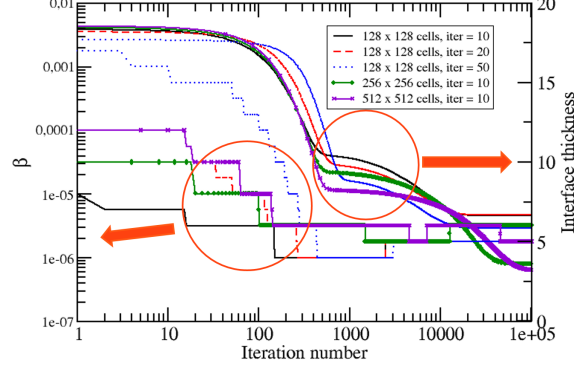


Figure 4.1: Effect of the interface sharpening equation on interfaces with different initial diffusions and on different grids, the left axis refers to the quantity β (defined in section 4.4), which represents the ratio between the volume variation of the interface after each iteration of the recompression equation and the initial interface volume, the interface thickness on the right axis is given in cell numbers, the X axis corresponds to the iteration number of the interface sharpening equation, iter refers to the iteration of the diffusion equation, the higher iter, the more diffused the initial interface, the orange circles and the arrows indicate which curves refer to which axes.

interface sharpening equation (4.6) is solved after the α -P loop. After solving the recompression equation, the volume fractions are updated. Mass fluxes are defined in this equation, which have to be considered to be consistent with the new volume fractions. These mass fluxes are taken into account in the next time step (time step $n+1$) as input of the α -P loop. Therefore, they do not modify immediately the velocity field, that is to say at time step n , since the pressure increment is not corrected after the resolution of the interface sharpening equation.

Thus, to ensure mass conservation, the recompression mass fluxes have to be added in the total mass fluxes. In other words, the total mass fluxes have to be corrected to include the recompression mass fluxes. To determine the expression of the corrected mass fluxes, we first consider the discretized mass balance equation solved in the α -P loop:

$$\rho_k \frac{\alpha_k^* - \alpha^n}{\Delta t} \Omega + \nabla \cdot (\rho_k \alpha_k^n \mathbf{u}_k^*) \Omega = 0 \quad (4.4)$$

with α_k^* the intermediate volume fraction evaluated in the α -P loop, α^n the volume fraction at time step n and Ω the cell volume.

Let us introduce the following notation for the mass flux term $\sum_{ij} \alpha_{ij} \phi_{ij} A_{ij} = \nabla \cdot (\rho_k \alpha_k^n \mathbf{u}_k^*) \Omega$, such that the discretized mass balance equation can be written simply as a sum between an unsteady term and a mass flux term:

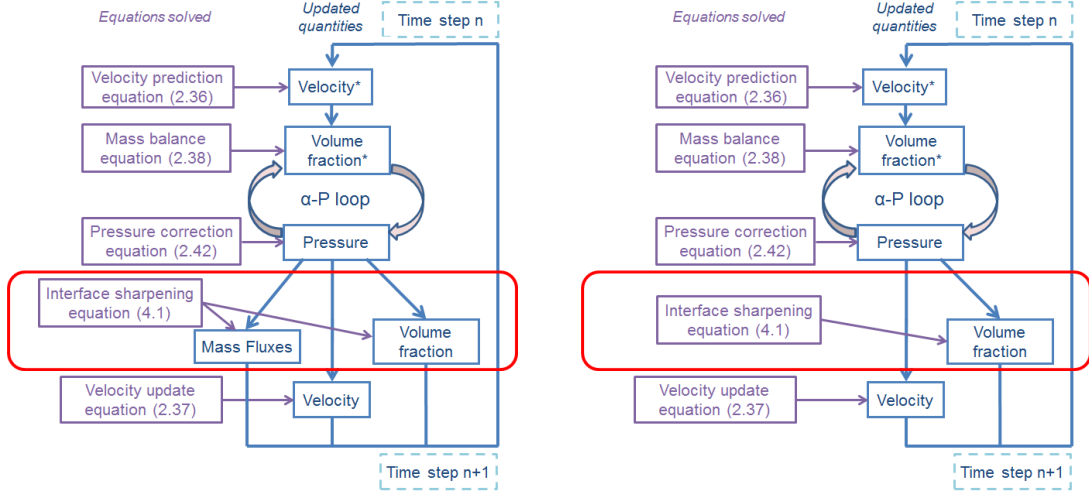


Figure 4.2: Schematic view of the numerical scheme used in the code NEPTUNE_CFD, left: conservative implementation of the interface sharpening equation, right: non conservative implementation, * denotes the intermediate values.

$$\rho_k \frac{\alpha_k^* - \alpha_k^n}{\Delta t} \Omega + \sum_{ij} \alpha_{ij} \phi_{ij} A_{ij} = 0 \quad (4.5)$$

with ϕ_{ij} the value at the cell faces, \sum_{ij} the sum over the cell faces, A_{ij} the face area and $\sum_{ij} \alpha_{ij} \phi_{ij} A_{ij}$ the intermediate mass fluxes evaluated in the α -P loop.

After the α -P loop, the interface sharpening equation is solved using the intermediate volume fraction α_k^* . The discretized interface sharpening equation can also be expressed as a sum between an unsteady term and a mass flux term:

$$\frac{\alpha_k^{n+1} - \alpha_k^*}{\Delta \tau} \Omega + \sum_{ij} \psi_{ij} A_{ij} = 0 \quad (4.6)$$

with $\sum_{ij} \psi_{ij} A_{ij} = (\nabla \cdot \alpha_k^* (1 - \alpha_k^*) \mathbf{n}^* - \varepsilon \nabla \cdot (\nabla \alpha_k^*)) \Omega$ the compressive and diffusive fluxes defined in the interface sharpening equation (4.1) and calculated using an upwind scheme.

The mass balance equation (4.5) allows obtaining an intermediate volume fraction α_k^* , which is used to solve the interface sharpening equation (4.6). After the sharpening step, the volume fraction is updated and equal to α_k^{n+1} . Then, the mass fluxes evaluated in the interface sharpening equation have to be added in the total mass fluxes such that:

$$\rho_k \frac{\alpha_k^{n+1} - \alpha_k^n}{\Delta t} \Omega + \sum_{ij} \alpha'_{ij} \Phi_{ij} A_{ij} = 0 \quad (4.7)$$

with $\sum_{ij} \alpha'_{ij} \Phi_{ij} A_{ij}$ the corrected mass fluxes, which take into account the inter-

mediate mass fluxes $\sum_{ij} \alpha_{ij} \phi_{ij} A_{ij}$ and the mass fluxes of the interface sharpening equation $\sum_{ij} \psi_{ij} A_{ij}$:

$$\sum_{ij} \alpha'_{ij} \Phi_{ij} A_{ij} = \sum_{ij} \alpha_{ij} \phi_{ij} A_{ij} + \frac{\rho_k \Delta \tau}{\Delta t} \sum_{ij} \psi_{ij} A_{ij} \quad (4.8)$$

In a non conservative implementation, the total mass fluxes are not calculated at the end of time step n . Only the mass fluxes evaluated in the mass balance equation are used to predict the velocity field at time step $n+1$ (see Figure 4.2 right). The volume fractions α_k^{n+1} at the beginning of time step $n+1$ are not consistent with the value of the mass fluxes, which induces large discrepancies on mass conservation. This is a major drawback of most of CMFD tools using a recompression equation.

4.3.2 Effect of the conservative implementation on simulation results

To illustrate the quantitative effect of the conservative implementation, an oscillating bubble is simulated.

In this case, a bubble of air is stretched in a still liquid. We observe the relaxation of the bubble until it recovers a round shape (see Figure 4.3).

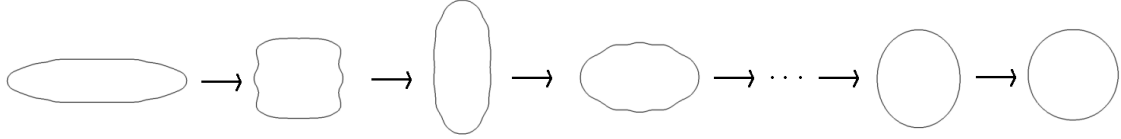


Figure 4.3: Pictures illustrating the evolution of the bubble shape over time, the bubble is intentionally more stretched than in the real simulation.

4.3.2.1 Theory

For small deformations, the interface position of a bubble with an initial radius of R_0 is given in polar coordinates by [93]:

$$R(\theta, t) = R_0 \left(1 + \tilde{\epsilon} \cos(2\theta) \cos(\omega_0 t) \exp\left(-\frac{t}{\tau_0}\right) \right) \quad (4.9)$$

with $\tilde{\epsilon}$ the initial perturbation of the bubble, θ the angular coordinate, ω_0 the oscillation frequency and τ_0 the characteristic time of decay due to viscous damping:

$$\omega_0^2 = \frac{6\sigma}{(\rho_{cl} + \rho_{cg}) R_0^3} \quad \text{and} \quad \tau_0 = \frac{R_0^2 (\rho_{cl} + \rho_{cg})}{4(\mu_{cl} + 3\mu_{cg})} \quad (4.10)$$

σ corresponds to the surface tension coefficient and R_0 to the final radius of the bubble equal to 1 cm.

4.3.2.2 Simulation

The properties of the air bubble and the liquid are given in Table 4.1 [24]. Surface tension coefficient is equal to 1.5 N.m^{-1} . The liquid viscosity is chosen higher than in the Caltagirone *et al.* paper [24] to limit the displacement of the bubble due to spurious velocities (see Chapter 5). With the fluid properties given in Table 4.1, the expected bubble frequency is equal to 5.71 s^{-1} and the characteristic time of decay to 4.37 s .

	Density (kg.m^{-3})	Viscosity (Pa.s)
Air bubble (subscript: <i>cg</i>)	1.17683	$1.85.10^{-5}$
Liquid (subscript: <i>cl</i>)	$7.0.10^3$	$4.0.10^{-2}$

Table 4.1: Properties of the gas and liquid phases for the simulation of the oscillating bubble.

The mesh used for this simulation is a square uniform Cartesian grid with 5 cm side length. Symmetry boundary planes are imposed everywhere. The bubble is initialized with an ellipsoidal shape and an initial perturbation $\tilde{\epsilon} = 0.05$, corresponding to a semi-minor axis equal to 0.95 cm and a semi-major axis of 1.05 cm . The oscillating bubble is simulated with two different meshes: 128×128 cells and 256×256 cells with a conservative implementation of the interface sharpening equation and a non conservative one. The time steps are constant and given in Table 4.2. Smaller values are used for the non conservative approach to ensure that the Courant–Friedrichs–Lewy (CFL) number is kept under 0.9.

Implementation of the interface sharpening equation	128 x 128 cells	256 x 256 cells
Conservative	0.5 ms	0.25 ms
Non conservative	0.05 ms	0.025 ms

Table 4.2: Time steps according to the mesh refinement and the implementation of the interface sharpening equation for the oscillating bubble test case.

The evolution of the major axis of the bubble is displayed in Figure 4.4. Irregularities on the curves corresponding to the non conservative implementation are observed. They are due to spurious oscillations of the bubble in diagonal directions. Moreover, the decay of the oscillation amplitude is quicker with the non conservative implementation. More quantitatively, in Table 4.3, the oscillation frequency and the characteristic time of decay are compared for the two grids and the two implementations of the interface sharpening equation with the results of Caltagirone *et al.* [24]. These two parameters are underestimated by the non conservative approach.

Mesh convergence study on this test case can be find in section 7.2 (Chapter 7).

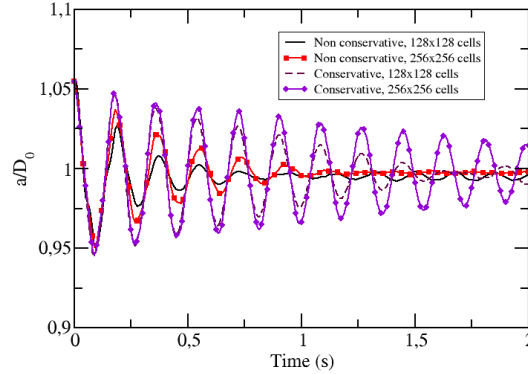


Figure 4.4: Evolution of the dimensionless bubble diameter over time for the oscillating bubble test case, the conservative and non conservative implementations of the interface sharpening equation are compared with the two grids 128 x 128 cells and 256 x 256 cells.

Mesh refinement	128 x 128 cells		256 x 256 cells	
	Conservative	Non conservative	Conservative	Non conservative
ω_0 (s^{-1})	5.56 (2.6 %) [4.95]	5.56 (2.6 %) [4.95]	5.68 (0.5 %) [4.99]	5.56 (2.6 %) [4.99]
τ_0 (s)	0.56 (87 %)	0.17 (96 %)	1.82 (58 %)	0.31 (93 %)

Table 4.3: Frequency ω_0 and characteristic time of decay τ_0 of the bubble oscillations according to the mesh refinement and the conservative implementation for an initial deformation rate of 0.05, the corresponding relative errors are given in brackets and the results of Caltagirone et al. [24] in square brackets.

Finally, concerning mass conservation, the mass balance error by time step in the whole domain is equal to 10^{-11} % with the non conservative approach and is reduced at 10^{-17} % with the conservative approach.

This study confirms that the non conservative implementation of the interface sharpening equation does not ensure mass conservation to almost computer error. Moreover, not considering the mass fluxes appearing in the recompression equation affects badly the simulations by decreasing the accuracy of the results.

4.4 Recompression threshold

4.4.1 Implementation of the criterion

Two main phenomena are in competition when the interface sharpening equation is solved. The first one is mass conservation which is ensured by the correction of the mass fluxes described in the previous section. The second one is the production of spurious velocities (added to those induced by the surface tension model) due to these mass fluxes, injected in the momentum balance equation. The objective of this part is then to find an equilibrium between these opposite contributions and to reach a favorable effect on the simulations in terms of mass conservation and limitation of the spurious velocities. Thus, we propose to introduce a recompression threshold which stops the resolution as soon as the final interface thickness is reached. As illustrated in Figure 4.1, up to a certain iteration number depending on the initial diffusion of the interface, the final thickness is reached. The extra iterations do not affect this thickness. This threshold allows limiting the quantity of mass fluxes added in the momentum balance equation for the prediction of the velocity field.

The recompression threshold is based on the ratio between the variation of the volume occupied by the interface and its initial volume: $\frac{\delta V^{Int}}{V^{Int}} < \beta$. Thus, the criterion is evaluated at the interface, where $\alpha_{cl}\alpha_{cg} > 0.02$ and has the following expression:

$$\sum_I^{ncel} \delta\alpha_k^I (1 - 2\alpha_k^I) \Omega^I < \beta^I \sum_I^{ncel} \alpha_{cl}^I \alpha_{cg}^I \Omega^I \quad (4.11)$$

with $\delta\alpha_k$ the volume fraction variation after each iteration of the interface sharpening equation. Since the equation is solved for each continuous field k in each cell, the criterion is applied for each continuous field in each cell.

In this expression, the term on the right-hand side $\sum_I^{ncel} \alpha_{cl}^I \alpha_{cg}^I \Omega^I$ denotes the volume occupied by the interface before the resolution of the interface sharpening equation. The term on the left-hand side $\sum_I^{ncel} \delta\alpha_k^I (1 - 2\alpha_k^I)$ evaluates its variation after each resolution of the interface sharpening equation. The recompression threshold β^I has the following expression:

$$\beta^I = \beta \frac{\Delta x^I}{\Delta x_{min}} \quad (4.12)$$

with β a constant which has the same value in the whole domain fixed for all the test cases. The recompression is then stopped when the variation of the interface volume tends to zero, which corresponds to a coefficient β^I equal to zero computer error. However, the conservative implementation of the interface sharpening equation induces a modification of the velocity field through the recompression mass fluxes (see section 4.3). Thus, if the equation is iterated many times, non zero mass fluxes

are constantly added and result in the definition of spurious velocities. The value of β has then to be optimized to have the following properties:

- It has to be small enough to stop the recompression only when the variation of the interface volume tends to zero.
- The interface thickness has to be equal to 5 cells when the recompression is stopped.
- It has to be large enough to limit the addition of spurious velocities.

The best choice for β according to Figure 4.1 corresponds to the first time the interface thickness is equal to 5 cells. The optimization is made by simulating a large range of test cases, as will be illustrated in the following section and Appendix B. Moreover, the recompression threshold is cell-dependent for unstructured grids. However, for uniform meshes, the threshold is equal to β since $\Delta x^I = \Delta x_{min}$. Indeed, the two parameters τ and ε are defined by using the minimum cell size Δx_{min} such that the final interface thickness is equal to 5 small cells. Therefore, with unstructured grids, the inclusions will be well resolved in regions where the cells are small. In the other regions where the cells are larger, the structures has to be considered less resolved. Thus, the recompression effort in these larger cells has to be smaller than in small cells. To take into account this requirement, the ratio $\frac{\Delta x^I}{\Delta x_{min}}$ is considered so that in larger cells the recompression threshold is higher, which stops the resolution of the interface sharpening equation earlier than in small cells. Validations of the efficiency of the interface sharpening equation and the recompression threshold with unstructured grids are proposed in Appendix C.

4.4.2 Optimization of the threshold β

To fix the threshold value β , simulations of the Bhaga and Weber's rising bubbles test case [16] are performed.

In this test case, an air bubble is rising up in viscous water. The simulation results are compared with the Bhaga and Weber's experimental data [16]. Two cases with two different liquid viscosities are simulated. They correspond to case b and case d in Bhaga and Weber's publication [16]. Their main characteristics are given in Table 4.4. Surface tension is equal to 0.0785 N.m^{-1} . Moreover, for the two cases:

$$\begin{aligned}\rho_{cl} &= 1350 \text{ kg.m}^{-3} \\ \frac{\rho_{cl}}{\rho_{cg}} &= 1000 \\ \mu_{cg} &= 1.8 \cdot 10^{-5} \text{ Pa.s}\end{aligned}$$

An hydrostatic pressure is imposed in the column:

$$P = P_0 + \rho g (z_{max} - z) \quad (4.13)$$

with P_0 the atmospheric pressure.

In the Bhaga and Weber's experiment, the bubbles have an initial volume of 9.3 cm^3 . Therefore, in the assumption of spherical bubbles, the initial value of the bubble radius is fixed at 1.3 cm in our simulations. Moreover, the bubble is initialized at 3.9 cm from the top of the mesh which corresponds to three radii.

Simulation	Experimental Reynolds number	Liquid viscosity ($Pa.s$)	Experimental final velocity ($cm.s^{-1}$)
Case b	3.57	2.02	20.5
Case d	13.3	0.77	29.0

Table 4.4: Characteristics of the two cases used for the Bhaga and Weber's rising bubble test case.

For the simulation, the dimensions of the computational domain are chosen large enough to avoid wall effects on the bubble and high enough to reach the limit velocity. Hua and Lou [73] and Denèfle [38] showed that for rising bubbles simulations, the computational domains must be of width equal to 4 times the bubble diameter and of height 12 times the diameter. Therefore, to limit CPU consumption, a 2D axisymmetric mesh, whose schematic view is given in Figure 4.5, is used. The mesh contains 179×540 cells. Thus, the initial bubble radius is around equal to 23 cells. The mesh length depends on the case: $L = 10.38 \text{ cm}$ for case b and $L = 10.33 \text{ cm}$ for case d. Indeed, the peak at the symmetric axis is difficult to compute since the mesh dimension in the y direction is very small. Thus, the deformation of the bubble is not well predicted in this region especially in case d since the liquid viscosity is smaller, which induces more bubble deformations. The mesh truncation is then higher for case d. The time step is kept constant, equal to 1.10^{-5} s for case b and 1.10^{-4} s for case d. These values are chosen to keep a CFL number under 0.9. Because the mesh is less truncated for case b, the mesh dimensions are smaller close to the symmetric axis and the time step has to be smaller.

To analyze the results, the final shape of the bubble (at 0.6 s) and its average vertical velocity are compared to Bhaga and Weber's experimental data. The average vertical velocity u_{av} obtained in the simulations is defined as follows:

$$u_{av} = \frac{\sum_I^{ncel} \alpha_{cg}^I u_{cg}^I \Omega}{\sum_I^{ncel} \alpha_{cg}^I \Omega} \quad (4.14)$$

with u_{cg}^I considered only in the vertical direction.

For the first study, case d is simulated with three different threshold values β : 5.10^{-3} , 1.10^{-3} and 5.10^{-4} . Indeed, Denèfle [38] showed that this case was more challenging in terms of bubble shape prediction.

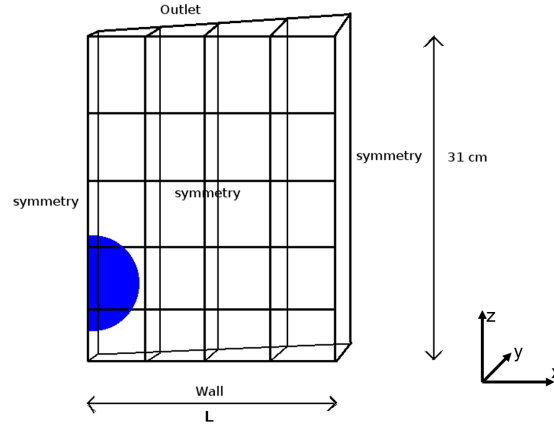


Figure 4.5: Schematic view of the simulation domain used for the simulation of the Bhaga and Weber's rising bubbles, $L = 10.38$ cm for case b and $L = 10.33$ cm for case d.

The simulated bubbles are superimposed to the experimental results in Figure 4.6. The first threshold value 5.10^{-3} induces a non physical elongation of each bubble side due to the lack of compression at each time step. The second threshold value 1.10^{-3} corrects this effect. Nevertheless, the bubble extremities remain not enough sharpened and detached twice (see Figure 4.6 middle picture). Thus, at 0.6 s, the final bubble is smaller than expected in terms of volume. Moreover, these detachments slow down the bubble which has a final velocity (at 0.6 s) equal to 28.3 $cm.s^{-1}$ compared to the experimental value (deducted from the Reynolds number) of 29 $cm.s^{-1}$. Therefore, the threshold value is one more time decreased at 5.10^{-4} . The prediction is in reasonable agreement with the experimental data. Moreover, the simulated final velocity is equal to 28.9 $cm.s^{-1}$, which corresponds to a relative error of 0.3 %.

Case b is also simulated with $\beta = 5.10^{-4}$. The bubble shape is shown in Figure 4.7. The simulation results agree well with the Bhaga and Weber's experimental data. Furthermore, the final velocity is found equal to 24.5 $cm.s^{-1}$, corresponding to a relative error of 19.5 % (experimental final velocity 20.5 $cm.s^{-1}$).

In terms of recompression efficiency, Figure 4.1 shows that whatever the mesh refinement and the initial interface diffusion, the final thickness is reached by fixing the recompression threshold at 5.10^{-4} . This value will be chosen in the rest of the thesis work and referred as the optimized recompression threshold.

Finally, one can note that, with the conservative implementation of the interface sharpening equation, the mass balance error by time step in the whole domain is equal to 10^{-16} %.

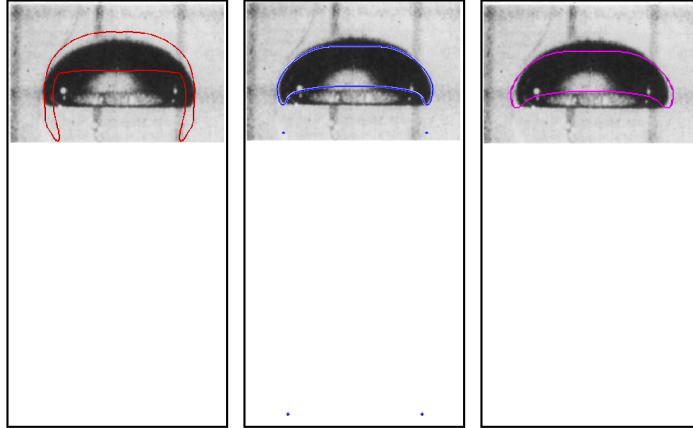


Figure 4.6: Comparison of the simulated bubble shape in case d at 0.6 s with the Bhaga and Weber's experimental observations [16], left to right: $\beta = 5.10^{-3}$, $\beta = 1.10^{-3}$ and $\beta = 5.10^{-4}$, the middle part of the domain is shown to highlight the creation of four small bubbles caused by the breakup of the large bubble for $\beta = 1.10^{-3}$.

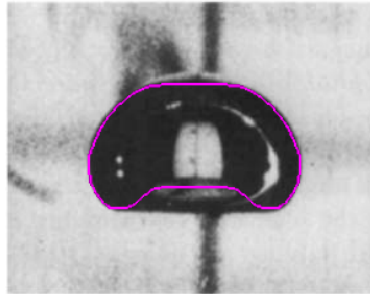


Figure 4.7: Comparison of the simulated bubble shape at 0.6 s with the Bhaga and Weber's experimental observations [16], case b, $\beta = 5.10^{-4}$.

4.5 Identification of diffused interfaces

4.5.1 Interface smearing criterion

The identification of the diffusion state of an interface plays also an important role with the conservative formulation of the interface sharpening equation. Indeed, as previously explained with the recompression threshold, the resolution of the equation has to be limited to avoid adding mass fluxes which will induce spurious velocities. Therefore, another criterion has been implemented to apply the interface sharpening equation only when a large interface is diffused.

This criterion is based on the gradient of the volume fraction. An interface is considered diffused if its thickness is higher than the thickness obtained after the resolution of the interface sharpening equation which is fixed at 5 cells. Therefore,

the criterion is based on the value of the volume fraction gradient over the interface. Two conditions are then required to activate the compression equation resolution. The first one is to locate a large interface spread over few cells, which means to have cells in which $\alpha_{cl}^I \alpha_{cg}^I > 0.02$. In Figure 4.8, the first situation does not meet this criterion. Therefore, the interface sharpening equation will not be solved. If the first criterion is satisfied, then the volume fraction gradient over the interface is evaluated in the cells containing the interface. Finally, this gradient $\nabla \alpha_k^I \cdot \mathbf{n}^I$, also equal to $\|\nabla \alpha_k^I\|$, is compared to $\frac{1}{5\Delta x^I}$. Indeed, as we can see in Figure 4.8 (middle picture), $\frac{1}{5\Delta x^I}$ corresponds to the volume fraction gradient over an interface with a thickness of 5 cells. Therefore, if an interface is diffused, then its thickness will be higher than 5 cells (Figure 4.8 right picture). The volume fraction gradient will be smaller than $\frac{1}{5\Delta x^I}$.

This new criterion ensures that the interface sharpening equation is activated only when the interface has a thickness larger than 5 cells.

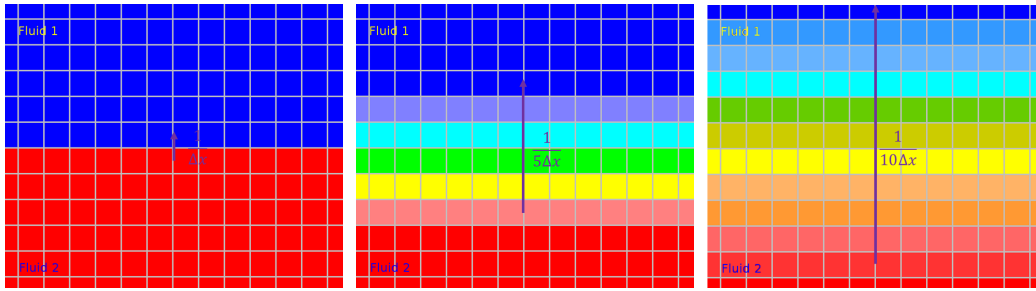


Figure 4.8: Schematic view of different diffusion state of an interface, the color scale represents the volume fraction of field 1, red corresponds to $\alpha_1 = 0$ and dark blue to $\alpha_1 = 1$, left to right : sharp interface (not spread over few cells), interface with a 5 cells thickness, diffused interface with a 10 cells thickness, the purple arrow displays the volume fraction gradient over the interface.

4.5.2 Illustration with Thorpe's experiment

The Kelvin-Helmholtz instability in Thorpe's experimental configuration [193] is a good example of an interface with limited diffusion. Indeed, in this experiment, two immiscible fluids are contained in a rectangular tank which is tilted for a small angle, $\sin(\gamma) = 0.072$ (see Figure 4.9). The velocities in each field vary in opposite directions. These velocities conduct to the existence of a shear stress at the interface which prevents it against diffusion.

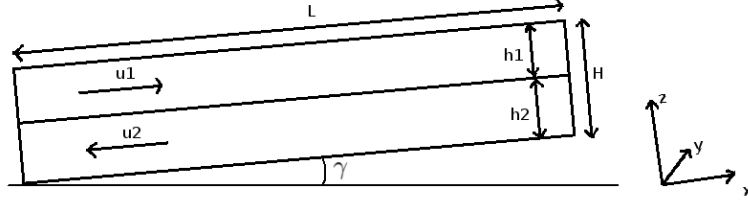


Figure 4.9: Schematic view of the Thorpe's experiment [193] at initial conditions.

4.5.2.1 Theory

In this test case, an inviscid fluid flow is considered with:

$$\rho = \begin{cases} \rho_2 & \text{for } 0 < z < h \\ \rho_1 & \text{for } h < z < H \end{cases} \quad (4.15)$$

with $h = h_1 = h_2 = \frac{H}{2}$. The steady velocity distribution along the rectangular tank is:

$$u = \begin{cases} -\frac{\Delta u}{2} & \text{for } 0 < z < h \\ \frac{\Delta u}{2} & \text{for } h < z < H \end{cases} \quad (4.16)$$

This parallel flow is assumed to be a solution of Euler equations upon which is superposed a small perturbation proportional to $\exp(i(kx + \omega t))$ with k a wavenumber and ω a pulsation. The linearization of the Euler equations gives the following dispersion relation:

$$\omega = k \frac{\Delta u (\rho_2 - \rho_1)}{2(\rho_1 + \rho_2)} \pm \sqrt{\frac{\sigma k^3 + gk(\rho_2 - \rho_1) \tanh(kh)}{\rho_1 + \rho_2} - \frac{k^2 \Delta u^2 \rho_1 \rho_2}{(\rho_1 + \rho_2)^2}} \quad (4.17)$$

The system is unstable when the complex part of ω is non-zero, which provides the condition for the minimum critical velocity difference:

$$\Delta u^2 > \frac{(\rho_1 + \rho_2)}{\rho_1 \rho_2} \left(\sigma k + \frac{g}{k} (\rho_2 - \rho_1) \right) \tanh(kh) \quad (4.18)$$

The critical wavenumber is then obtained by calculating the minimum of the right-hand side of Equation (4.18):

$$k_c = \sqrt{\frac{g(\rho_2 - \rho_1)}{\sigma}} \quad (4.19)$$

This corresponds to a theoretical value of 232 m^{-1} in Thorpe's experimental configuration. Experimentally, the measured values were equal to $k_c = 197 \pm 58 \text{ m}^{-1}$.

Moreover, if viscosity and closed-end effects are neglected, the velocity distribution at the beginning of the simulation is:

$$\begin{cases} u_1 = \frac{(\rho_2 - \rho_1)h_2 g \sin \gamma}{(\rho_1 h_2 + \rho_2 h_1)} t \\ u_2 = -\frac{(\rho_2 - \rho_1)h_1 g \sin \gamma}{(\rho_1 h_2 + \rho_2 h_1)} t \end{cases} \quad (4.20)$$

From this equation, Thorpe [193] predicted the time of the instability onset between 1.5 s and 1.7 s and observed experimentally $t_{onset} = 1.88 \pm 0.07$ s. Finally, Thorpe evaluated the wave velocity at $u_{waves} = 2.38$ cm.s⁻¹ and observed $u_{waves} = 2.6$ cm.s⁻¹.

4.5.2.2 Simulation

Both fluid layers have the same initial height $h_1 = h_2 = 1.5$ cm. The properties of the two fluids are presented in Table 4.5. Surface tension coefficient is equal to 0.04 N.m⁻¹.

	Density ($kg.m^{-3}$)	Viscosity ($Pa.s$)
Paraffin	780	0.0015
Water	1000	0.001

Table 4.5: Properties of the two liquid phases for the simulation of Kelvin-Helmholtz instability in Thorpe’s experimental configuration [193].

The dimensions of the computational domain are $L = 1.83$ m and $H = 3$ cm (see Figure 4.9). The mesh contains 80 x 4880 cells. A wall boundary condition is imposed everywhere except in front of and behind, where symmetry boundary planes are defined. The simulation is performed with a constant time step equal to 0.5 ms.

Two simulations are considered: one with a criterion on the interface smearing which limits the recompression to diffused interfaces and another without this criterion. The evolution of the interface shape for the two cases is displayed in Figure 4.10. The interface deformation is similar with and without the criterion.



Figure 4.10: Influence of the interface smearing criterion in terms of interface shape, left: no interface smearing criterion, right: with the interface smearing criterion, mesh with 80 x 4880 cells, constant time step equal to 0.5 ms, only the middle 0.6 meters long section of the channel is shown.

The interface profile at 3 s is then extracted to determine the critical wavenumber (see Figure 4.11). This time corresponds to the time where enough instabilities are observed and before they begin to fall down and break up. Therefore, the critical wavenumber obtained without the criterion is equal to 202 m^{-1} and to 219 m^{-1} with the criterion. These results are both in good agreement with the experimental, theoretical and simulated data (see Table 4.6).

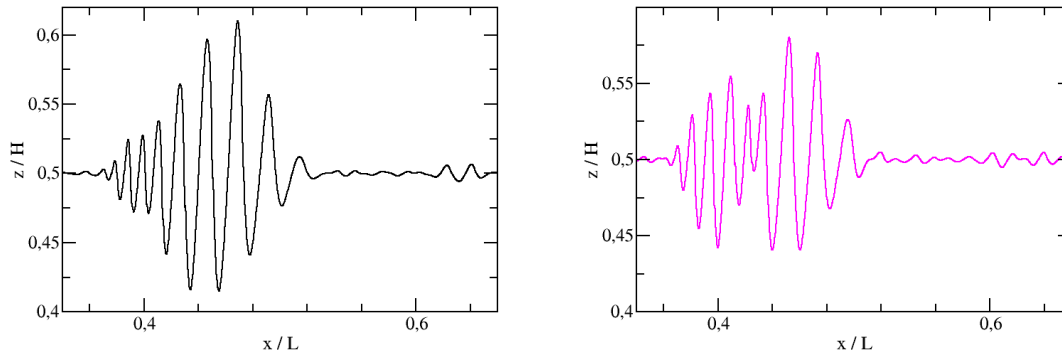


Figure 4.11: Physical location of the interface at 3 s, left: no interface smearing criterion, right: with the interface smearing criterion, only the middle 0.6 meters long section of the channel is shown, this representation is used to evaluate the wavenumber.

The time of the instability onset t_{onset} is also compared. For this purpose, the standard deviation of the interface is evaluated every 0.2 s between 1 s and 3.4 s. The evolution of this value allows estimating the amplitude growth of the instability. The result is shown in Figure 4.12. Then, the time of the instability onset is obtained by taking the intersection between the tangent of the linear behavior and the level of zero growing rate at the beginning of the simulations (see Figure 4.13). In the two simulations, the time of the instability onset is equal to 2.1 s.

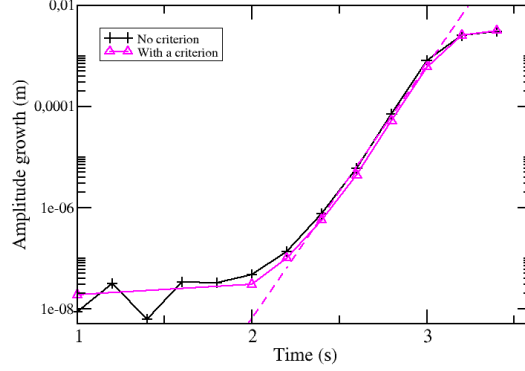


Figure 4.12: Amplitude growth obtained by evaluating the standard deviation of the interface over time, only the middle 0.6 meters long section of the channel is used for this analysis, the dashed line corresponds to the asymptotic amplitude growth used to determine the time of the instability onset.

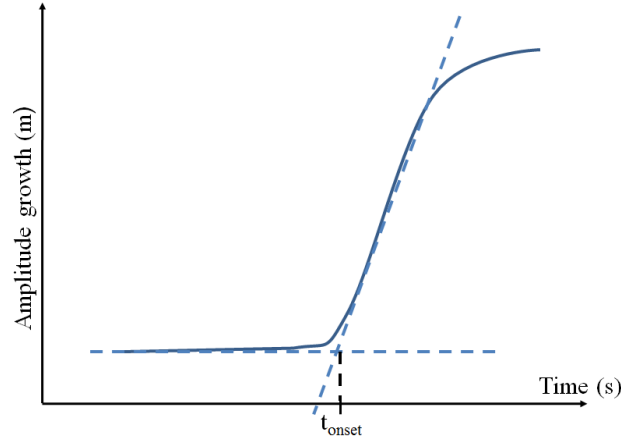


Figure 4.13: Methodology followed to evaluate the time of the instability onset using the evolution of amplitude growth over time.

Then, Figure 4.14 presents the maximum value of the average interface velocity \mathbf{U} over time defined as follows:

$$\mathbf{U} = \frac{\alpha_1 \rho_1 \mathbf{u}_1 + \alpha_2 \rho_2 \mathbf{u}_2}{\alpha_1 \rho_1 + \alpha_2 \rho_2} \quad (4.21)$$

This velocity refers to a weighted average of the fluid velocities at the interface. The results are compared with Equation (4.20) which is valid at short times, where

the linear approximation can be applied. The two simulations predict well the evolution of this velocity.

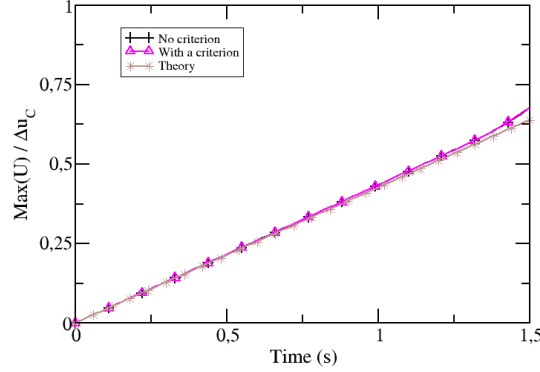


Figure 4.14: Average interface velocity \mathbf{U} normalized by the critical velocity over time with and without the interface smearing criterion, \mathbf{U} is defined in Equation (4.21), the theory is given by Equation (4.20), the three curves are superposed.

Finally, the wave speed u_{waves} is compared by calculating the crest-to-crest distance at different positions in the tank. Figure 4.15 gives an example of the waves used for this calculation. We find $u_{waves} = 1.6 \text{ cm.s}^{-1}$ without the criterion and $u_{waves} = 3.1 \text{ cm.s}^{-1}$ with the criterion. In comparison with the experimental, theoretical and simulated data displayed in Table 4.6, the simulation without the criterion does not well predict this parameter.

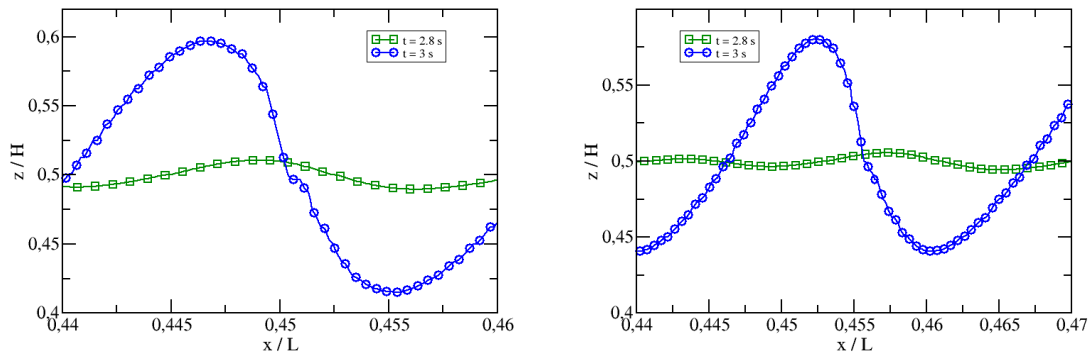


Figure 4.15: Physical location of the interface at different times for the evaluation of the wave speed, left: no interface smearing criterion, right: with the interface smearing criterion.

Results	k_c (m^{-1})	t_{onset} (s)	u_{waves} ($cm.s^{-1}$)
With the interface smearing criterion	219	2.1	3.1
Without the interface smearing criterion	202	2.1	1.6
Theory	232	1.5 – 1.7	2.38
Experiments	197 ± 58	1.88 ± 0.007	2.6
Bartosiewicz <i>et al.</i> [13]	143	1.9	2.5
Štrubelj [188]	157	2.0	3.0

Table 4.6: Comparison of the critical wavenumber k_c , the time of the instability onset t_{onset} and the wave speed u_{waves} with and without the interface smearing criterion, the theoretical and experimental data and the simulations of Bartosiewicz *et al.* [13] and Štrubelj [188].

Thus, the criterion controlling the activation of the interface sharpening equation does not change dramatically the simulations but it can affect some specific parameters. Therefore, to simulate accurately such flows and to limit the addition of spurious velocities, the activation of the recompression equation is restricted to diffused interfaces.

4.6 Conclusion

For an accurate simulation of the large interfaces, the implementation of the interface sharpening equation is a crucial point. Thus, in this chapter and Appendix B, the different parameters relative to the sharpening equation have been compared with five isothermal laminar test cases. A summary of the simulations is displayed in Table 4.7. This study highlights the importance of a conservative implementation to ensure mass conservation. As an example, the simulations of the Kelvin-Helmholtz instability with a non conservative formulation produced a mass balance error in the whole domain at each time step equal to 10^{-10} %. This error is reduced at 10^{-17} % with a conservative implementation. Nevertheless, we showed that this implementation requires a correction of the mass fluxes which are then used to evaluate the velocity field. Therefore, the resolution of the interface sharpening equation has to be limited to avoid creating spurious velocities by adding extra mass fluxes. For this purpose, two criteria have been developed. The first one is used to stop the recompression when the interface has reached its final thickness. It is based on the volume variation of the interface induced by the compression. An analysis of the spurious velocities with a stationary bubble and a validation with the Bhaga and Weber’s rising bubble, the oscillating bubble test case (two large bubble simulations) and the Thorpe’s experiment (an interfacial liquid/liquid test case) allowed optimizing the value of the threshold β . This value has been fixed at 5.10^{-4} . The second criterion evaluates the diffusion state of the interface thanks

CHAPTER 4. CONSERVATIVE IMPLEMENTATION OF THE INTERFACE SHARPENING EQUATION

to the volume fraction gradient and has been validated with the simulation of the Kelvin-Helmholtz instability.

In the rest of this thesis report, this optimized implementation of the interface sharpening equation will be used.

Implementa- tion	Drag force model	Threshold value	Interface smearing criterion	Test cases						
				Square bubble	Oscillating bubble	Stationary bubble	Bhaga's bubble	Kelvin- Helmholtz instability		
Non conservative	Law 1	$\beta = 5.10^{-4}$	ON	X						
	Law 2			✓						
	Law 3			✓	X					
Conservative	Law 2	$\beta = 5.10^{-4}$	ON					X		
			OFF					X		
	Law 3	$\beta = 1.10^{-2}$	ON		X	X				
				$\beta = 5.10^{-3}$				X		
				$\beta = 1.10^{-3}$		✓	X	X	X	
				$\beta = 5.10^{-4}$	ON		✓		✓	✓
				OFF					X	
$\beta = 1.10^{-4}$	ON		✓	X						

Table 4.7: Summary of the test cases and parameters simulated in this chapter and Appendix B, the crosses symbolize that no reasonable results were obtained whereas the ticks correspond to an accurate simulation of the cases, law 1 refers to the drag force law in Equation (6.1), law 2 to Equation (3.15) and law 3 to Equation (6.7).

Chapter 5

Evaluation of the spurious velocities induced by the surface tension model

In the previous chapter, we studied the implementation of the interface sharpening equation which is a crucial point for the simulation of the large interfaces with the Large Bubble Model but induces spurious velocities. The choice and the implementation of the surface tension model is also involved in the production of such velocities. Thus, in this chapter, the intensity of these velocities and their effects are evaluated on a standard test case: the stationary bubble. Then, the notion of critical Capillary number is introduced and estimated. Two cases are taken into account an air bubble in still water at 298.15 K and a steam bubble in water at 378.15 K . In both cases, no thermal and mass transfers across interfaces are taken into account. Like the previous chapter, the flows considered here are laminar and isothermal with only continuous fields the surface tension model is used for the simulation of large interfaces between two continuous fields.

5.1 Résumé du chapitre

Ce chapitre s'intéresse au deuxième élément du Modèle Large Bulle : la tension de surface. Le modèle utilisé est connu pour induire des vitesses parasites. Par conséquent, on évalue ces vitesses parasites dans différentes configurations pour en déduire le nombre Capillaire critique de notre modèle. Ce nombre adimensionnel permet d'évaluer la part des vitesses parasites dans les simulations afin de s'assurer que les phénomènes observés sont bien d'origine physique.

5.2 Air bubble in still water at 298.15 K

In the LBMo, the choice has been made to implement a volumetric expression of the CSF model proposed by Brackbill *et al.* [21]. Nevertheless, this model is known to induce spurious velocities [89, 148]. To evaluate the spurious velocities induced by both the surface tension model and the interface sharpening equation, a

stationary bubble is simulated. In this test case, a bubble is simulated in still water at 298.15 K with an initial round shape and without gravity forces. The interface is initialized at the equilibrium. All the fluids are at rest. Thus, the fluids velocities are supposed to be equal to zero. The bubble motion and the interface deformation are only due to spurious velocities. Therefore, this test case is particularly severe since, in most industrial configurations, the spurious velocities do not have a predominant effect on the observed phenomena. Indeed, the velocity intensities are usually higher thanks to the fluids motion.

The properties of the two fluids are given in Tables 5.1. The surface tension coefficient is equal to 0.08 N.m^{-1} . The initial bubble diameter is taken equal to 2 cm . The mesh is a square uniform Cartesian grid with 5 cm sides. A wall boundary condition is imposed everywhere. The simulations are performed for 1 s . At this time, we assume that the bubble has reached its equilibrium state.

	Density ($kg.m^{-3}$)	Viscosity ($Pa.s$)
Air bubble (subscript: cg)	1.29	1.10^{-5}
Water (subscript: cl)	1000	1.10^{-3}

Table 5.1: Properties of water and air for the stationary bubble test case, the simulation is performed at 298.15 K .

5.2.1 Theory

The circularity of the bubble is defined as follows:

$$C = \frac{2\pi R_0}{L} \quad (5.1)$$

with σ the surface tension coefficient, R_0 the bubble radius and L the bubble perimeter.

Concerning the pressure field, the Laplace equation in two dimensions is valid:

$$P_{in} - P_{out} = \frac{\sigma}{R_0} \quad (5.2)$$

with P_{in} the pressure in the bubble and P_{out} out of the bubble.

We can also introduce the Capillary number, defined for the evaluation of the spurious velocities:

$$Ca = \frac{\mu_{cl} U_{cg}}{\sigma} \quad (5.3)$$

Two definitions of U_{cg} are considered in this chapter. They are defined in Equations (5.7) and (5.8).

5.2.2 Simulation

Seven different mesh refinements are tested: 45 x 45 cells, 64 x 64 cells, 91 x 91 cells, 128 x 128 cells, 181 x 181 cells, 256 x 256 cells and 512 x 512 cells. The time step is constant and equal to 0.1 *ms*. Therefore, the CFL number is kept under 0.9.

In this case, the criterion used to solve the interface sharpening equation only on smeared interfaces is not activated to see the effect of this compression on the spurious velocities intensity.

The quantities observed are the relative error for the circularity C , evaluated using Equation (5.1), for the pressure, defined by the Laplace Equation (5.2) and the average bubble velocity in the bubble (Equation (5.7)) and within the interface (Equation (5.8)). The pressure fields in and out of the bubble are evaluated using the average expressions:

$$P_{in} = \frac{\sum_I^{ncel} \alpha_{cg} P \Omega}{\sum_I^{ncel} \alpha_{cg} \Omega} \quad \text{and} \quad P_{out} = \frac{\sum_I^{ncel} \alpha_{cl} P \Omega}{\sum_I^{ncel} \alpha_{cl} \Omega} \quad (5.4)$$

The final radius of the bubble is obtained as follows:

$$R_0 = \sqrt{\frac{S_n}{\pi}} \quad (5.5)$$

with S_n , the estimated bubble surface:

$$S_n = \sum_I^{ncel} \alpha_{cg} \quad (5.6)$$

$$U_{cg} = \frac{\sum_{\alpha_{cg} > 1.10^{-3}} \alpha_{cg} \rho_{cg} u_{cg}}{\sum_{\alpha_{cg} > 1.10^{-3}} \alpha_{cg} \rho_{cg}} \quad (5.7)$$

$$U_{cg}^{Int} = \frac{\sum_{\alpha_{cl} \alpha_{cg} > 0.1} \alpha_{cg} \rho_{cg} u_{cg}}{\sum_{\alpha_{cl} \alpha_{cg} > 0.1} \alpha_{cg} \rho_{cg}} \quad (5.8)$$

For the pressure, the relative error is obtained by comparing $R_0 (P_{in} - P_{out})$ to σ .

The results of the convergence test are given in Figures 5.1 and 5.2. The X axis of the six graphs corresponds to the dimensionless quantity obtained by dividing the bubble diameter by the cell length. In Figure 5.1, one can note a convergence of the three quantities. Therefore, the intensity of spurious velocities decreases with the mesh refinement and remains low even with coarse meshes.

To evaluate the order of convergence x for the quantity f , the following expression [160] is applied. It is based on the Richardson's extrapolation (see Appendix D for more details):

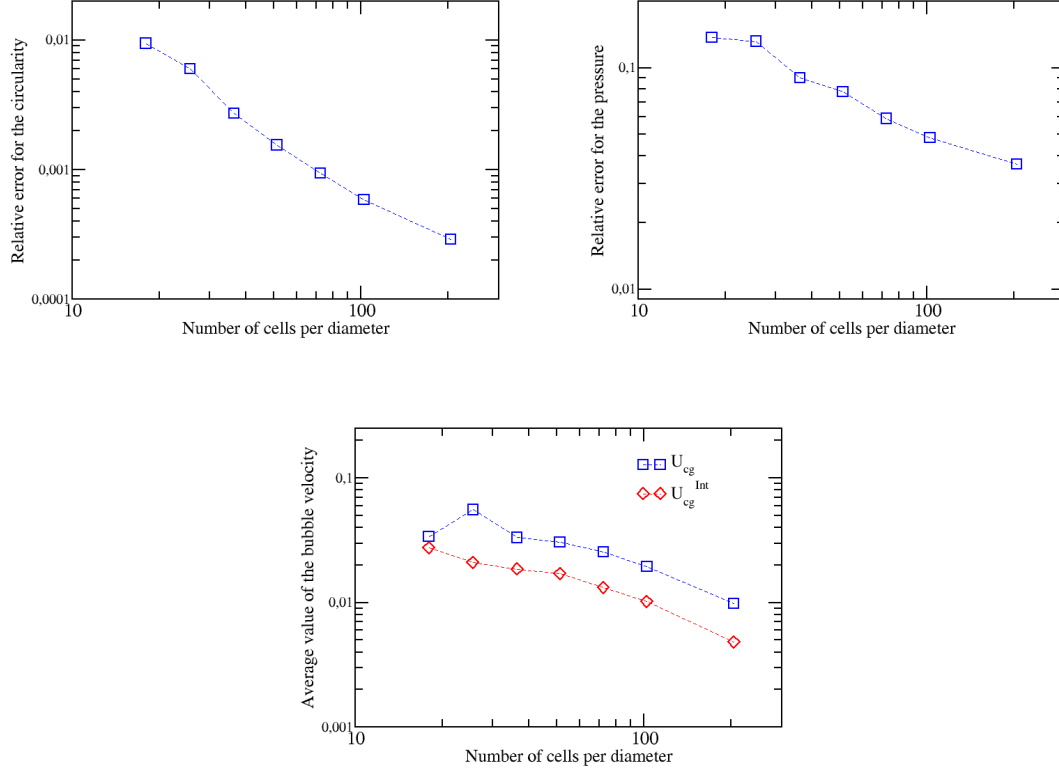


Figure 5.1: Convergence of the relative error for the circularity, for the pressure and the average bubble velocity (squares: U_{cg} , diamonds: U_{cg}^{Int}), logarithmic scales for both axes.

$$x = \frac{\ln\left(\frac{f_{m_3} - f_{m_2}}{f_{m_2} - f_{m_1}}\right)}{\ln\left(\frac{1}{2}\right)} \quad (5.9)$$

with m_1 , m_2 and m_3 three mesh refinements, such as:

$$\Delta x_{m_3} = \frac{\Delta x_{m_2}}{2} = \frac{\Delta x_{m_1}}{4} \quad (5.10)$$

To determine the order of convergence, the meshes with 128×128 cells, 256×256 cells and 512×512 cells are used. Indeed, as we can see in Figure 5.2, these meshes belong to the asymptotic regions, where the Richardson's extrapolation is valid. Therefore, for the circularity, the order of convergence is equal to 1.7, for the pressure to 1.4 and for the average velocity to 0.22 and 0.35 respectively in the whole domain and at the interface. The order of convergence of spurious velocity is low compared to pressure and circularity obtained values. This is mainly due to the non-linear coupling between discretization errors on curvature and the amplification in the momentum conservation equation. However, few codes observe a mesh convergence for the spurious velocities (see Figure B.5 in Appendix B).

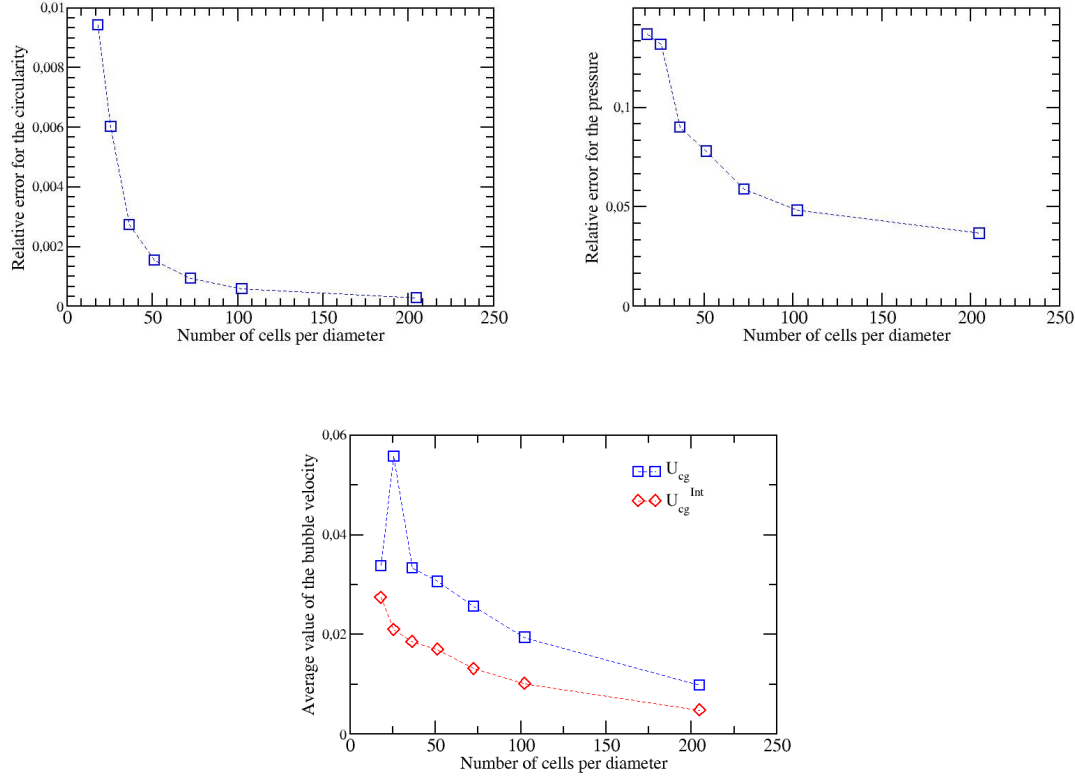


Figure 5.2: Location of the asymptotic region for the estimation of the order of convergence of the circularity, the pressure and the average bubble velocity (squares: U_{cg} , diamonds: U_{cg}^{Int}), linear axes.

5.3 Steam bubble in still water at 378.15 K

This second study consists in a preliminary work for the simulation of water/steam flows in order to have an evaluation of the existing spurious velocities in such flows. Thus, the same study is performed with three mesh refinements: 128 x 128 cells, 256 x 256 cells and 512 x 512 cells. The time step is constant and equal to 0.1 ms. The same definitions are used for the average velocities. The only difference is the fluid properties, given in Table 5.2 for this case. Surface tension coefficient is equal to $0.057 N.m^{-1}$. In this case, mass transfers due to phase change are not taken into account. The simulation is performed at 378.15 K, which only means that the fluid properties are taken at this temperature, at the atmospheric pressure.

The average velocities and the corresponding Capillary numbers are presented in Figure 5.3 and compared to the previous case. First, the level of spurious velocities is comparable in the two studies. In the water/steam flow, the interface velocity is higher than the velocity obtained in the whole domain. This means that the spurious velocities are more concentrated at the interface compared to the previous

	Density ($kg.m^{-3}$)	Viscosity ($Pa.s$)
Steam bubble (subscript: cg)	0.578	$1.39.10^{-5}$
Water (subscript: cl)	986.5	$2.7.10^{-4}$

Table 5.2: Properties of water and steam for the stationary bubble test case, water at 378.15 K.

case.

Moreover, Figure 5.3 right presents the corresponding Capillary numbers. In these two cases, the Capillary number is non zero due to the existence of spurious velocities. The Capillary number due to spurious velocities corresponds to the critical Capillary number for a CMFD tool. In a simulation with fluids in motion, a corresponding Capillary number will be calculated using the characteristic velocities of the flow. If this number is smaller than the critical Capillary number, the simulation will be only driven by the spurious velocities. It won't be possible to predict the correct physical behavior. In our case, the critical Capillary number is equal to 0.001 since whatever the test case and the grid, the Capillary number is always smaller than 0.001. As a comparison, Pan *et al.* [148] and Lafaurie *et al.* [89] evaluated their critical Capillary number at 0.01 without special treatment of the surface tension force.

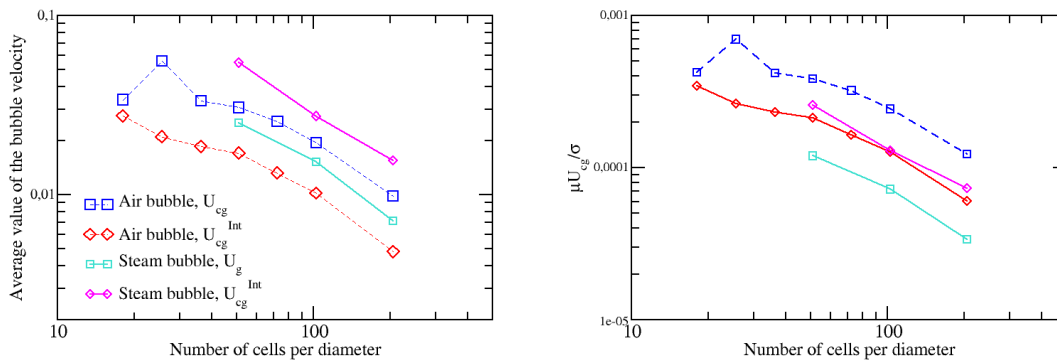


Figure 5.3: Evaluation of the spurious velocities according to the mesh refinement, left: average velocity, right: corresponding Capillary number, the results are compared with the air/water stationary bubble test case, logarithmic scales for both axes.

5.4 Conclusion

The stationary bubble is a very interesting test case for the evaluation of the induced spurious velocities since the flow is at rest. This study showed that the

intensity of these velocities remains at an acceptable level whatever the case: air bubble or steam bubble. The mesh refinement induces a decrease of these velocities. Moreover, this work allows evaluating the critical Capillary number which is in the order of 0.001 in our method. Test cases with moving fluids characterized by a Capillary numbers higher than 0.001 will not be affected by these spurious velocities. This analysis has been performed on structured grids. The same analysis on unstructured meshes is proposed in Appendix C. Finally, the surface tension model has been validated.

Chapter 6

Implementation and validation of a new drag force model

The conservative implementation of the interface sharpening equation and the surface tension model are two crucial elements for an accurate simulation of the large interfaces. Nevertheless, the choice of the drag force model has also a significant influence on the simulation. Thus, in this chapter, a new drag force model suitable for the simulation of large interfaces within the multifield approach is detailed. The new expression is compared to the standard drag force law (section 6.2) and the previous expression used with the multifield approach (see section 3.4.1) with different laminar isothermal test cases. For the sake of clarity, only one bubble and one interfacial liquid/liquid test case will be presented to validate the new drag force law. Extra validations can be found in Appendix E. All the laminar and isothermal flows considered in this chapter and Appendix E are simulated with continuous fields. No dispersed fields are considered since the drag force law developed in this chapter is devoted to the simulation of large interfaces between two continuous fields.

The main part of this chapter has been presented at the 6th International Symposium on Advances in Computational Heat Transfer (CHT-15, 25-29 May 2015) [47] and has been published in [48, 130].

6.1 Résumé du chapitre

Ce chapitre est centré sur le dernier élément du Modèle Large Bulle : la loi de traînée. Cette loi permet de coupler les vitesses des deux champs continus au niveau des grandes interfaces. Une version déjà implémentée de cette loi a montré des difficultés à prédire les formes et vitesses finales de bulles dans des liquides à viscosité faible. Par conséquent, ce chapitre propose d'établir une nouvelle loi de traînée qui prend en considération les propriétés physiques des fluides et qui s'intègre dans l'approche multi-champ.

6.2 Standard drag force model

The standard drag force model is applied for the simulations of interfaces within the Large Interface Model (LIM), see section F. It has the following expression:

$$\mathbf{F}_{Drag,cl \rightarrow cg} = \alpha_{cl} \alpha_{cg} C_D (\mathbf{u}_{cl} - \mathbf{u}_{cg}) \quad (6.1)$$

with C_D the two-phase flow standard interfacial coefficient, built from the bubble/droplet models [34].

Nevertheless, to simulate large interfaces with the multifield approach, it seems necessary to consider the physical properties of the two continuous fields in the drag force coefficient. Thus, a specific drag force law was proposed and described in Equation (3.15) (section 3.4.1). This expression gave quite good results on a large range of test cases but failed to simulate rising bubbles in liquid with small viscosities. In the next section, a new expression is proposed which takes into account the liquid viscosity for bubbly flows and which is more suitable to the simulations of large interfaces with a multifield approach.

6.3 New drag force expression

The new formulation is based on the drag force expression applied to the dispersed fields in the approximation of spherical bubbles/droplets. Thus, in the example of a bubbly flow:

$$\mathbf{F}_{Drag,cl \rightarrow cg} = \frac{\rho_{dg}}{\alpha_{cl}} \frac{1}{\tau} (\mathbf{u}_{cl} - \mathbf{u}_{dg}) \quad (6.2)$$

If we use the Ishii's definition for τ [75]:

$$\frac{1}{\tau} = \frac{3\rho_{cl} C_D \|\mathbf{u}_{cl} - \mathbf{u}_{dg}\|}{4\rho_{dg} d_p} \quad (6.3)$$

The drag coefficient is given by the Stokes drag force on a spherical particle:

$$C_D = \frac{24}{Re_d} \quad (6.4)$$

with:

$$Re_d = \frac{\rho_{cl} \|\mathbf{u}_{cl} - \mathbf{u}_{dg}\| d_p}{\mu_{cl}} \quad (6.5)$$

By combining Equations (6.2), (6.3), (6.4) and (6.5), the following drag force expression is obtained:

$$\mathbf{F}_{Drag,cl \rightarrow cg} = \frac{18\mu_{cl}}{\alpha_{cl} d_p^2} (\mathbf{u}_{cl} - \mathbf{u}_{dg}) \quad (6.6)$$

The obtained formulation is extended to large interfaces using a continuous approximation. The large interfaces are considered as a series of aligned dispersed

structures, which form a continuous boundary between two continuous fields, as shown in Figure 6.1.

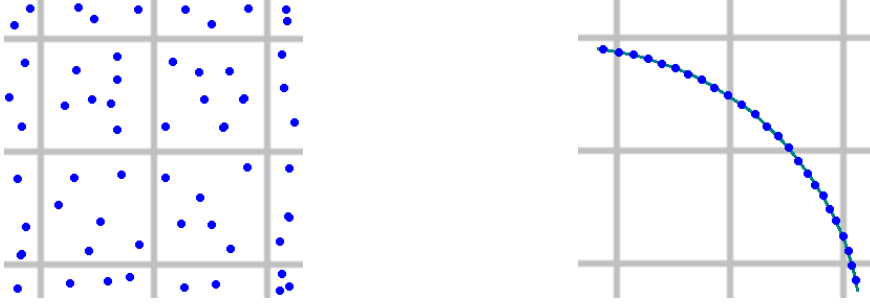


Figure 6.1: Schematic view explaining the extension of the drag force expression to large interfaces based on a continuous approximation, left: dispersed approach with dispersed particles distributed statistically over the domain, right: aligned dispersed particles forming a continuous boundary between two continuous fields.

To adapt this expression, the drag force is multiplied by $\alpha_{cl}\alpha_{cg}$ to restrict its application at the interface when the value of $\alpha_{cl}\alpha_{cg}$ is non zero. Then, it is split into three regions according to the flow properties:

$$\begin{aligned}
 \alpha_{cg} < 0.3 : \quad & \mathbf{F}_{bubble,cl \rightarrow cg} = \alpha_{cl}\alpha_{cg} \frac{18\mu_{cl}}{\alpha_{cl}d_p^2} (\mathbf{u}_{cl} - \mathbf{u}_{cg}) \\
 \alpha_{cg} > 0.7 : \quad & \mathbf{F}_{droplet,cl \rightarrow cg} = \alpha_{cl}\alpha_{cg} \frac{18\mu_{cg}}{\alpha_{cg}d_p^2} (\mathbf{u}_{cl} - \mathbf{u}_{cg}) \\
 0.3 \leq \alpha_{cg} \leq 0.7 : \quad & \mathbf{F}_{mix,cl \rightarrow cg} = \frac{0.7-\alpha_{cg}}{0.7-0.3} \mathbf{F}_{bubble} + \frac{\alpha_{cg}-0.3}{0.7-0.3} \mathbf{F}_{droplet}
 \end{aligned} \tag{6.7}$$

The critical volume fraction fixed at 0.3 and used to define the different regions is based on experimental studies of bubbly flows [57, 139, 191]. The peculiarity of this new definition is that the viscosity becomes a parameter of the drag force intensity. Moreover, the new drag force integrates the concept of the multifield approach. Indeed, the expression depends on the properties of the dominant continuous field, which is determined in each cell by the value of α_{cg} :

- $\alpha_{cg} < 0.3$: dominant continuous liquid field with large bubbles,
- $\alpha_{cg} > 0.7$: dominant continuous gas field with large droplets,
- $0.3 \leq \alpha_{cg} \leq 0.7$: mixture of gas and liquid, no predominant field.

Therefore, this drag force allows dealing with a large variety of flow types. Smooth transitions between these regimes are ensured by the definition of \mathbf{F}_{mix} .

The multifield model is also taken into account in the definition of the characteristic distance d_p . The large interfaces and the small spherical bubbles which belong to a dispersed field, are distinguished according to the value of $\alpha_{cl}\alpha_{cg}$. Thus, in the region of large interfaces, $0.1 < \alpha_{cl}\alpha_{cg} < 0.25$, which corresponds to the interface thickness obtained after resolution of the interface sharpening equation, d_p is evaluated by a local quantity $\frac{\alpha_p}{\|\nabla\alpha_p\|}$ (the subscript p corresponding to cg for \mathbf{F}_{bubble} and to cl for $\mathbf{F}_{droplet}$) corrected by the factor $\sqrt{\frac{\mu_{cg}}{\mu_{cl}}}$. This factor is necessary since the drag force model has been initially developed for spherical particles and is applied to large interfaces without any assumptions on their shape. It involves the viscosity of the two fluids since these quantities have an effect on velocities on each side of the interface. Then, in cells containing a dispersed field, like dispersed bubbles for instance, $\alpha_{cg} \ll \alpha_{cl}$. Therefore, for $\alpha_{cl}\alpha_{cg} < 0.02$, d_p is chosen equal to the diameter of the dispersed bubbles/droplets. Between these two regions, d_p is evaluated by interpolation of its two extreme values:

$$d_p = \frac{\alpha_{cl}\alpha_{cg} - b}{a - b}d_{pdisp} + \frac{\alpha_{cl}\alpha_{cg} - a}{b - a} \sqrt{\frac{\mu_{cg}}{\mu_{cl}}} \frac{\alpha_p}{\|\nabla\alpha_p\|} \quad (6.8)$$

with $a = 0.02$ and $b = 0.1$. An illustration of the method chosen to define d_p is proposed in Figure 6.2.

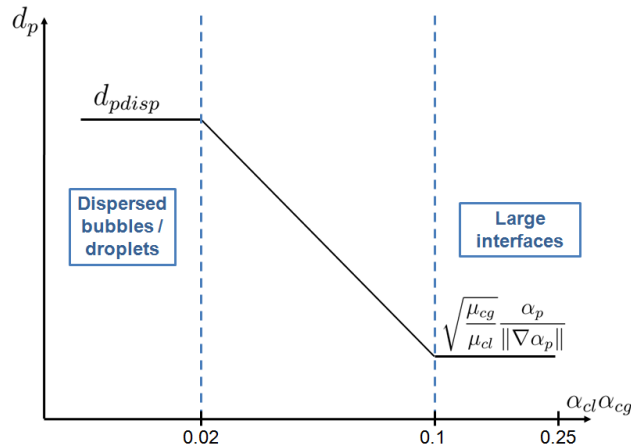


Figure 6.2: Distribution of d_p along the domain, d_{pdisp} corresponds to the diameter of the dispersed bubbles/droplets, large interfaces are located at high values of $\alpha_{cl}\alpha_{cg}$, the subscript p corresponds to cg for \mathbf{F}_{bubble} and to cl for $\mathbf{F}_{droplet}$.

This distribution of the characteristic distance d_p ensures a smooth transition between this drag force, applied to the interfaces separating two continuous fields, and the drag force between a dispersed and a continuous field.

6.4 Validation of the new drag force expression

To validate this new drag force, four different test cases (two large bubbles and two interfacial liquid/liquid test cases) were simulated: the Bhaga and Weber's bubbles [16], the Thorpe's experiment [193], the oscillating bubble and the Rayleigh-Taylor instability with the three drag force expressions. The results of the Bhaga and Weber's rising bubble test case and the Thorpe's experiment [193] are presented in this section. The other results can be found in Appendix E.

6.4.1 Bhaga and Weber's rising bubbles

With this test case, the new drag force expression developed in section 6.3 with and without the adding factor $\sqrt{\frac{\mu_{cg}}{\mu_{cl}}}$ (see the definition of d_p in Equation (6.8)) is compared with the previous drag force defined in Equation (3.15) with $\tau = 1.10^{-7}$ s and the standard drag force in Equation (6.1). The simulation parameters can be found in section 4.4.2. The bubble shapes for case b and case d are displayed in Figures 6.3 and 6.4. The simulation with the standard drag force expression (Equation (6.1)) has only been performed in case d. Indeed, as soon as the bubble begins to rise, it breaks up (see Figure 6.5). No physical results can be obtained with this drag force. For the three other drag force expressions, the simulation results agree well with the Bhaga and Weber's experimental data. No differences are observed between the three drag forces for case b. Thus, only the result obtained with the new drag expression given by Equation (6.7) is presented in Figure 6.3. However, in case d, the new drag force expression, especially without the adding factor $\sqrt{\frac{\mu_{cg}}{\mu_{cl}}}$, induces the lateral extension of the bubble.

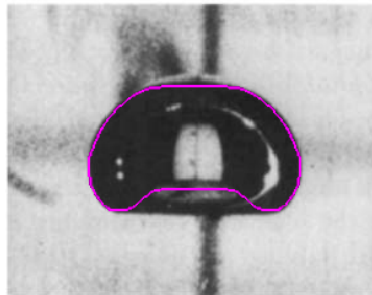


Figure 6.3: Comparison between the simulated bubble shape obtained with the new drag force expression given by Equation (6.7) at 0.6 s and the Bhaga and Weber's experimental data.

This difference is also visible in the final bubble velocity, given by Table 6.1. The final velocity is well predicted in case d with the new drag force expression. In case b, the relative errors are higher and close for the three drag forces.

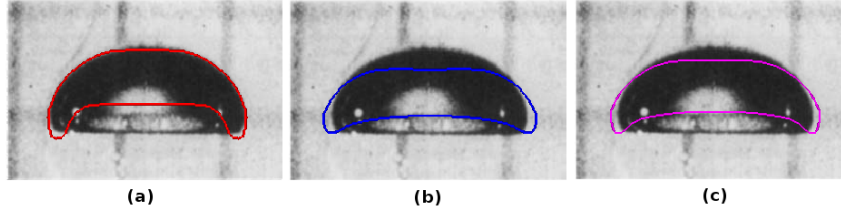


Figure 6.4: Comparison between the three drag forces with case d in terms of bubble shape at 0.6 s, (a) corresponds to the drag force defined in Equation (3.15) with $\tau = 1.10^{-7}$ s, (b) to the new drag force without the adding factor $\sqrt{\frac{\mu_{cg}}{\mu_{cl}}}$ and (c) to the new drag force given by Equation (6.7), the isosurfaces of α_{cg} ($\alpha_{cg} = 0.5$) are superposed on the Bhaga and Weber's experimental data.

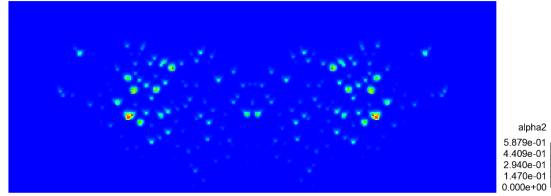


Figure 6.5: Bubble shape obtained with the standard drag force (Equation (6.1)) at 0.6 s, the bubble breaks up as soon as it begins to rise, case d.

Simulation	$\tau = 1.10^{-7}$ s	New drag force without $\sqrt{\frac{\mu_{cg}}{\mu_{cl}}}$	New drag force
Case b	24.4 $cm.s^{-1}$ (19.0 %)	24.5 $cm.s^{-1}$ (19.5 %)	24.5 $cm.s^{-1}$ (19.5 %)
Case d	29.3 $cm.s^{-1}$ (1.0 %)	27.9 $cm.s^{-1}$ (3.8 %)	28.9 $cm.s^{-1}$ (0.3 %)

Table 6.1: Final velocities (at 0.6 s) of the two cases obtained with the previous drag force (3.15) with $\tau = 1.10^{-7}$ s, the new drag force without the adding factor $\frac{\mu_{cl}}{\mu_{cg}}$ and the new drag force displayed in Equation (6.7), the relative errors are given in brackets.

To conclude, the new drag force allows the simulation of Bhaga and Weber's bubbles in liquids with different viscosities by increasing (case d) or maintaining (case b) the accuracy of the results.

6.4.2 Kelvin-Helmholtz instability

Now, the four drag force expressions are compared with an interfacial liquid/liquid test case. For this purpose, the Thorpe's experiment (see section 4.5.2) is simulated

with the four drag force laws. The results are compared in terms of interface shape, critical wavenumber, wave velocity, time of the instability onset and evolution of the maximum value of the average interface velocity \mathbf{U} (see Equation (4.21)) at the beginning of the simulation.

In Figure 6.6, an illustration of the evolution of the Kelvin Helmholtz instability over time is displayed for the four drag forces. The waves appear later with the previous drag force (3.15) with $\tau = 1.10^{-7}$ s.

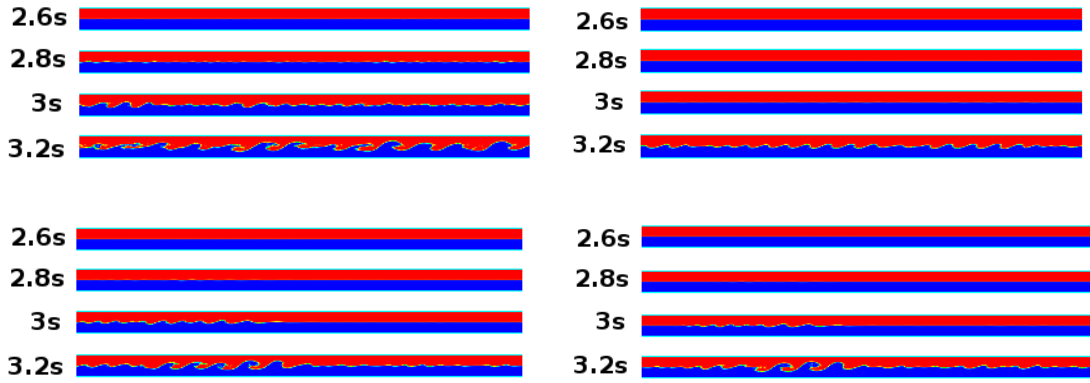


Figure 6.6: Influence of the drag force expression in terms of interface shape, left to right, top to bottom: standard drag force given by Equation (6.1), previous drag force (3.15) with $\tau = 1.10^{-7}$ s, new drag force without the adding factor $\sqrt{\frac{\mu_{cg}}{\mu_{cl}}}$, new drag force given by Equation (6.7), only the middle 0.6 meters long section of the channel is shown.

To determine the critical wavenumber, the interface profile is extracted at 3 s and the waves distance is evaluated. The results are displayed in Table 6.2 and compared with Bartosiewicz *et al.* and Štrubelj [188] results. All the obtained wavenumbers have the same order of magnitude.

The interface is also examined in terms of amplitude growth in order to evaluate the time of the instability onset. The results are presented in Figure 6.7 and Table 6.2. These results agree well with the simulations of Bartosiewicz *et al.* [13] with $t_{onset} = 1.9$ s and Štrubelj [188] with $t_{onset} = 2$ s. The previous drag force (3.15) with $\tau = 1.10^{-7}$ s overpredicts the time of the instability onset compared to the three other drag force expressions.

Moreover, Figure 6.8 presents the maximum value of the average interface velocity \mathbf{U} (Equation (4.21)) over time. The results are compared with Equation (4.20) which is valid at short times, where the linear approximation can be applied. The four drag forces ensure an accurate prediction of the interface velocity.

In Figure 6.9, the velocity profiles over time obtained with the new drag force expression are displayed. The three other drag forces predict the same profiles. These profiles are symmetrical. Indeed, in our case: $h_1 = h_2 = 1.5$ cm. Thus, Equation (4.20) predicts that, for short times, the velocity of each field has the same magnitude and evolves in an opposite direction. In Figure 6.9, we see that, from 2 s,

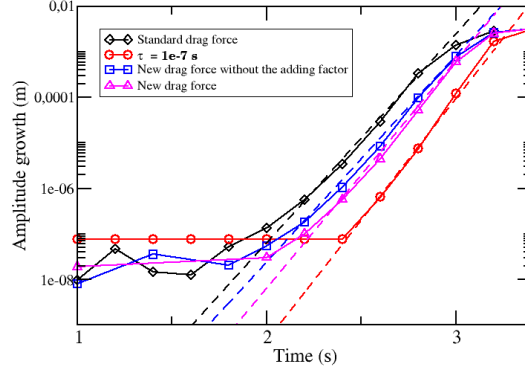


Figure 6.7: Amplitude growth obtained by evaluating the standard deviation of the interface over time.

the symmetry begins to disappear. In the middle of the domain corresponding to the position of the liquid/liquid interface at $\frac{z}{H} = 0.5$, no velocity jump is observed. Thus, at the interface, the drag force ensures the coupling of the two velocities.

Finally, the wave speed u_{waves} is evaluated by calculating the crest-to-crest distance at different positions in the tube. Table 6.2 summarizes the results for the four drag force expressions. The new drag force without the adding factor $\sqrt{\frac{\mu_{cg}}{\mu_{cl}}}$ overpredicts the wave speed whereas the three other expressions give the same results.

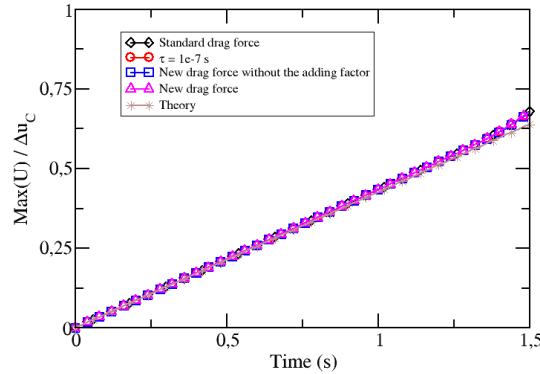


Figure 6.8: The velocity \mathbf{U} (see Equation (4.21)) normalized by the critical velocity difference (Equation 4.18), the theory is given in Equation (4.20), all the curves are superposed.

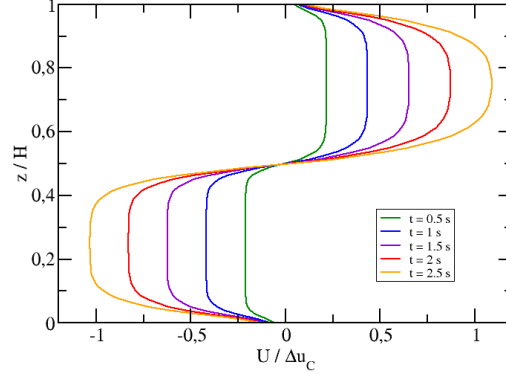


Figure 6.9: Variation of the average interface velocity \mathbf{U} normalized by the critical velocity difference (Equation (4.21)) along the tube width, new drag force given by Equation (6.7).

In Table 6.2, all the parameters defined in this simulation are summarized and compared with the theoretical and experimental data and other simulations. This test case does not allow discriminating the new drag force law and the standard one contrary to the Bhaga and Weber’s rising bubble test case. Nevertheless, we showed the necessity of the adding factor in the drag force expression especially for an accurate evaluation of the wave speed. Moreover, we highlighted the meaningful input of the new drag force, particularly for the prediction of the time of the instability onset compared to the previous drag force law (3.15) with $\tau = 1.10^{-7}$ s. Furthermore, the results obtained with the new drag force expression are in good agreement with the other data.

Results	k_c (m^{-1})	t_{onset} (s)	u_{waves} ($cm.s^{-1}$)
Standard drag force	223	1.8	3.0
Previous drag force with $\tau = 1.10^{-7}$ s	222	2.4	3.3
New drag force without $\sqrt{\frac{\mu_{cg}}{\mu_{cl}}}$	222	1.9	4.4
New drag force	219	2.1	3.1
Theory	232	1.5 – 1.7	2.38
Experiments	197 ± 58	1.88 ± 0.007	2.6
Bartosiewicz <i>et al.</i> [13]	143	1.9	2.5
Štrubelj [188]	157	2.0	3.0

Table 6.2: Comparison between the different drag force laws, the theoretical and experimental data and the simulations of Bartosiewicz *et al.* [13] and Štrubelj [188].

6.5 Conclusion

In this chapter, a new drag force expression (6.7) has been developed. The comparison with different test cases showed its ability to simulate bubble and interfacial liquid/liquid test cases with a reasonable accuracy compared to the previous drag force expression (3.15) and the standard one (6.1). Improvement in terms of shapes, velocity and pressure predictions have been highlighted. Therefore, in the following chapters, we will only consider this new drag force.

Chapter 7

Comparison between the Large Bubble Model (LBMo) and dedicated large interface tracking methods

After studying each element of the LBMo separately, this chapter compares the ability of the optimized version of the LBMo to simulate accurately large interfaces on various configurations (bubble and interfacial liquid/liquid test case) in laminar isothermal flows to other dedicated large interface tracking methods. The first section is devoted to a comparison with a VOF-PLIC approach for the simulation of an oscillating bubble. Then, in the second section, results obtained with different codes using one-fluid and two-fluid approaches are compared with the Rayleigh-Taylor instability in the Štrubelj's set of data [188]. Finally, a comparison of the LBMo with the LIM, the other method dedicated to the simulation of large interfaces in the code NEPTUNE_CFD, is proposed with the Kelvin-Helmholtz instability in the Thorpe's experimental configuration. Further comparisons are presented in Appendix G. The flows simulated in this chapter and Appendix G are laminar and isothermal with only continuous fields. No dispersed fields are considered since the LBMo is a method dedicated to the simulation of large interfaces between two continuous fields.

7.1 Résumé du chapitre

Après avoir optimisé le Modèle Large Bulle dans les trois chapitres précédents, des comparaisons du modèle avec des approches 1-fluide et bi-fluide dédiées à la simulation de grandes interfaces sont présentées. Les cas tests couvrent une variété d'écoulements à grandes interfaces : des écoulements à bulles aux écoulements interfaciaux liquide/liquide. Les comparaisons sont réalisées sur la base de données expérimentales et de solutions analytiques pour permettre une validation la plus complète possible du modèle.

7.2 Comparison with a one-fluid approach

For this comparison, the oscillating bubble test case is simulated (see section 4.3.2 for the case description). This work corresponds to the paper of Caltagirone *et al.* [24], who simulated the test case with a VOF-PLIC method (see section 2.4.4).

Contrary to Caltagirone *et al.*, the mesh refinement test is performed with an initial bubble deformation rate equal to 0.05. Indeed, Caltagirone *et al.* [24] did this analysis with an initial deformation rate equal to 0.2. However, the authors showed that this initial deformation rate is too large to be in the linear theory assumption. Deformation rate smaller than 0.1 are required to fulfill this assumption.

The four meshes are composed with: 64 x 64 cells, 128 x 128 cells, 256 x 256 cells and 512 x 512 cells. The time step is kept constant and is respectively equal to 0.1 *ms*, 0.05 *ms*, 0.025 *ms* and 0.0125 *ms*.

The results are presented in Table 7.1. As a comparison, the oscillation frequency of the bubble obtained by Caltagirone *et al.* [24] with an initial deformation rate equal to 0.2 are also given in this table. With the coarser mesh, spurious oscillations in diagonal directions are observed. Therefore, we have to be cautious with the values displayed in this table. This phenomenon was expected since the Capillary number for this simulation is approximately equal to 4.10^{-4} . Therefore, for the coarser mesh, the Capillary number is slightly smaller than the critical Capillary number (see Figure 5.3) especially at the end of the simulation when the oscillation velocity is small. The bubble oscillation is then affected by the spurious velocities which become predominant at the end of the simulation and induce spurious deformation in diagonal directions. For the frequency and the characteristic time of decay of the bubble oscillations, a convergence with the mesh refinement is observed. The oscillation frequency predicted by the LBMO is more accurate than with the VOF-PLIC. Nevertheless, these results do not allow concluding that the LBMO achieves better the simulation of the oscillating bubble. Indeed, the initial deformation rate is not the same for the two sets of data and can explain the higher relative errors obtained with the VOF-PLIC. However, we can still be confident about the small level of error, in brackets, observed with the LBMO.

In the second study, the mesh refinement is fixed (512 x 512 cells) and four different initial bubble deformation rates are simulated: $\tilde{\epsilon} = 0.4$, $\tilde{\epsilon} = 0.2$, $\tilde{\epsilon} = 0.1$ and $\tilde{\epsilon} = 0.05$. The results are shown in Table 7.2. A convergence is also observed when the deformation rate decreases, as expected [24]. Indeed, the smaller the deformation rate is, the better the bubble oscillations satisfy the linear theory, presented in section 4.3.2. The LBMO has a better prediction of the bubble oscillation frequency than the VOF-PLIC method.

7.3. COMPARISON WITH OTHER CODES ON THE RAYLEIGH-TAYLOR
INSTABILITY TEST CASE

Mesh refinement	f_0 (s^{-1})		τ_0 (s)
	NEPTUNE_CFD	VOF-PLIC [24]	
64 x 64 cells	5.71 (-)	4.79187 (16 %)	0.55 (87 %)
128 x 128 cells	5.56 (2.6 %)	4.95222 (13 %)	0.56 (87 %)
256 x 256 cells	5.68 (0.5 %)	4.98973 (13 %)	1.82 (58 %)
512 x 512 cells	5.67 (0.7 %)	5.03814 (12 %)	3.16 (28 %)

Table 7.1: Frequency and characteristic time of decay of the bubble oscillations according to the mesh refinement, obtained with the LBMo for an initial deformation rate equal to 0.05 and with the VOF-PLIC in [24] for an initial deformation rate equal to 0.2.

Deformation rate	f_0 (s^{-1})		τ_0 (s)
	NEPTUNE_CFD	VOF-PLIC [24]	
$\tilde{\epsilon} = 0.4$	5.23 (8.4 %)	4.66479 (18 %)	2.17 (50 %)
$\tilde{\epsilon} = 0.2$	5.43 (4.9 %)	5.03814 (12 %)	2.50 (43 %)
$\tilde{\epsilon} = 0.1$	5.52 (3.3 %)	5.21205 (8.7 %)	2.81 (36 %)
$\tilde{\epsilon} = 0.05$	5.67 (0.7 %)	5.50479 (3.5 %)	3.16 (28 %)

Table 7.2: Frequency and characteristic time of decay of the bubble oscillations according to the initial deformation rate, mesh with 512 x 512 cells, obtained with the LBMo and the VOF-PLIC in [24].

7.3 Comparison with other codes on the Rayleigh-Taylor instability test case

Then, another comparison is made with an interfacial liquid/liquid test case: the Rayleigh-Taylor instability in the Štrubelj’s set of data [188]. The Rayleigh-Taylor instability occurs in a system with two immiscible fluids of different densities in the presence of a gravity field, perpendicular to the interface. The fluid with higher density is initially located above the fluid with lower density.

7.3.1 Theory

As long as the flow can be analyzed with linearized Navier-Stokes’ equations, the amplitude of the interface deformation has the following expression:

$$a(t) = \delta_0 \exp(\omega t) \tag{7.1}$$

with δ_0 the initial amplitude of the interface equal to 1 *mm*.

The pulsation ω is given by:

$$\omega^2 = gkA_t - \frac{k^3\sigma}{\rho_1 + \rho_2} \quad (7.2)$$

with $A_t = \frac{\rho_1 - \rho_2}{\rho_1 + \rho_2}$, the Atwood number and $k = \frac{\pi}{L}$ the wavenumber of the initial perturbation.

7.3.2 Simulation

The simulations are performed without surface tension. Gravity is equal to 10 *m.s*⁻². The properties of the two fluids are given in Table 7.3. The Atwood number is equal to 0.5.

	Density (<i>kg.m</i> ⁻³)	Viscosity (<i>Pa.s</i>)
Liquid 1	3	0.03
Liquid 2	1	0.01

Table 7.3: Properties of the two liquid phases for the simulation of the Rayleigh-Taylor instability with Štrubelj's set of data [188].

The two immiscible liquids are contained in a closed box ($H = 5$ *m*, $L = 1$ *m*). The interface between the two fluids is initialized at 4.5 *m* high as a small cosine wave with an amplitude equal to 1 *mm*. The following expression is implemented for the initialization [188]:

$$\delta = 4.5 + \delta_0 \left(\cos\left(\frac{2\pi x}{L} - \pi\right) + 1 \right) \quad (7.3)$$

with $0 < x < L$.

The mesh contains 96 x 480 cells. A wall boundary condition is imposed at the top and the bottom of the mesh and symmetry boundary planes everywhere else. A variable time step is chosen for the simulation. Its initial value is taken equal to 1 *ms* and the maximum CFL number is fixed at 0.9.

Figure 7.1 proposes a comparison of our results with other codes, based on one-fluid and two-fluid approaches, in terms of interface shape. The smearing of the interface is well controlled by the use of interface sharpening or the geometrical interface reconstruction in the code FLUENT. Moreover, the shape of the mushroom obtained with the different codes remains the same except with FLUENT, where the mushroom is more lately extended. With the Štrubelj's in-house code [188], some particles of the above fluid are early created and detached due to the mushroom extension. This is caused by the implementation of a transition criterion between a stratified flow and a dispersed flow. Moreover, at $t = 4$ *s*, the mushroom keeps its symmetrical shape with CFX and with the Štrubelj's in-house code but not with

FLUENT and the LBMo. This loss of symmetry is probably caused by spurious velocities. CFX and the Štrubelj’s in-house code produce less spurious velocities. These adding velocities affect the mushroom motion and can induce its deformation in a non symmetrical way. Nevertheless, this effect is well controlled in the LBMo and was analyzed in Chapter 5 with the simulation of the stationary bubble.

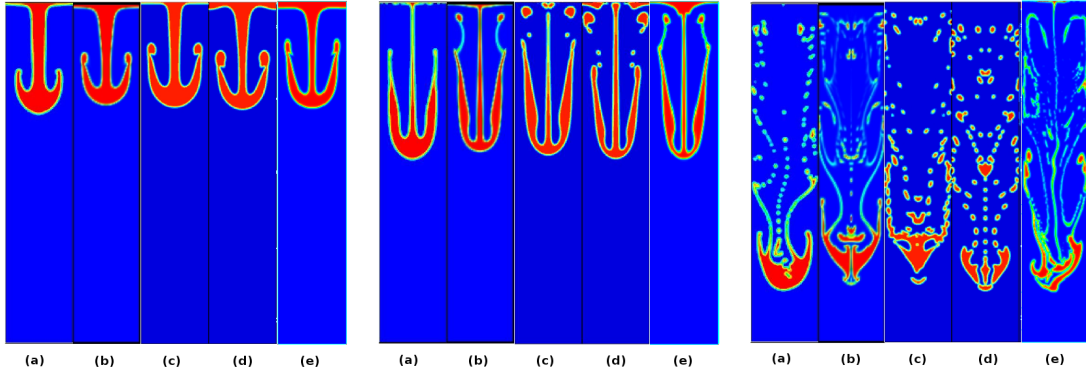


Figure 7.1: Evolution of the Rayleigh Taylor instability obtained with various models, (a) VOF with geometrical interface reconstruction in FLUENT [188], (b) VOF with interface sharpening in CFX [188], (c) single-fluid model with interface sharpening with Štrubelj’s in-house code [188], (d) two-fluid model with interface sharpening with Štrubelj’s in-house code [188], (e) LBMo, left to right: $t = 2$ s, $t = 2.5$ s and $t = 4$ s.

This test case gives another illustration in favor of the LBMo which is able to simulate large interfaces with comparable solutions to the existing numerical methods for interfacial flows.

7.4 Comparison with LIM

In this section, the comparison is only made with the Kelvin-Helmholtz instability in the Thorpe’s experimental configuration. Other comparisons can be found in Appendix G.

As previously done in section 4.5.2, the LIM and LBMo will be compared in terms of interface shape, critical wavenumber, wave velocity, time of the instability onset and evolution of the maximum value of the average interface velocity U (Equation (4.21)) at the beginning of the simulation. As a reminder, LIM simulations are performed using the same interface sharpening equation used in the LBMo and detailed in Chapter 4. A description of LIM, a method existing in the code NEPTUNE_CFD for handling large scale interfaces, is proposed in Appendix F. The simulation parameters can be found in section 4.5.2.

In Figure 7.2, a picture of the evolution of the Kelvin Helmholtz instability over time is displayed for the LBMo and the LIM. The waves appear earlier with the LIM.

The critical wavenumber is then evaluated from the interface profile at 3 s for the LBMo and 2.8 s for the LIM. We obtain 219 m^{-1} in the first case and 303 m^{-1}



Figure 7.2: Influence of the model in terms of interface shape, left: LBMo and right: LIM, only the middle 0.6 meters long section of the channel is shown.

with the LIM. These results are compared with the experimental and theoretical data and other simulation results in Table 7.4. The LBMo gives good results and the LIM does not predict accurately the wavenumber.

The interface is also examined in terms of amplitude growth in order to calculate the time of the instability onset. The results are presented in Figure 7.3. With the LBMo, t_{onset} is equal to 2.1 s and with the LIM to 2.3 s. These values correspond to a relative error of respectively 12 % and 22 %, by taking 1.88 s, the experimental results, as the reference time. Moreover, contrary to the LBMo, the amplitude growth predicted by the LIM is quicker and conducts to a higher time of the instability onset whereas the waves are visible earlier (see Figure 7.2).

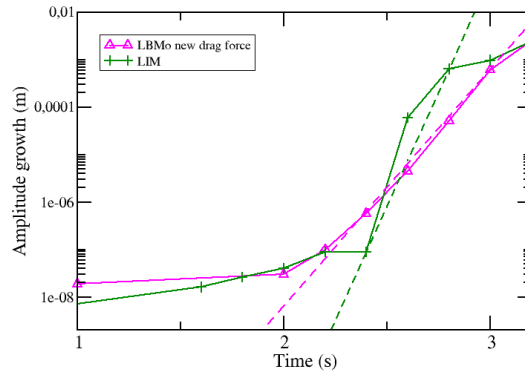


Figure 7.3: Amplitude growth obtained by evaluating the standard deviation of the interface over time.

Moreover, Figure 7.4 presents the maximum value of the average interface velocity \mathbf{U} (Equation (4.21)) over time. All the curves are superposed, which was expected since we showed in Chapter 4 that the interface velocity was not affected by the drag force if the interface sharpening equation was implemented with respect to the mass conservation and with criteria to limit the spurious velocities.

Finally, the wave speed u_{waves} is evaluated by calculating the crest-to-crest distance at different positions in the tube. We find $u_{waves} = 3.1 \text{ cm.s}^{-1}$ with the LBMo and $u_{waves} = 3.9 \text{ cm.s}^{-1}$ with the LIM. The LIM overpredicts the wave speed as previously observed in the section 6.4.2 with the new drag force expression which

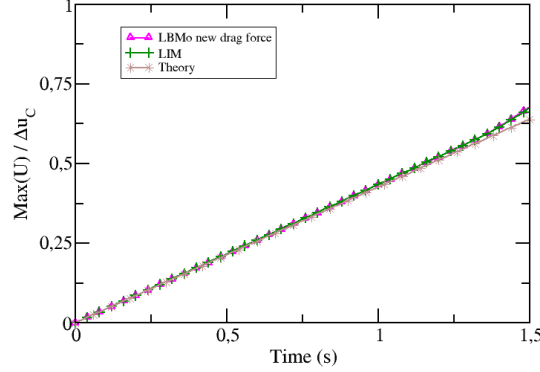


Figure 7.4: The velocity \mathbf{U} (see Equation (4.21)) normalized by the critical velocity difference (Equation 4.18), the theory is given in Equation (4.20), all the curves are superposed.

did not consider the adding factor $\sqrt{\frac{\mu_{cg}}{\mu_{cl}}}$. Thus, a smaller intensity of the drag force, due to the absence of the adding factor $\sqrt{\frac{\mu_{cg}}{\mu_{cl}}}$ or the use of an anisotropic friction model in the LIM, induced an increase of the wave speed.

In Table 7.4, all the parameters defined in this simulation are summarized and compared with the theoretical and experimental data and other simulations. This study showed that the LIM overestimates the critical wavenumber and the wave speed. For the other parameters, the two methods are comparable.

Results	k_c (m^{-1})	t_{onset} (s)	u_{waves} ($cm.s^{-1}$)
LBMo	219	2.1	3.1
LIM	303	2.3	3.9
Theory	232	1.5 – 1.7	2.38
Experiments	197 ± 58	1.88 ± 0.007	2.6
Bartosiewicz <i>et al.</i> [13]	43	1.9	2.5
Štrubelj [188]	157	2.0	3.0

Table 7.4: Comparison between the LBMo, the LIM, the theoretical and experimental data, the simulations of Bartosiewicz *et al.* [13] and Štrubelj [188].

7.5 Conclusion

This chapter combined with Appendix G confirms that the LBMo with the conservative implementation of the interface sharpening equation, the CSF model and

the new drag force expression developed in section 6.3 is able to simulate accurately a wide range of separated phases flows. The results are in good agreement with the analytical and experimental data. The same level of errors are obtained with the LBMo and other dedicated approaches for large interfaces simulations.

In the following chapters, the LBMo is retained as the model for the simulation of large interfaces in the framework of a multifield approach with a two-fluid model.

Chapter 8

Conclusion

A summary of the different test cases and parameters simulated in this part to optimize the LBMo is displayed in Table 8.1. This table compares a large variety of flows from large bubbles to interfacial liquid/liquid test cases. This study highlights that all the three elements of the LBMo which are the interface sharpening equation, the surface tension model and the drag force law, are crucial for the simulation of large interfaces within the multifield approach with a two-fluid model.

After a review of the two-phase flow modeling strategies and the description of the multifield approach, the third chapter highlighted the importance of a conservative implementation of the recompression equation not only to ensure mass conservation but also to predict with accuracy the flow behavior. Then, criteria have been implemented to solve the equation only when the interface is diffused to limit the spurious velocities induced by the recompression mass fluxes. In the fourth chapter, these velocities have been evaluated to determine the critical Capillary number. This number allows determining the level of the spurious velocities according to the characteristic velocities in the flow. Under this critical number, the physical phenomena cannot be reproduced since the simulation is driven by spurious currents. In the fifth chapter, a new drag force law suitable for the simulation of large interfaces in the framework of the multifield approach has been developed and compared to classical drag force laws. The results showed the ability of the new expression to couple precisely the velocities of the two continuous fields at the interface. To finish, the last chapter proposed a comparison of the LBMo with other methods dedicated to large interfaces within one-fluid and two-fluid models, such as the LIM. This study proved that the LBMo was able to compute with the same accuracy and computational cost different phenomena.

In this part, only laminar and isothermal flows with two continuous fields have been simulated. Thus, in the next parts, interfaces with thermal transfers and phase change, three field flows with two continuous and one gaseous dispersed field and turbulent flows will be studied. In this work, the LBMo will be used to simulate large interfaces considering the optimized implementation of each element described and validated in this part.

CHAPTER 8. CONCLUSION

	Implementa- tion	Drag force model	Threshold value	Activation of the interface smearing criterion	Test cases						
					Square bubble	Oscillating bubble	Stationary bubble	Bhaga's bubble	Kelvin- Helmholtz instability	Rayleigh- Taylor instability	
LBMo	Non conservative	Law 1	$\beta = 5.10^{-4}$	ON	X						
		Law 2			✓						
		Law 3			✓	X					
	Conservative	Law 1	$\beta = 5.10^{-4}$	ON				X	✓	✓	
		Law 2	$\beta = 5.10^{-4}$	ON		X		X	X	✓	
				OFF				X			
		Law 3	$\beta = 1.10^{-2}$ $\beta = 5.10^{-3}$ $\beta = 1.10^{-3}$	ON		X	X				
								X	X	X	
						✓	✓	✓	✓	✓	✓
						✓				X	
	$\beta = 5.10^{-4}$	ON		✓							
	$\beta = 1.10^{-4}$	ON			✓	X					
LIM	Conservative	Law 1	$\beta = 5.10^{-4}$	ON		✓		X	X	✓	

Table 8.1: Summary of the test cases and parameters simulated in the first part of the thesis: Treatment of the large interfacial structures, the crosses symbolize that no reasonable results were obtained whereas the ticks correspond to an accurate simulation of the cases, for the drag force model, law 1 refers to the drag force model in Equation (6.1), law 2 to Equation (3.15) and law 3 to Equation (6.7).

Part II

Computation of heat and mass transfers

In the previous part, the LBMo has been improved to simulate accurately large and deformable inclusions in the framework of the multifield approach based on a two-fluid model. However, only isothermal flows have been considered. Moreover, simulations were performed with only two continuous fields. Small spherical structures were not considered. In this part, we are now interested in heat and mass transfers. Two types of mass transfers appear in complex boiling flows. The first type which corresponds to the first chapter is the mass transfer due to phase change between liquid water and steam. Since the simulation of large interfaces with a two-fluid model is quite new, a specific mass transfer term is proposed and validated. The second type of mass transfer is intrinsically linked to the multifield approach. Indeed, the gaseous phase is split into two fields: a continuous and a dispersed one. Therefore, coalescence of small spherical bubbles and breakup of large ones have to be considered. In the second chapter, three field simulations are performed to highlight the ability of the existing mass transfer term, presented in section 3.6, to simulate accurately these two phenomena (coalescence and breakup). Finally, in the third chapter, the multifield approach is used to predict various flow regimes. An improvement of the transfer term dealing with the coalescence of small spherical bubbles is also presented.

Chapter 9

Simulation of large interfaces with phase change

This chapter is devoted to phase change occurring at large interfaces. Thus, in this chapter, the test cases contain only continuous fields. No dispersed fields are considered. The main goal is to detail the required adjustments of the Large Bubble Model to simulate accurately phase change. Moreover, the implementation and validation of a new heat and mass transfer term is discussed. These developments will be illustrated by different simulations involving water/steam flows.

9.1 Résumé du chapitre

Après avoir amélioré et validé le Modèle Large Bulle dans le cas d'écoulements laminaires et isothermes, on s'intéresse ici à sa mise en application pour les grandes interfaces avec changement de phase de type eau/vapeur. Une première étape vers cette extension du modèle consiste à modifier l'implémentation de l'équation de recompression pour s'assurer de la cohérence entre la température, la pression, la fraction volumique et la densité de chaque phase et ainsi de conserver la masse. Dans un second temps, il est nécessaire de développer un modèle de transfert de masse consistant avec le Modèle Large Bulle et l'approche bi-fluide. Ce nouveau modèle est validé sur plusieurs cas tests académiques de condensation et d'évaporation dans des conditions de pression allant de la pression atmosphérique aux pressions observées en centrale nucléaire. Comme pour les chapitres précédents, les champs sont continus. Aucun champ dispersé n'est considéré. Les écoulements sont laminaires, incompressibles mais anisothermes. L'équation d'énergie est donc résolue.

9.2 Adjustment of the numerical scheme

To deal with phase change flows, new quantities such as enthalpy, temperature but also density have to be taken into account. To evaluate the enthalpy and so the temperature fields, the energy balance equation (see Equation (2.31)) is solved.

Nevertheless, these two parameters are coupled with the density, the pressure and the volume fraction by the thermodynamics laws. Therefore, the resolution of the energy balance equation has to be integrated in the numerical scheme so that all the physical properties of the flow are consistent. The equation is thus solved in the α -P-H loop, as shown in Figure 9.1. At the end of this loop, volume fraction, pressure and enthalpy of each field are determined with respect to the thermodynamics laws. These three quantities can then be used to calculate the temperature and the density of each field. This step is done at the very beginning of each time step (see Figure 9.1).

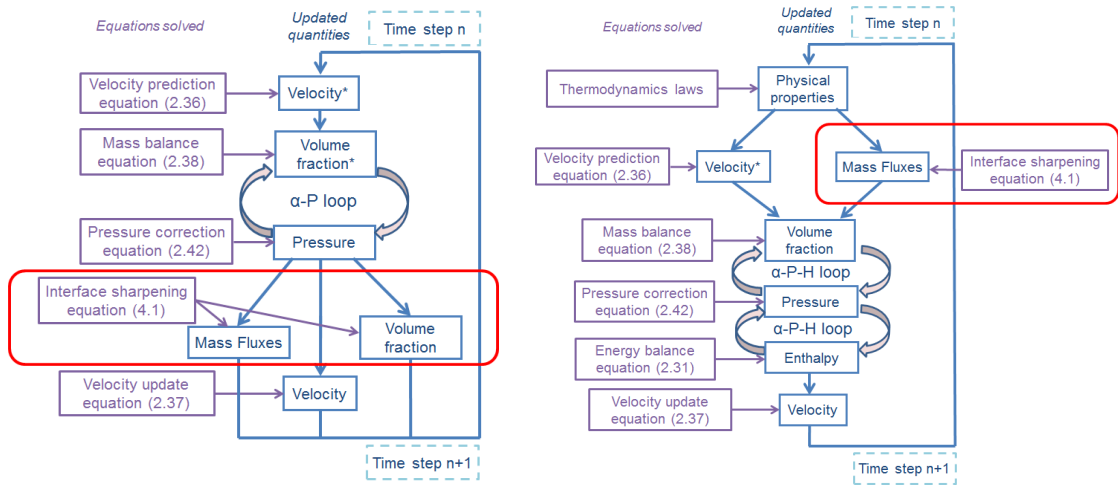


Figure 9.1: Schematic view of the numerical scheme used in the code `NEPTUNE_CFD`, left: for isothermal test cases, right: for test cases with phase change, the physical properties refer here to the temperature and the density, * denotes the intermediate values.

9.3 Adjustment of the Large Bubble Model

In water/steam flows, the steam density can vary in space and in time. Therefore, the interface sharpening step has to be adapted to ensure mass conservation with variable densities.

In a first approach, simulation of phase change flows have been performed with the interface sharpening equation implemented in Chapter 4. Nevertheless, the mass balance error in the whole domain at each time step reached 10^{-10} %, which means that the method did not ensure mass conservation. After the resolution of the α -P-H loop, the mass balance error was equal to zero. However, after the interface sharpening step, the error jumped. Indeed, with these flows and contrary to the isothermal test cases studied previously, the densities vary according to the thermodynamic laws. They are then updated at the beginning of each time step (see Figure 9.1) according to the value of the volume fractions, the pressure and the enthalpy which are iteratively calculated in the α -P-H loop. Nevertheless, the modification of the volume fraction in the interface sharpening equation is done regardless of the other quantities which are not corrected. Thus, the solution of

this issue is to find a way to correct the volume fraction when the enthalpy and the pressure are calculated, which means in the α -P-H loop. Therefore, the interface sharpening equation is moved before the loop (instead of after, see in Figure 9.1). The same equation is solved. However, the sharpened volume fractions obtained after the resolution are not used directly as done before. Instead, the mass fluxes evaluated are injected in the α -P-H loop to find the new volume fraction with regard to the pressure and the enthalpy. With these modifications, the mass balance error in the whole domain at each time step is decreased at 10^{-17} % corresponding to the same error level obtained with the isothermal test cases.

9.4 Implementation of a new heat and mass transfer source term

In this section, different mass transfer models for phase change used in the literature are detailed. Then, these models are adapted to the multifield approach. For this purpose, the relation between the heat and mass transfer terms is explained before proposing a new model for the heat transfer term, suitable for interfaces treated with the Large Bubble Model.

9.4.1 Relation between mass transfer terms and heat fluxes

In the energy balance equation (2.31), the term $E_{p \rightarrow k}^{Int}$ refers to the energy transfers occurring at large interfaces. This term can be split into two contributions, one related to mass transfer and the second to heat transfer:

$$E_{p \rightarrow k}^{Int} = \Gamma_{p \rightarrow k} H_{p \rightarrow k}^{Int} + q_{p \rightarrow k} \quad (9.1)$$

$\Gamma_{p \rightarrow k}$ corresponds to the mass transfer term in the mass balance equation (2.29) and $q_{p \rightarrow k}$ the interfacial heat flux. To obtain the expression of this term, we consider that the enthalpy jump for the vapor phase is independent on the jump for the liquid phase, ie $H_{cl \rightarrow cg}^{Int} \neq H_{cg \rightarrow cl}^{Int}$. Within this assumption, the relation $E_{cl \rightarrow cg}^{Int} + E_{cg \rightarrow cl}^{Int} = 0$ allows writing:

$$\Gamma_{p \rightarrow k} = \frac{q_{p \rightarrow k} + q_{k \rightarrow p}}{H_{p \rightarrow k}^{Int} - H_{k \rightarrow p}^{Int}} \quad (9.2)$$

For a water/steam flow, the following assumption is made:

$$H_{p \rightarrow k}^{Int} = H_k \quad (9.3)$$

After introducing independent models for heat transfers,

$$q_{p \rightarrow k} = q_k^V \quad (9.4)$$

the mass transfer term can be presented as follows:

$$\Gamma_k = \frac{q_k^V + q_p^V}{H_p - H_k} \quad (9.5)$$

with $|H_p - H_k| = L$ the latent heat.

9.4.2 Available models in the literature

Different phase change models are available in the literature. The most widely used is the model proposed by Lee [99], based on an empirical expression to quantify the interfacial heat and mass transfer term:

$$\begin{aligned} \Gamma_{cl} = -\Gamma_{cg} &= r\alpha_{cl}\rho_{cl}\frac{T-T_{sat}}{T_{sat}} & \text{if } T > T_{sat} \\ \Gamma_{cl} = -\Gamma_{cg} &= r\alpha_{cl}\rho_{cl}\frac{T_{sat}-T}{T_{sat}} & \text{if } T < T_{sat} \end{aligned} \quad (9.6)$$

with r the empirical mass transfer intensity factor. The r factor is fixed to bring the temperature of the cells containing the interface close to the saturation temperature. However, a large range of values has been obtained in the literature from 0.1 s^{-1} [4, 174, 215] to 100 s^{-1} [46, 219]. It has also been shown that too large values could induce numerical instabilities with oscillations of the temperature around the saturation temperature.

To avoid the issue of fixing an empirical coefficient, the development of a formulation based on theoretical considerations is necessary. Thus, to estimate the heat flux jump at the interface, the Fourier's law is applied. The interfacial heat flux can then be written as follows:

$$q^{Int} = q_l^S + q_v^S \quad (9.7)$$

with:

$$q_l^S = -\lambda_l \nabla T_l \cdot \mathbf{n} \quad (9.8)$$

and

$$q_v^S = \lambda_v \nabla T_v \cdot \mathbf{n} \quad (9.9)$$

with \mathbf{n} the normal vector to the interface pointing from the vapor phase to the liquid phase, ∇T_l and ∇T_v the temperature gradients in respectively the liquid and the vapor phases and λ the thermal conductivity.

Therefore, the mass transfer flux has the following expression:

$$\Gamma_{cl} = -\Gamma_{cg} = \frac{q^{Int} \cdot \mathbf{n} A^{Int}}{L\Omega} \quad (9.10)$$

with A^{Int} the interface area in a grid cell and L the latent heat. This model and other similar approaches have been used by several research groups [54, 86, 117, 142, 189] with VOF or Level-Set methods to track the interface. Nevertheless, all these models are applied to interfaces contained in one grid cell. In the framework of the multifield approach with the two-fluid model, the large interfaces are diffused over a few cells. The expression of q^{Int} in Equation (9.7) has to be adapted to interfaces with a

non zero thickness. Thus, the development and implementation of the heat transfer model within the multifield approach is detailed in the next section.

9.4.3 New heat transfer term

The expressions of the interfacial heat fluxes q_l^S and q_v^S ($W.m^{-2}$) given in Equations 9.8 and 9.9 are valid for interfaces with zero thickness. Therefore, the term has to be adapted to large interfaces treated with the LBMo (with a 5 cells thickness). For this purpose, a volume reformulation is used, based on the procedure applied to the surface tension force by Brackbill *et al.* [21]. Indeed, we know that the exact expression of the liquid heat flux is:

$$q_l^S = \lambda_l \nabla T_l \cdot \mathbf{n} \quad (9.11)$$

For the demonstration here, only the liquid term is considered. Nevertheless, the same process can be followed to obtain the volume reformulation of the vapor term. As done for the surface tension model, the volume expression of the heat fluxes q_l^V can be obtained by considering:

$$\lim_{h \rightarrow 0} \int_{V^{Int}} q_l^V(x) dx^3 = \int_{A^{Int}} q_l^S(x^{Int}) dA \quad (9.12)$$

with h the interface thickness, V^{Int} the volume of an interface with a thickness equal to h and A^{Int} the area of a zero thickness interface.

Thus,

$$\begin{aligned} \int_{A^{Int}} q_l^S(x^{Int}) dA &= \int_{V^{Int}} q_l^S(x) \delta(\mathbf{n}(x^{Int}) \cdot (x - x^{Int})) dx^3 \\ &= \int_{V^{Int}} \lambda_l \nabla T_l(x) \cdot \mathbf{n}(x) \delta(\mathbf{n}(x^{Int}) \cdot (x - x^{Int})) dx^3 \end{aligned}$$

with δ the Dirac function. In [21], the interface is located with a color function c , using a VOF approach. Thus, by introducing the notations of this article, we can write the following relation between the color function gradient of the diffused interface and the normal vector \mathbf{n} :

$$\lim_{h \rightarrow 0} \nabla c(x) = \mathbf{n}(x) \delta(\mathbf{n}(x^{Int}) \cdot (x - x^{Int})) [c] \quad (9.13)$$

with $[c]$ the jump of the color function over the interface.

Using this expression, we obtain:

$$\int_{A^{Int}} q_l^S(x^{Int}) dA = \lim_{h \rightarrow 0} \int_{V^{Int}} \lambda_l \nabla T_l(x) \frac{\nabla c(x)}{[c]} dx^3 \quad (9.14)$$

Therefore, the volume expression of the heat fluxes q_l^V with the color function c is:

$$q_l^V(x) = \lambda_l \nabla T_l(x) \frac{\nabla c(x)}{[c]} \quad (9.15)$$

In the two-fluid formulation, this expression is rewritten:

$$q_k^V(x) = \beta_k \lambda_k \nabla T_k(x) \nabla \alpha_k(x) \quad (9.16)$$

with $\nabla T_k = \frac{T_{sat} - T_k}{d^{Int}}$ and d^{Int} the distance to the interface. β_k is introduced to distribute the term over the two phases. For this parameter, the mass and the volume formulation will be considered in the validation section.

$$\beta_k = \frac{\alpha_k \rho_k}{\sum \alpha_i \rho_i} \quad (9.17)$$

or

$$\beta_k = \alpha_k \quad (9.18)$$

One can note that the volume formulation has been chosen for the surface tension model.

9.5 Validation of the new heat transfer model

To validate the Large Bubble Model with phase change and the specific mass transfer source terms, five different academic test cases with steam and water are simulated. In this section, only two cases will be shown. Extra validations can be found in Appendix I. In all these simulations, the interface motion is only driven by heat transfer. The results will be compared with the LIM heat transfer model (see Appendix F). The effect of the volume and the mass formulations will also be studied.

9.5.1 Sucking problem

In the sucking problem, steam and liquid water are contained in a 1D tube with a heated wall (see Figure 9.2). The liquid is superheated at T_{max} and the wall temperature is fixed at $T_{wall} = T_{sat}$ so that steam is at the saturation temperature (see Figure 9.3). Therefore, there is no temperature gradient in the vapor. Both fields are at the rest at $t = 0$ s. For $t > 0$ s, the liquid begins to boil at the interface, which induces a displacement of the steam/water interface.

9.5.1.1 Theory

The theory of the sucking problem is given in [212]. In this section, we are just going to give the energy balance equations in the liquid phase and its solution. In Appendix H, details about the calculation are given.

First, let us make a transformation of the spatial coordinates such as the steam/water is located at $\xi = 0$:

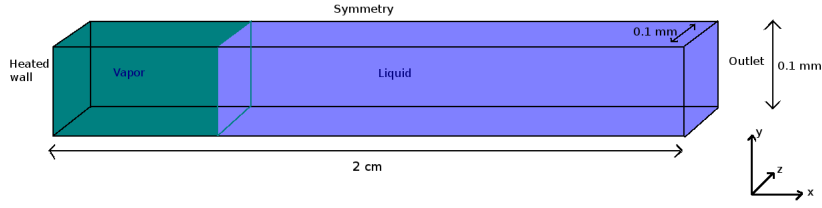


Figure 9.2: Definition sketch of the 1D computational domain used for the simulation of the sucking problem.

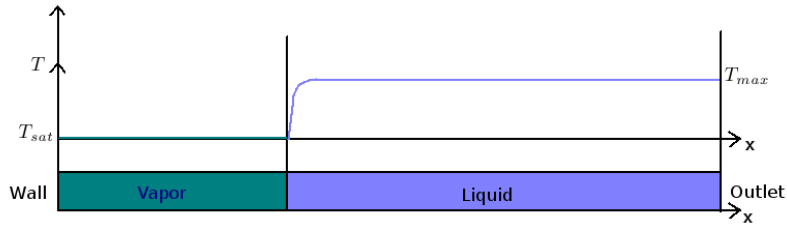


Figure 9.3: Simulation conditions at a given time for the sucking problem, the liquid boils and the interface moves to the right side due to volume expansion of the liquid-vapor phase change.

$$\xi = x - \int_0^t v_s(t') dt' \quad (9.19)$$

With v_s the interface velocity.

With this new coordinate, the energy balance equation in the liquid phase can be written:

$$\frac{\partial T}{\partial t} + (v - v_s) \frac{\partial T}{\partial \xi} = \chi_l \frac{\partial^2 T}{\partial \xi^2} \quad (9.20)$$

To solve this equation, different constants are introduced:

$$B = \frac{\chi_l \rho_l}{C \rho_v}, \quad C = \frac{\lambda_l}{L \rho_v} \quad \text{and} \quad \beta = \frac{\rho_v}{\rho_l} \quad (9.21)$$

χ_l being the thermal diffusivity of the liquid phase, λ_l its thermal conductivity and L the latent heat between steam and liquid water.

By using the following boundary conditions:

$$\begin{aligned} T(\xi = 0, t) &= T_{sat} \\ T(\xi \rightarrow \infty, t) &= T_{max} \\ T(\xi, t = 0) &= T_{max} \end{aligned}$$

and the following notation:

$$T(x, t) = B\phi(\eta) \quad (9.22)$$

with $\eta = \frac{\xi}{\sqrt{2\chi t}}$.

We finally obtain:

$$T = T_{sat} + B\phi'(0)\exp(x_0^2)\sqrt{\frac{\pi}{2}}\operatorname{erf}(x_0, x) \quad (9.23)$$

with $x = \frac{\eta+\phi'(0)}{\sqrt{2}}$, $x_0 = \frac{\phi'(0)}{\sqrt{2}}$ and $\operatorname{erf}(x_0, x) = \frac{2}{\sqrt{\pi}}\int_{x_0}^x \exp(-t^2) dt$, the error function.

With the same energy balance equation, the evolution of the interface position can be obtained:

$$X(t) = \frac{\phi'(0)}{\beta}\sqrt{2\chi t} \quad (9.24)$$

9.5.1.2 Simulation

The study is based on Sato's and Welch's publications [171, 212]. The physical properties of steam and water are given in Table 9.1. They are updated at each time step (see Figure 9.1 right) using the standard set of thermodynamic Equations Of State based on CATHARE functions [44]. The pressure of the system is equal to $1.013.10^5 Pa$ (the atmospheric pressure), the latent heat to $2.27.10^6 J.kg^{-1}$ and the liquid temperature in the bulk to $T_{max} = 378.15 K$.

	Density ($kg.m^{-3}$)	Viscosity ($Pa.s$)	Heat capacity ($J.kg^{-1}.K^{-1}$)	Thermal conductivity ($W.m^{-1}.K^{-1}$)
Steam	0.578	$1.3.10^{-5}$	$1.5.10^3$	$2.52.10^{-2}$
Liquid water	956.5	$2.7.10^{-4}$	$4.2.10^3$	0.687

Table 9.1: Properties of the two fluids for the simulation of the sucking problem with a pressure of $1.013.10^5 Pa$.

The tube length is equal to 2 cm. A heated wall boundary condition ($T_{wall} = T_{sat}$) is imposed on the left face, an outlet boundary condition on the right face and symmetry planes everywhere else (see Figure 9.2). The liquid temperature is initialized by using Equation (9.23) at $t = 0.1 s$. Therefore, the interface position at the beginning of the simulation is compared to the theoretical position at $t = 0.1 s$. Finally, for the error function (used to initialize the temperature profile), two approximated expression have been implemented according to the values of x_0 and x :

$$\begin{aligned}
 x \leq 0.5 : \quad erf(x) &= \frac{2exp(-x^2)}{\sqrt{\pi}} \left(x + \frac{2}{3}x^3 + \frac{4}{15}x^5 \right) \\
 x > 0.5 : \quad erf(x) &= 1 - exp(-1.9x^{1.3})
 \end{aligned}
 \tag{9.25}$$

Four different mesh refinements have been used with cell sizes equal to: $1.10^{-4} m$, $5.10^{-5} m$, $2.5.10^{-5} m$ and $1.25.10^{-5} m$. The time step is kept constant and fixed according to the grid and the heat transfer model to ensure a constant Fourier number in all the simulations:

$$F_0 = \frac{\chi_v \Delta t}{\Delta x^2} \tag{9.26}$$

with Δt the time step, Δx the cell size, χ_v the thermal diffusivity of steam. The time steps are respectively equal to $4.10^{-4} s$, $1.10^{-4} s$ and $2.5.10^{-5} s$ for the LIM and the LBMo with the mass formulation and to $1.6.10^{-3} s$, $4.10^{-4} s$, $1.10^{-4} s$ and $2.5.10^{-5} s$ for the LBMo with the volume formulation. With the LIM and the LBMo with the mass formulation, the most refined mesh is not simulated since it would require a time step smaller than the time steps allowed by the code NEPTUNE_CFD.

It is important to note that the initialization of the interface depends on the model used to track large interfaces. Indeed, with the LI3C used with the LIM, three cells have to be detected: one with a higher quantity of steam, one with a higher quantity of liquid and the last one with the two fluids in the same proportion. Thus, steam is defined in the first four cells, the following cell contains 75 %, 50 % and 25 % of steam and the rest of the domain is full filled with liquid. For the LBMo, the interface have a five cell thickness. Therefore, steam is also defined in the first four cells, the five next cells are composed with a mixture of the two phases and the rest of the domain is full filled with liquid. The five mixed cells have the following composition in steam: 87.5 % for the first one, 75 %, 50 %, 25 % and 12.5 %.

In all the simulations even with the LIM, the interface sharpening equation is solved. Indeed, without this step, the interface diffuses when it moves. Thus, the initialized mixed cells have to be consistent with the interface thickness imposed by the interface sharpening equation (see section 3.4.3). With the LIM, the final interface thickness defined by the two parameters τ and ε is decreased and equal to 3 cells.

This case under atmospheric pressure is really interesting to compare methods since the temperature gradient at the interface is significant. Thus, the different approaches are well discriminated.

To compare the analytical solution with the simulation results, special care has to be taken concerning the interface and the temperature profile position. Indeed, in the analytical view of the test case (see Figure 9.4), the interface has a zero thickness and the temperature jump corresponds to the interface position. In the simulation, the temperature jump begins where the liquid is present, that is to say at one extremity of the interface (see Figure 9.4). In the post-processing procedure, the position of the interface is taken where $\alpha_{cg} = \alpha_{cl} = 0.5$ corresponding to the center of the smeared interface. Since we consider that the analytical interface position

corresponds to the position of the temperature jump, we have to shift the simulated results. Thus, an initial time onset is evaluated using the analytical expression of the interface position over time by taking the analytical interface position at 0.1 s (the temperature profile is initialized at 0.1 s) decreased by $2.5\Delta x$ for the LBMo (5 cells thickness) and $1.5\Delta x$ for the LIM (3 cells thickness). The simulated results are shifted using this time onset. Moreover, the interface position at 0.1 s in all the curves is considered as the zero position.

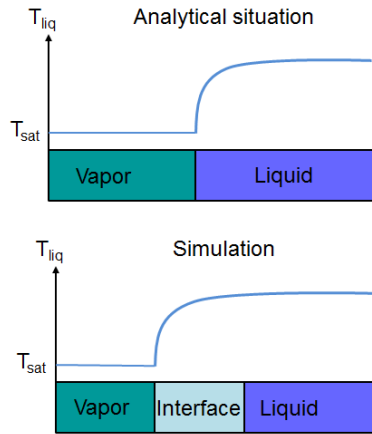


Figure 9.4: Schematic view of the temperature profile and vapor/liquid interface in the analytical test case (top) and the simulation (bottom), sucking problem.

The results are given in Figure 9.5. The LBMo with the mass formulation seems not suitable for the heat transfer model since it does not converge to the theoretical curve. Concerning the LIM results, numerical instabilities appear. Steam is created in the liquid bulk, which affects the results and makes comparison difficult. Moreover, the more refined the mesh is, the closer to the analytical solution the results are with the LBMo and the volume formulation. The results obtained with the most refined mesh and the LBMo combined with the volume formulation are very close to the analytical results. This confirms the ability of the developed model to predict an interface motion only driven by the heat transfer term. Figure 9.6 presents the corresponding average relative error for the interface position between 0.1 s and 1.5 s . When the mesh is refined, the error increases with the LBMo and the mass formulation, which means that the simulated results move away from the analytical solution. For the LBMo with the volume formulation, the error decreases. This study allows defining the order of convergence (using the Richardson's extrapolation (4.8)) of the LBMo with the volume formulation, equal to 1.1.

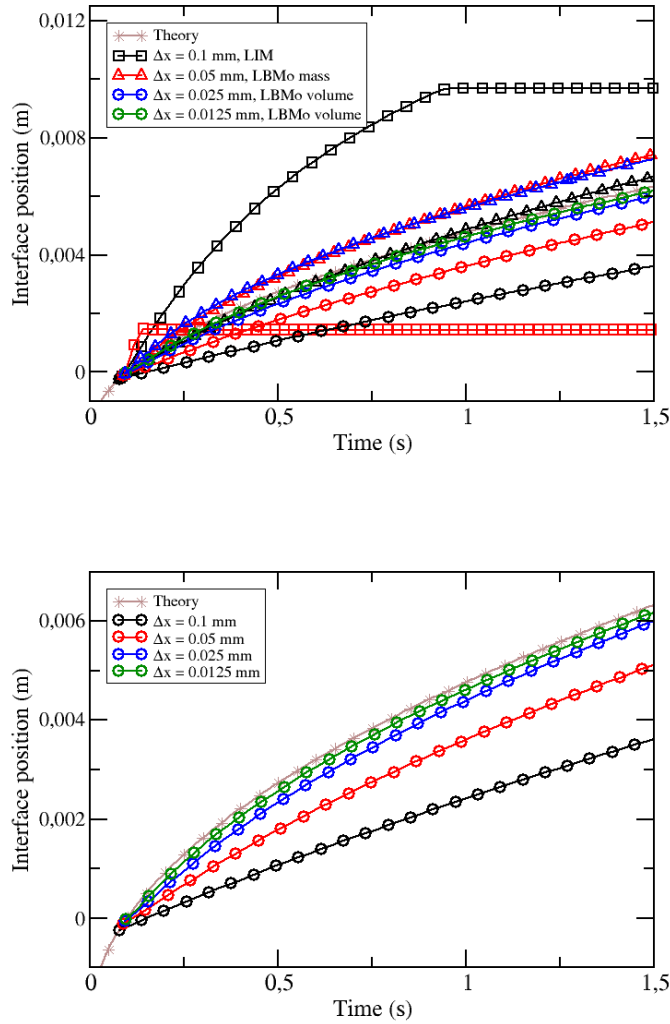


Figure 9.5: Evolution of the interface position obtained with different heat transfer models and mesh refinements, sucking problem at an atmospheric pressure, all the notations and colors are not given in the top picture for sake of clarity, squares: LIM, triangles: LBMo with a mass formulation, circles: LBMo with a volume formulation, black curves: $\Delta x = 1.10^{-4} \text{ m}$, red curves: $\Delta x = 5.10^{-5} \text{ m}$, blue curves: $\Delta x = 2.5.10^{-5} \text{ m}$ and green curves: $\Delta x = 1.25.10^{-5} \text{ m}$, bottom picture: results obtained with the LBMo and a volume formulation only.

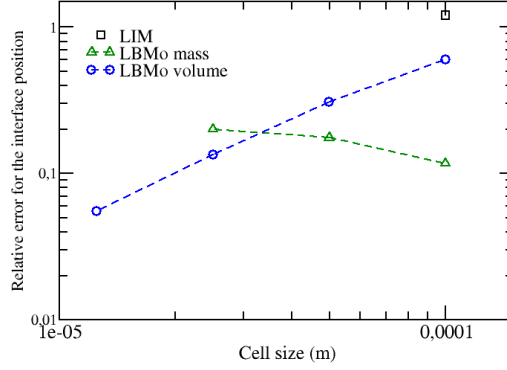


Figure 9.6: Average relative error for the interface position compared to the theoretical results between 0.1 s and 1.5 s, sucking problem at an atmospheric pressure.

This study highlights that the volume formulation is the more suitable one. This formulation will be chosen for the rest of this report.

9.5.2 Stefan problem

The Stefan problem is very close to the sucking problem. Vapor and liquid are contained in a 1D tube with a heated wall under atmospheric pressure. But, in this case, vapor is superheated and the liquid temperature is equal to the saturation temperature $T_{sat} = 373.15 \text{ K}$. The wall temperature keeps a constant value during the simulation: $T_{wall} = 398.15 \text{ K}$. As a consequence, there is a temperature gradient in the vapor phase (see Figure 9.7).

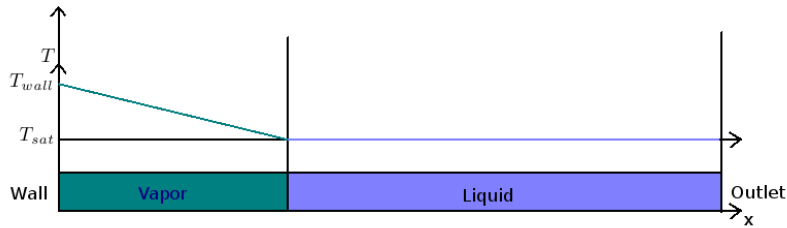


Figure 9.7: Simulation conditions at a given time for the Stefan problem, the liquid boils and the interface moves to the right side due to volume expansion of the liquid-vapor phase change.

9.5.2.1 Theory

The evolution of the interface position is given by the equation [212]:

$$X(t) = 2\beta\sqrt{\chi_v t} \quad (9.27)$$

with $\chi_v = \frac{\lambda_v}{\rho_v C_{pv}}$ the thermal diffusivity, λ_v the thermal conductivity and C_{pv} the specific heat capacity of vapor.

The temperature profile is equal to :

$$T(x, t) = T_{wall} + \left(\frac{T_{sat} - T_{wall}}{\text{erf}(\beta)} \right) \text{erf}\left(\frac{x}{2\sqrt{\chi_v t}} \right) \quad (9.28)$$

$\text{erf}(x)$ corresponds to the error function.

β is the solution of the equation :

$$\beta \exp(\beta^2) \text{erf}(\beta) = \frac{C_{pv}(T_{wall} - T_{sat})}{\sqrt{\pi} L} \quad (9.29)$$

with L the latent heat of vaporization.

9.5.2.2 Simulation

The physical properties of steam and water are the same as the sucking problem at $1.013 \cdot 10^5 \text{ Pa}$ (see Table 9.1). They are also updated at each time step (see Figure 9.1 right) using the standard set of thermodynamic Equations Of State based on CATHARE functions [44]. The pressure of the system is equal to $1.013 \cdot 10^5 \text{ Pa}$, the latent heat to $2.27 \cdot 10^6 \text{ J.kg}^{-1}$. The same grids have been used with the same boundary conditions. The only difference is the wall temperature which is equal to 398.15 K , that is to say $T_{sat} + 25 \text{ K}$, in the Stefan problem instead of T_{sat} in the sucking problem. The time steps are respectively equal to $1.6 \cdot 10^{-3} \text{ s}$, $4 \cdot 10^{-4} \text{ s}$ and $1 \cdot 10^{-4} \text{ s}$ for the two approaches (the LBMo with the volume formulation and the LIM). The interface sharpening equation is solved in all cases with a 5 cells thickness for the LBMo and 3 cells for the LIM.

The volume fractions are initialized as previously done with the sucking problem. The initial vapor temperature is approximated using an affine function:

$$T_v(x) = T_{wall} - \frac{(T_{wall} - T_{sat})x}{d} \quad (9.30)$$

with $d = 9\Delta x$ (four cells full of vapor and five mixed cells) for the LBMo and $d = 7\Delta x$ (four cells full of vapor and three mixed cells) for the LIM, which corresponds to the ‘‘end’’ of the interface (see Figure 9.8) and x the position of the cell center.

Concerning the comparison of the simulation results and the analytical solution, the same observations can be done with the location of the interface and temperature deflection, as shown in Figure 9.8. The time onset is calculated using the initial computed interface center position increased by $2.5\Delta x$ for the LBMo and $1.5\Delta x$ for the LIM.

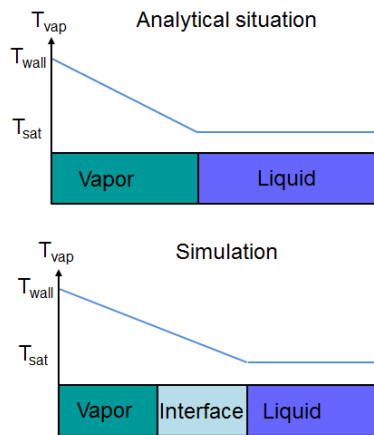


Figure 9.8: Schematic view of the temperature profile and vapor/liquid interface in the analytical test case (top) and the simulation (bottom), Stefan problem.

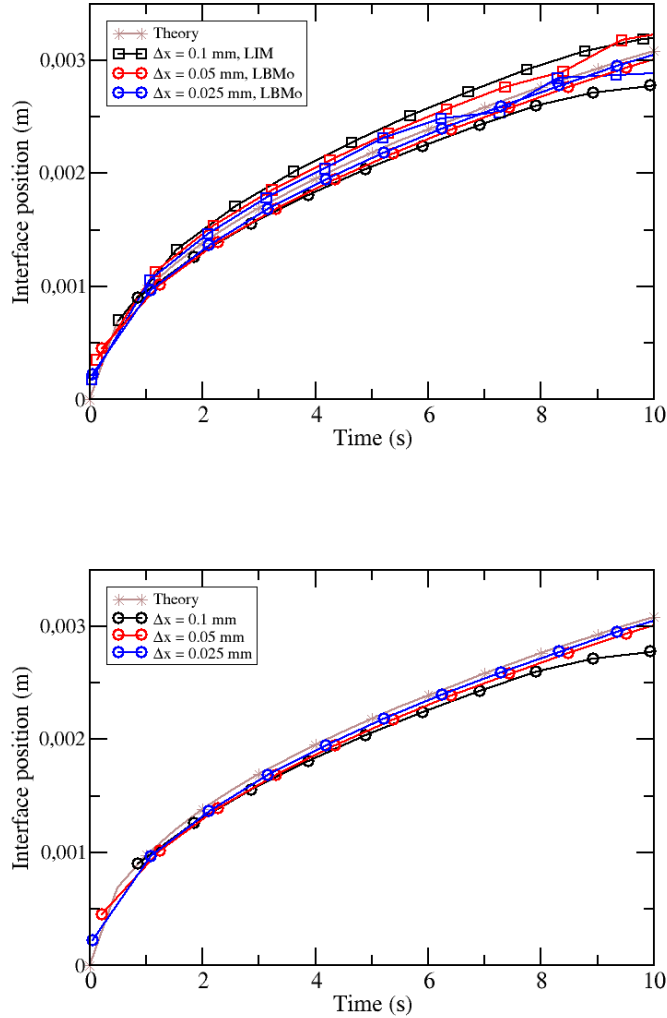


Figure 9.9: Evolution of the interface position obtained with different heat transfer models and mesh refinements, Stefan problem at an atmospheric pressure, all the notations and colors are not given in the top picture for sake of clarity, squares: LIM, circles: LBMo with a volume formulation, black curves: $\Delta x = 1.10^{-4} m$, red curves: $\Delta x = 5.10^{-5} m$ and blue curves: $\Delta x = 2.5.10^{-5} m$, bottom picture: results obtained with the LBMo with a volume formulation only.

The results are given in Figure 9.9. Contrary to the sucking problem, the two methods are very close. This result can be explained by the fact that the local temperature gradient at the interface is smaller even if in the whole domain the temperature difference is higher (equal to $25 K$ versus $5 K$ in the sucking problem). Thus, the two approaches can handle it more easily. The LIM overestimates the interface position whereas the LBMo underestimates it. Numerical instabilities remains with the LIM. Figure 9.10 presents the corresponding average relative error for the interface position for the first $10 s$. When the mesh is refined, the error

decreases for the two approaches. The order of convergence (using the Richardson's extrapolation (4.8)) of the LIM is equal to 0.53 and the LBMo with the volume formulation to 0.74.

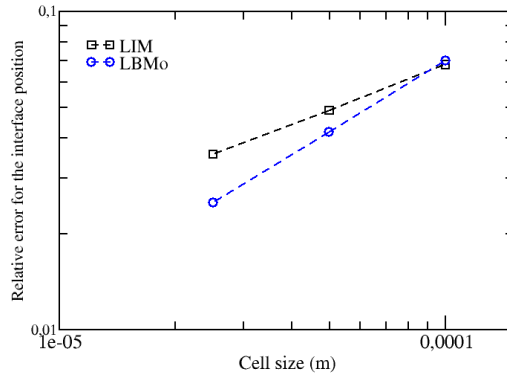


Figure 9.10: Average relative error for the interface position compared to the theoretical results for the first 10 s, Stefan problem at an atmospheric pressure.

9.6 Conclusion

The error obtained with the LBMo using the volume formulation for the five test cases presented in this chapter and Appendix I are summarized in Figure 9.11. The order of convergence is around equal to 1. All the simulations performed highlighted that the mass formulation was not suitable. Results were comparable to the LIM which is a method dedicated to the simulation of large interfaces. Moreover, the model is able to simulate phase change under pressure conditions occurring in the primary and secondary circuits in nuclear reactor vessel or steam generators. Finally, the extension to 3D simulations was straightforward (see Appendix I).

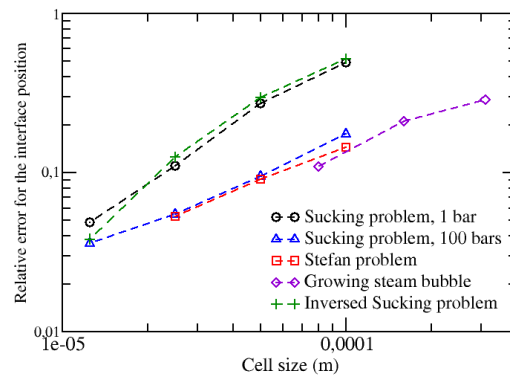


Figure 9.11: Average relative error for the interface position compared to the theoretical results obtained for the five test cases presented in Chapter 9 and Appendix I with LBMo and a volume formulation.

Chapter 10

Simulation of multifield flows with coexistence of large interfaces and a dispersed gas field

In the previous chapters, only two-phase flows with two continuous fields have been considered. Thus, in this chapter, a validation of the multifield approach using the LBMo optimized in Part I is proposed. After showing the benefits of the Large Bubble Model and improving the implementation of the interface sharpening equation and the drag force law, we want to validate the approach on multifield flows. The mass transfer terms presented in section 3.6 and dedicated to the coalescence and breakup of bubbles are also assessed to ensure an accurate simulation of complex flows containing a large range of bubble sizes and shapes. An extra validation of the multifield approach can be found in Appendix K.

In all this chapter, the flows are considered isothermal. The mass transfer term developed in the previous chapter between a continuous gas field and a continuous liquid field is not used. This work is only devoted to mass transfers occurring between two fields of the same phase, that is to say transfers between the continuous gas field and the dispersed gas field. The large deformable bubbles are treated using the LBMo whereas the small spherical bubbles are considered as a dispersed field.

10.1 Résumé du chapitre

Dans le chapitre précédent un premier type de transfert entre champs a été étudié. Ces transferts sont de type anisotherme et impliquent deux champs issus de deux phases différentes. Cependant, avec l'approche multi-champ, un second type de transfert apparaît. En effet, la phase gazeuse est scindée en deux champs: un champ dispersé gaz contenant les petites bulles sphériques et un champ continu gaz dans les grosses poches déformables. La coalescence des petites bulles sphériques pouvant générer de grosses inclusions déformables, il faut être capable de transférer le champ dispersé vers le champ continu gaz. A l'inverse, les grosses poches de gaz peuvent se fractionner pour former des petites structures sphériques. Pour modéliser ces

phénomènes de coalescence et de fractionnement, un terme de transfert isotherme entre champs d'une même phase doit être développé. Dans ce chapitre, la capacité de l'approche multi-champ couplée au Modèle Large Bulle à simuler des écoulements contenant des structures de tailles très variées est donc évaluée. Les simulations sont cette fois menées avec trois champs: un champs continu liquide, un champ continu gaz et un champ dispersé gaz.

10.2 Test case description

The validation will be performed on the Hänsch's bubble column. Thus, this first section is devoted to the description of the test case. In the test case proposed by Hänsch *et al.* [64], a free surface between water and air located initially at 0.3 m in a rectangular box with dimensions of $0.2\text{ m} \times 0.5\text{ m} \times 0.05\text{ m}$ (see Figure 10.1) is considered. Dispersed air is injected at the bottom of the box with a maximum mass flow rate of $6.10^{-4}\text{ kg.s}^{-1}$ following a parabolic shape. During the column rising, the dispersed bubbles coalesce and form larger bubbles. These large bubbles can then disappear by fragmentation, contributing to the transition from the continuous gas field to the dispersed field. When the bubbles, whatever their sizes, reach the free surface, they merge with the free surface and induce deformations (waves). The results obtained by Hänsch *et al.* [64] are displayed in Figure 10.2.

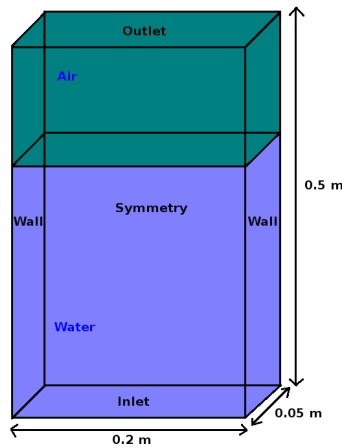


Figure 10.1: Schematic view of the Hänsch's bubble column [64] at initial conditions, dispersed bubbles are injected at the inlet with a maximum mass flow rate of $6.10^{-4}\text{ kg.s}^{-1}$.

The boundary conditions are given in Figure 10.1. Two mesh refinements are used: $40 \times 100 \times 10$ cells ($\Delta x = 5\text{ mm}$) and $80 \times 200 \times 20$ cells ($\Delta x = 2.5\text{ mm}$). The time step is kept constant equal to 0.1 ms for the two meshes. The time step used to evaluate the transitions terms $\Gamma_{cg \rightarrow dg}$ and $\Gamma_{dg \rightarrow cg}$ (see section 3.6) is also fixed at 0.1 ms for all the simulations. No turbulence models have been used for all the simulations in this chapter, corresponding to the use of a MILES modeling (see section 14.4). In Appendix J, it is shown that, for this particular test case, the

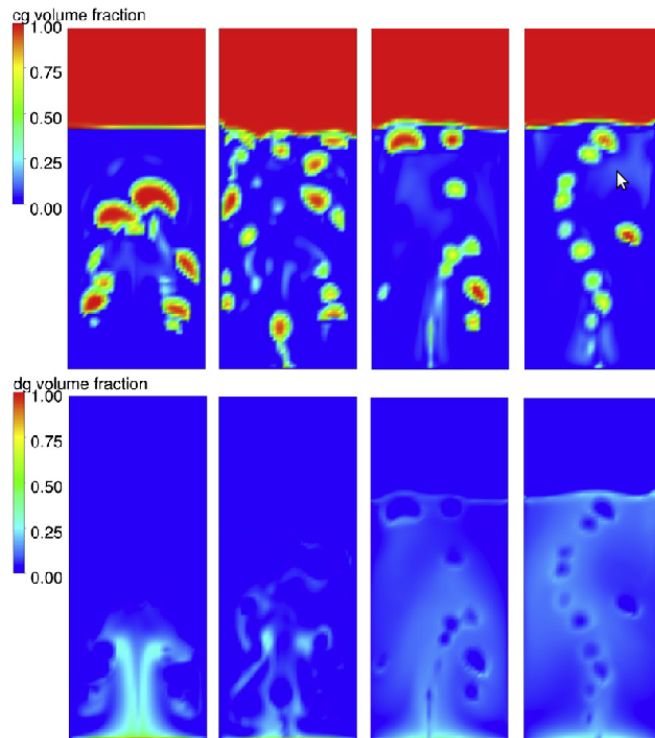


Figure 10.2: Volume fraction of the continuous gas field (top) and the polydispersed gas field (bottom) in the middle cross section of the bubble column domain at different time: from left to right 1 s, 2 s, 3 s and 5 s, results obtained by Hänsch *et al.* [64].

turbulence model has a minor effect on the flow evolution. In the whole chapter, the dispersed bubble diameter is constant, equal to 1 mm.

10.3 Effect of the interface sharpening equation on three field simulations

A first simulation of the Hänsch’s bubble column has been performed with the criteria defined in Chapter 4 for the interface sharpening equation and the coarse grid. Pictures of the column with the distribution of the dispersed bubbles and large gas bubbles are displayed at 5 s in Figure 10.3. The dispersed bubbles are concentrated in certain regions contrary to the results obtained by Hänsch *et al.* [64] (see Figure 10.2). Indeed, in the liquid part of the domain, where the dispersed bubbles are, the interface sharpening equation is activated by the criteria previously defined. Therefore, the recompression equation contributes to the concentration of the dispersed bubbles which then are transferred to the continuous gas field. Without this non physical concentration, these large bubbles would not have been created. Thus, to fix this issue, the interface sharpening equation resolution is deactivated in cells containing dispersed bubbles.

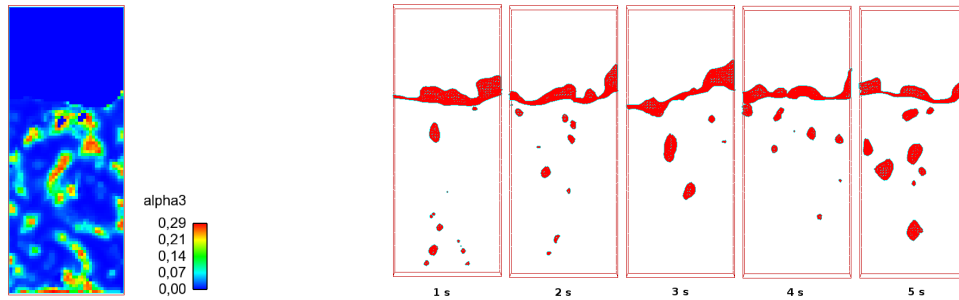


Figure 10.3: Hänsch’s bubble column over time with interface sharpening in the whole domain, left: distribution of the dispersed bubbles volume fraction (α_3) at 5 s, right: isosurfaces of the continuous gas volume fraction $\alpha_{cg} = 0.5$, mesh with $40 \times 100 \times 10$ cells.

With the modification of the interface sharpening equation described above, a new simulation is performed. The results are proposed in Figures 10.4 and 10.5. These two simulations highlight the two main steps occurring in the system. In the first step, the dispersed bubbles injected at the bottom of the column begin to rise until they reach the free surface and merge. This corresponds to the initial slope of the four curves in Figure 10.5. The total volume of dispersed gas increases linearly and, at the same time, the volume of continuous gas decreases and goes outside of the computational domain due to the rise of the free surface. Then, in the second step, an equilibrium between the volume of each field is obtained which corresponds to the flat part of the four curves in Figure 10.5. The large bubbles of continuous gas appear where the concentration of dispersed gas is higher and disappear if their characteristic scales are too small. The viable bubbles continue to grow when rising in the column and merge with the free surface.

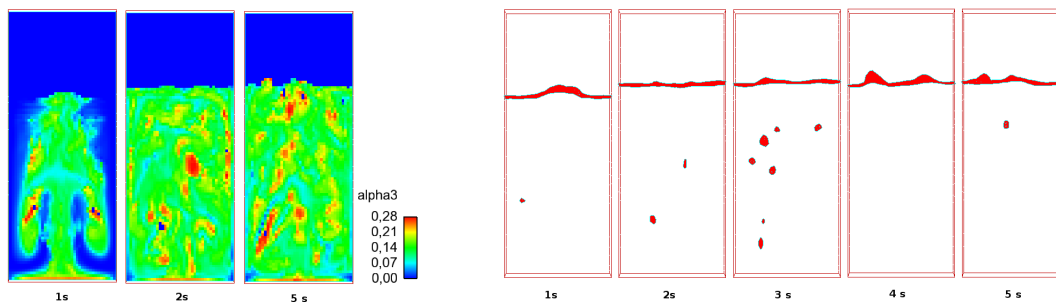


Figure 10.4: Hänsch’s bubble column over time, left: distribution of the dispersed bubbles volume fraction (α_3), right: isosurfaces of the continuous gas volume fraction $\alpha_{cg} = 0.5$, deactivation of the interface sharpening equation in cells containing dispersed bubbles, mesh with $40 \times 100 \times 10$ cells.

Furthermore, with these two simulations, the effect of the partial interface sharpening equation deactivation in the liquid domain is visible. Indeed, Figures 10.3 and 10.4 shows that more large bubbles are created in the first simulation and earlier. The free surface is then wavier due to the higher number of large bubbles. This ob-

ervation is correlated to the agglomeration of dispersed bubbles in certain regions, which increases the volume fraction of dispersed gas and induces the transition to the continuous gas field ($\alpha_{dg} > 0.3$).

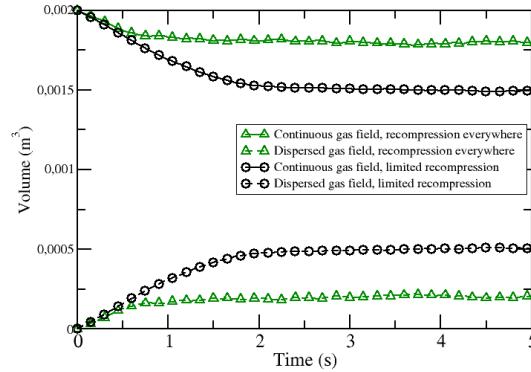


Figure 10.5: Evolution of the volume occupied by the dispersed and the continuous gas fields over time, solid lines: volume occupied by the continuous gas field, dashed lines: volume occupied by the dispersed gas field, black circles: deactivation of the interface sharpening equation in cells containing dispersed bubbles, green triangles: interface sharpening equation activated everywhere.

In multifield simulations, the interface sharpening equation must be deactivated in cells containing a non negligible quantity of a dispersed field to ensure an accurate simulation of the physical phenomena. This modification will be used in all the rest of this thesis.

10.4 Transition between the continuous gas field and the dispersed gas field

The goal of these simulations is to show the ability of the model to deal with two gas fields with transitions between them.

10.4.1 Transition from the dispersed gas field to the continuous gas field

First, the previous simulation will be reproduced with the modified interface sharpening equation by allowing only the transitions from the dispersed gas field to the continuous gas field. The results are presented in Figures 10.6 and 10.7. As expected, the quantity of large bubbles is increased in the liquid region since these bubbles can not collapse into dispersed bubbles. Therefore, the volume occupied by

the dispersed bubbles is smaller. The results are comparable to the first simulation (green curve in Figure 10.5) since the activation of the interface sharpening equation in the liquid region concentrated the dispersed bubbles and so enhanced the creation of large bubbles. However, the simulation allows the existence of large bubbles, which are actually not well resolved and should return in the dispersed field to be better modeled (see Figure 10.6).

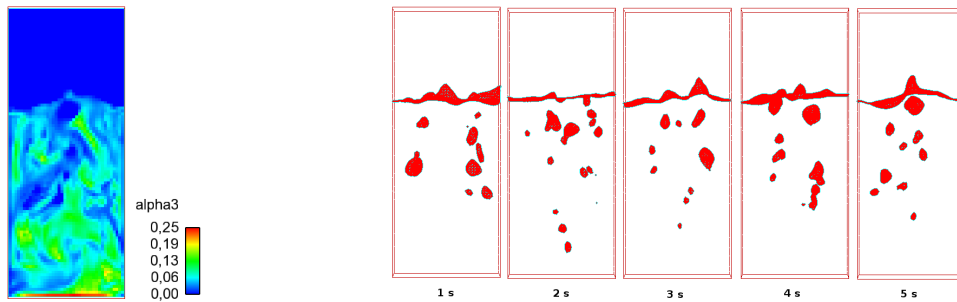


Figure 10.6: Hänsch's bubble column over time without transfers from the continuous gas field to the dispersed gas field, left: distribution of the dispersed bubbles volume fraction (α_3) at 5 s, right: isosurfaces of the continuous gas volume fraction $\alpha_{cg} = 0.5$, mesh with $40 \times 100 \times 10$ cells.

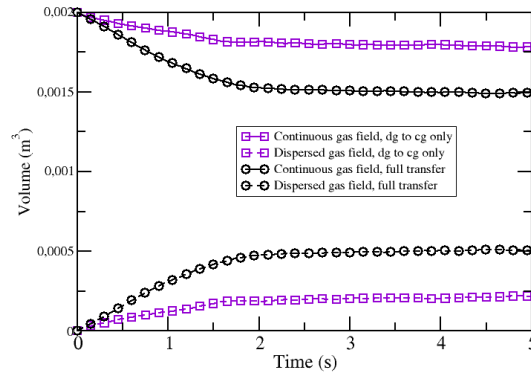


Figure 10.7: Evolution of the volume occupied by the dispersed and the continuous gas fields over time, solid lines: volume occupied by the continuous gas field, dashed lines: volume occupied by the dispersed gas field, black circles: transitions between the dispersed and the continuous gas fields, purple squares: transitions only from the dispersed gas field to the continuous gas field.

10.4.2 Effect of the mesh refinement

The effect of the mesh refinement on the transfer rate between the two gas fields (Figures 10.8 and 10.9) is studied. With the more refined mesh, more large

10.4. TRANSITION BETWEEN THE CONTINUOUS GAS FIELD AND THE DISPERSED GAS FIELD

bubbles are created. Nevertheless, due to the smaller cell size, the created bubbles are smaller. In terms of volume occupied by each field, the results are very similar for the two mesh refinements, as expected. Thus, the mesh convergence has been reached. Moreover, these results showed that the gas volume is conserved when the mesh is refined.

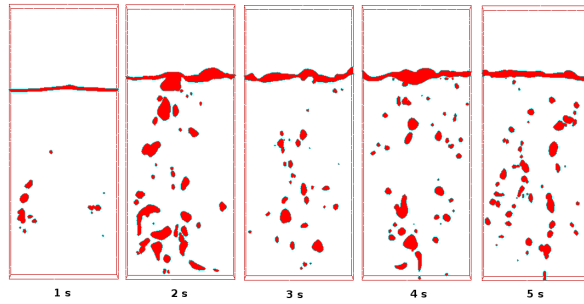


Figure 10.8: Distribution of the large bubbles in the Hänsch's bubble column over time, the isosurfaces of the continuous gas volume fraction $\alpha_{cg} = 0.5$ are represented in red, mesh with $80 \times 200 \times 20$ cells.

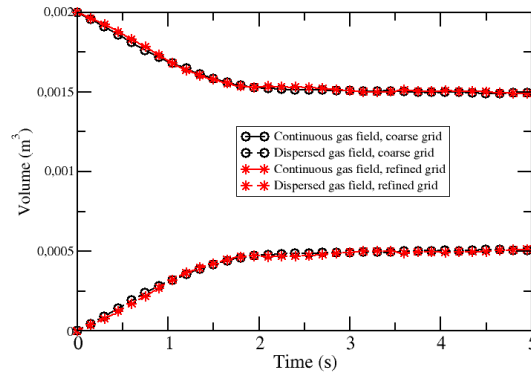


Figure 10.9: Evolution of the volume occupied by the dispersed and the continuous gas fields over time, solid lines: volume occupied by the continuous gas field, dashed lines: volume occupied by the dispersed gas field, black circles: coarser mesh ($40 \times 100 \times 10$ cells), red stars: more refined mesh ($80 \times 200 \times 20$ cells).

It should be also interesting to know if the interfacial area is conserved when the mesh is refined. For this purpose, the total dispersed field and the total continuous gas field interfacial areas are extracted. The total dispersed field interfacial area is obtained using the following expression:

$$A_{disp} = \sum_I^{ncel} \frac{6\alpha_{dg}^I}{d_{disp}^I} \Omega \quad (10.1)$$

with d_{disp}^I the diameter of the dispersed field in the cell I , which is constant in the whole domain, equal to 1 mm.

The total continuous gas field interfacial area is evaluated by post-treating the area of the isosurface: $\alpha_{cg} = 0.5$.

Results are available in Figure 10.10. First, we see that, contrary to the volume, the steady state is reached later for the area. In the left picture, we then observe that the interfacial area of the continuous gas field increases when the mesh is refined, which is consistent with the fact that more large bubbles are created (see Figure 10.8). Whatever the grid, the interfacial area of the continuous gas field is negligible compared to the dispersed field which is in larger quantity in the flow. Finally, in the right picture, we see that the total interfacial area depends on the grid. The effect of a dispersed diameter variation of 10 % is plotted for the refined grid. The two curves highlight that the difference between the two grids corresponds to a diameter variation larger than 10 %. At the end of the simulation, the interfacial area difference between the two grids is equal to 25 %. Thus, the interfacial area is not conserved when the mesh is refined. This point should be improved since the interfacial area appears in several terms in the balance equations. This work is not performed with the current mass transfer terms because they are going to be improved in the next chapter.

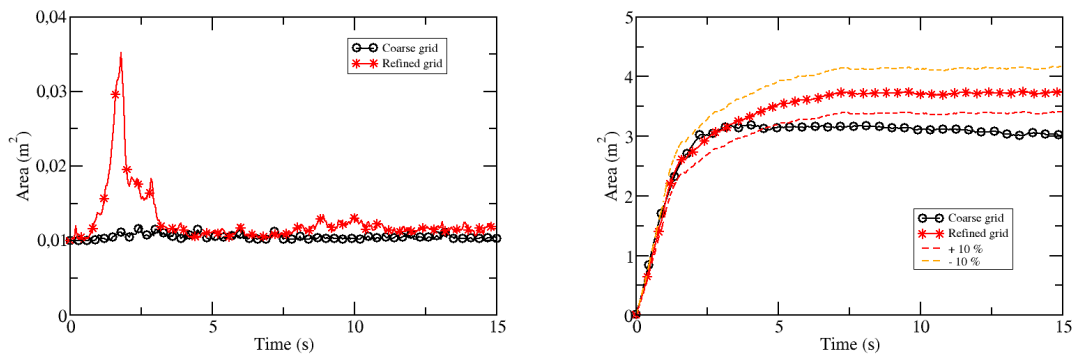


Figure 10.10: Evolution of the interfacial area of the dispersed and the continuous gas fields over time, left: interfacial area of the continuous gas field only, right: total interfacial area of the gas field (continuous and dispersed), coarse mesh with 40 x 100 x 10 cells, refined mesh with 80 x 200 x 20 cells.

This simulation highlights also that the transfer term allows creating large bubbles without any predictions on their shapes and so to be closer to physical results.

10.4.3 Effect of the time step

In this section, the effect of the time step on the simulations with the mesh containing $40 \times 100 \times 10$ cells is studied. Three time steps are considered: 0.1 ms , 0.2 ms and 0.4 ms . For all these simulations, the characteristic time step of the transfer term between the two gas fields is fixed at 0.1 ms to be comparable. The results in terms of volume occupied by each field is displayed in Figure 10.11. Once again, the results are very similar. The transition dynamics is not affected by the time step modification.

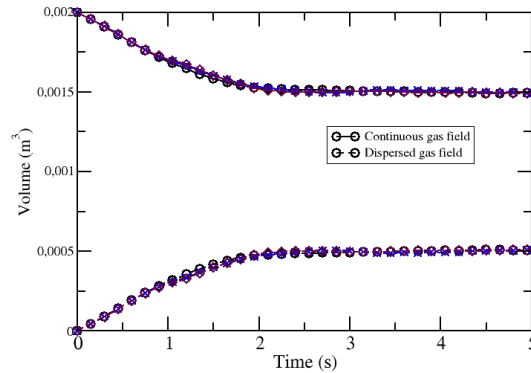


Figure 10.11: Evolution of the volume occupied by the dispersed and the continuous gas fields over time, all the notations and colors are not given in the picture for sake of clarity, solid lines: volume occupied by the continuous gas field, dashed lines: volume occupied by the dispersed gas field, black circles: time step equal to 0.1 ms , blue crosses: time step equal to 0.2 ms , brown diamond: time step equal to 0.4 ms .

10.4.4 Effect of the characteristic time step of the transition

Finally, the effect of the characteristic time step of the transfer term is observed. The Hänsch's column is simulated with the coarse mesh ($40 \times 100 \times 10$ cells) and a time step equal to 0.4 ms . Three characteristic time steps of the transfer term are compared: 0.4 ms , 0.1 ms and 0.025 ms . All these characteristic time steps are smaller than the time step of the simulation since it corresponds to a convergence time step for the transition term. The results are displayed in Figure 10.12. This figure highlights that the smaller the characteristic time step is, the more continuous gas is created and the less dispersed bubbles is contained in the liquid phase. However, these results do not allow concluding on the evolution of the large bubble size versus quantity.

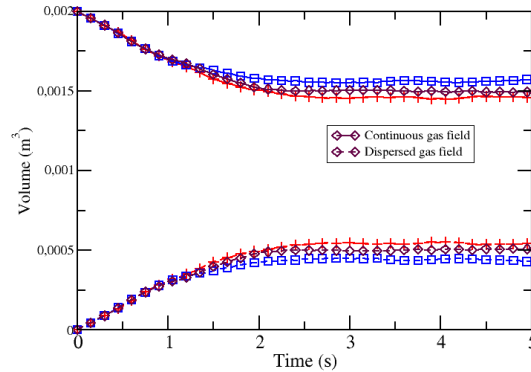


Figure 10.12: Evolution of the volume occupied by the dispersed and the continuous gas fields over time, all the notations and colors are not given in the picture for sake of clarity, solid lines: volume occupied by the continuous gas field, dashed lines: volume occupied by the dispersed gas field, red plus: characteristic time step of the transfer term equal to 0.4 ms, brown diamond: 0.1 ms, blue squares: 0.025 ms, mesh with 80 x 200 x 20 cells, time step equal to 0.4 ms.

10.5 Conclusion

The simulation of the Hänsch's bubble column highlights the ability of the code to compute three field flows and to create large deformable bubbles without assumptions on their initial shapes. After few modifications of the interface sharpening equation, transitions between the two gas fields were possible. The volume fraction ratio between the two gas fields was not affected by the mesh refinement and the time step of the simulation. A more refined mesh only allowed creating smaller continuous bubbles. Nevertheless, a decrease of the characteristic time step of the transfer term induced a decrease of the dispersed bubbles quantity and so an increase of the continuous gas volume fraction.

Chapter 11

Prediction of flow regimes: improvement of the isothermal mass transfer terms

After showing the ability of the Large Bubble Model to compute three field simulations with transitions between the dispersed and the continuous gas fields, the effect of the model on the prediction of flow regimes is studied. This information is crucial in nuclear power plants where the knowledge of flow regimes should be improved in some components, as shown in Chapter 1. Indeed, these data allow identifying regions of early aging and then increasing performance and lifetime of these components. Improvements of the coalescence term is then proposed. In the version validated in the previous chapter, the activation of the transfer was based on the volume fraction of the dispersed field. Thus, the critical value was fixed according to experimental observations.

In this chapter, like in the previous one, the flows are isothermal. Three fields are defined: a continuous liquid field, a continuous gas field and a dispersed gas field. Mass transfers are only considered between the two gas fields.

The section dealing with the ability of the multifield approach to predict flow regimes corresponds to a communication [131] presented at the 9th International Conference on Multiphase Flow 2016 (ICMF 2016, 22-27 May 2016) and a paper accepted for publication in Nuclear Engineering and Design [130].

11.1 Résumé du chapitre

Après avoir validé l'approche multi-champ, ce chapitre propose d'appliquer la méthode à la prédiction de régimes d'écoulement variés. Cette donnée est très importante pour des entreprises comme EDF qui n'ont pas toujours accès aux caractéristiques (taille de bulles, trajectoires) des écoulements dans certaines parties des centrales nucléaires. Or, cette information peut permettre d'identifier des zones de vieillissement précoce et d'augmenter ainsi le rendement et la durée de vie de ces éléments. Dans un deuxième temps, le cas test est utilisé pour améliorer le terme

de coalescence des bulles sphériques initialement basé sur une valeur empirique de fraction volumique critique.

11.2 METERO test case

The METERO experiment has been developed in the frame of the NEPTUNE project, jointly developed by CEA, EDF, AREVA and IRSN in order to improve numerical CMFD tools by contributing to model validations. The experiment consists in an horizontal cylindrical pipe (see Figure 11.1 for the schematic view), in which water and air can be injected at the same time with different superficial velocities (from 0 m.s^{-1} to 5 m.s^{-1} for water and from 0 m.s^{-1} to 0.7 m.s^{-1} for air). The air injection tubes have been set to ensure uniform bubble injection in the inlet section. The test section is 5.4 m long for an inner diameter of 0.1 m . The flow properties are extracted at three different positions along the pipe. More informations on the experiment can be found in [20].

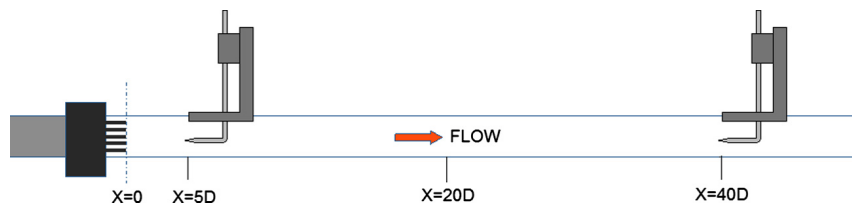


Figure 11.1: Schematic view of the horizontal pipe of the METERO experiment [20].

This experiment allows establishing a flow pattern map in Figure 11.2 according to the injection superficial velocity of water and air. Figure 11.4 proposes an illustration of each flow regime observed in the METERO experiment.

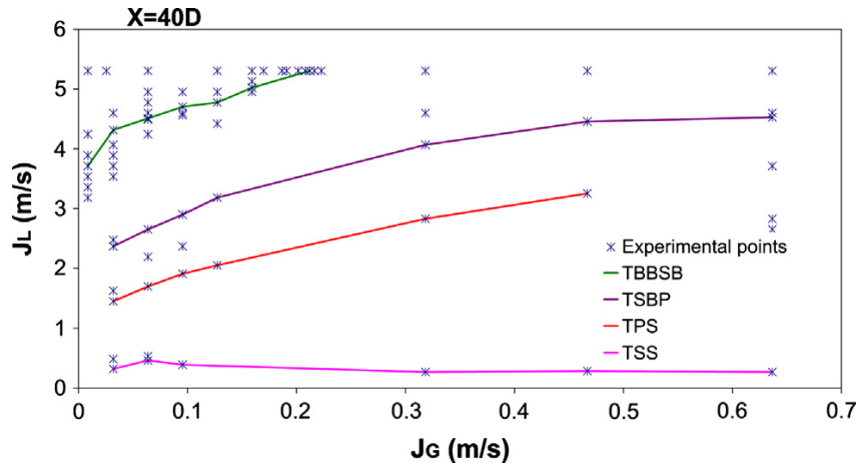


Figure 11.2: METERO flow pattern for $\frac{X}{D} = 40$, J_L corresponds to the water velocity and J_G to the air velocity at the injection, TSS refers to the transition from slug to stratified flow (pink line), TPS to the transition from plug to slug flow (orange line), TSBP to the transition from stratified bubbles regime to plug (purple line) and TBBSB to the transition from buoyant bubble flow to stratified bubble flow (green line), crosses correspond to video acquisitions [20].

The simulations of the experiment have been performed with three different cylindrical grids containing respectively 277200, 966168 and 2327808 cells (see Figure 11.3). The boundary conditions are standard: inlet on the right, outlet: on the left and walls everywhere else. The properties of the two phases are presented in Table 11.1. Surface tension coefficient is equal to 0.075 N.m^{-1} . The simulations are performed until they reach 13 s including 5 s of averaging.

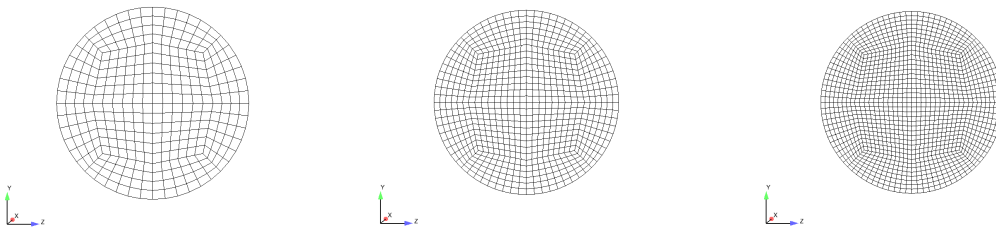


Figure 11.3: Slice of the mesh used for the simulation of the METERO test case, left to right: coarse grid with 277200 cells, intermediate grid with 966168 cells and refined grid with 2327808 cells.

	Density ($kg.m^{-3}$)	Viscosity ($Pa.s$)
Air	1.29	$1.8.10^{-5}$
Water	1000	$1.3.10^{-3}$

Table 11.1: Properties of water and air for the METERO test case.

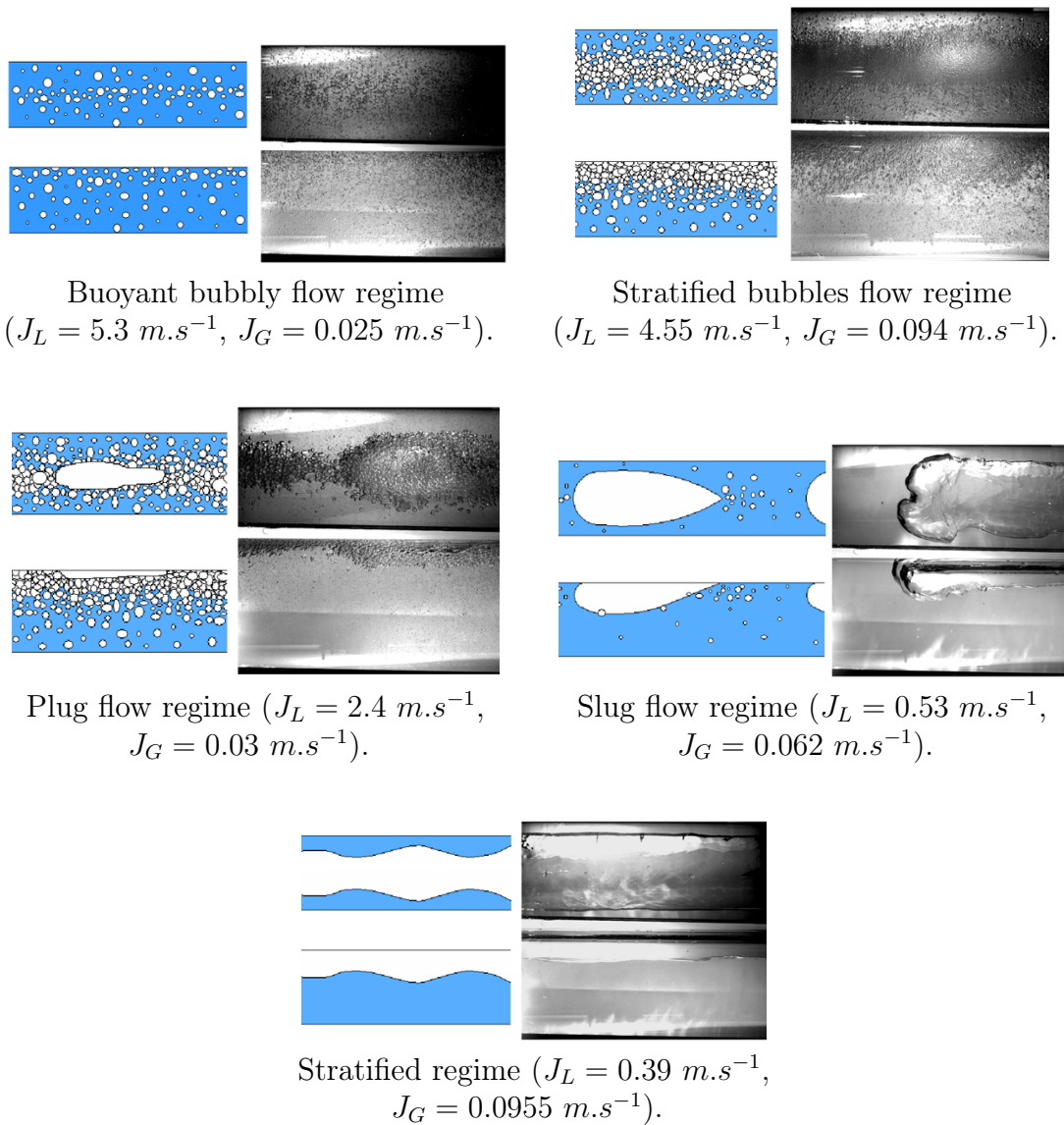


Figure 11.4: Illustration of the different flow regimes observed in the METERO experiment according to the water and air superficial velocities, top: top view and bottom: side view, the fluid is flowing from the right to the left [20].

11.3 Prediction of flow regimes

For this purpose, the METERO test case is simulated with different injection superficial velocities of water 1.59 m.s^{-1} , 2.65 m.s^{-1} , 4.42 m.s^{-1} and 5.31 m.s^{-1} and a given air superficial velocity of 0.127 m.s^{-1} . In a first approach, a RANS turbulence model is considered in the liquid phase as our work on LES was not achieved when we first considered the METERO test case. LES modeling will be investigated in the next part (in Chapter 17 for this test case). The simulations are performed with the multifield approach using the standard dispersed approach described in section 3.3 and the LBMo improved in the previous part. An interfacial area transport equation based on the Ruyer-Seiler model [178] is solved to evaluate the dispersed bubble-size distribution which is not constant in the whole domain. The simulations are performed with the three grids to assess mesh convergence. The time steps are constant and are given in Table 11.2 for the three grids and the four water superficial velocities.

Flow regime	Coarse grid	Intermediate grid	Refined grid
Slug flow ($J_L = 1.59 \text{ m.s}^{-1}$)	0.3 ms	0.12 ms	0.1 ms
Plug flow ($J_L = 2.65 \text{ m.s}^{-1}$)	0.3 ms	0.25 ms	0.1 ms
Dispersed bubble flow ($J_L = 4.42 \text{ m.s}^{-1}$)	0.5 ms	0.5 ms	0.25 ms
Gravity flow ($J_L = 5.31 \text{ m.s}^{-1}$)	0.5 ms	0.5 ms	0.25 ms

Table 11.2: Time steps according to the flow regime and the grid for the METERO test case with the RANS approach.

The objective of these simulations is to show the ability of the approach to predict flow regimes. We begin with the smallest liquid superficial velocity. According to the flow map in Figure 11.2, we expect a slug flow with large, long and deformable bubbles followed by a limited number of small spherical inclusions (see Figure 11.4). Figure 11.5 shows that the simulations results are in good agreement with the expected flow. The large bubbles occupy an important part of the tube and are followed by small ones treated in the dispersed field.

Then, the liquid superficial velocity is increased at $J_L = 2.65 \text{ m.s}^{-1}$. This time, the flow is supposed to belong to the plug flow type. The large deformable inclusions are supposed to be smaller and surrounded by a larger number of small spherical bubbles. Once again, the simulation (see Figure 11.6) corresponds to the expected results. A higher quantity of dispersed field is observed. The small spherical bubbles are located between two large inclusions.

The liquid superficial velocity is increased one more time at $J_L = 4.42 \text{ m.s}^{-1}$, corresponding to a stratified bubbles flow. According to Figure 11.4, large deformable

bubbles have disappeared in this flow regime. Only small spherical bubbles are expected. Figure 11.7 displays the absence of a continuous gas field. Finally, the liquid superficial velocity is fixed at $J_L = 5.31 \text{ m.s}^{-1}$. The buoyant bubbles flow regime looks like the previous one with a smaller quantity of dispersed bubbles. We observe this decrease in the simulation (see Figure 11.8) if we look at the volume fraction scale of the dispersed field.

This analysis gave a qualitative validation of the multifield approach. However, void fraction and liquid velocity profiles can also be compared to the experimental data to have a quantitative study. Figure 11.9 presents the results for the four liquid superficial velocities and the three grids. The results are in reasonable agreements with the experimental data. The curves are very close for the three grids. Thus, in what follows, the simulations will be performed with the intermediate mesh.

This study showed that the implementation of the LBMo combined with the dispersed field approach allows an accurate simulation of a large range of flow regimes without considering any additional criteria to select a flow type. The precise treatment of the large interfaces with the development of transition terms between the continuous and the dispersed gas fields are sufficient to predict properly flow regimes according to the injection conditions and phase properties.

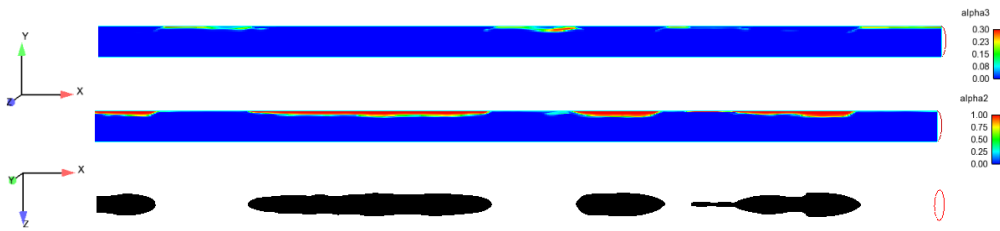


Figure 11.5: Simulation results of the METERO test case with $J_L = 1.59 \text{ m.s}^{-1}$ and $J_G = 0.127 \text{ m.s}^{-1}$, corresponding to a slug flow regime, top to bottom: volume fraction of the dispersed gas field (side view), volume fraction of the continuous gas field (side view) and isosurface $\alpha_{cg} = 0.5$ (top view), the fluid is flowing from the left to the right, RANS model, intermediate mesh.

11.4 Improvement of the isothermal mass transfer term

The isothermal mass transfer term presented in section 3.6 is split into two terms. The first term, corresponding to Equation (3.26), deals with the breakup of large deformable bubbles into small ones. Dispersed gas field is created. In the second term, corresponding to Equation (3.27), the coalescence of small spherical bubbles is treated inducing the creation of continuous gas field. However, this term is based on the volume fraction of the dispersed gas field. To activate the transfer, the volume fraction has to be larger than 0.3. This value has been fixed empirically

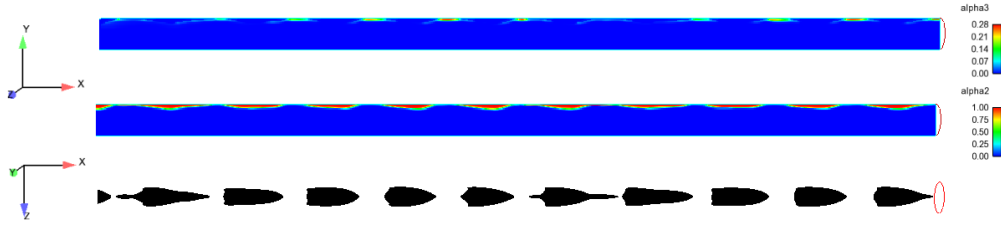


Figure 11.6: Simulation results of the METERO test case with $J_L = 2.65 \text{ m.s}^{-1}$ and $J_G = 0.127 \text{ m.s}^{-1}$, corresponding to a plug flow regime, top to bottom: volume fraction of the dispersed gas field (side view), volume fraction of the continuous gas field (side view) and isosurface $\alpha_{cg} = 0.5$ (top view), the fluid is flowing from the left to the right, RANS model, intermediate mesh.



Figure 11.7: Simulation results of the METERO test case with $J_L = 4.42 \text{ m.s}^{-1}$ and $J_G = 0.127 \text{ m.s}^{-1}$, corresponding to a stratified bubbles flow regime, top to bottom: volume fraction of the dispersed gas field (side view), volume fraction of the continuous gas field (side view) and isosurface $\alpha_{cg} = 0.5$ (top view), the fluid is flowing from the left to the right, RANS model, intermediate mesh.

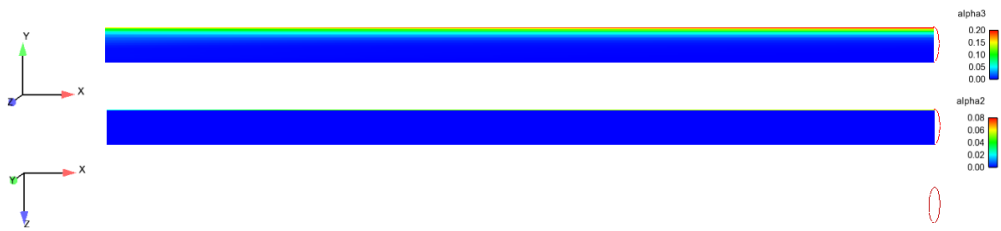


Figure 11.8: Simulation results of the METERO test case with $J_L = 5.31 \text{ m.s}^{-1}$ and $J_G = 0.127 \text{ m.s}^{-1}$, corresponding to a buoyant bubbles flow regime, top to bottom: volume fraction of the dispersed gas field (side view), volume fraction of the continuous gas field (side view) and isosurface $\alpha_{cg} = 0.5$ (top view), the fluid is flowing from the left to the right, RANS model, intermediate mesh.

using experimental observations [57, 139, 191]. Nevertheless, it can vary according to the flow properties especially to the pressure. As an example, Khafisov *et al.* [84] showed that in sodium boiling flows, the critical void fraction to reach slug flow regimes can be on the order of 2.5 % (see Figure 11.10).

CHAPTER 11. PREDICTION OF FLOW REGIMES: IMPROVEMENT OF THE ISOTHERMAL MASS TRANSFER TERMS

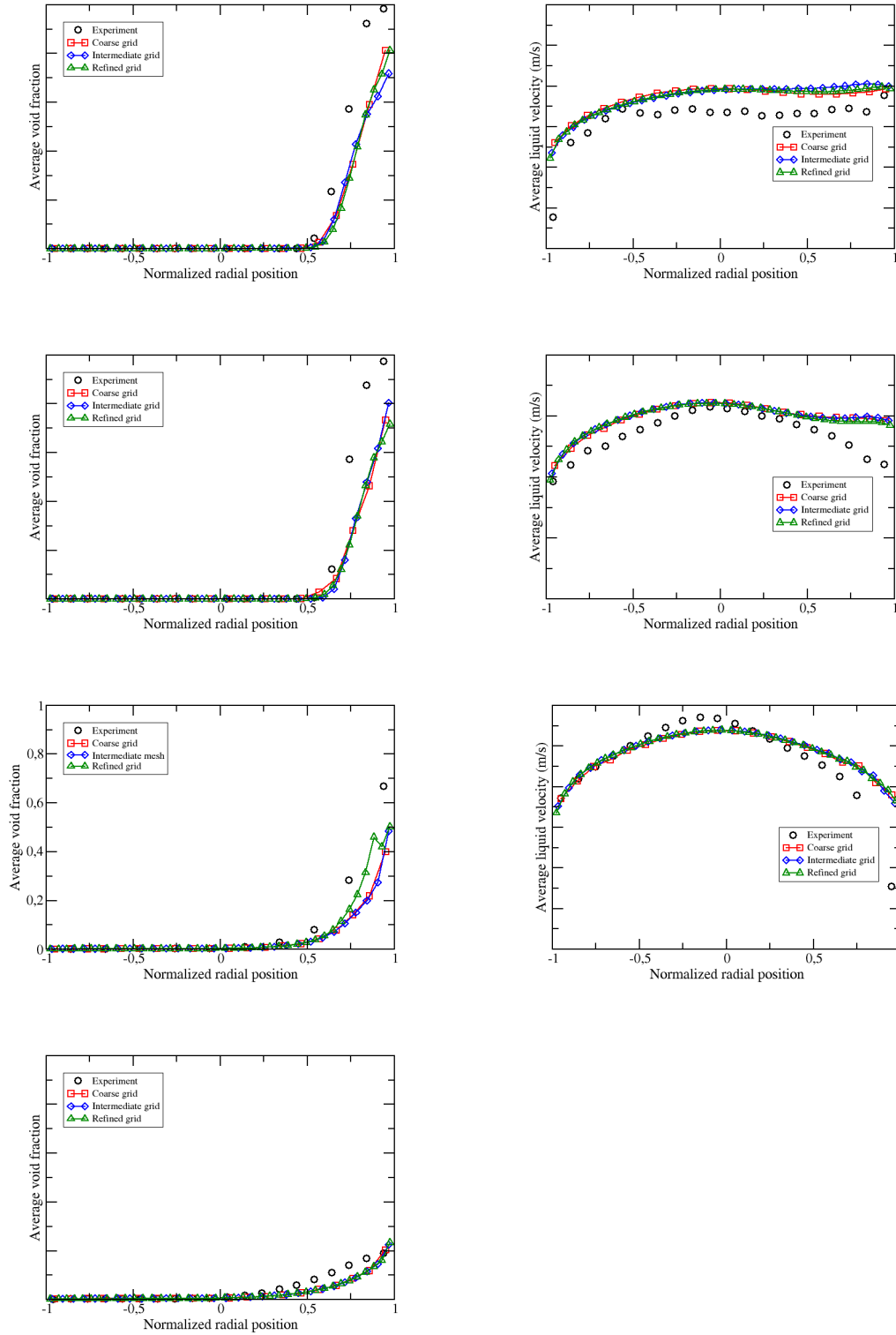


Figure 11.9: Average void fraction and average liquid velocity at $X = 40D$, top to bottom: slug flow ($J_L = 1.59 \text{ m.s}^{-1}$), plug flow ($J_L = 2.65 \text{ m.s}^{-1}$), stratified bubble flow ($J_L = 4.42 \text{ m.s}^{-1}$) and buoyant bubble flow ($J_L = 5.31 \text{ m.s}^{-1}$), $J_G = 0.127 \text{ m.s}^{-1}$, RANS model.

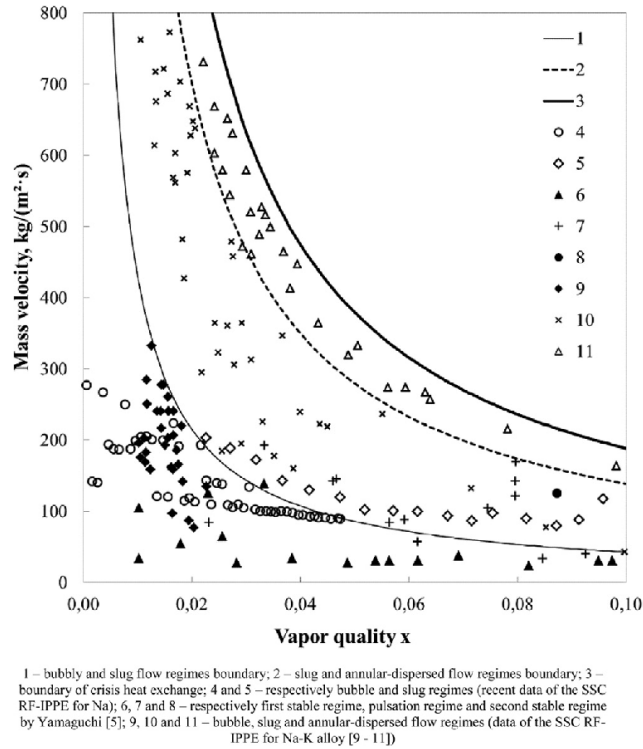


Figure 11.10: Flow map obtained by Khafisov et al. [84] with liquid metal two-phase flow, 1 refers to bubbly and slug flow regimes boundary

11.4.1 Improved coalescence term

The objective here is to find another criterion to activate or not the coalescence process. In the multifield approach, the inclusions contained in the dispersed field are assumed to be spherical or slightly ellipsoidal. Thus, if these inclusions begin to deform and the error made by considering them with a dispersed approach is too large, they are not supposed to remain in the dispersed field. This assumption allows defining a new transition criterion based on the shape of the dispersed bubbles. If their shape is closer to an ellipsoidal shape, the transfer to the continuous gas field is activated. Due to confidentiality, the expression of the new transfer term is not given.

11.4.2 Validation

To validate this new term, the four liquid superficial velocities of the METERO test case are simulated with the RANS approach and the intermediate mesh. The void fraction and liquid velocity profiles are compared in Figure 11.12. For the slug and the plug flows, the results are slightly improved with the new criterion for the coalescence activation. However, for the two other flow regimes, the improvement can be discussed. Indeed, these two flow regimes contain more dispersed bubbles.

Thus, the dispersed bubble diameter prediction is more crucial. Nevertheless, the previous coalescence term did not depend on this parameter, contrary to the new one. Thus, it was not affected by the error made on the bubble diameter. It has to be noted that the dispersed bubble diameter prediction is totally independent on the coalescence model and is only evaluated using an interfacial area transport equation based on the Ruyer-Seiler model [178]. To have an idea of the error made on this prediction, Figure 11.11 displays the Sauter diameter profile of the dispersed field obtained with this model for the buoyant bubble flow regime. This quantity is underestimated. With the previous coalescence model, the diameter prediction had no effect on the coalescence process whereas with the new criterion, it is crucial. This can explain the limited improvement of the new coalescence model on the buoyant bubble and the stratified bubble flow regimes.

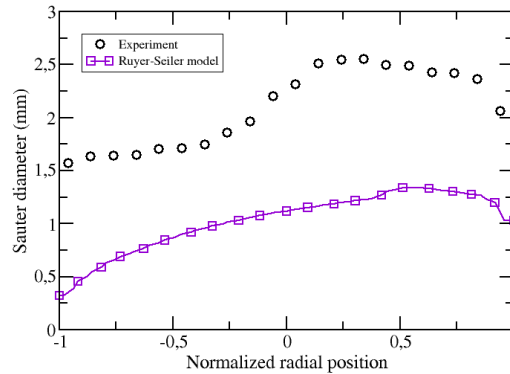


Figure 11.11: Sauter diameter obtained with Ruyer-Seiler model [178] in the buoyant bubble flow configuration, $J_L = 5.31 \text{ m.s}^{-1}$, $J_G = 0.127 \text{ m.s}^{-1}$, RANS model, intermediate mesh.

11.4.3 Interfacial area conservation

In section 10.4.2, we showed that the previous transfer terms did not ensure interfacial area conservation when the mesh was refined. In this section, this point is assessed with the new transfer model. For this purpose, the Hänsch's bubble column is simulated with the two grids (see section 10.2 for the details on the simulations parameters). Contrary to Chapter 10, the interfacial area transport equation based on the Ruyer-Seiler model [178] is solved to evaluate the diameter of the dispersed bubble, which is necessary to apply the new coalescence criterion.

The results are presented in Figure 11.13. In the left picture, the interfacial area of continuous gas field are displayed. For the two grids, the interfacial area of continuous gas field is larger than with the previous coalescence model. Thus,

11.4. IMPROVEMENT OF THE ISOTHERMAL MASS TRANSFER TERM

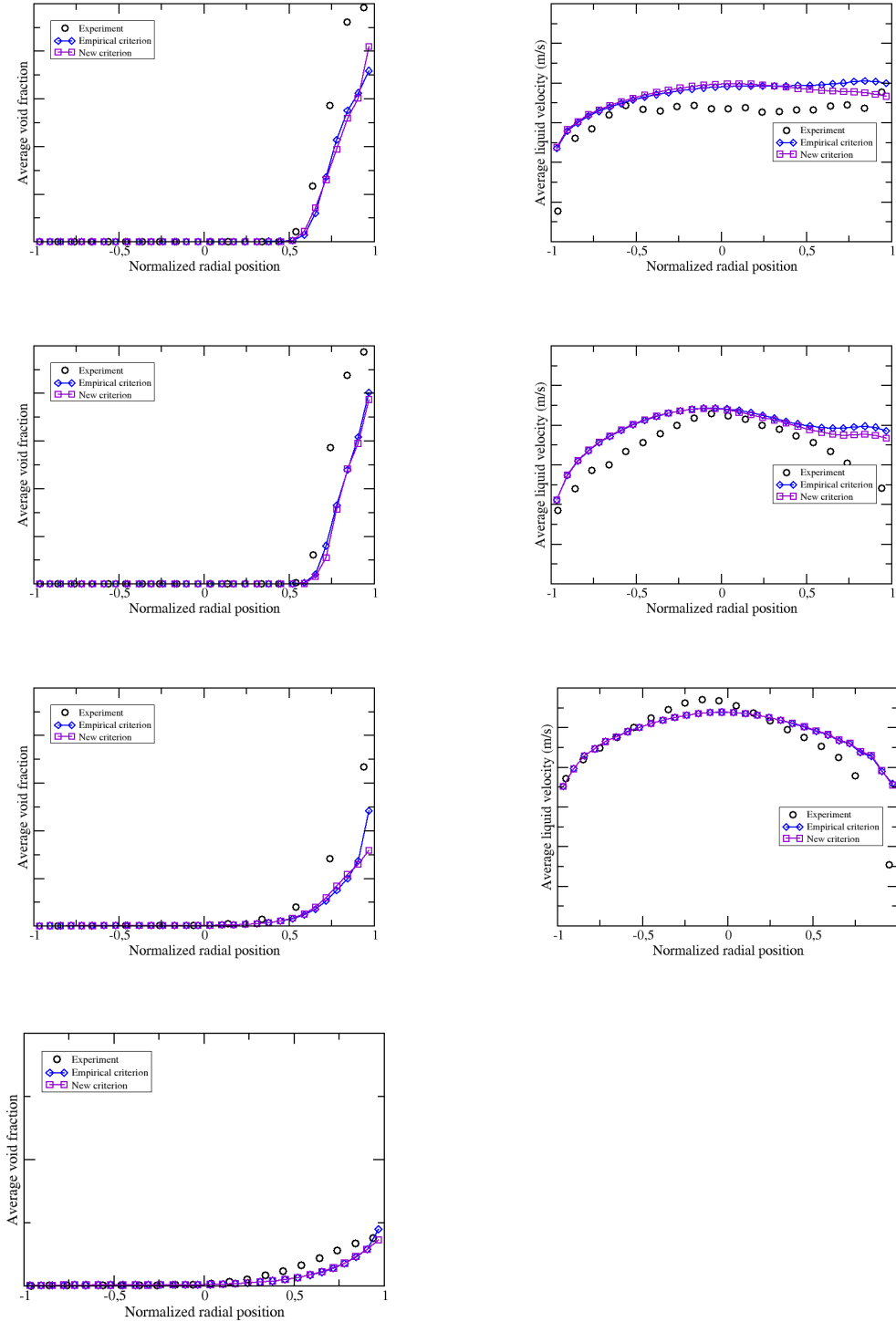


Figure 11.12: Average void fraction and average liquid velocity at $X = 40D$, top to bottom: slug flow ($J_L = 1.59 \text{ m.s}^{-1}$), plug flow ($J_L = 2.65 \text{ m.s}^{-1}$), stratified bubble flow ($J_L = 4.42 \text{ m.s}^{-1}$) and buoyant bubble flow ($J_L = 5.31 \text{ m.s}^{-1}$), $J_G = 0.127 \text{ m.s}^{-1}$, RANS model, blue diamonds: previous coalescence term (Equation 3.27), purple squares: new coalescence term (section 11.4.1).

more continuous gas field has been created with the new coalescence term. The same trend is observed when the grid is refined: more large bubble are created. However, the contribution of the interfacial area induced by the continuous gas field remains negligible. Finally, in the right picture, we see that the total interfacial area is smaller than with the previous model. However, contrary to the previous model, the difference between the two grids correspond to a dispersed diameter variation on the order of 10 %. The error on the interfacial area at the end of the simulation is equal to 13 %. Thus, the interfacial area is better conserved with the new transfer model. This is probably due to the resolution of the interfacial area transport equation for the dispersed bubbles. The equation adapts the bubble diameter and so its interfacial area according to the grid refinement. Nevertheless, a specific term should be added to compensate this loss of interfacial area when the transfer occurs.

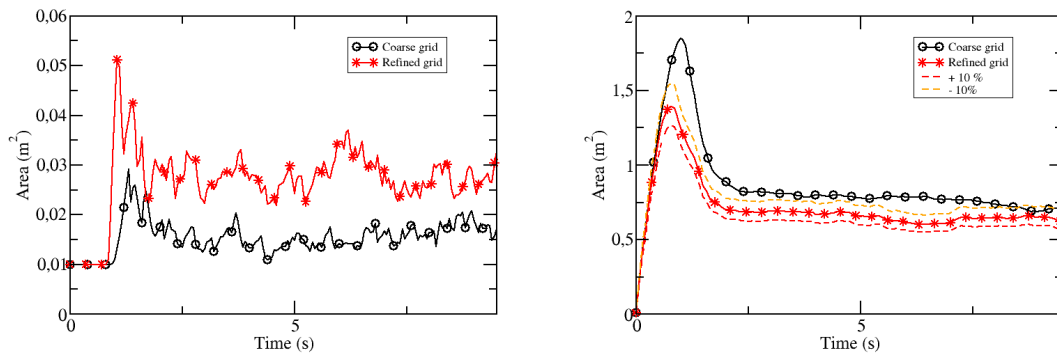


Figure 11.13: Evolution of the interfacial area of the dispersed and the continuous gas fields over time, left: interfacial area of the continuous gas field only, right: total interfacial area of the gas field (continuous and dispersed), coarse mesh with $40 \times 100 \times 10$ cells, refined mesh with $80 \times 200 \times 20$ cells, new coalescence term (section 11.4.1).

11.5 Conclusion

In this chapter, the ability of the multifield approach to predict accurately flow regimes has been showed. A new transfer term to model the coalescence of the small spherical inclusions has been presented and validated. A study of the grid refinement effect on the interfacial area highlighted that the quantity is better conserved with the new coalescence model. This is an important issue since the interfacial area appears in several terms in the balance equations. A specific term should be implemented when a transfer occurs to improve conservation.

Chapter 12

Conclusion

This second part was devoted to mass transfers in order to perform simulations of phase change effects on water/steam flows on one hand and to deal with transitions between fields from the same phase on the other hand. In the first case, non isothermal flows containing only continuous fields have been studied. The use of the two-fluid model and the LBMo required the implementation of a specific mass transfer term. Validations of this term have been presented with five different academic test cases with both superheated water and steam and also liquid under the saturation temperature in 1D and 3D. For the first time, a simulation of a moving water/steam interface has been performed at a pressure of $1.013 \cdot 10^7 Pa$ closer to the nuclear power plant configurations. After studying phase change effects, the multifield approach has been assessed on various flows with a large range of bubble sizes and shapes. The optimized LBMo coupled to the dispersed approach allowed predicting flow regimes with a reasonable accuracy. Finally, the improvement of the transition term to model coalescence of the dispersed gas field gave encouraging results.

Part III

Investigation of Large Eddy Simulation for turbulent flows

An efficient and accurate modeling of turbulence effects is of great importance to simulate complex two-phase flows. For single-phase flows, Large Eddy Simulation (LES) models have been extensively studied and are implemented in various CMFD tools. However, for two-phase flows, work is still in progress to formulate and to apply these models to flows containing inclusions of different sizes. The one-fluid model equations have already been filtered. *A priori* LES studies have been performed to evaluate the obtained subgrid terms and to compare different turbulence models. Some research groups have even implemented successfully some of these turbulence models for the convective [200] and the surface tension subgrid terms in their CMFD tools [6]. For two-fluid models, the equations have only been filtered in the case of a continuous carrier field with a dispersed field [90].

After improving the large interface modeling within the two-fluid model in Part I, we are now interested in the turbulence modeling with a LES approach. For this purpose, in the first two chapters, a review of the turbulence properties and the different approaches available to model the turbulence effects are detailed. In the code NEPTUNE_CFD, different turbulence models based on RANS and URANS approaches have been implemented and optimized. However, these two approaches are based on an ensemble average description of turbulence effects which seems not suitable for the simulation of unsteady two-phase flows using the multifield approach. Indeed, an interface tracking method is added to the dispersed model for the simulation of large and deformable inclusions. For such interfacial structures, a deterministic description is used. Thus, LES models seem more suitable. In the third chapter, a feasibility study of LES with the code NEPTUNE_CFD is first performed on a single-phase flow. In the fourth chapter, a two-phase flow is simulated to perform an *a priori* LES study. The two-fluid model equations are filtered in the context of large interface simulations with the LBM_o. Different turbulence models are compared. The more suitable one is implemented in the last chapter. Preliminary results are detailed on single and two-phase flows.

Thus, in this part, only isothermal and incompressible flows containing one or two continuous fields are considered.

Chapter 13

Properties of turbulent flows and modeling strategies

In the previous chapters, the turbulence effects in two-phase flows have not been discussed. RANS models were used as they were the only available turbulence models in NEPTUNE_CFD at the beginning of the PhD. However, turbulence occurs in a variety of situations, scales and areas (aeronautics, meteorology, chemistry, etc). In two-phase flows, it is responsible for inter-phase exchange and scale separations. Therefore, its understanding is a requirement to be able to simulate properly industrial flows especially in nuclear power plants where the installations safety mainly depends on these flows. This chapter proposes an overview of the properties of turbulent flows and the different modeling strategies available in the literature.

13.1 Résumé du chapitre

Dans les deux premières parties de ce manuscrit, la notion de turbulence n'a pas été discuté. Cependant, pour simuler des écoulements complexes tels que ceux rencontrés en centrale nucléaire, la modélisation de la turbulence est fondamentale. Dans ce chapitre, les propriétés des écoulements turbulents sont décrites. Différentes stratégies de modélisation sont ensuite détaillées.

13.2 Properties of homogeneous isotropic turbulence: single-phase flows

13.2.1 Main characteristics

The first researcher interested in the turbulent phenomena was Osborne Reynolds [157] at the end of the 19th century. He showed that if the convection is largely higher than dissipation, the laminar flow becomes turbulent. Thus, he defined the dimensionless Reynolds number as the ratio between the convection effect and the dissipative contribution:

$$Re = \frac{dU}{\nu} \quad (13.1)$$

with U the velocity scale, d the characteristic length and ν the cinematic viscosity. The transition between the two flow regimes (laminar and turbulent) which corresponds to a critical Reynolds number highly depends on the system configurations. For example, in a cylinder with a circular section, the transition is observed for a Reynolds number equal to 2300, whereas for the flow over a wing profile, the critical Reynolds number can reach $5 \cdot 10^5$.

Behind the diversity of turbulent flows, some universal characteristics can be defined [9, 29, 103]:

- Turbulent flows are mainly three dimensional (except in some particular cases such as stratified flows),
- They are unsteady and chaotic: a small perturbation of the flow is amplified over time.
- They are highly diffusive: the mass, momentum and heat transfers increase with turbulence. Thus, the mixtures are quicker and more efficient, which explains the interest of the chemistry industry for the chemical reactor.
- a variety of scales are represented in turbulent flows without discontinuities: the spectral energy density is continuous.
- the vorticity is not zero.

13.2.2 A multitude of scales

In a turbulent flow, different scales of length, time and velocity are observed. The largest ones are controlled by the geometry of the system and the boundary conditions. Therefore, their properties are dictated by the mean flow which has a velocity \mathbf{U} and a characteristic length d . They are responsible for the transport and the diffusion of the momentum. The turbulent kinetic energy is mainly contained in these structures. The existence of shear stress in the flow induces their division into small eddies, with a velocity \mathbf{u}_η and a characteristic length η . The motion of these structures is more isotropic and more sensible to the viscosity effects. The different scales of the turbulent flows are summarized in Table 13.1. The energy spectral density presented in Figure 13.1 gives another view of these scales and their energetic properties.

13.2. PROPERTIES OF HOMOGENEOUS ISOTROPIC TURBULENCE:
SINGLE-PHASE FLOWS

	Velocity	Length	Time	Reynolds number
Large scale	\mathbf{u}	Λ	Te	$Re_\Lambda = \frac{\Lambda \ \mathbf{u}\ }{\nu}$
Mean flow	\mathbf{U}	d	T	$Re_d = \frac{d \ \mathbf{U}\ }{\nu}$
Kolmogorov scales	$u_\eta = \nu \epsilon^{1/4}$	$\eta = \nu^{3/4} \epsilon^{-1/4}$	$t_\eta = (\frac{\nu}{\epsilon})^{1/2}$	$Re_\eta = \frac{\eta \ \mathbf{u}_\eta\ }{\nu} = 1$

Table 13.1: Characteristic quantities of isotropic turbulent flows.

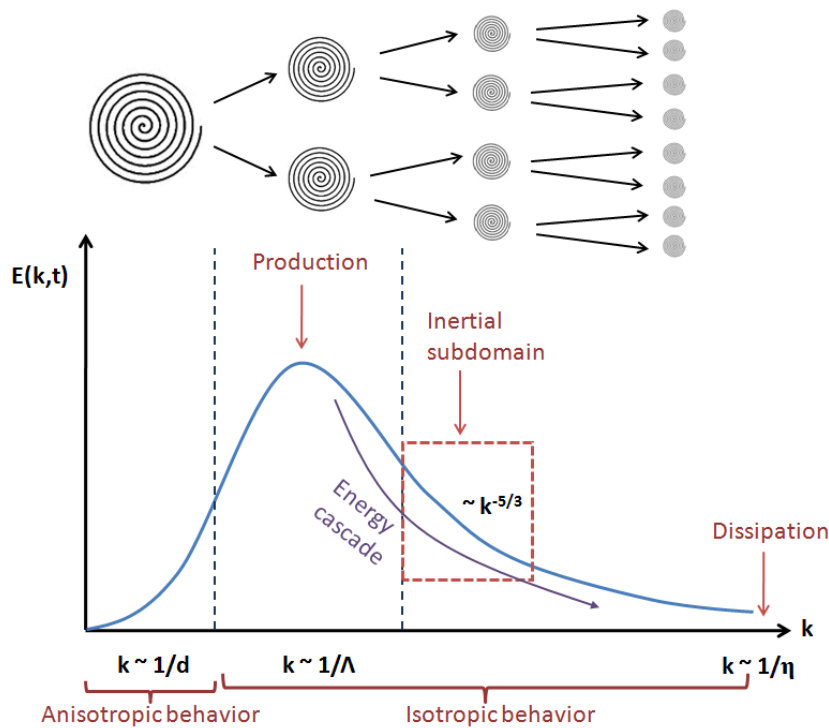


Figure 13.1: Energy spectral density $E(k,t)$ according to the wavenumber k for a turbulent flow.

13.2.3 Kolmogorov's energy cascade

At the beginning of the 20th century, Kolmogorov focused his work on the smallest eddies of turbulent flows. He first showed that the structures smaller than the Kolmogorov's length dissipate the energy from the largest structures by heating up the system. Indeed, at this scale, the viscosity effects are responsible for the temporal

velocity variations. The mathematical formulation of this statement allows defining the Kolmorov's scale:

$$\frac{\partial \mathbf{u}_\eta}{\partial t} = \nu \frac{\partial^2 \mathbf{u}_\eta}{\partial x^2} \quad (13.2)$$

with $\frac{\partial u_\eta}{\partial t} \simeq \frac{u_\eta^2}{\eta}$ the temporal velocity variation and $\nu \frac{\partial^2 u_\eta}{\partial x^2} \simeq \nu \frac{u_\eta}{\eta^2}$ the viscous term. Therefore, the Kolmogorov's Reynolds number is defined:

$$Re_\eta = \frac{\eta u_\eta}{\nu} = 1 \quad (13.3)$$

As we can see in Figure 13.1, the energy spectral density is continuous and the energy transfer begins from the large scales to the smallest ones. Therefore, the energy from the energetic structures is equal to the dissipation rate of turbulent kinetic energy, which leads to the following relation:

$$\frac{u_\eta^3}{\eta} = \frac{u^3}{\Lambda} \quad (13.4)$$

Since the dissipation rate of turbulent kinetic energy can be approximated by:

$$\epsilon = \frac{\nu}{2} \sum_{i,j} \left(\frac{\partial u_i}{\partial x_j} + \frac{\partial u_j}{\partial x_i} \right)^2 \simeq \nu \frac{u_\eta^2}{\eta^2} \quad (13.5)$$

Equations (13.3) and (13.5) lead to the relation given in Table 13.1:

$$u_\eta = (\nu \epsilon)^{\frac{1}{4}} \quad (13.6)$$

and

$$\eta = \nu^{\frac{3}{4}} \epsilon^{-\frac{1}{4}} \quad (13.7)$$

These last two relations illustrate the Kolmogorov's assumption that at high Reynolds numbers, the equilibrium state of the dissipative structures are entirely described with ν and ϵ . The second Kolmogorov's assumption is related to the energetic transfer between the different structures. He showed that depending on the Reynolds number of the large scales, the transition between the inertial domain and the viscous domain can include a viscous or inertial subdomain, as displayed in Figure 13.2. For $Re_\Lambda > 10^4$, an inertial subdomain appears and induces a decreasing of the energy density following the so called $-\frac{5}{3}$ law, visible in Figure 13.1:

$$\eta = C_K \epsilon^{\frac{2}{3}} k^{-\frac{5}{3}} \quad (13.8)$$

with $C_K \simeq 1.5$ the Kolmogorov's constant.

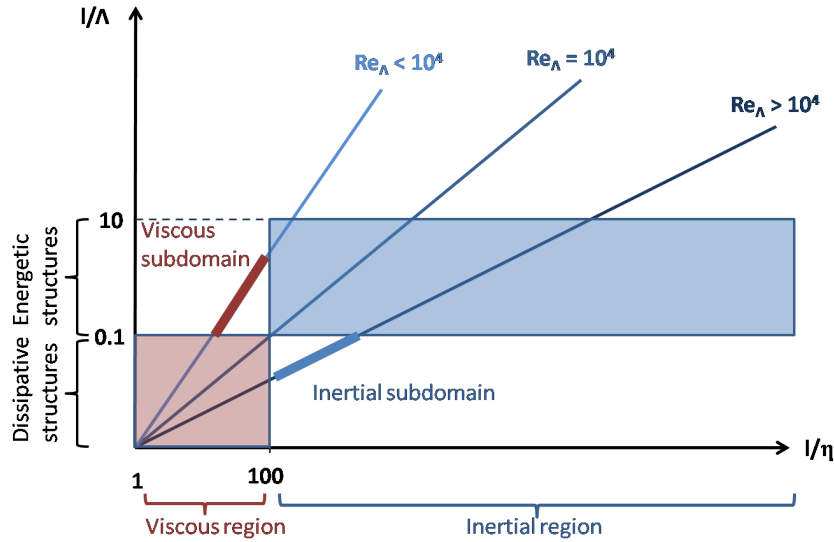


Figure 13.2: Map of the different energetic domains in a turbulent flow according to the observed scale l .

13.3 Properties of turbulent two-phase flows

Bubbles immersed in liquid generate an agitation, called pseudo-turbulence. This induced turbulence is on certain points similar to shear-induced turbulence for its random character but also different for the energy distribution over the wavelength. Indeed, the presence of bubbles in a flow modify the energy production, transfer and dissipation. Lance and Bataille [94] distinguish three types of mechanism:

- The first one concerns the extra turbulent fluctuations induced by the bubbles in their relative motion. This mechanism is predominant in rising bubbles test cases [118].
- The second mechanism is related to shear-induced turbulence in the wake of bubbles.
- The last one is the reverse coupling phenomenon: turbulent structures in the liquid induce bubbles deformations. Serizawa and Kataoka [179] showed that the bubble deformation could absorb the turbulent energy in the liquid and modify its dissipation even at low gas fractions.

These mechanisms strongly interact and induce non linear coupling effects which make the turbulence modeling very challenging.

In terms of energy spectrum, Lance and Bataille [94] found that, at high Reynolds numbers, for increasing gas fraction, the Kolmogorov energy spectrum exponent equal to $-\frac{5}{3}$ in homogeneous single-phase turbulence progressively decrease to reach

$-\frac{8}{3}$ due to wake dissipation effects. The authors also showed that quantity of spectral energy in the small scale eddies is larger and in the large scale eddies smaller.

More recently, several experimental works have investigated the agitation generated by bubbles rising at Reynolds numbers of order 100-1000, with millimetre-size air bubbles in water [119, 120, 158, 159, 162]. They found that:

- Each bubble wake is shorter than a single rising bubble wake due to the interaction with the wakes of the surrounding bubbles.
- The velocity fluctuations scale is a function of the gas fraction ($\alpha^{0.4}$).
- The vertical fluctuations are anisotropic and predominant in the upward direction.
- The integral length scale becomes equal to $\Lambda = \frac{d}{C_D}$ with C_D the bubble drag coefficient.
- The energy spectrum exhibits a k^{-3} for wavelengths smaller than Λ .

Bunner and Tryggvason [23] showed that the interaction between deformable bubbles and a pseudo-turbulent flow is dominated by wake effect, which leads to the formation of large scale flow structures. Moreover, the deformable bubbles induces larger velocity fluctuations. Hosokawa and Tomiyama [72] studied experimentally pseudo-turbulence in laminar pipe flows and made some other conclusions:

- Turbulence kinetic energy of bubble-induced turbulence and local void fraction are proportional.
- The ratio among axial turbulence intensity is twice the radial and azimuthal components of turbulence intensity respectively.
- The Reynolds shear stress of bubble-induced turbulence depends on velocity and void fraction gradients.
- The dissipation process of bubble-induced turbulence and shear-induced turbulence are similar.

13.4 Simulation of turbulent flows

As discussed in the previous section, turbulent flows are complex since a variety of time, velocity and length scales coexists. Therefore, different modeling and numerical strategies have been developed to simulate them.

13.4.1 Direct Numerical Simulation (DNS)

In Direct Numerical Simulation, the operators are discretized by choosing a time step and a cell size as small as possible to solve all the spatial and temporal scales. Therefore, for turbulent flows, this means that the cell size has to be smaller than the Kolmogorov's length η . The number of cells N^3 , necessary for the simulation, is then proportional to the ratio between the largest and the smallest scales: $\frac{\Lambda}{\eta}$. This implies that the total number of cells is of the order of $Re_{\Lambda}^{\frac{9}{4}}$. In Table 13.2, the total number of cells is given for different Reynolds numbers. As we can see in this table, the number of cells becomes quickly high. Therefore, DNS can be easily too much CPU consuming, which is not suited to simulations in industrial context. Thus, DNS is used as a "numerical experiment" in order to understand interactions and to evaluate the weight of some terms. For example, Bunner and Tryggvason [23] used DNS to study the interaction between deformable bubbles and a pseudo-turbulent flow generated by the bubble swarm. Lakehal *et al.* [91] investigated the impact of the interfacial dynamics on turbulent heat transfer at a sheared gas-liquid interface and the influence of the Prandtl number on the transport. These DNS highlighted the increase of the vertical turbulent heat transfer due to the enhancement of the velocity fluctuating field normal to the interface and allowed establishing a variation law for the heat transfer velocity according to the Prandtl number. However, this is only possible for low turbulent Reynolds numbers.

Reynolds number	Number of cells
10	178
100	31623
1000	$5.6 \cdot 10^6$
10^6	$3.2 \cdot 10^{13}$

Table 13.2: Number of cells necessary for the DNS of turbulent flows at different Reynolds numbers.

To simulate complex turbulent flows, other approaches have been developed. They use different types of averages to reduce the CPU consumption. These methods are introduced below.

13.4.2 Reynolds Average Navier-Stokes (RANS) / Unsteady Reynolds Average Navier-Stokes (URANS)

The Reynolds Average Navier-Stokes (RANS) and Unsteady Reynolds Average Navier-Stokes (URANS) approaches are based on an ensemble average description of the turbulence effects. Only the average flow in time and space is simulated.

Therefore, each quantity Φ is split into an average value and an instantaneous one. The first part is solved to obtain a stationary solution and the second part is modeled:

$$\Phi(x, t) = \underbrace{\overline{\Phi}(x, t)}_{\text{Average value}} + \underbrace{\Phi'(x, t)}_{\text{Instantaneous value}} \quad (13.9)$$

Moreover, in the RANS approach, a time averaging is defined to solve the averaged Navier-Stokes' equations. If this time scale becomes smaller than the one of the studied physical phenomenon, the average values depend on time and the calculation of their temporal derivations in the balance equations is required. In this case, we speak about Unsteady Reynolds Average Navier-Stokes (URANS) [185].

The corresponding energy spectral densities are displayed in Figure 13.3 for the RANS model and Figure 13.4 for the URANS model. These representations, proposed by Sagaut [164], show the distribution between the resolved and modeled parts for each approach.

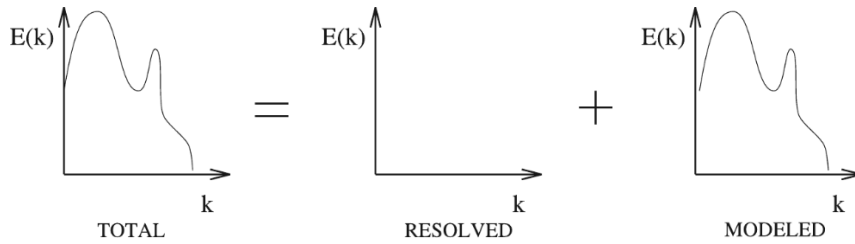


Figure 13.3: Schematic representation of the energy spectrum splitting between the resolved and modeled parts with the RANS approach [164].

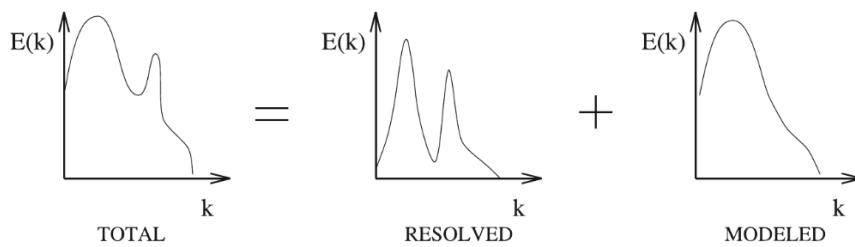


Figure 13.4: Schematic representation of the energy spectrum splitting between the resolved and modeled parts with the URANS approach [164].

To model the fluctuating quantities, the Reynolds stress tensor is defined as follows:

$$R = \overline{\mathbf{u}'\mathbf{u}'} = \nu^T \nabla \cdot \mathbf{u} + \frac{2}{3} K I_d \quad (13.10)$$

with ν^T the eddy viscosity. Models are then developed for the eddy viscosity.

A first available approach for the eddy viscosity modeling is the $K - \epsilon$ model [164]. In this case, two transport equations are solved: one for the turbulent kinetic

energy K and the other for the dissipation rate of turbulent kinetic energy ϵ . The eddy viscosity is then defined as:

$$\nu^T = \rho C_\nu \frac{K^2}{\epsilon} \quad (13.11)$$

This approach requires to fix different parameters such as C_ν by data fitting. Even though this model and its derivative version $K - \omega$ have been widely used to simulate turbulent flows [114, 136], Mimouni *et al.* [128] showed several shortcomings and deficiencies for industrial applications in nuclear industry. But, the main issue with the $K - \epsilon$ model is its inability to deal with anisotropic turbulent flows. An illustration of this difficulty can be found in [38]. Indeed, a simulation of the Deen *et al.* experiment [36] which is a column of water with bubbles rising up has been performed with the $K - \epsilon$ model. The model predicts an isotropic path for the bubbles in total disagreement with the expected results.

The second most used approach is the Reynolds Stress Transport Models (RSTM) or $R_{ij} - \epsilon$ model [127, 164]. In this family of models, the dissipation rate of turbulent kinetic energy ϵ and the six terms of the Reynolds stress tensor are transported. Therefore, compared to the previous model, the computational time is higher. Nevertheless, in the Deen *et al.* experiment, this model gave better results in terms of flow anisotropy [38].

However, these two approaches are based on an ensemble average description of turbulence effects which is not suitable for the simulation of unsteady two-phase flows using the multifield approach. Indeed, simulations using a dispersed approach are based on an ensemble average view of the small and spherical inclusions. The RANS and URANS approaches are then appropriate for the simulation of such flows. In the multifield approach, an interface tracking method is added to the dispersed model for the simulation of large and deformable inclusions. For such interfacial structures, a deterministic description is used. Thus, the ensemble average view of the RANS and URANS cannot be applied anymore.

13.4.3 Large Eddy Simulation

Contrary to the previous methods, the Large Eddy Simulations considered a deterministic description of turbulence based on filtered quantities. The large scales are solved whereas the small dissipative structures are modeled. Figure 13.5 gives an illustration of this approach in terms of energetic spectrum.

This method requires the use of large scale-pass filter G with a filter width $\bar{\Delta}$. The filtered variable $\bar{\Phi}$ is then defined as:

$$\bar{\Phi} = \int_{-\infty}^{-\infty} \int_{-\infty}^{-\infty} G(\bar{\Delta}, x - y, t - t') \Phi(y, t') dy dt' \quad (13.12)$$

After applying the filter G , the quantity Φ can be split into a resolved part and a modeled part:

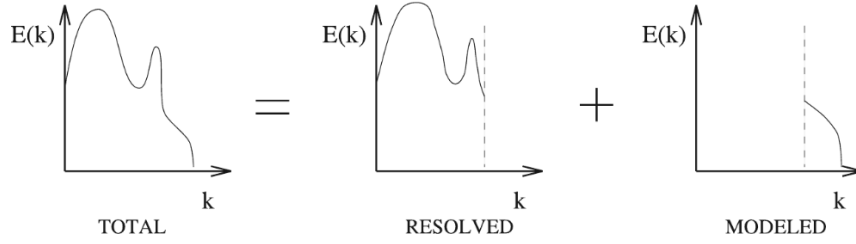


Figure 13.5: Schematic representation of the energy spectrum splitting between the resolved and modeled parts with the LES approach [164].

$$\Phi(x, t) = \underbrace{\bar{\Phi}(x, t)}_{\text{Solved scales}} + \underbrace{\Phi'(x, t)}_{\text{Modeled scales}} \quad (13.13)$$

The large scale-pass filter G has the following properties.:

- A filtered constant is equal to itself:

$$\begin{aligned} \bar{a} &= \int_{-\infty}^{-\infty} \int_{-\infty}^{-\infty} G(\bar{\Delta}, x - y, t - t') a dy dt' \\ &= a \int_{-\infty}^{-\infty} \int_{-\infty}^{-\infty} G(\bar{\Delta}, x - y, t - t') dy dt' \\ &= a \end{aligned} \quad (13.14)$$

- Linearity:

$$\overline{\Phi + \psi} = \bar{\Phi} + \bar{\psi} \quad (13.15)$$

- Commutation with the derivatives:

$$\frac{\partial \bar{\Phi}}{\partial s} = \bar{\frac{\partial \Phi}{\partial s}} \quad (13.16)$$

The commutation with the spatial derivatives is ensured if the filter is homogeneous in space.

- The idempotence property is not assumed:

$$\bar{\bar{\Phi}} \neq \bar{\Phi} \text{ and } \overline{\bar{\Phi}\psi} \neq \bar{\Phi}\bar{\psi} \quad (13.17)$$

The LES approach has been used more recently as an alternative to the RANS methods. In the framework of the multifield approach, the deterministic description of the turbulence effects proposed by the LES seems more suitable. Thus, the next chapter will be devoted to LES. The filtered equations will be presented. Some associated turbulence models available in the literature will be detailed. Finally, the effect of interfaces and dispersed structures on the modeling will be discussed.

Chapter 14

Large Eddy Simulation of turbulent two-phase flows

To simulate two-phase flows with the multifield approach, large interfaces are located thanks to the volume fraction updated using the mass balance equation. Thus, they are described in a deterministic way contrary to the dispersed fields which are considered using an ensemble average point of view. Choosing ensemble average methods such as RANS or URANS to model turbulence effects in the framework of the multifield approach seems then not suitable. Therefore, in this chapter, LES of two-phase flows which is based on a deterministic description of turbulence effects is detailed. First, the filtered one-fluid equations are presented for pedagogical purposes. The objectives are first to explain the methodology to filter the equations and then to apply this methodology in Chapter 16 to filter the two-fluid equations. The second objective is to highlight the subgrid terms obtained with the filtered one-fluid equations and to compare them to the corresponding terms in the filtered two-fluid equations. Then, different LES models are detailed. Finally, recent works and difficulties appearing when interfaces and dispersed phases are present in flows are discussed. In this chapter, only isothermal and incompressible flows are considered. Thus, the filtering of the energy balance equation is not detailed in a first approach.

14.1 Résumé du chapitre

Au sein de l'approche multi-champ, les grandes interfaces sont localisées dans le domaine grâce à la distribution des fractions volumiques, actualisées à chaque pas de temps via la résolution de l'équation de bilan de masse. Elles sont donc décrites de manière déterministe contrairement au champ dispersé qui est vu en moyenne d'ensemble. Le choix du modèle de turbulence à associer doit donc être cohérent avec le type de modélisation choisi pour les structures diphasiques. Les approches de type RANS et URANS sont basées sur une description en moyenne d'ensemble de la turbulence tandis que la simulation aux grandes échelles (LES) est un modèle déterministe. La LES semble donc la plus appropriée pour la simulation d'écoulements contenant des grandes interfaces. Ce chapitre est donc dédié à la

LES. Dans un premier temps, les équations du modèle 1-fluide sont filtrées. Cette première partie a pour objectif de montrer l'effet du filtre LES sur les équations et de présenter la méthodologie suivie pour le filtrage car elle sera ensuite appliquée dans le Chapitre 16 aux équations bi-fluide avec le Modèle Large Bulle. Après avoir identifié les termes sous-mailles apparaissant dans les équations, différents modèles disponibles dans la littérature sont présentés de manière non exhaustive. Enfin, les modifications de l'écoulement induites par la présence de petites bulles sphériques et de grandes interfaces sont décrites. Dans ce chapitre, on ne considère que des écoulements isothermes. le filtrage de l'équation du bilan d'énergie n'est donc pas présenté.

14.2 LES filtering of the single-fluid model equations

LES of turbulent two-phase flows containing large interfaces has never been performed with two-fluid models since the treatment of such interfaces with the two-fluid model has been first proposed by Denèfle [38]. Thus, the filtered two-fluid equations in this particular case have never been presented. On the contrary, the filtering of the single-fluid model equations for the simulation of large interfaces has been performed by several research groups [88, 96, 207]. In order to understand the effect of the LES filter and to highlight the methodology to obtain the filtered equations, this section is devoted to the filtering of the single-fluid model equations. The equations of the two-fluid model for large interface simulations (with the LBMo) will then be filtered in Chapter 16 following the same procedure as apply to the one-fluid model.

In this section, we consider that the interfaces are followed using a VOF approach with a color function C (see section 2.4.4). For incompressible isothermal flows, three equations are solved [83, 116, 173]: a mass balance equation, a momentum balance equation and the advection equation for the color function C :

$$\begin{cases} \nabla \cdot \mathbf{u} = 0 \\ \frac{\partial \rho \mathbf{u}}{\partial t} + \nabla \cdot (\rho \mathbf{u} \otimes \mathbf{u}) = \nabla \cdot (\underline{\underline{\mu S}}) - \nabla P + \rho \mathbf{g} + \sigma \kappa \nabla C \\ \frac{\partial C}{\partial t} + \mathbf{u} \cdot \nabla C = 0 \end{cases} \quad (14.1)$$

with $\nabla C = \mathbf{n}^{Int} \delta^{Int}$.

After applying the filter G and assuming the commutation with the time and space derivatives, we obtain:

$$\begin{cases} \overline{\nabla \cdot \mathbf{u}} = 0 \\ \frac{\partial \overline{\rho \mathbf{u}}}{\partial t} + \nabla \cdot (\overline{\rho \mathbf{u} \otimes \mathbf{u}}) = \nabla \cdot (\overline{\underline{\underline{\mu S}}}) - \nabla \overline{P} + \overline{\rho \mathbf{g}} + \overline{\sigma \kappa \nabla C} \\ \frac{\partial \overline{C}}{\partial t} + \overline{\mathbf{u} \cdot \nabla C} = 0 \end{cases} \quad (14.2)$$

Two systems of filtered quantities can be used to solve these equations: $(\bar{\mathbf{u}}, \bar{P}, \bar{C}, \bar{\rho}, \bar{\mu}, \hat{\kappa})$ or $(\tilde{\mathbf{u}}, \bar{P}, \bar{C}, \bar{\rho}, \bar{\mu}, \hat{\kappa})$, with $\tilde{\mathbf{u}} = \frac{\overline{\rho \mathbf{u}}}{\bar{\rho}}$ the Favre's velocity. In what follows, we will show the resulted subgrid terms for the two approaches. One can note that the derivation is confined to equidistant grids for which the commutativity of the filtering operation with respect to the differential operators is valid.

14.2.1 Simple filtering

In this section, the first system of filtered quantities $(\bar{\mathbf{u}}, \bar{P}, \bar{C}, \bar{\rho}, \bar{\mu}, \hat{\kappa})$ is used to obtain the final filtered equations and subgrid terms.

14.2.1.1 Advection equation

The term on the left-hand side of the filtered advection equation has the following expression:

$$\frac{\partial \bar{C}}{\partial t} + \overline{\mathbf{u} \cdot \nabla C} = \frac{\partial \bar{C}}{\partial t} + \bar{\mathbf{u}} \cdot \nabla \bar{C} + (\overline{\mathbf{u} \cdot \nabla C} - \bar{\mathbf{u}} \cdot \nabla \bar{C}) \quad (14.3)$$

Thus, the filtered equation can be written:

$$\frac{\partial \bar{C}}{\partial t} + \bar{\mathbf{u}} \cdot \nabla \bar{C} + \bar{\tau}_{interf} = 0 \quad (14.4)$$

with $\bar{\tau}_{interf}$ the first subgrid term defined as:

$$\bar{\tau}_{interf} = (\overline{\mathbf{u} \cdot \nabla C} - \bar{\mathbf{u}} \cdot \nabla \bar{C}) \quad (14.5)$$

This subgrid term highlights the relationship between the filtered velocity $\bar{\mathbf{u}}$ and the interface topology through the term $\nabla \bar{C}$.

14.2.1.2 Mass balance equation

We have the following filtered mass balance equation [88, 96]:

$$\overline{\nabla \cdot \mathbf{u}} = 0 \quad (14.6)$$

Since the commutativity between the differential operator is assumed, the divergence free condition is still valid for the filtered velocity. Thus, the filtered mass balance equation does not include subgrid terms:

$$\nabla \cdot \bar{\mathbf{u}} = 0 \quad (14.7)$$

14.2.1.3 Momentum balance equation

For a conservative formulation in time and space, we have the following filtered momentum balance equation:

$$\frac{\partial \bar{\rho} \bar{\mathbf{u}}}{\partial t} + \bar{\tau}_{time} + \bar{\rho} \bar{\mathbf{u}} \nabla \cdot \bar{\mathbf{u}} + \bar{\tau}_{conv} = \nabla \cdot (\bar{\mu} \underline{\underline{S}}) + \bar{\tau}_{diff} - \nabla \bar{P} + \bar{\rho} \mathbf{g} + \sigma \hat{\kappa} \nabla \bar{C} + \bar{\tau}_{superf} \quad (14.8)$$

with $\bar{\tau}_{time}$, $\bar{\tau}_{conv}$, $\bar{\tau}_{diff}$ and $\bar{\tau}_{superf}$ four additional subgrid terms:

$$\bar{\tau}_{time} = \frac{\partial \bar{\rho} \bar{\mathbf{u}}}{\partial t} - \frac{\partial \bar{\rho} \bar{\mathbf{u}}}{\partial t} \quad (14.9)$$

$$\begin{aligned} \bar{\tau}_{conv} &= \nabla \cdot (\overline{\rho \mathbf{u} \otimes \mathbf{u}}) - \nabla \cdot (\bar{\rho} \bar{\mathbf{u}} \otimes \bar{\mathbf{u}}) \\ &= \overline{\rho \mathbf{u} \nabla \cdot \mathbf{u}} - \bar{\rho} \bar{\mathbf{u}} \nabla \cdot \bar{\mathbf{u}} \end{aligned} \quad (14.10)$$

One can note that these two formulations are equal because $\overline{\nabla \cdot (\rho \mathbf{u})} = 0$.

$$\bar{\tau}_{diff} = \nabla \cdot (\underline{\underline{\mu S}}) - \nabla \cdot (\bar{\mu} \underline{\underline{S}}) \quad (14.11)$$

$$\bar{\tau}_{superf} = \sigma (\overline{\kappa \nabla C} - \hat{\kappa} \nabla C) \quad (14.12)$$

with $\hat{\kappa} = -\nabla \cdot \left(\frac{\nabla C}{\|\nabla C\|} \right)$ the filtered curvature.

To understand the effect of the convective subgrid term $\bar{\tau}_{conv}$, let us consider the Leonard's decomposition of the term. Taking the same notations introduced in section 13.4.3, the filtered velocity can be split into a resolved part $\bar{\mathbf{u}}$ and a subgrid part \mathbf{u}' :

$$\mathbf{u} = \bar{\mathbf{u}} + \mathbf{u}' \quad (14.13)$$

Thus, Leonard [102] proposed a decomposition for the convective term $\overline{\mathbf{u} \otimes \mathbf{u}} = \overline{u_i u_j}$ using the previous expression:

$$\begin{aligned} \overline{u_i u_j} &= \overline{(\bar{u}_i + u'_i) (\bar{u}_j + u'_j)} \\ &= \overline{\bar{u}_i \bar{u}_j} + \overline{\bar{u}_i u'_j} + \overline{\bar{u}_j u'_i} + \overline{u'_i u'_j} \end{aligned} \quad (14.14)$$

This decomposition highlights two contributions. The first one, $\underline{\underline{C}}_{ij}$, corresponds to the interactions between the subgrid and resolved scales. The second contribution depicts the interactions between the subgrid scales themselves and is denoted $\underline{\underline{R}}_{ij}$:

$$\underline{\underline{C}}_{ij} = \overline{\bar{u}_i u'_j} + \overline{\bar{u}_j u'_i} \quad (14.15)$$

$$\underline{\underline{R}}_{ij} = \overline{u'_i u'_j} \quad (14.16)$$

The second order filtered term $\overline{\bar{u}_i \bar{u}_j}$ is split once again [102]:

$$(\overline{\bar{u}_i \bar{u}_j} - \bar{u}_i \bar{u}_j) + \bar{u}_i \bar{u}_j = \underline{\underline{L}}_{ij} + \bar{u}_i \bar{u}_j \quad (14.17)$$

The new tensor appearing in this equation, denoted L_{ij} and called the Leonard's tensor, contains the interactions between the large resolved scales. This decomposition allows rewriting the filtered convective term as follows:

$$\frac{\partial \overline{u_i u_j}}{\partial x_j} = \frac{\partial \overline{u_i} \overline{u_j}}{\partial x_j} + \underline{\underline{\tau}}_{ij} \quad (14.18)$$

with $\underline{\underline{\tau}}_{ij} = \frac{\partial}{\partial x_j} \left(\underline{\underline{C}}_{ij} + \underline{\underline{R}}_{ij} + \underline{\underline{L}}_{ij} \right)$. The convective subgrid term is then a combination of the three contributions $\underline{\underline{C}}_{ij}$, $\underline{\underline{R}}_{ij}$ and $\underline{\underline{L}}_{ij}$.

Finally, the two last subgrid terms $\underline{\underline{\tau}}_{diff}$ and $\underline{\underline{\tau}}_{surf}$ refers respectively to the correlation between the velocity and the viscosity which is discontinuous at the interface and the subgrid fluctuations of the surface tension force.

14.2.2 Favre's averaging

The second system of filtered quantities $(\tilde{\mathbf{u}}, \overline{P}, \overline{C}, \overline{\rho}, \overline{\mu}, \hat{\kappa})$ is now considered, with $\tilde{\mathbf{u}} = \frac{\overline{\rho \mathbf{u}}}{\overline{\rho}}$ the Favre's velocity.

14.2.2.1 Advection equation

The same method is applied to filter the advection equation with the Favre's averaging:

$$\frac{\partial \overline{C}}{\partial t} + \tilde{\mathbf{u}} \cdot \nabla \overline{C} + \tilde{\tau}_{interf} = 0 \quad (14.19)$$

with:

$$\tilde{\tau}_{interf} = (\overline{\mathbf{u} \cdot \nabla C} - \tilde{\mathbf{u}} \cdot \nabla \overline{C}) \quad (14.20)$$

14.2.2.2 Mass balance equation

To obtain the divergence of the Favre's velocity, let us evaluate the term $\overline{\rho \nabla \cdot \mathbf{u}}$ [88, 96]. This term can be expressed using the definition of ρ (see Equation (2.21)) and the filtered advection equation:

$$\overline{\rho \nabla \cdot \mathbf{u}} = (\rho_1 - \rho_2) \underbrace{\left(\frac{\partial \overline{C}}{\partial t} + \mathbf{u} \cdot \nabla \overline{C} \right)}_{=0} \quad (14.21)$$

This leads to:

$$\overline{\rho \nabla \cdot \mathbf{u}} = 0 \quad (14.22)$$

Developing the term on the left-hand side of this equation:

$$\begin{aligned}
\overline{\rho \nabla \cdot \mathbf{u}} &= \overline{\nabla \cdot (\rho \mathbf{u})} - \overline{\mathbf{u} \nabla \rho} \\
&= \overline{\nabla \cdot (\bar{\rho} \tilde{\mathbf{u}})} - \overline{\mathbf{u} \nabla \bar{\rho}} \\
&= (\bar{\rho} \nabla \cdot \tilde{\mathbf{u}} + \tilde{\mathbf{u}} \nabla \bar{\rho}) - \overline{\mathbf{u} (\rho_1 - \rho_2) \nabla C} \\
&= (\bar{\rho} \nabla \cdot \tilde{\mathbf{u}} + \tilde{\mathbf{u}} (\rho_1 - \rho_2) \nabla \bar{C}) - \overline{\mathbf{u} (\rho_1 - \rho_2) \nabla C}
\end{aligned} \tag{14.23}$$

with $\bar{\rho} = \bar{C} \rho_1 + (1 - \bar{C}) \rho_2$. One can note that for constant density flows, we consider [90]: $\bar{\rho} = \tilde{\rho} = \rho$.

Therefore, from these two equations, we deduce the filtered mass balance equation:

$$\nabla \cdot \tilde{\mathbf{u}} = \frac{\rho_1 - \rho_2}{\bar{\rho}} \tilde{\tau}_{interf} \tag{14.24}$$

$$\text{with } \tilde{\tau}_{interf} = (\overline{\mathbf{u} \cdot \nabla C} - \tilde{\mathbf{u}} \cdot \nabla \bar{C}).$$

14.2.2.3 Momentum balance equation

With the Favre's averaging, the following filtered momentum balance equation is obtained:

$$\frac{\partial \bar{\rho} \tilde{\mathbf{u}}}{\partial t} + \nabla \cdot (\bar{\rho} \tilde{\mathbf{u}} \otimes \tilde{\mathbf{u}}) + \tilde{\tau}_{conv} = \nabla \cdot (\underline{\underline{\bar{\mu} \tilde{S}}}) + \tilde{\tau}_{diff} - \nabla \bar{P} + \bar{\rho} \mathbf{g} + \sigma \hat{\kappa} \nabla \bar{C} + \tilde{\tau}_{superf} \tag{14.25}$$

with $\tilde{\tau}_{conv}$, $\tilde{\tau}_{diff}$ and $\tilde{\tau}_{superf}$:

$$\tilde{\tau}_{conv} = \nabla \cdot (\overline{\rho \mathbf{u} \otimes \mathbf{u}}) - \nabla \cdot (\bar{\rho} \tilde{\mathbf{u}} \otimes \tilde{\mathbf{u}}) \tag{14.26}$$

$$\tilde{\tau}_{diff} = \nabla \cdot (\underline{\underline{\bar{\mu} \tilde{S}}}) - \nabla \cdot (\underline{\underline{\bar{\mu} \tilde{S}}}) \tag{14.27}$$

$$\tilde{\tau}_{superf} = \sigma (\hat{\kappa} \nabla \bar{C} - \hat{\kappa} \nabla C) = \bar{\tau}_{superf} \tag{14.28}$$

With the conservative formulation of the momentum balance equation, the sub-grid term $\tilde{\tau}_{time}$ is equal to 0 since:

$$\begin{aligned}
\tilde{\tau}_{time} &= \frac{\partial \bar{\rho} \tilde{\mathbf{u}}}{\partial t} - \frac{\partial \bar{\rho}}{\partial t} \tilde{\mathbf{u}} \\
&= \frac{\partial \bar{\rho} \tilde{\mathbf{u}}}{\partial t} - \frac{\partial}{\partial t} \left(\bar{\rho} \frac{\bar{\rho} \tilde{\mathbf{u}}}{\bar{\rho}} \right) \\
&= 0
\end{aligned} \tag{14.29}$$

However, one can note that for a non conservative formulation of the equation in time, an extra source term appears:

$$\frac{\partial \bar{\rho} \tilde{\mathbf{u}}}{\partial t} = \bar{\rho} \frac{\partial \tilde{\mathbf{u}}}{\partial t} + \tilde{\mathbf{u}} \frac{\partial \bar{\rho}}{\partial t} \tag{14.30}$$

The second term on the right-hand side can be written:

$$\tilde{\mathbf{u}} \frac{\partial \bar{\rho}}{\partial t} = \tilde{\mathbf{u}} (\rho_1 - \rho_2) \frac{\partial \bar{C}}{\partial t} \quad (14.31)$$

Using the filtered advection equation (14.19), we obtain:

$$\frac{\partial \bar{\rho} \tilde{\mathbf{u}}}{\partial t} = \bar{\rho} \frac{\partial \tilde{\mathbf{u}}}{\partial t} + \tilde{\mathbf{u}} (\rho_2 - \rho_1) (\tilde{\mathbf{u}} \cdot \nabla \bar{C} + \tilde{\tau}_{interf}) \quad (14.32)$$

The filtered momentum balance equation becomes:

$$\begin{aligned} \bar{\rho} \frac{\partial \tilde{\mathbf{u}}}{\partial t} + \tilde{\mathbf{u}} (\rho_2 - \rho_1) (\tilde{\mathbf{u}} \cdot \nabla \bar{C} + \tilde{\tau}_{interf}) + \nabla \cdot (\bar{\rho} \tilde{\mathbf{u}} \otimes \tilde{\mathbf{u}}) + \tilde{\tau}_{conv} = \nabla \cdot (\bar{\mu} \underline{\underline{S}}) + \tilde{\tau}_{diff} \\ - \nabla \bar{P} + \bar{\rho} \mathbf{g} + \sigma \hat{\kappa} \nabla \bar{C} + \tilde{\tau}_{superf} \end{aligned} \quad (14.33)$$

To summarize, all the subgrid terms obtained with the simple filtering and the Favre's averaging are displayed in Table 14.1. The choice between each system affects the number of subgrid terms and the modeling strategy. For the first system (simple filtering), an advantage is the absence of subgrid terms for the mass balance equation. Nevertheless, for the momentum balance equation, a subgrid term which is time dependent appears and is difficult to model. This approach was chosen by Toutant [197]. However, the second system was recommended by different authors [88, 109, 110, 198, 207].

Subgrid terms	Simple filtering	Favre's averaging
τ_{time}	$\frac{\partial \bar{\rho} \bar{\mathbf{u}}}{\partial t} - \bar{\rho} \frac{\partial \bar{\mathbf{u}}}{\partial t}$	—
τ_{conv}	$\overline{\rho \mathbf{u} \nabla \cdot \mathbf{u}} - \bar{\rho} \bar{\mathbf{u}} \nabla \cdot \bar{\mathbf{u}}$	$\nabla \cdot (\bar{\rho} \mathbf{u} \otimes \mathbf{u}) - \nabla \cdot (\bar{\rho} \tilde{\mathbf{u}} \otimes \tilde{\mathbf{u}})$
τ_{diff}	$\nabla \cdot (\bar{\mu} \underline{\underline{S}}) - \nabla \cdot (\bar{\mu} \underline{\underline{S}})$	$\nabla \cdot (\bar{\mu} \underline{\underline{S}}) - \nabla \cdot (\bar{\mu} \underline{\underline{S}})$
τ_{superf}	$\sigma (\bar{\kappa} \nabla \bar{C} - \hat{\kappa} \nabla \bar{C})$	$\sigma (\bar{\kappa} \nabla \bar{C} - \hat{\kappa} \nabla \bar{C})$
τ_{interf}	$(\bar{\mathbf{u}} \cdot \nabla \bar{C} - \bar{\mathbf{u}} \cdot \nabla \bar{C})$	$(\bar{\mathbf{u}} \cdot \nabla \bar{C} - \tilde{\mathbf{u}} \cdot \nabla \bar{C})$

Table 14.1: Summary of the subgrid terms appearing in the filtered single-fluid model equations with the simple filtering ($\bar{\mathbf{u}}, \bar{P}, \bar{C}, \bar{\rho}, \bar{\mu}, \hat{\kappa}$) and the Favre's averaging ($\tilde{\mathbf{u}}, \bar{P}, \bar{C}, \bar{\rho}, \bar{\mu}, \hat{\kappa}$).

14.2.3 Discussion

The subgrid terms that appear in the filtered conservation equations are characteristic of the turbulent and interfacial motion subgrid behavior and their interactions. Therefore, they have to be modeled properly to simulate these turbulent flows. Since models are not yet available for all these subgrid terms, first DNS

studies have been performed to evaluate and compare their relative contributions. Therefore, several research groups [96, 198, 207] have been working on the hierarchy of these subgrid terms in the case of separated phases flows [96], turbulence-bubble interaction [88, 198, 207] or spray atomization [30]. They found that the predominant subgrid term is τ_{conv} . The three other terms are highly dependent on the flow configuration and the two-phase description. Therefore, *a posteriori* LES have been performed by modeling only τ_{conv} [109, 110, 156].

14.3 Models for the subgrid terms

Two main approaches to model the subgrid terms can be distinguished. The first ones, called the functional models, are based on the Kolmogorov's energetic cascade and the second ones, the structural models, use a reconstructed real velocity according to the filtered solved velocity. With this second type of models, the mathematical structure of the subgrid term is preserved. In this section, different methods are detailed for each range of models. The objective is not to give an exhaustive overview of all the existing models since it has been previously done in [164] but to present only the models which will be compared in this thesis.

14.3.1 Functional models

In these models, some assumptions based on the Kolmogorov's theory are necessary. First, the subgrid scales must be isotropic and energetically balanced with the resolved scales. Secondly, the main effect of subgrid scales is the energy dissipation. Thus, within these assumptions, the energy cascade mechanism can be assimilated to a molecular diffusion phenomenon, in which the molecular viscosity μ is completed with an eddy viscosity μ^T .

By assuming a linear relationship between the deviatoric part of the subgrid tensor $\bar{\tau}_{conv}^d$ and the resolved deformation rate tensor $\underline{\underline{S}}$. Thus, the subgrid term $\bar{\tau}_{conv}$ can be modeled as follows:

$$\bar{\tau}_{conv}^d = \bar{\tau}_{conv} - \frac{1}{3}tr(\bar{\tau}_{conv})\underline{\underline{I}}_d = -\mu^T\underline{\underline{S}} \quad (14.34)$$

with $tr(.)$ the trace of the matrix. This equation is called the Boussinesq's relation. The isotropic part of the subgrid stress tensor $\frac{1}{3}tr(\bar{\tau}_{conv})\underline{\underline{I}}_d$ is injected in the pressure term:

$$\bar{P}^* = \bar{P} + \frac{1}{3}tr(\bar{\tau}_{conv})\underline{\underline{I}}_d \quad (14.35)$$

The filtered momentum balance equation becomes then:

$$\frac{\partial \bar{\rho} \bar{\mathbf{u}}}{\partial t} + \nabla \cdot (\bar{\rho} \bar{\mathbf{u}} \otimes \bar{\mathbf{u}}) = \nabla \cdot ((\bar{\mu} + \mu^T)\underline{\underline{S}}) - \nabla \bar{P}^* + \bar{\rho} \mathbf{g} + \bar{\tau}_{diff} + \sigma \hat{\kappa} \nabla \bar{C} + \bar{\tau}_{superf} \quad (14.36)$$

To close the system, different approaches have been proposed to model the eddy viscosity $\nu^T = \frac{\mu^T}{\rho}$. However, since they are based on the energy cascade mechanism, they can only be applied to the convective subgrid term $\bar{\tau}_{conv}$ and the interfacial subgrid term $\bar{\tau}_{interf}$.

14.3.1.1 Smagorinsky's model

This model was proposed by Smagorinsky [182]. The eddy viscosity is defined as follows:

$$\nu^T = (C_S \bar{\Delta})^2 |\underline{\underline{S}}_{ij}| \quad (14.37)$$

$$\text{with } |\underline{\underline{S}}_{ij}| = \sqrt{2 \underline{\underline{S}}_{ij} \underline{\underline{S}}_{ij}} \text{ and } \underline{\underline{S}}_{ij} = \frac{1}{2} \left(\frac{\partial \bar{u}_i}{\partial x_j} + \frac{\partial \bar{u}_j}{\partial x_i} \right).$$

The constant value C_S is defined in order to have the equilibrium between energy production and dissipation. Lilly introduced the following expression [106]:

$$C_S = \frac{1}{\pi} \left(\frac{2}{3C_K} \right)^{3/4} \simeq 0.18 \quad (14.38)$$

with $C_K \simeq 1.5$ the Kolmogorov's constant. Nevertheless, these two constants C_K and C_S are fixed for isotropic homogeneous turbulence in single-phase flows. Therefore, for two-phase flows, their values depend on the situation and have to be adjusted. The authors in [92, 110] recommend $C_S = 0.1$.

This model is convenient to deal with complex geometries since it is based on local evaluation of the velocity gradient. However, it fails to predict the asymptotic behavior of turbulence approaching a wall [110]. Indeed, the eddy viscosity has a non zero value near the walls due to the existence of velocity gradients. Therefore, a common remedy has been to use a near-wall treatment such as the van Driest damping function [205]. Nevertheless, the implementation of this method becomes difficult for complex geometries. Then, Germano *et al.* [55] proposed to vary dynamically the coefficient C_S in order to cancel the eddy viscosity near walls. In what follows, this version of the Smagorinsky's model is referred as the Smagorinsky's model with the dynamic procedure. For this purpose, they consider a second filter, called test filter. This filter is twice the size of the grid filter: $\hat{\Delta} = 2\bar{\Delta}$, with $\hat{\Delta}$ corresponding to the test filter. The expression of the coefficient C_S becomes [107]:

$$C_S^I = \sqrt{\frac{1}{2} \frac{\underline{\underline{L}}_{ij}^I \underline{\underline{M}}_{ij}^I}{(\underline{\underline{M}}_{ij}^I)^2}} \quad (14.39)$$

with:

$$\underline{\underline{L}}_{ij}^I = \hat{\hat{u}}_i^I \hat{\hat{u}}_j^I - \widehat{\widehat{u}_i^I u_j^I} \quad (14.40)$$

and

$$\underline{\underline{M}}_{ij}^I = \hat{\Delta}^2 |\hat{\hat{S}}_{ij}^I| \hat{\hat{S}}_{ij}^I - \widehat{\widehat{\Delta}^2 |\underline{\underline{S}}_{ij}^I| \underline{\underline{S}}_{ij}^I} \quad (14.41)$$

In this approach, the coefficient C_S varies over time and space depending on the velocity field. However, the method requires to average C_S in space to avoid numerical instabilities generated by the prediction of negative values for the coefficient. Benhamadouche [14] showed that the results were improved with this extra averaging step especially for the simulation of the fully developed turbulent channel flow. In all this report, if we refer to the Smagorinsky's model with the dynamic procedure, it means that the Smagorinsky's constant C_S vary dynamically according to the Germano's procedure [55] and is space-averaged using the neighbors. Other derivative versions of the Smagorinsky's model have been proposed such as the Inertial Range Consistent (IRC) and the multi-scales Inertial Range Consistent [125].

14.3.1.2 Wall-Adapting Local Eddy-Viscosity (WALE)

This model has been developed to reproduce the proper turbulent scaling at the wall [143]. It also ensures that the eddy viscosity has a non zero value near walls:

$$\nu^T = (C_W \bar{\Delta})^2 \frac{\left(\overline{\underline{S}}_{ij}^d \overline{\underline{S}}_{ij}^d\right)^{\frac{3}{2}}}{\left(\overline{\underline{S}}_{ij} \overline{\underline{S}}_{ij}\right)^{\frac{5}{2}} + \left(\overline{\underline{S}}_{ij}^d \overline{\underline{S}}_{ij}^d\right)^{\frac{5}{4}}} \quad (14.42)$$

with $\overline{\underline{S}}_{ij}^d = \frac{1}{2} \left(\frac{\partial \bar{u}_i}{\partial x_k} \frac{\partial \bar{u}_k}{\partial x_j} + \frac{\partial \bar{u}_j}{\partial x_k} \frac{\partial \bar{u}_k}{\partial x_i} \right) - \frac{1}{3} \delta_{ij} \frac{\partial \bar{u}_k}{\partial x_k}^2$ and $C_W = 0.5$.

With this formulation, the eddy viscosity takes into account both the strain and the rotation rate of the smallest turbulent structures through the specific term $\overline{\underline{S}}_{ij}^d \overline{\underline{S}}_{ij}^d$ [214]. Moreover, as for the Smagorinsky's model, it is suitable for complex geometries involving structured or unstructured methods because it is only based on local parameters.

14.3.2 Structural models

One of the main drawback of the functional models is that they are only able to model the energy transfer from the large scales to the small scales. Thus, they can only be applied to two subgrid terms. Contrary to the functional models, the structural models are not based on the effect of the subgrid terms but their mathematical structures. Therefore, in these models, the goal is to find an approximated value of the initial quantities before the application of the filter Φ (velocity, density, viscosity, color function) thanks to the resolved quantities $\bar{\Phi}$, that is to say to find the relationship F between Φ and $\bar{\Phi}$ such as $\Phi = F(\bar{\Phi})$ by using series expansions. For this purpose, different approaches have been developed. Two of them are presented here.

14.3.2.1 Bardina's model or similarity subgrid-scale model

In this model proposed by Bardina *et al.* [10, 11], the subgrid terms are assumed statistically similar to the smallest resolved scales. The energetic spectrum is then

divided into three parts as shown in Figure 14.1. This assumption has been generalized by the Liu *et al.* [111] which divided the energetic spectrum into any number of consecutive regions. The similarity subgrid-scale assumption is then valid between two consecutive domains.

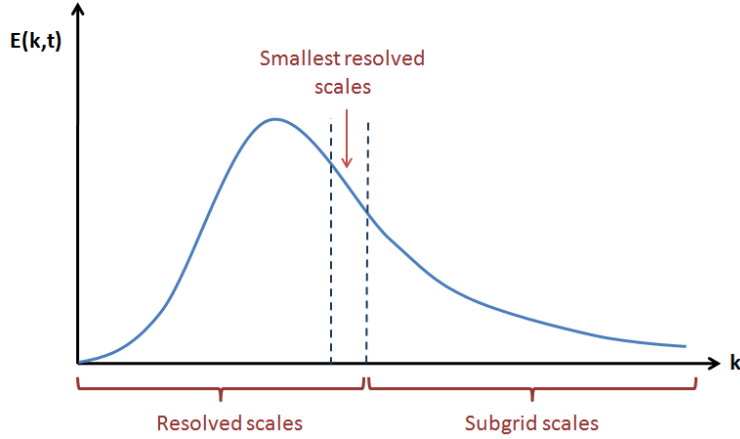


Figure 14.1: Schematic view of the energy spectrum in the Bardina's model configuration.

Thus, using this assumption, the subgrid scales are approximated as follows [10]:

$$\overline{\Phi'} = \overline{\Phi} - \overline{\overline{\Phi}} \quad (14.43)$$

By considering the following approximation:

$$\overline{ab} \simeq \overline{a}\overline{b} \quad (14.44)$$

We can rewrite the $\underline{\underline{C}}_{ij}$ and $\underline{\underline{R}}_{ij}$ terms of the Leonard's decomposition:

$$\underline{\underline{C}}_{ij} = (\overline{u_i} - \overline{\overline{u_i}}) \overline{\overline{u'_j}} + (\overline{u_j} - \overline{\overline{u_j}}) \overline{\overline{u'_i}} \quad (14.45)$$

$$\underline{\underline{R}}_{ij} = (\overline{u_i} - \overline{\overline{u_i}}) (\overline{u_j} - \overline{\overline{u_j}}) \quad (14.46)$$

The expression of the Leonard's term $\underline{\underline{L}}_{ij}$ is not modified by this assumption since it only depends on resolved scales. Finally, the convective subgrid term can be expressed as follows:

$$\frac{\partial \overline{\overline{u_i u_j}}}{\partial x_j} = \frac{\partial \overline{\overline{u_i}} \overline{\overline{u_j}}}{\partial x_j} + \overline{\overline{\tau_{conv}^{bard}}} \quad (14.47)$$

$$\text{with } \overline{\overline{\tau_{conv}^{bard}}} = \frac{\partial}{\partial x_j} \left(\underline{\underline{C}}_{ij} + \underline{\underline{R}}_{ij} + \underline{\underline{L}}_{ij} \right)$$

Contrary to the functional model, this expression can be applied to all the subgrid terms since no assumptions are made on their mathematical structures.

14.3.2.2 Approximate Deconvolution Model (ADM)

This model proposed by Adams and Stolz [2, 187] is based on the approximative evaluation of the inverse of the filter G through a deconvolution operator, Q_N . This operator can be used to find an approximation of the quantities Φ before applying the filter G , denoted Φ^* :

$$\Phi^* = Q_N * \bar{\Phi} \quad (14.48)$$

with $*$ the convolution operator. Q_N has the following expression:

$$Q_\infty = \sum_{l=0}^{\infty} (I_d - G)^l \simeq G^{-1} \quad (14.49)$$

$$Q_N = \sum_{l=0}^N (I_d - G)^l \simeq G_N^{-1} \quad (14.50)$$

N represents the order of the ADM. In their publication, Adams and Stolz [2] obtained a good agreement by choosing $N = 3$ and showed that an order larger than 5 did not improve the results. Thus, for single-phase flows, N is usually taken equal to 4 or 5. With this model, we can then rewrite the convective subgrid term:

$$\overline{\tau}_{conv}^{ADM} = \nabla \cdot (\overline{\rho^* \mathbf{u}^* \otimes \mathbf{u}^*} - \bar{\rho} \bar{\mathbf{u}} \otimes \bar{\mathbf{u}}) \quad (14.51)$$

Nevertheless, one can note that replacing \mathbf{u} by \mathbf{u}^* is not sufficient to model the effect of the subgrid scales on the resolved ones. Chow and Street [31] proposed a very interesting illustration to understand the effect of deconvolution models. As shown in Figure 14.2, the total energy spectrum can be split into three parts: the resolvable structures, the Resolvable SubFilter-Scale (RSFS) and the Unresolvable SubFilter-Scale (USFS) also called SubGrid Scale (SGS). The RSFS can be theoretically reconstructed by the inverse filter operation. This procedure is limited by the Numerical Errors (NE) which increase close to the grid cutoff [133]. The SGS are not reconstructed after applying deconvolution models. Thus, an additional relaxation term in the momentum balance equation is required to reproduce the energy dissipation of the subgrid scales [6, 165, 175]. This term has the following structure: $\Lambda_u (Id - Q_N * G) * \bar{\mathbf{u}}$. Different methods have been developed to implement this term and especially to evaluate the value of the parameter Λ_u [165].

One of these methods consist in applying a Smagorinsky's formulation with a Germano's procedure [55]. This choice requires to adapt the subgrid term expression so that the predicted model coefficient has a non zero value:

$$\overline{\tau}_{conv}^{ADM} = \nabla \cdot (\overline{\rho^* \mathbf{u}^* \otimes \mathbf{u}^*} - \bar{\rho}^* \bar{\mathbf{u}}^* \otimes \bar{\mathbf{u}}^*) \quad (14.52)$$

The expression of the Smagorinsky's coefficient (Equation (14.39)) has also to be modified:

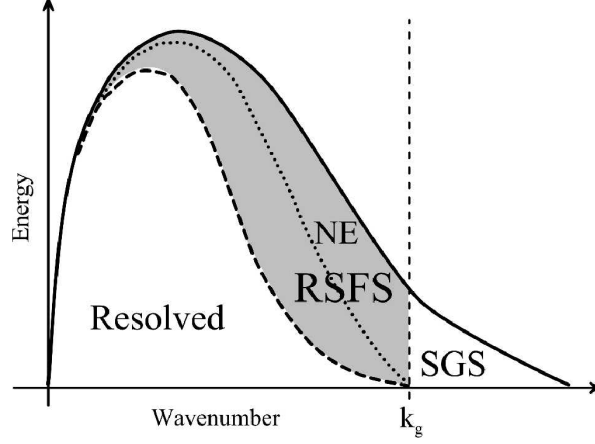


Figure 14.2: Schematic view of the velocity energy spectrum with linear axis, RSFS refers to the resolvable subfilter-scales, NE to the numerical errors done during the deconvolution process (located above the dotted line) and SGS to the subgrid scales, the grid filter corresponds to the dashed line at the wavenumber k_g and the explicit filter to the curved dashed line [31].

$$C_S = \sqrt{\frac{1}{2} \frac{\left(\underline{\underline{L}}_{ij} - \underline{\underline{H}}_{ij} \right) \underline{\underline{M}}_{ij}}{\underline{\underline{M}}_{ij}^2}} \quad (14.53)$$

with:

$$\underline{\underline{H}}_{ij} = \widehat{\widehat{u_i u_j}} - \widehat{\widehat{u_i}} \widehat{\widehat{u_j}} \quad (14.54)$$

This approach has been implemented by different research groups [31, 58, 62, 63, 81, 121].

14.3.3 Mixed scale models

In previous comparisons of turbulence models, it has been shown that the functional models were able to reproduce the correct energetic transfers contrary to the structural models which predicted better the structure of the subgrid terms. Thus, the idea of the mixed models is to combine a functional model with a structural one to benefit from the advantages of each. In this report, only the Smagorinsky-Bardina model proposed by Bardina *et al.* [11] is considered. Thus, the deviatoric part of the convective subgrid tensor is written:

$$\tilde{\tau}_{conv} - \frac{1}{3} \text{tr}(\tilde{\tau}_{conv}) \underline{\underline{I}}_d = -\nu^T \tilde{\underline{\underline{S}}} + \frac{1}{2} \left(\underline{\underline{L}}_{ij} - \frac{1}{3} \underline{\underline{L}}_{kk} \underline{\underline{I}}_d \right) \quad (14.55)$$

with $\underline{\underline{L}}_{ij} = \frac{\partial \overline{\overline{u_i u_j}}}{\partial x_j} - \frac{\partial \overline{\overline{u_i}} \overline{\overline{u_j}}}{\partial x_j}$ and $\nu^T = (C_S \overline{\Delta})^2 |\underline{\underline{S}}_{ij}|$, using Equation (14.53) for C_S [210, 223].

One can note that the implementation of the ADM combined with a dynamic Smagorinsky's model for the relaxation term can be considered as a mixed scale model.

14.3.4 Boundary conditions in LES

There are essentially two ways to treat boundary conditions in LES [151]. The first method consists in decreasing the filter width to zero at the boundaries. This approach implemented in [81] is called the Near Wall Resolution [151]. Its main advantage is its ability to capture the important flow features near the boundary. However, to achieve this, refined grids at the boundaries are required, which increase the CPU consumption. On the contrary, the second method, referred as the Near Wall Modeling, uses physical modeling such as conditions on the shear stress [31, 218] or logarithmic law [134] to deal with boundary conditions. These models are added to the turbulent LES models acting in the bulk of the flow. With the Near Wall Modeling, it is not necessary to refine the grids at the boundaries, which allows simulations of larger computational domain for industrial applications. More recently, a new method, called Approximate Deconvolution Boundary Conditions, has been proposed by Borggaard and Iliescu [18]. This approach is based on approximate deconvolution and computes the boundary commutation error term. An advantage of this method compared to the two others is that it is suited for turbulent flows with time-dependent boundary conditions.

14.4 Monotonically Integrated Large Eddy Simulation (MILES)

This new approach of the Large Eddy Simulation has been introduced by Boris *et al.* [19] as an alternative to the models for the unresolved subgrid scales. Initially developed to improve shock-capturing schemes, the MILES integrates the subgrid models in the code algorithm through the functional reconstruction of the convective fluxes. Thus, the truncation error induced by the high-order algorithm generates numerical diffusion which acts as a turbulent viscosity. The implicit filter is then the mesh cell discretization in the finite volume discretization.

Fureby and Grinstein [53] applied this method to free shear flows, especially transitional free jets. They showed that the same results quality was obtained with subgrid models and with the MILES approach. Moreover, they concluded that the method was suitable for the simulation of moderately high Reynolds number free shear flows.

A detailed review of this approach can be found in Grinstein and Fureby [59].

14.5 Filter notion

Two levels of filtering can be distinguished. The first one is the implicit filtering related to the cell size, the numerical scheme and the subgrid model. To fix the implicit filter width, the assumption is usually made that the effect of the grid cell plays a lead role [163]. Therefore, for a three dimensional mesh, Deardoff [35] proposed the following filter width:

$$\bar{\Delta} = \frac{1}{3} (\Delta x \Delta y \Delta z)^{\frac{1}{3}} \quad (14.56)$$

The choice of the cell size is then a crucial issue especially when dispersed phases and interfaces are present in the flow. Indeed, the filter width must be small enough but higher than the diameter of the dispersed bubbles [92, 126]. Milelli [126] showed that the best ratio between the filter width and the bubble diameter is: $1.2 < \frac{\bar{\Delta}}{d_{dg}} < 1.8$. Moreover, in case of large interfaces, the mesh has to be enough refined to solve both the turbulent scales and the interface deformation [90]. Therefore, a compromise between all these limitations has to be defined in complex flows.

The second level of filtering, called explicit filtering or test filtering, selects the smallest resolved scales. The choice for this filter is important since it is explicitly applied in structural turbulence models or dynamic procedures (see section 14.3) based on a scale-similarity assumption. To satisfy this assumption and so to limit numerical errors, the test filter, corresponding to the hat operator, has to be similar to the implicit filter, referred to as the overbar filter. Usually, for a second order numerical scheme, the explicit filter width $\hat{\Delta}$ is twice the implicit filter width [167]. Different types of explicit filter have been used in the literature:

- Box or top hat filter:

$$G(x) = \frac{1}{\hat{\Delta}} H \left(\frac{\hat{\Delta}}{2} - |x| \right) \quad (14.57)$$

with H the Heaviside function.

Because of its simplicity, this filter is widely used for *a priori* LES studies [88, 96, 207]. For *a posteriori* simulations, two main discrete box filters are used: the trapezoidal filter based on the trapezoidal rule [31, 62, 210, 223] which has the following expression in 1D at second order:

$$\bar{\Phi}_i = \frac{1}{4} (\Phi_{i+1} + 2\Phi_i + \Phi_{i-1}) \quad (14.58)$$

and the Simpson's filter using the Simpson's rule [168]:

$$\bar{\Phi}_i = \frac{1}{6} (\Phi_{i+1} + 4\Phi_i + \Phi_{i-1}) \quad (14.59)$$

where Φ_i refers to the value of the quantity Φ in the cell i . The main advantage of the trapezoidal filter is that, in spectral space, the transfer function goes to zero at the grid cutoff contrary to the Simpson's filter and therefore eliminates the highest wavenumber that could be sustained by the grid [140].

- Gaussian filter:

$$G(x) = \sqrt{\frac{6}{\pi \hat{\Delta}^2}} \exp\left(\frac{-6x^2}{\hat{\Delta}^2}\right) \quad (14.60)$$

In the Fourier space, the Gaussian filter is still Gaussian. Thus, it does not have a sharp cutoff in the Fourier space.

- Sharp spectral filter:

$$G(x) = \frac{\sin\left(\frac{\pi x}{\Delta}\right)}{\pi x} \quad (14.61)$$

This filter corresponds to an Heaviside function in the Fourier space with a sharp cutoff. It has been used in [113, 175].

- Padé or Compact discrete filter: Lele proposed in [101] different compact discrete filters. Such filters provide a greater control over the shape of the transfer function. The order and parameter numbers can be easily managed. Many research groups have chosen these filters at different orders as test filter for deconvolution procedures [2, 81, 121, 154].

Several researchers have worked on the filter choice. One main difference between all these available filters is the cutoff in the Fourier space which is either sharp or smooth. Thus, De Stefano and Vasilyev [186] showed that if LES was based on smooth filter, then subgrid scale models should also model the effect of the filter on large scales and remove (or add) energy at the resolved scales. Otherwise, to minimize the effect of filter on large scales dynamics and energy transfer, the filter has to be chosen with a sharp cut-off. Lund [113] also showed that non-sharp filters in the Fourier space lead to an incorrect dissipation, proportional to the degree to which the filter departs from a sharp-cut-off. A comparison of different explicit filters associated to ADM has been proposed on a single-phase flow by San *et al.* [168] and with the Smagorinsky's model with a dynamic procedure by Gullbrand and Chow [62].

14.6 Interactions between turbulence and interfaces

In a flow, the interface motion induces energetic transfers between the two continuous phases, which can produce turbulence. Some studies have been performed to determine the influence of this motion. In [110], the authors showed that the

interface deformation induces an exponential decrease of the turbulence intensity. Therefore, they proposed a correction of the eddy viscosity:

$$\nu^T = f_{int} \sqrt{2} (C_S \bar{\Delta})^2 \underline{\underline{S}}_{ij} \quad (14.62)$$

with f_{int} a damping model function extracted from DNS results of Fulgosi *et al.* [52]:

$$f_{int} = 1 - \exp\left(-1.3 \cdot 10^{-5} y_{int}^+ - 3.6 \cdot 10^{-5} (y_{int}^+)^2 - 1.08 \cdot 10^{-5} (y_{int}^+)^3\right) \quad (14.63)$$

with $y_{int}^+ = \frac{\Delta y \rho_{cl} u_\tau}{\mu_{cl}}$ the wall distance and u_τ the shear velocity at the interface.

Moreover, for interfaces with surface tension, an adding subgrid term appears in the momentum balance equation:

$$\tau_{superf} = \sigma (\bar{\kappa} \bar{\mathbf{n}} - \bar{\kappa} \bar{\mathbf{n}}) \quad (14.64)$$

Usually, this subgrid term is neglected. Nevertheless, some *a priori* DNS studies, such as in [110], highlighted that the negligibility assumption can be challenged and can cause spurious currents. Therefore, in [6], the authors developed a method based on the Approximate Deconvolution Model (ADM) to evaluate this subgrid term.

For explicit filtering, the existence of interfaces in a flow has also an impact. Indeed, to ensure the commutation assumption between the filter and the time and space derivatives, the convolution kernel has to be independent on time and space. In a two-phase flow, this means that the filter is also applied over interfaces, where discontinuities occur. Sagaut [166] showed that the jump of the average field appears in the subgrid fluctuation. It can even be predominant compared to the turbulent contribution. This conclusion is very interesting since the LES models are based on the assumption that all the subgrid fluctuations come from turbulence effects. Thus, for two-phase flows, the explicit filter has to be adapted. For example, Trontin presented in [200] a phase conditioned filtering suitable for the one-fluid approach.

14.7 Interactions between turbulence and dispersed fields

The existence of dispersed fields in a flow is an adding issue for the LES simulation. Specific subgrid terms appear in the conservation equation that have to be modeled. The classical LES models have to be adapted to simulate flows containing small spherical inclusions.

14.7.1 LES filtering of the two-fluid model equations

With the same method described in section 14.2, Lakehal [90] proposed a filtering of the two-fluid model with a continuous field and a dispersed one. The same analysis will be performed with the LBMo considering two continuous fields in Chapter 16.

For constant density flows, the subgrid term τ_{un} appearing in the mass conservation equation can be neglected since $\overline{\rho_k} = \overline{\alpha_k} \tilde{\rho}_k = \overline{\alpha_k} \rho_k$. To determine the coefficients of the filtered interfacial forces, Lakehal [90] simulated a vertical bubbly flow using the Smagorinsky's model for the subgrid term $\tau_{\rho uu}$ and neglected τ_{un} and τ_c . He took the same value for the coefficient of the filtered and non filtered added mass force, C_A equal to 0.5. He found that the coefficient of the filtered lift force should be equal to 0.25 instead of 0.5.

14.7.2 Effect on the subgrid models

The dispersed fields interact with the unresolved scale and contribute to the momentum dissipation. Therefore, it requires to adapt the model for the subgrid terms. Different expressions have been developed. Sato *et al.* [172] proposed:

$$\nu^T = \nu_{Smag}^T \left(1 + C_f \alpha_g 6\pi \frac{d_b \nu}{\overline{\Delta} \nu_{Smag}^T} \right)^{\frac{1}{3}} \quad (14.74)$$

with $\nu_{Smag}^T = \sqrt{2} (C_S \overline{\Delta})^2 |S_{ij}|$ and d_b the bubble diameter.
Tran [199]:

$$\nu^T = \nu_{Smag}^T + \frac{1}{2} C_{nu_b} \alpha_g d_b \|\tilde{\mathbf{u}}_{dg} - \tilde{\mathbf{u}}_{cl}\| \quad (14.75)$$

and Milelli [126]:

$$\nu^T = \nu_{Smag}^T + (C_S \overline{\Delta}) \alpha_g \|\tilde{\mathbf{u}}_{dg} - \tilde{\mathbf{u}}_{cl}\| \quad (14.76)$$

The last formulation was validated on bubble plumes simulations in [126] and bubbly mixing layers in [90]. The main advantage of this approach is that it gives the same good results than the Tran's formulation without additional empirical constants such as C_f or C_{nu_b} in the other formulations. Usually, C_S is taken equal to the Smagorinsky's constant: $C_S = 0.12$.

Chapter 15

Feasibility study of LES on a single-phase flow

In the code `NEPTUNE_CFD`, different turbulence models based on RANS and URANS approaches have been implemented and optimized. However, LES models have not yet been implemented and validated. In this chapter, the Smagorinsky's model with the dynamic procedure (section 14.3.1.1) and the WALE model (section 14.3.1.2) are implemented. The implementation is validated using a single-phase flow test case. Finally, the results are compared to the MILES (section 14.4) approach. Since the objective of this thesis is not the simulation of single-phase flows, this chapter is only devoted to a feasibility study to assess the ability of the code `NEPTUNE_CFD` to perform LES. Comparison of improved turbulence models will not be presented here. This work will be done in Chapters 16 and 17 for two-phase flows.

The test case is a single phase flow. Thus, only one continuous field is defined in this chapter. The flow is isothermal and turbulent.

15.1 Résumé du chapitre

Pour modéliser les phénomènes de turbulence avec le code `NEPTUNE_CFD`, différents modèles basés sur des approches RANS et URANS ont été implémentés et validés. Cependant, aucun calcul n'a été réalisé avec la simulation aux grandes échelles (LES). Ce chapitre constitue donc un test de faisabilité numérique pour les modèles de type Smagorinsky dynamique, WALE et MILES. Un cas de turbulence pleinement développée dans un canal monophasique a donc été simulé. Les résultats des simulations sont comparés à des données expérimentales. L'écoulement étant monophasique, un seul champ continu est défini dans ce chapitre. De plus, aucun transfert thermique n'est modélisé de sorte que la simulation est isotherme.

15.2 Description of the test case

To validate the LES models, a fully developed turbulent channel flow is simulated. This test case belongs to the identified validation test cases for the Large Eddy Simulations [144]. The fully developed turbulent channel flow consists in an idealized turbulent flow between two parallel plates driven by a mean pressure gradient parallel to the wall. Experimental [33, 144, 211] and DNS [161] data are available for a large range of Reynolds numbers.

15.2.1 Notations

Near the wall, viscous stress is predominant, which affects turbulence. Therefore, in addition to the usual flow parameters such as the fluid velocity and the Reynolds number, new parameters are defined to characterize the effect of the wall shear stress. A wall shear velocity u_τ is introduced:

$$u_\tau = \sqrt{\frac{\tau_w}{\rho}} \quad (15.1)$$

with $\tau_w = \mu \left. \frac{\partial u}{\partial y} \right|_{y=0}$ the wall shear stress. This new velocity allows defining a turbulent Reynolds number:

$$Re_\tau = \frac{u_\tau \delta}{\nu} \quad (15.2)$$

with δ the channel mid-height. This turbulent Reynolds number should not be confused with the Reynolds number based on the bulk mean velocity: $Re_{deb} = \frac{u_{deb} \delta}{\nu}$ with u_{deb} the bulk mean velocity.

The turbulent Reynolds number allows defining a dimensionless distance to the wall y^+ :

$$y^+ = \frac{u_\tau y}{\nu} \quad (15.3)$$

which is also equal to:

$$y^+ = Re_\tau \frac{y}{\delta} \quad (15.4)$$

15.2.2 Characteristics of the flow

In a channel, the turbulent flow is affected by the walls. Thus, different regions can be distinguished according to the distance to the wall.

As shown in Figure 15.1, the viscous sublayer goes up to $y^+ = 5$. In this region, the fluid is dominated by viscous shear in absence of turbulent shear stress effects. It can be assumed that the shear stress is almost equal to the wall shear stress throughout the layer, which leads to:

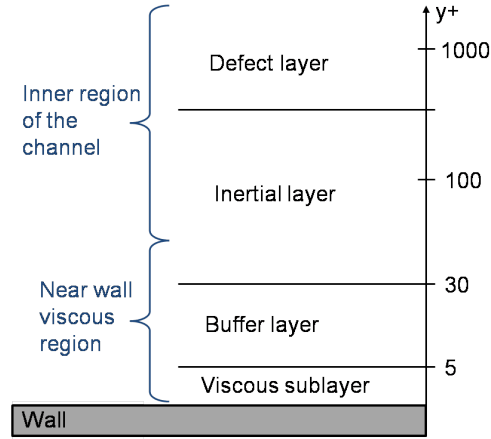


Figure 15.1: Schematic view of the different regions near a wall according to the dimensionless distance y^+ .

$$u^+ = y^+ \quad (15.5)$$

Then, comes the buffer layer ($5 < y^+ < 30$) as an intermediate layer between the viscous sublayer and the inertial layer. In this region, a high quantity of turbulent energy is produced. For $30 < y^+ < 500$, the fluid enters in the inertial layer also called log-law layer. At this distance from the wall, the viscous and turbulent effects are both important so that the shear stress is assumed to be constant and equal to the wall shear stress. The relation between u^+ and y^+ is given by:

$$u^+ = \frac{1}{B} \ln(y^+) + C \quad (15.6)$$

where B and C are constants, found from measurements.

For $y^+ > 500$, wall effects are considered negligible. In this part of the domain, turbulence becomes homogeneous.

15.3 Simulation parameters

15.3.1 Flow parameters

To simulate the fully developed turbulent channel flow, the experiment of Niederschulte *et al.* [144] is used to compare the simulation results. This experiment has been chosen because it belongs to the validation test cases for LES of *Code_Saturne*. Moreover, the Reynolds number is higher to those available with DNS, which allows going further in the validation of LES models. In the experiment, the turbulent Reynolds number is equal to 921, corresponding to a wall shear velocity $u_\tau = 1 \text{ m.s}^{-1}$ and a Reynolds number based on the bulk mean velocity: $Re_{deb} = 18339$. The experimental data give a bulk mean velocity equal to 20.06 m.s^{-1} . The fluid properties

are: $\rho = 1 \text{ kg.m}^{-3}$, $\mu = 1.08578.10^{-3} \text{ Pa.s}$. The simulation is performed without gravity.

To initialize the velocity field, a Poiseuille flow type is superposed to a random perturbation which obeys the zero divergence condition. The random distribution must have a mean value equal to zero to avoid interfering on the mass flow rate. For this purpose, a Box-Müller distribution is used [80]. As a reminder, the Box-Müller distribution is defined in its Cartesian form as follows:

$$z_0 = x\sqrt{\frac{-2 \ln s}{s}} \text{ and } z_1 = y\sqrt{\frac{-2 \ln s}{s}}. \quad (15.7)$$

with x and y two independent numbers chosen uniformly between -1 and 1 and $s = x^2 + y^2$ such that s belongs to $]0, 1[$.

15.3.2 Mesh

In the buffer layer, some researchers [85] have identified structures responsible for the turbulent energy production, called “streak“. These long thin lines of fluid stretched along the flow direction are characterized by a mean length in the z direction of $\lambda_z^+ = 100$ and in the x direction of $\lambda_x^+ = 1000$. Thus, the choice of the mesh dimensions has to be done with respect to these characteristic length scales. The schematic view of the simulation domain is displayed in Figure 15.2. In dimensionless values, the dimensions of the mesh are (with a turbulent Reynolds number of 921 and a channel mid-height of 1 m): $L_x^+ = 5784$, $L_y^+ = 1842$ and $L_z^+ = 2892$.

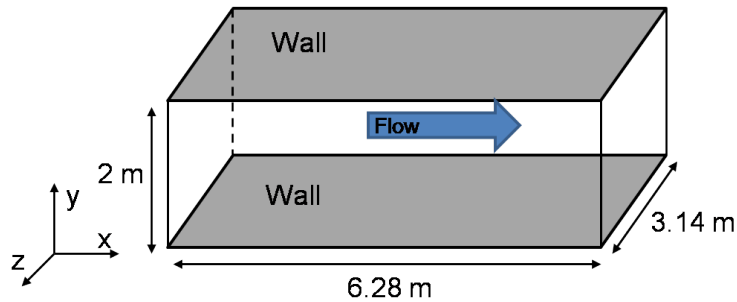


Figure 15.2: Schematic view of the simulation domain used for the simulation of the fully developed turbulent channel flow.

Concerning the mesh refinement, Zhang [222] proposed the following criteria for an accurate simulation of the large turbulent scales: $\Delta x^+ < 80$ and $\Delta z^+ < 40$ with 3 cells in the viscous sublayer $y^+ < 5$. In our study, four meshes have been considered. Table 15.1 gives the characteristics of the four grids. To reduce the number of cells and so to minimize computation time, the distance between the cells is not constant in the y direction (see Figure 15.3).

	Number of cells	Δx^+	Δz^+	y_{min}^+
Grid 1	80 x 68 x 90	72	32	1
Grid 2	145 x 68 x 145	40	20	1
Grid 3	145 x 44 x 145	40	20	5
Grid 4	145 x 34 x 145	40	20	10

Table 15.1: Characteristics of the four grids used to simulate the fully developed turbulent channel flow, y_{min}^+ refers to the position of the first cell center in the y direction.

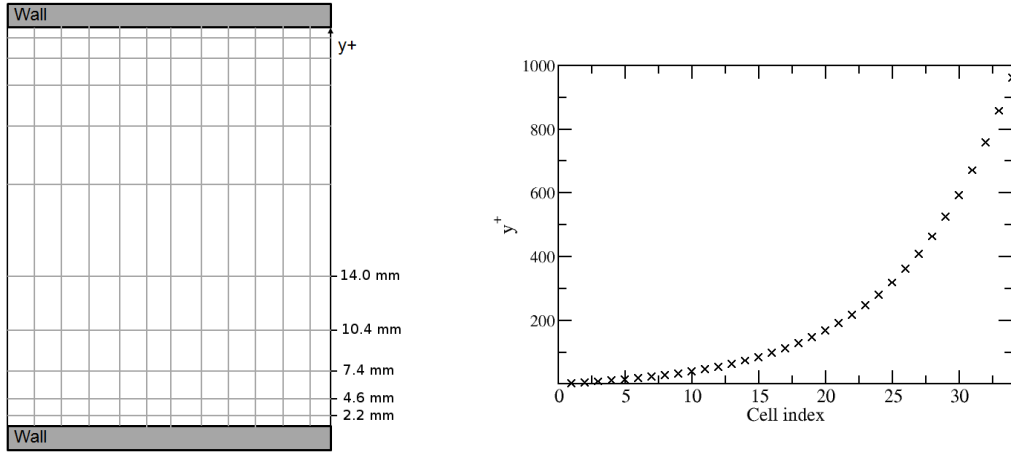


Figure 15.3: Left: schematic view of the mesh in the y direction, right: position of the cell center of each cell in the y direction of Grid 1.

For the boundary conditions, the flow comes from the left face and goes out from the right face which are both defined as periodic faces. The same boundary condition is applied to the faces in front of and behind (faces perpendicular to the z direction). These conditions correspond to an infinite flow in the x and z directions. A wall boundary condition is imposed for the two parallel plates.

With the use of periodic boundary conditions, the mean pressure gradient has to be dynamically adapted after each iteration so that the bulk Reynolds number is brought towards its target value. For this purpose, the procedure proposed by Zhang and Vicquelin in [224] is implemented. It consists in adding an extra source terms B in the momentum equations which has the following expression:

$$\frac{dB}{dt} = \frac{\mu_b}{\delta} \left(\frac{2}{\tau} \frac{dRe_{deb}}{dt}(t) + \frac{Re_{deb}(t) - Re_{deb}^t}{\tau^2} - \frac{d}{dt} \left(\frac{\tau_{w,1} + \tau_{w,2}}{2\mu_b} \right) \right) \quad (15.8)$$

with μ_b the bulk viscosity, δ the middle height, $\tau = \frac{\delta}{10u_\tau^t}$, u_τ^t the target value of the wall shear velocity, Re_{deb}^t the target value of the bulk Reynolds number and $\tau_{w,1}$

and $\tau_{w,2}$ respectively the average wall shear stresses on the lower and upper wall. This extra source term is added all along the simulations.

15.3.3 Numerical parameters

For the simulation, the time step is kept constant and depends on the grid. The simulation is performed for 50 *s* to reach convergence. Then, time averages of the velocity field are calculated for an extra 100 *s*.

15.4 Results

The following quantities are defined: u^r the velocity in the x direction, U' the fluctuating velocity in the x direction and V' the fluctuating velocity in the y direction. To link the quantities obtained with LES and the experimental data of Niederschulte *et al.* [144], the quantities u^r , $U'U'$, $U'V'$ and $V'V'$ are averaged in time and space (see Appendix L for more details). The space average is done over each plane in the span-wise direction, that is to say over the cells with the same y coordinate. The average quantities are defined using the following notation: $\langle . \rangle$.

15.4.1 Averaging effects

A first study has been performed to validate the averaging time with the MILES model. The test case is simulated using Grid 1 and a constant time step equal to 0.2 *ms*. The evolution of the quantities $\langle u^r \rangle$, $\langle U'U' \rangle$, $\langle U'V' \rangle$ and $\langle V'V' \rangle$ obtained in the middle of the domain and normalized by the simulated bulk mean velocity are presented in Figure 15.4. For all the quantities except $\langle U'U' \rangle$, convergence is reached quickly. Nevertheless, for $\langle U'U' \rangle$, 100 *s* are necessary to have a converged average value.

The same conclusion can be drawn with the WALE and Smagorinsky's model with the dynamic procedure.

15.4.2 Turbulence model comparison

In the second study, the flow is simulated with the three different turbulence models: MILES, WALE and Smagorinsky's model with the dynamic procedure and the coarse grid (Grid 1). It has to be noted that in this chapter and the following, the Smagorinsky's constant C_S is averaged using the neighbors since it has been shown that the results were improved especially for the simulation of the fully developed turbulent channel flow [14]. As a reminder, in the MILES model, no subgrid scale models are implemented. The modeling is done implicitly through the grid cell discretization and the numerical scheme. The time step is equal to 0.2 *ms* such that the CFL number is smaller than 0.1.

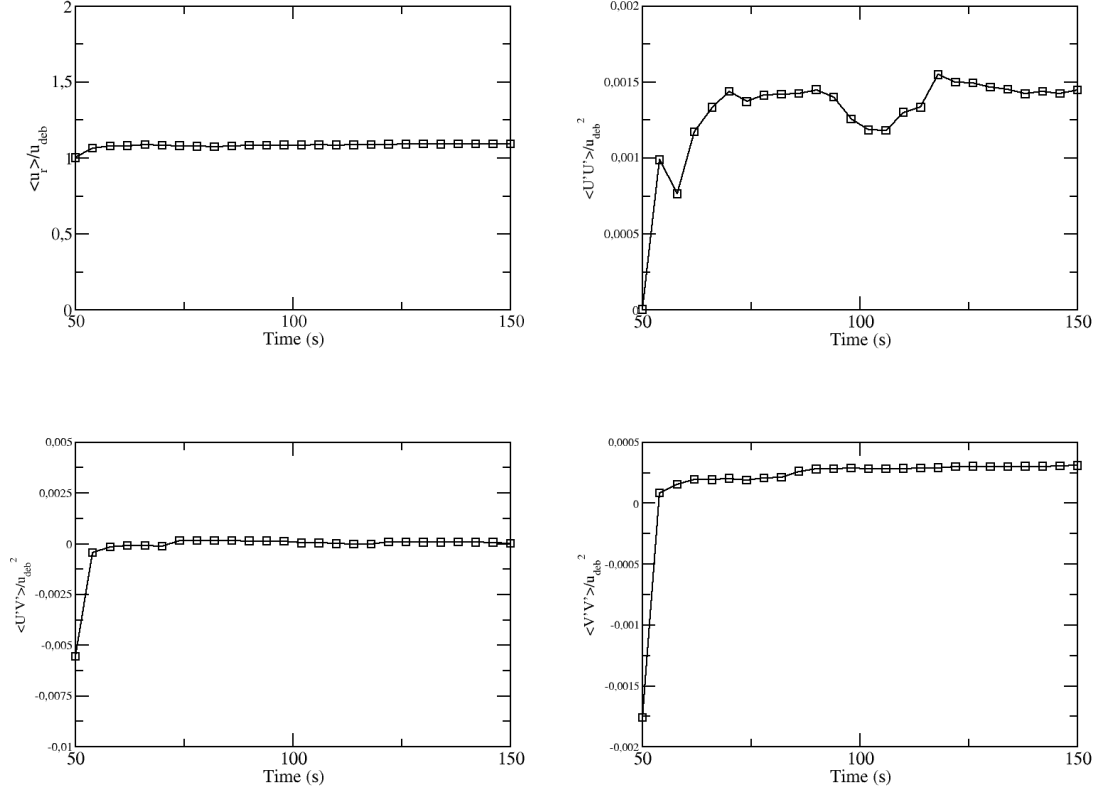


Figure 15.4: Comparison of the average quantities $\langle u^r \rangle$, $\langle U^*U^* \rangle$, $\langle U^*V^* \rangle$ and $\langle V^*V^* \rangle$ according to the average time, the normalization is done with the computed bulk mean velocity, MILES model.

	$u_{deb} \text{ (m.s}^{-1}\text{)}$	$u_\tau \text{ (m.s}^{-1}\text{)}$
MILES	19.65 (2.0 %)	0.90 (10 %)
WALE	19.65 (2.0 %)	0.83 (17 %)
Smagorinsky	19.65 (2.0 %)	0.85 (15 %)

Table 15.2: Computed bulk mean velocity and wall shear velocity for the three turbulence models, the relative error based on the experimental data are given in brackets.

Table 15.2 presents the bulk mean velocity and the wall shear velocity predicted by the simulations. The results are comparable with the three models. The same level of errors has been obtained with improved turbulence models and a discretization order of 2 by Lubin in [112] and Montreuil [135]. In [135], the error for the wall shear velocity goes from 1.1 % to 22 % with a turbulent Reynolds number Re_τ equal to 180, which is smaller than in this test case. However, Sarghini and Pionmelli [169] reported an increase of the error on the wall shear velocity when the

turbulent Reynolds number was increased. At $Re_\tau = 180$, the error was equal to 6 % and reaches 18 % for $Re_\tau = 1050$ (with a fourth order in time and eight in space and a comparable mesh refinement). The second main point which can explain the difference is the order of the time discretization which is equal to 1 in our case. Concerning the bulk mean velocity, Montreuil [135] obtains errors from 3.0 % to 5.8 %, which is consistent with our results (see Table 15.2). The bulk mean velocity is better predicted than the wall shear velocity, as also observed by Lubin in [112] and Montreuil [135]. Indeed, Härtel and Kleiser [66] showed that the dissipative effects of the subgrid models are more efficient on the center of the channel than close to the walls.

Then, the profiles of $\langle u^r \rangle$, $\langle U'U' \rangle$, $\langle U'V' \rangle$ and $\langle V'V' \rangle$ are compared with the experimental data [144]. Figure 15.5 displays the profile of the average resolved velocity. The dimensionless quantities are obtained by considering the computed turbulent Reynolds number and wall shear velocity not the theoretical values. This explains why the first point is located at $y^+ < 1$. In the left picture, for $y^+ < 5$, the simulations follow well the linear law whatever the turbulence model. Nevertheless, for $y^+ > 10$, the simulations overpredict the velocity. As shown in [135], these discrepancies are due to the error on the wall shear velocity which is used to normalize the resolved velocity. The discrepancies are larger when the error on the wall shear velocity is larger. In the right picture, the normalization is done with the bulk mean velocity which is equal for the three models. This normalization is kept for the fluctuating quantities. This picture shows that for $y^+ < 5$ the velocity is underestimated, which agrees with the underestimation of the wall shear velocity. Thus, for $y^+ > 10$, the velocity is overestimated due to the conservation of the bulk mean velocity. However, the bulk mean velocity is quite well predicted. Thus, the results are in reasonable agreement with the experimental data.

Finally, Figure 15.6 presents the fluctuating velocities normalized by the bulk mean velocity. The same trends are observed with the three turbulence models. The intensity of $\langle U'U' \rangle$ at the peak is overestimated and shifted to higher y^+ values, especially with MILES, in agreement with Montreuil's results [135]. The dispersion of the different curves is also larger for this component. Montreuil [135] showed that when the turbulent Reynolds number increased, this dispersion was increased. On the contrary, the intensities of $\langle U'V' \rangle$ and $\langle V'V' \rangle$ are underestimated. If we compare the intensities of the three quantities, we see that $\langle U'U' \rangle$ is larger by a factor of 10. In fact, $\langle U'U' \rangle$ corresponds to the contribution in the flow direction, where the kinetic turbulent energy is concentrated. To compare the turbulence models, the best criterion is to assess its ability to predict the turbulent kinetic energy thus to predict the $\langle U'U' \rangle$ profile. For $\langle U'V' \rangle$ and $\langle V'V' \rangle$, MILES gives the best profile prediction, which is consistent with the results obtained with the coarser grid in [14]. However, MILES does not predict accurately $\langle U'U' \rangle$. Thus, MILES fails at predicting properly the turbulent kinetic energy. On the contrary, the WALE and especially the Smagorinsky's model reproduce better the $\langle U'U' \rangle$ profile. In fact, the addition of a turbulent viscosity induce energy dissipation. The turbulent kinetic energy is then smaller and at the same time, the

average kinetic energy is increased (see Figure 15.5).

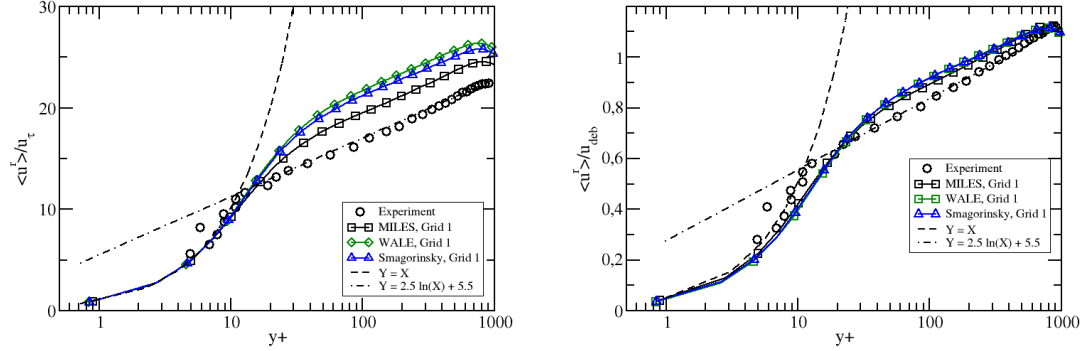


Figure 15.5: Comparison of the profiles of $\langle u^r \rangle$ with the experimental data [144] and three different LES models: MILES (black curve with squares), WALE (green curve with diamonds) and Smagorinsky (blue curve with triangles), left: normalization by the computed wall shear velocity, right: by the computed bulk mean velocity, Grid 1.

15.4.3 Sensibility to the mesh refinement in the span-wise direction

In the previous simulations, Grid 1 has been used. In this section, the effect of the mesh refinement in the x and z directions is studied for the three turbulence models. For this purpose, the same simulations are performed using Grid 2. This mesh is obtained by increasing the number of cells in the x and z directions (see Table 15.1) and keeping the same space discretization along the y direction. The time step is equal to 0.1 ms with Grid 2 such that the CFL number is smaller than 0.1. Except the modification of the mesh and the time step, all the simulations parameters remain unchanged.

	$u_{deb} (m.s^{-1})$		$u_\tau (m.s^{-1})$	
	Grid 1	Grid 2	Grid 1	Grid 2
MILES	19.65 (2.0 %)	19.65 (2.0 %)	0.90 (10 %)	0.96 (4.0 %)
WALE	19.65 (2.0 %)	19.65 (2.0 %)	0.83 (17 %)	0.90 (10 %)
Smagorinsky	19.65 (2.0 %)	19.65 (2.0 %)	0.85 (15 %)	0.89 (11 %)

Table 15.3: Computed bulk mean velocity and wall shear velocity for the three turbulence models and the two grids, the relative error based on the experimental data are given in brackets.

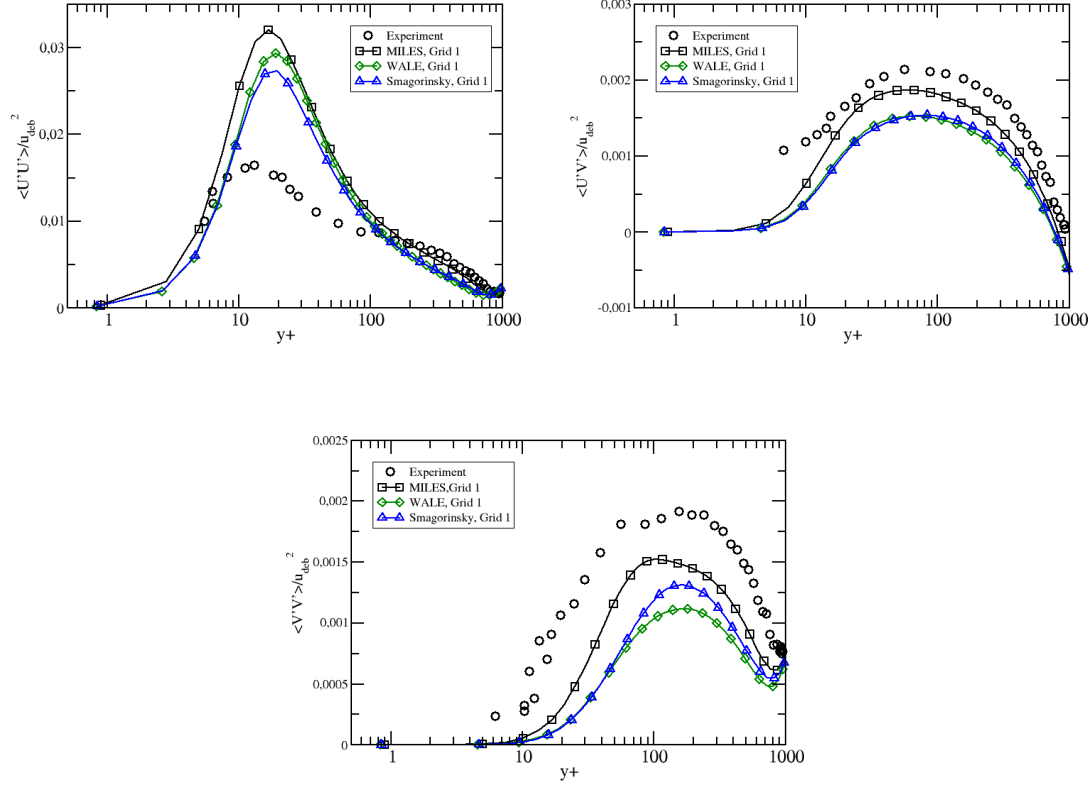


Figure 15.6: Comparison of the profiles of $\langle U'U' \rangle$, $\langle U'V' \rangle$ and $\langle V'V' \rangle$ with the experimental data [144] and three different LES models: MILES (black curve with squares), WALE (green curve with diamonds) and Smagorinsky (blue curve with triangles), all the quantities are normalized by the computed bulk mean velocity, Grid 1.

Table 15.3 compares the bulk mean velocity and the wall shear velocity predicted by the simulations with the two grids and the three turbulence models. The bulk mean velocity remains unchanged. This is probably due to the dynamic procedure used to vary the mean pressure gradient which is not affected by the mesh refinement. On the contrary, the wall shear velocity prediction is improved, which is consistent with previous results reported in [14, 135].

The profiles comparisons are presented in Figure 15.7 for $\langle u^r \rangle$ and Figure 15.8 for $\langle U'U' \rangle$, $\langle U'V' \rangle$ and $\langle V'V' \rangle$. For the sake of clarity, only the results with the MILES model are shown. The dimensionless quantities are obtained with the computed values. The same trend is obtained with the three turbulence models. The results for the WALE and Smagorinsky's model are available in Appendix M. For all the quantities, the results are improved by the grid refinement in the spanwise direction. One reason of this global improvement is the reduction of the grid anisotropy especially close to walls where the cells are particularly small in the y direction.

In the next sections and chapters, the level of refinement in the x and z directions

of Grid 2 is chosen.

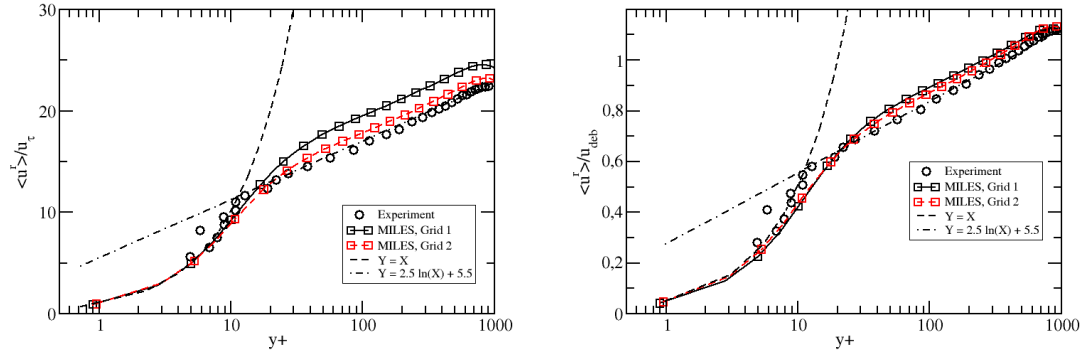


Figure 15.7: Comparison of the profiles of $\langle u^r \rangle$ with the experimental data [144] and the MILES model for the two grids, left: normalization by the computed wall shear velocity, right: by the computed bulk mean velocity.

15.4.4 Sensibility to the mesh refinement in the stream-wise direction

In the previous simulations, the first cell of the mesh has been fixed at $y^+ = 1$. Nevertheless, in the objective of industrial simulations at high Reynolds numbers in a large domain, this condition on the first cell size can highly increase the computational cost. Therefore, in this section, a quantification of the effect of a larger first cell on the simulation results is proposed. For this purpose, two new grids are defined with a first cell size respectively at $y^+ = 5$ (Grid 3) and $y^+ = 10$ (Grid 4). The mesh dimensions, the cell size at the middle height of the domain and the refinement in the x and z directions are conserved compared to Grid 2. The time step is equal to 0.1 ms . Except the modification of the mesh, all the simulation parameters remain unchanged.

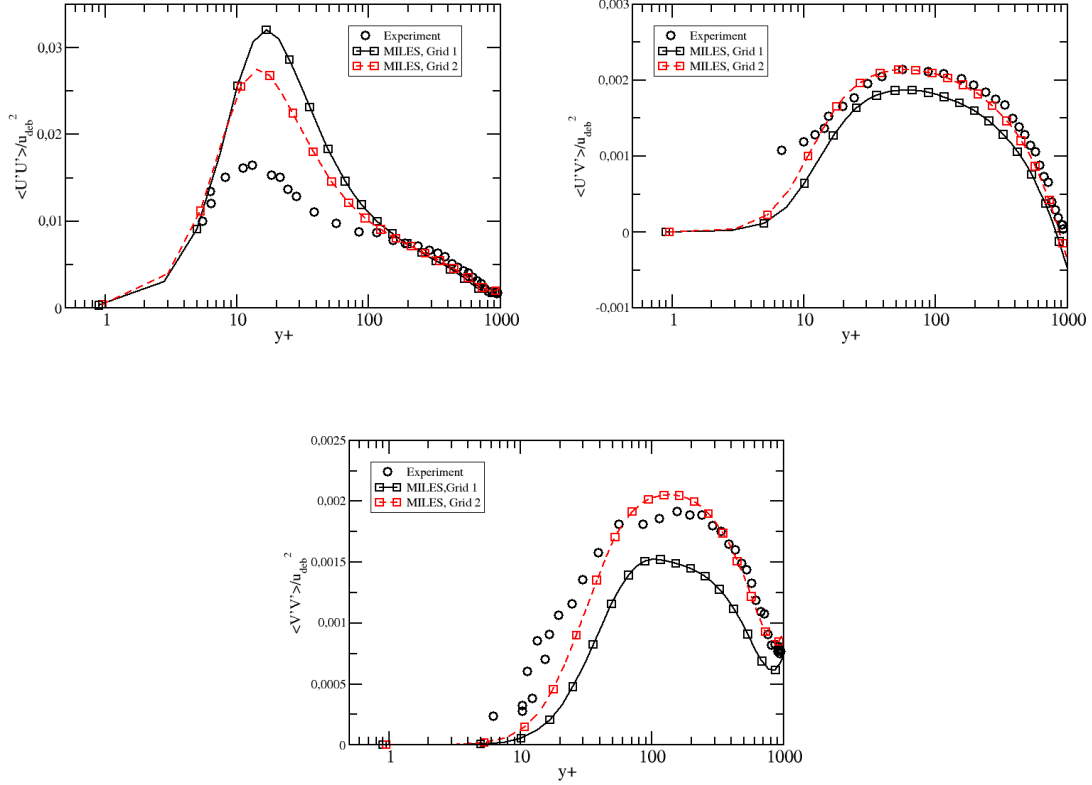


Figure 15.8: Comparison of the profiles of $\langle U'U' \rangle$, $\langle U'V' \rangle$ and $\langle V'V' \rangle$ with the experimental data [144] and the MILES model for the two grids, all the quantities are normalized by the computed bulk mean velocity.

	$u_{deb} (m.s^{-1})$			$u_{\tau} (m.s^{-1})$		
	Grid 2	Grid 3	Grid 4	Grid 2	Grid 3	Grid 4
MILES	19.65 (2.0 %)	19.88 (0.90 %)	19.26 (4.0 %)	0.96 (4.0 %)	0.89 (11 %)	0.76 (24 %)
WALE	19.65 (2.0 %)	19.88 (0.90 %)	19.26 (4.0 %)	0.90 (10 %)	0.86 (14 %)	0.73 (27 %)
Smagorinsky	19.65 (2.0 %)	19.88 (0.90 %)	19.26 (4.0 %)	0.89 (11 %)	0.88 (12 %)	0.76 (24 %)

Table 15.4: Computed bulk mean velocity and wall shear velocity for the three turbulence models and the three grids, the relative error based on the experimental data are given in brackets.

Table 15.4 compares the bulk mean velocity and the wall shear velocity predicted

by the simulations with the three grids and the three turbulence models. The alteration of the results due to the mesh coarsening is limited and depends on the turbulence model. Surprisingly, the error on the bulk mean velocity is decreased when Grid 3 is used whereas the first cell position is fixed at $y^+ = 5$. However, for $y^+ = 10$, the bulk mean velocity begins to decrease. To compare the error level, Zahrai *et al.* [221] reported an error on the center velocity equal to 10 % with a first cell located at $y^+ = 5$. Thus, the error level obtained in our simulation is slightly smaller. For the wall shear velocity, as expected, the grid refinement plays an important role to limit the error. Thus, when the mesh is coarsened, the error increases.

The profiles comparisons are presented for the MILES model in Figure 15.9 for $\langle u^r \rangle$ and Figure 15.10 for $\langle U'U' \rangle$, $\langle U'V' \rangle$ and $\langle V'V' \rangle$. The dimensionless quantities are obtained with the computed values. The results for the other turbulence models are available in Appendix M. The same trends are observed for the three models. The results are comparable for the two more refined grids (Grid 2 and Grid 3). The effect of the mesh coarsening is limited for high y^+ . The main differences are observed for $y^+ < 30$.

The weak effect of a mesh coarsening for $y^+ < 5$ is an important point for the simulation of industrial test cases with limited computational costs.

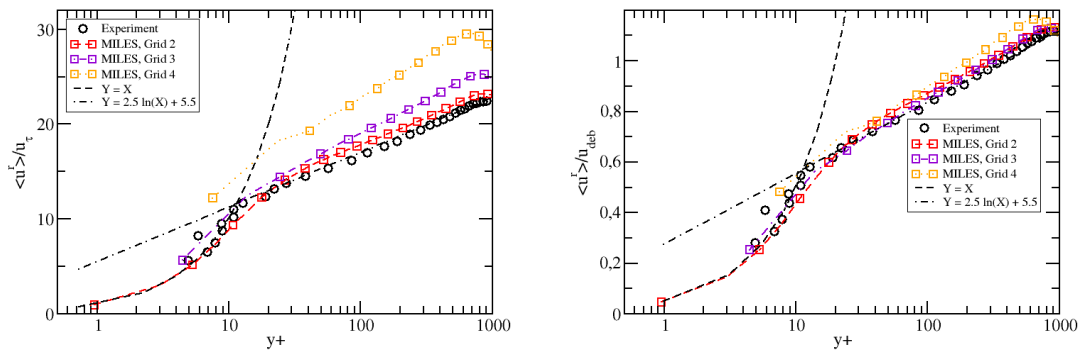


Figure 15.9: Comparison of the profiles of $\langle u^r \rangle$ with the experimental data [144] and the MILES model for the three grids, left: normalization by the computed wall shear velocity, right: by the computed bulk mean velocity.

15.4.5 Sensibility to the time scheme order

In all the simulations, a centered scheme is used in space. However, the time scheme is at 1st order. To assess the effect of the time order on the simulation, the 2nd order is implemented and used to simulate the test case. Grid 2 is chosen for this study. The time step is equal to 0.1 ms. Except the time order, all the simulation parameters remain unchanged.

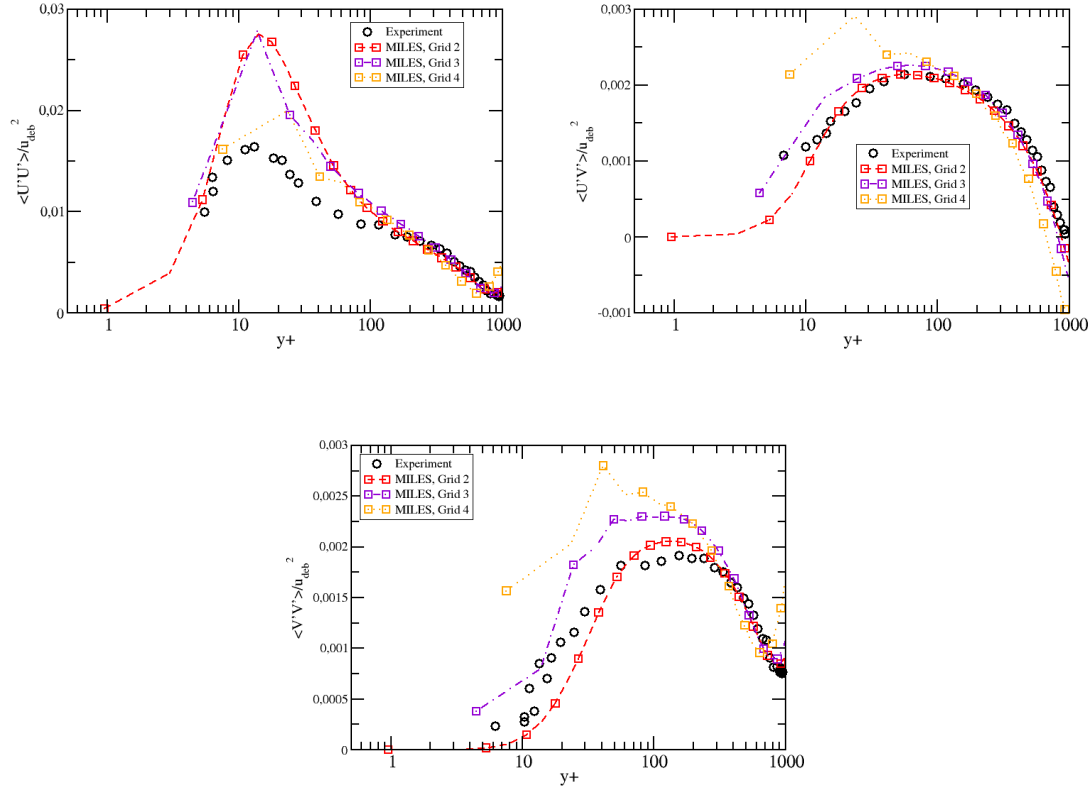


Figure 15.10: Comparison of the profiles of $\langle U'U' \rangle$, $\langle U'V' \rangle$ and $\langle V'V' \rangle$ with the experimental data [144] and the MILES model for the three grids, all the quantities are normalized by the computed bulk mean velocity.

	$u_{deb} (m.s^{-1})$		$u_{\tau} (m.s^{-1})$	
	1 st order scheme	2 nd order scheme	1 st order scheme	2 nd order scheme
MILES	19.65 (2.0 %)	19.65 (2.0 %)	0.96 (4.0 %)	1.03 (3.0 %)
WALE	19.65 (2.0 %)	19.65 (2.0 %)	0.90 (10 %)	0.92 (8.0 %)
Smagorinsky	19.65 (2.0 %)	19.65 (2.0 %)	0.89 (11 %)	0.92 (8.0 %)

Table 15.5: Computed bulk mean velocity and wall shear velocity for the three turbulence models and the 1st and 2nd time scheme order, the relative error based on the experimental data are given in brackets, Grid 2.

The bulk velocity and the wall shear velocity are compared in Table 15.5. The bulk mean velocity remains unchanged. This is probably due to the dynamic procedure used to vary the mean pressure gradient which is not affected by the time

scheme order. The main difference is obtained for the wall shear velocity. The increase of the time scheme order improves the prediction of the wall shear velocity. These results are also visible in the left picture in Figure 15.11. The curves corresponding to the 2nd order are closer to the experimental results.

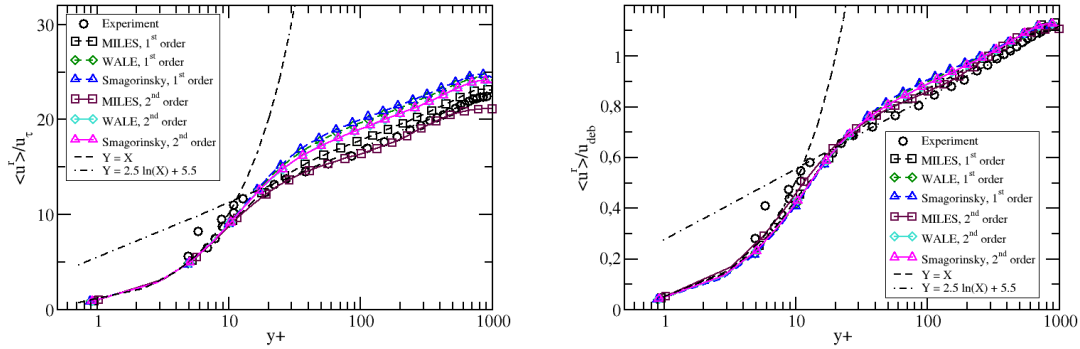


Figure 15.11: Comparison of the profiles of $\langle u^r \rangle$ with the experimental data [144] with a 1st and a 2nd time scheme order and the three turbulence models, Grid 2, left: normalization by the computed wall shear velocity, right: by the computed bulk mean velocity.

Figure 15.12 compares the turbulent components of the velocity. The improvement due to the increase of the time order is visible but limited with the WALE and the Smagorinsky's model. This observation allows concluding that the time scheme order is not responsible for the overestimation of $\langle U'U' \rangle$. With the MILES model, the 2nd order badly affects the results. This is due to the reduction of the numerical viscosity induced by the scheme diffusivity. Thus, the effect of the time scheme order on the production of numerical viscosity is largely preponderant compared to the grid refinement. These results reinforce the assumption of a numerical turbulent viscosity with a 1st time scheme order, which allows performing implicit LES.

The use of the 2nd order improves slightly the results. The improvements are limited since the time step is small. Significant differences should be observed with larger time steps. The implementation of the 2nd order scheme have yet only been performed for single-phase flow simulations. Its extension to two-phase flow simulations is not currently available but should be done in few months. Thus, if the next chapters, the 1st time scheme order is used for all the simulations.

15.5 Conclusion

This study showed the ability of the code to simulate turbulent flows using Large Eddy Simulation. Reasonable agreements have been obtained with the experimental data. The same level of accuracy have been reported in the literature for such turbulence models [112, 135]. Moreover, a mesh coarsening study highlighted a limited effect on the results. Results with the WALE and the Smagorinsky's model

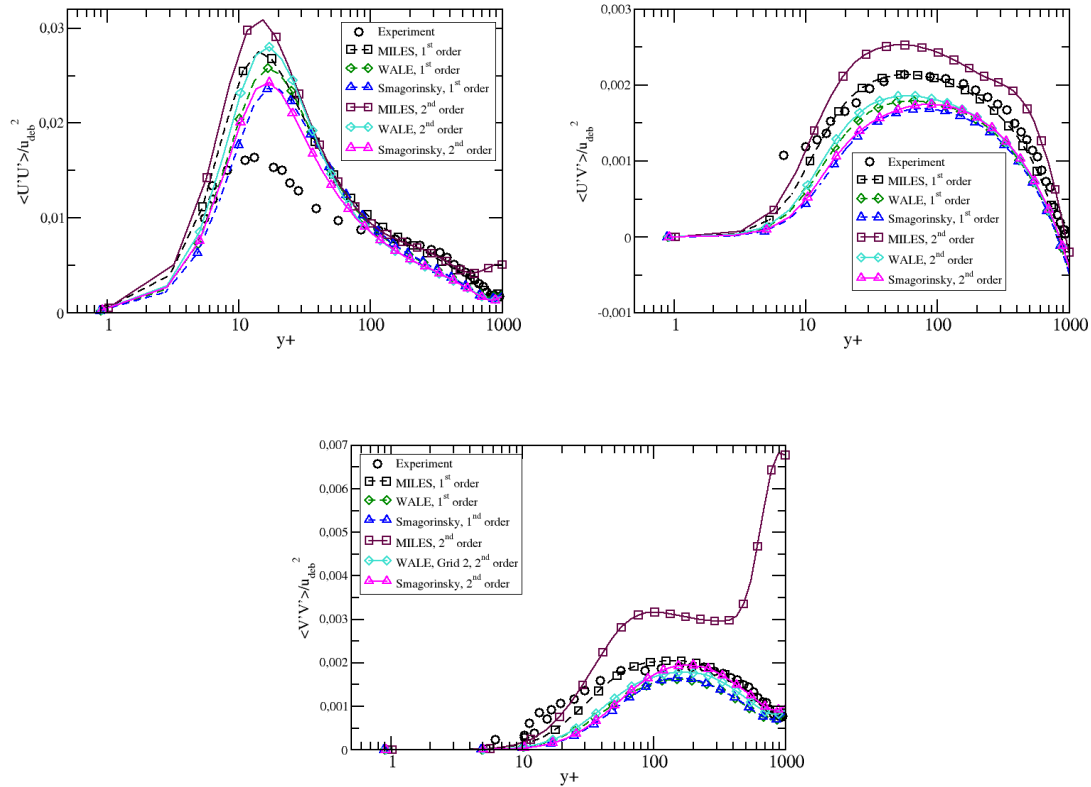


Figure 15.12: Comparison of the profiles of $\langle U'U' \rangle$, $\langle U'V' \rangle$ and $\langle V'V' \rangle$ with the experimental data [144] with a 1st and a 2nd time scheme order and the three turbulence models, Grid 2, all the quantities are normalized by the computed bulk mean velocity.

were improved by increasing the time scheme order. However, it is not yet available for two-phase flow simulations.

All these results could be improved by the use of more suitable turbulence models such as models presented in [135]. Thus, the development and comparisons of other models are proposed in the next two chapters on turbulent two-phase flows.

Chapter 16

A priori LES study on two-phase flows with the two-fluid model

In this chapter, the properties of the turbulent isothermal flows with two phases defined as two continuous fields are studied. For this purpose, the phase inversion benchmark [207] is simulated. This benchmark is a phase separation test case which have been previously used in different publications to study the role and to compare the order of magnitude of the two-phase subgrid terms for one-fluid models [88, 96, 207]. Here, exploratory simulations are performed with the two-fluid model using the LBMo (see Part I) to see if similar results are obtained. The subgrid terms appearing in the filtered two-fluid equations are evaluated and different turbulence models presented in section 14.3 are compared. This analysis is performed by considering only two continuous fields. No dispersed field is simulated.

In Appendix N, a second case of the phase inversion benchmark is simulated and used to perform the *a priori* LES study. This second case differs from the first one by the size of the computational domain and the surface tension coefficient.

This chapter corresponds to two proceeding communications presented at the 4th International Conference on Turbulence and Interactions 2015 (TI 2015, 2-6 November 2015) [50] and the 7th International Symposium on Advances in Computational Heat Transfer (CHT-17, 28 May - 2 June 2017) [51].

16.1 Résumé du chapitre

Après avoir démontré la faisabilité numérique de simulations LES, ce chapitre propose une analyse *a priori* de cette approche sur la base d'un cas de référence: l'inversion de phase. Dans un premier temps, la simulation est validée avec des codes de DNS dédiés. Puis, les équations bi-fluide sont filtrées pour faire apparaître les différents termes sous-maîles qui devront être modélisés. La simulation est ensuite utilisée pour évaluer l'ordre de grandeur de ces termes afin d'identifier ceux qui vont nécessiter un effort de modélisation plus important du fait de leur prépondérance. Enfin, différents modèles de turbulence disponibles dans la littérature sont comparées. Toute cette analyse est réalisée en ne considérant que des champs continus.

L'écoulement est isotherme comme dans le chapitre précédent.

16.2 Simulation of the phase inversion benchmark

16.2.1 Presentation of the test case

In this test case, an oil drop with a cubic shape (size of $\frac{L}{2}$) is initially placed in a cubic box (size $L = 0.1 \text{ m}$) containing liquid water (see Figure 16.1). The evolution of the system is driven by gravity forces in the z direction ($g = 9.81 \text{ m.s}^{-2}$). At the end of the simulation, the oil phase is supposed to be located in the top part of the box with the liquid water beneath. The fluid properties are given in Table 16.1. Surface tension coefficient is equal to 0.045 N.m^{-1} . Some significant physical parameters can be defined for this simulation: the Reynolds number, the Weber number and the Ohnesorge number:

$$Re = \frac{\rho_2 L U_2}{\mu_2} \quad (16.1)$$

with $U_g = \frac{\rho_2 - \rho_1}{\rho_1} \sqrt{\frac{Lg}{2}}$ the gravitational velocity. With the fluid properties given in Table 16.1, the Reynolds number is equal to 7000.

$$We = \frac{\rho_2 L U_2^2}{\sigma} \quad (16.2)$$

The Weber number is equal to 11.

$$Oh = \frac{\mu_2}{\sqrt{\sigma \rho_2 L}} \quad (16.3)$$

The Ohnesorge number is equal to $4.7 \cdot 10^{-4}$.

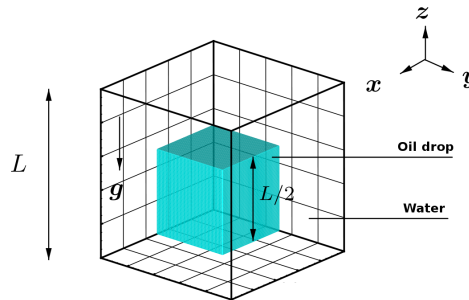


Figure 16.1: Initial conditions of the phase inversion benchmark.

	Density ($kg.m^{-3}$)	Viscosity ($Pa.s$)
Oil (phase 1)	900	0.1
Water (phase 2)	1000	1.10^{-3}

Table 16.1: Properties of oil and water for the phase inversion benchmark.

The test case is simulated with three different mesh refinements: 128^3 cells, 256^3 cells and 512^3 cells. The time steps are kept constant and are respectively equal to $0.8 ms$, $0.2 ms$ and $0.05 ms$ such that the CFL number is constant and always smaller than 0.9. The simulations have been performed with 144 cores for the first mesh and 1152 for the two others during respectively 7 hours, 47 hours and 2 months and a half to reach 13 physical seconds.

16.2.2 Validation of the macroscopic behavior

First, some macroscopic quantities are compared to validate the simulation. The evolution of the normalized kinetic energy for each field: $E_{c,k} = \frac{1}{2} \sum_I^{ncel} \alpha_k \rho_k u_k^2 \Omega$, potential energy: $E_{p,k} = \sum_I^{ncel} \alpha_k \rho_k g z \Omega$, enstrophy $E_{s,k} = \frac{1}{2} \sum_I^{ncel} \alpha_k \nabla \mathbf{u}_k \Omega$ and the volume ratio of oil in the top part of the box: $r = \frac{1}{V_1} \sum_I^{ncel} \alpha_k \Omega$, with $V_1 = \frac{L^3}{8}$ the volume of the upper layer of the box are assessed. These quantities are normalized using Table 16.2. Concerning the time scale, the normalized value is equal to $t^* = \frac{t}{t_c} = \frac{tL}{U_g}$.

	$E_{c,k}^n = \frac{1}{16} \rho_k U_g^2 L^3$	$E_{p,k}^n = \lim_{t \rightarrow +\infty} (E_{p,k})$	$E_{s,k}^n$ maximum of enstrophy for code DyJeAT with 512^3 grid [208]
Oil	$3.41.10^{-4} J$	$0.1035 J$	$7.33.10^{-2} m^3.s^{-2}$
Water	$3.78.10^{-4} J$	$0.3755 J$	$1.3759 m^3.s^{-2}$

Table 16.2: Macroscopic quantities normalization for the phase inversion benchmark.

The simulation is performed with the Large Bubble Model considering two continuous fields: oil and water and no dispersed one. To validate the simulation of the phase inversion benchmark, the evolution of the macroscopic quantities are compared in Figure 16.2 to the results obtained with the code DyJeAT (Dynamic of Jet ATomization) developed at ONERA. This code is dedicated to Direct Numerical Simulations. It uses a projection method to couple velocity and pressure on

a staggered grid. Surface tension forces are implemented through a ghost fluid approach. The interfaces are tracked thanks to a Level-Set method with a redistancing algorithm. A fifth order conservative WENO [180] scheme is applied to discretized space advection terms together with a 3^{rd} order Runge-Kutta TVD scheme for time derivatives [181]. More details can be found in [201, 202, 226].

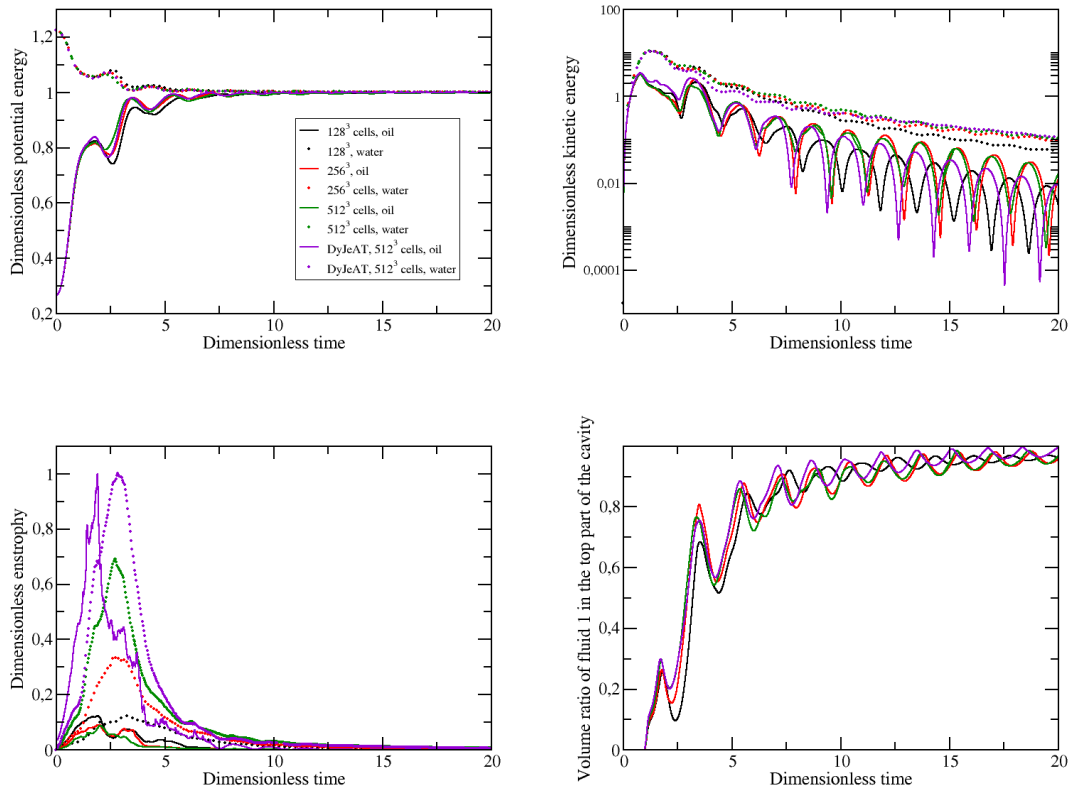


Figure 16.2: Evolution of the dimensionless potential energy, kinetic energy, enstrophy and volume ratio of oil, the solid lines correspond to the oil phase, the dashed lines to water, the black curves refer to the coarser mesh: 128^3 cells, the red ones to the intermediate mesh: 256^3 cells, the green ones to the refined mesh: 512^3 cells and the purple curves refer to the code DyJeAT with the 512^3 grid.

The Large Bubble Model reproduces the same trends obtained with DyJeAT and other DNS codes [208]. The potential energy oscillates before reaching its final value. These oscillations also observed with the kinetic energy and the volume ratio of oil are caused by the sloshing motion of oil at the top of the box. The frequency corresponds to the period of time for oil to go from the left of the box to the right and to come back to the left. Concerning the enstrophy, the amplitude decreases with the mesh refinement for the oil phase but increases for the water phase, as observed with other codes in [208]. This last point is very interesting since all the other quantities seem to have converged, suggesting that a real DNS was achieved.

The main difference then is that the potential and kinetic energies are dominated by large-scale motions whereas small-scale motions, especially vorticity, are the main contributors of enstrophy. Studies of vorticity magnitude [208] highlighted that, in this configuration, the high shear regions are located close to walls and interfaces. Such boundary layers seem clearly not fully resolved even with the finest grids (512^3 cells). In single-phase turbulent flows, DNS requires a number of grid points of the order of $Re^{\frac{9}{4}}$ so that the smallest scale corresponds to the Kolmogorov's length. Taking the definition of the Reynolds number presented in Equation (16.1), the grid should be divided into 448.10^6 cells. As a comparison, the finest mesh used in this study contains $512^3 = 134.10^6$ cells. Nevertheless, the use of the gravitational velocity for the definition of the Reynolds number can be criticized. Thus, in Table 16.3, the maximum and average velocity for water and the number of cells required for a DNS with each velocity are presented. These data illustrate well that with the average velocity, we can expect to be close to DNS with the finest mesh. However, locally, this refinement will not be sufficient. Thus, even with this mesh, no convergence can be expected for enstrophy. In the rest of the work, it will be considered that the 512^3 grid is enough for performing a DNS of the phase separation benchmark and provides a representative simulation of this complex two-phase flow. To finish, concerning the location of the enstrophy peak, as observed with DyJeAT and other DNS codes [208], it occurs at around 3 in dimensionless time. A picture of the flow close to this time is presented in Figure 16.3.

	Maximum velocity		Mean velocity	
	$U_{max}(m.s^{-1})$	DNS cells	$U_{mean}(m.s^{-1})$	DNS cells
128^3 cells	0.32	14.10^9	0.048	192.10^6
256^3 cells	0.34	16.10^9	0.044	158.10^6
512^3 cells	0.37	19.10^9	0.047	183.10^6

Table 16.3: Evaluation of the maximum ($U_{max} = \max_{\alpha_2 > 1.10^{-4}} (u_2)$) and mean water velocity

($U_{mean} = \frac{\sum_I^{ncel} \alpha_2^I \rho_2^I u_2^I}{\sum_I^{ncel} \alpha_2^I \rho_2^I}$) in the whole domain to evaluate the required cell numbers for a DNS.

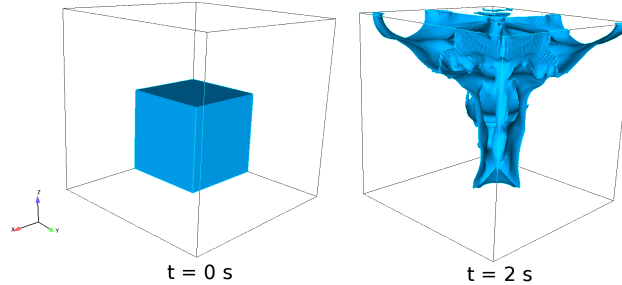


Figure 16.3: Picture of the phase inversion benchmark, at the initialized state and close to the peak of enstrophy.

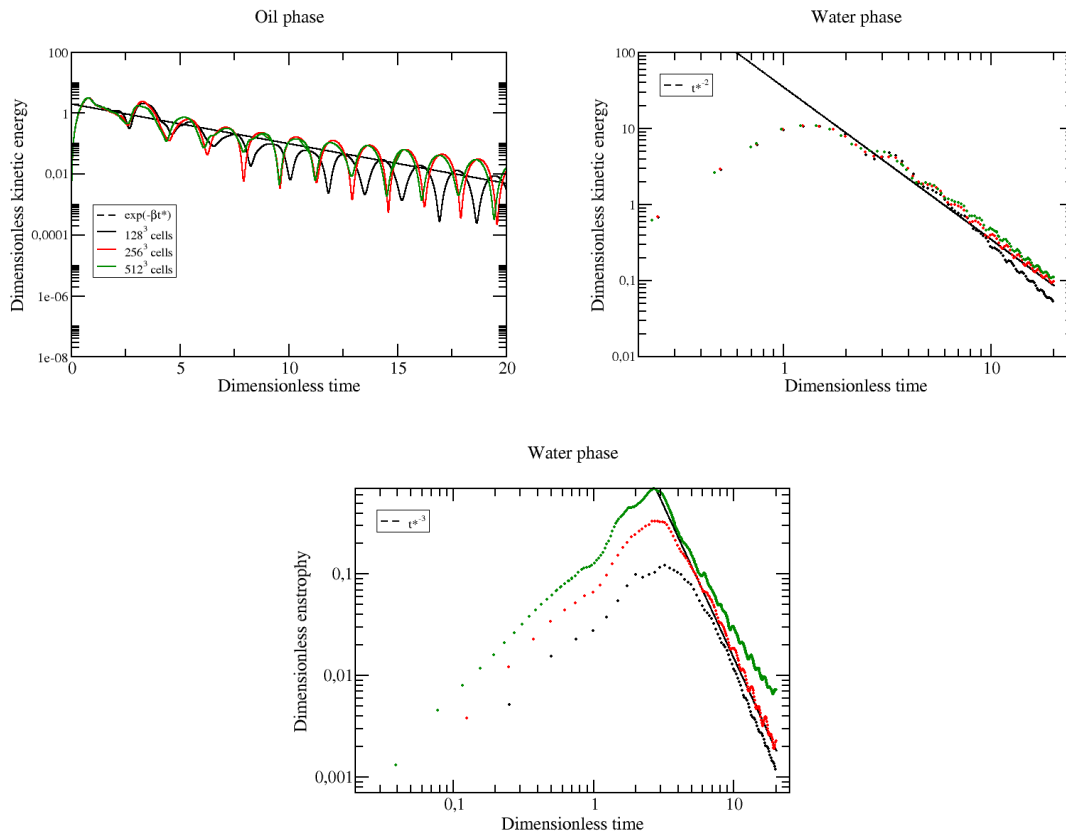


Figure 16.4: Evolution of the dimensionless kinetic energy for the two phases and the dimensionless enstrophy for water, the black dashed lines correspond to different laws that fit the macroscopic quantities after the enstrophy peak, the solid lines correspond to the oil phase, the dashed lines to water, the black curves refer to the coarser mesh: 128^3 cells, the red ones to the intermediate mesh: 256^3 cells and the green ones to the refined mesh: 512^3 cells.

Finally, Vincent *et al.* [208] proposed different evolution laws which characterize

the motion after the enstrophy peak, when the flow reaches its sloshing regime. Doing so, a Stokes' decay law $e^{-\beta t^*}$ was observed with the DNS codes for the kinetic energy of the oil phase. For the kinetic energy of the water phase, an evolution in t^{*-2} was obtained and t^{*-3} for the enstrophy of the water phase. These observations are also valuable with our two-fluid approach as shown in Figure 16.4.

16.3 Filtering of the two-fluid model equations

Contrary to section 14.7.1, in which the filtered two-fluid model equations have been written for a continuous field and a dispersed one [90], here, the filtering of these equations is considered for two continuous fields using the LBMo. Specific subgrid terms appear at the interface between the two continuous fields which do not exist in the previous filtered two-fluid equations. Therefore, let us write the filtered equations in isothermal conditions without mass transfers between two incompressible fields:

- The filtered mass balance equation:

$$\frac{\partial}{\partial t} (\overline{\alpha_k \rho_k}) + \overline{\nabla \cdot (\alpha_k \rho_k \mathbf{u}_k)} = 0 \quad (16.4)$$

- The filtered momentum balance equation:

$$\frac{\partial}{\partial t} (\overline{\alpha_k \rho_k \mathbf{u}_k}) + \overline{\nabla \cdot (\alpha_k \rho_k \mathbf{u}_k \otimes \mathbf{u}_k)} = \frac{-\overline{\alpha_k \nabla P} + \overline{\nabla \cdot (\alpha_k \mu_k \underline{S}_k)}}{\overline{\alpha_k \rho_k \mathbf{g}} + \overline{\mathbf{F}_{Drag,p \rightarrow k}} + \overline{\alpha_k \sigma_k \nabla \alpha_k}} \quad (16.5)$$

As previously done in section 14.2, the equations will be filtered using the simple filtering and the Favre's averaging. Contrary to the one-fluid equations, density and viscosity of each field are constant. Thus, $\overline{\rho_k} = \rho_k$ and $\overline{\mu_k} = \mu_k$. The Favre's averaging is defined as follows:

$$\tilde{\mathbf{u}}_k = \frac{\overline{\alpha_k \mathbf{u}_k}}{\overline{\alpha_k}} \quad (16.6)$$

16.3.1 Simple filtering

As previously done in section 14.2.1, the following filtered equations are obtained:

- The filtered mass balance equation:

$$\frac{\partial}{\partial t} (\overline{\alpha_k \rho_k}) + \rho_k \nabla \cdot (\overline{\alpha_k \mathbf{u}_k}) + \overline{\tau}_{interf} = 0 \quad (16.7)$$

with $\overline{\tau}_{interf} = \rho_k (\nabla \cdot (\overline{\alpha_k \mathbf{u}_k}) - \nabla \cdot (\overline{\alpha_k} \overline{\mathbf{u}_k}))$.

- The filtered momentum balance equation:

$$\begin{aligned} \frac{\partial}{\partial t} (\rho_k \overline{\alpha_k} \overline{\mathbf{u}_k}) + \overline{\tau}_{time} + \rho_k \nabla \cdot (\overline{\alpha_k} \overline{\mathbf{u}_k} \otimes \overline{\mathbf{u}_k}) + \overline{\tau}_{conv} = & -\overline{\alpha_k} \nabla \overline{P} - \overline{\tau}_{pressure} \\ & + \mu_k \nabla \cdot (\overline{\alpha_k} \overline{\underline{\underline{S}}_k}) + \overline{\tau}_{diff} \\ & + \overline{\alpha_k} \rho_k \mathbf{g} + \hat{\mathbf{F}}_{drag,p \rightarrow k} + \overline{\tau}_{drag} \\ & + \sigma \overline{\alpha_k} \hat{\kappa} \nabla \overline{\alpha_k} + \overline{\tau}_{superf} \end{aligned} \quad (16.8)$$

with $\overline{\tau}_{time}$, $\overline{\tau}_{conv}$, $\overline{\tau}_{diff}$ and $\overline{\tau}_{superf}$ four additional subgrid terms, comparable to the single-fluid formulation:

$$\overline{\tau}_{time} = \rho_k \left(\frac{\partial \overline{\alpha_k} \overline{\mathbf{u}_k}}{\partial t} - \frac{\partial \overline{\alpha_k}}{\partial t} \overline{\mathbf{u}_k} \right) \quad (16.9)$$

$$\overline{\tau}_{conv} = \rho_k (\nabla \cdot (\overline{\alpha_k \mathbf{u}_k \otimes \mathbf{u}_k}) - \nabla \cdot (\overline{\alpha_k} \overline{\mathbf{u}_k} \otimes \overline{\mathbf{u}_k})) \quad (16.10)$$

$$\overline{\tau}_{diff} = \mu_k \left(\nabla \cdot (\overline{\alpha_k \underline{\underline{S}}_k}) - \nabla \cdot (\overline{\alpha_k} \overline{\underline{\underline{S}}_k}) \right) \quad (16.11)$$

$$\overline{\tau}_{superf} = \sigma (\overline{\alpha_k \kappa \nabla \alpha_k} - \overline{\alpha_k} \hat{\kappa} \nabla \overline{\alpha_k}) \quad (16.12)$$

with $\hat{\kappa} = -\nabla \cdot \left(\frac{\nabla \overline{\alpha_k}}{\|\nabla \overline{\alpha_k}\|} \right)$ the filtered curvature.

The filtered equations highlight also new subgrid terms: $\overline{\tau}_{pressure}$ and $\overline{\tau}_{drag}$, whose expressions are:

$$\overline{\tau}_{pressure} = \overline{\alpha_k \nabla P} - \overline{\alpha_k} \nabla \overline{P} \quad (16.13)$$

$$\overline{\tau}_{drag} = \overline{\mathbf{F}_{drag}} - \hat{\mathbf{F}}_{drag} \quad (16.14)$$

with:

$$\begin{aligned} \overline{\alpha_{cg}} < 0.3 : \quad & \overline{\mathbf{F}}_{bubble,cl \rightarrow cg} = \overline{\alpha_{cl} \alpha_{cg} \frac{18\mu_{cl}}{\alpha_{cl} d_p^2} (\mathbf{u}_{cl} - \mathbf{u}_{cg})} \\ \overline{\alpha_{cg}} > 0.7 : \quad & \overline{\mathbf{F}}_{droplet,cl \rightarrow cg} = \overline{\alpha_{cl} \alpha_{cg} \frac{18\mu_{cg}}{\alpha_{cg} d_p^2} (\mathbf{u}_{cl} - \mathbf{u}_{cg})} \end{aligned} \quad (16.15)$$

$$0.3 \leq \overline{\alpha_{cg}} \leq 0.7 : \quad \overline{\mathbf{F}}_{mix,cl \rightarrow cg} = \overline{\frac{0.7 - \alpha_{cg}}{0.7 - 0.3} \mathbf{F}_{bubble} + \frac{\alpha_{cg} - 0.3}{0.7 - 0.3} \mathbf{F}_{droplet}}$$

and:

$$\begin{aligned}
 \overline{\alpha_{cg}} < 0.3 : \quad \hat{\mathbf{F}}_{bubble,cl \rightarrow cg} &= \overline{\alpha_{cl}} \overline{\alpha_{cg}} \frac{18\mu_{cl}}{\alpha_{cl}\hat{d}_p^2} (\overline{\mathbf{u}_{cl}} - \overline{\mathbf{u}_{cg}}) \\
 \overline{\alpha_{cg}} > 0.7 : \quad \hat{\mathbf{F}}_{droplet,cl \rightarrow cg} &= \overline{\alpha_{cl}} \overline{\alpha_{cg}} \frac{18\mu_{cg}}{\alpha_{cg}\hat{d}_p^2} (\overline{\mathbf{u}_{cl}} - \overline{\mathbf{u}_{cg}}) \\
 0.3 \leq \overline{\alpha_{cg}} \leq 0.7 : \quad \hat{\mathbf{F}}_{mix,cl \rightarrow cg} &= \frac{0.7-\overline{\alpha_{cg}}}{0.7-0.3} \hat{\mathbf{F}}_{bubble} + \frac{\overline{\alpha_{cg}}-0.3}{0.7-0.3} \hat{\mathbf{F}}_{droplet}
 \end{aligned} \tag{16.16}$$

The definition of \hat{d}_p is given in Figure 16.5.

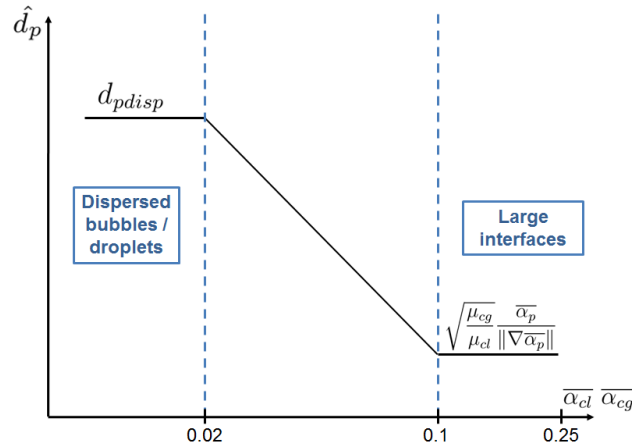


Figure 16.5: Distribution of \hat{d}_p along the domain, d_{pdisp} corresponds to the diameter of the dispersed bubbles/droplets, large interfaces are located at high values of $\overline{\alpha_{cl}} \overline{\alpha_{cg}}$, between the two extreme values d_{pdisp} and $\sqrt{\frac{\mu_{cg}}{\mu_{cl}} \frac{\overline{\alpha_p}}{\|\nabla \overline{\alpha_p}\|}}$, \hat{d}_p is equal to: $\hat{d}_p = \frac{\overline{\alpha_{cl}} \overline{\alpha_{cg}} - b}{a - b} d_{pdisp} + \frac{\overline{\alpha_{cl}} \overline{\alpha_{cg}} - a}{b - a} \sqrt{\frac{\mu_{cg}}{\mu_{cl}} \frac{\overline{\alpha_p}}{\|\nabla \overline{\alpha_p}\|}}$, with $a = 0.02$ and $b = 0.1$.

16.3.2 Favre's averaging

Now, the Favre's averaging is considered:

- The filtered mass balance equation:

$$\frac{\partial}{\partial t} (\overline{\alpha_k} \rho_k) + \rho_k \nabla \cdot (\overline{\alpha_k} \tilde{\mathbf{u}}_k) + \tilde{\tau}_{interf} = 0 \tag{16.17}$$

with

$$\begin{aligned}
 \tilde{\tau}_{interf} &= \rho_k (\nabla \cdot (\overline{\alpha_k \mathbf{u}_k}) - \nabla \cdot (\overline{\alpha_k} \tilde{\mathbf{u}}_k)) \\
 &= \rho_k \left(\nabla \cdot (\overline{\alpha_k \mathbf{u}_k}) - \nabla \cdot \left(\overline{\alpha_k} \frac{\overline{\alpha_k \mathbf{u}_k}}{\overline{\alpha_k}} \right) \right) \\
 &= 0
 \end{aligned} \tag{16.18}$$

Thus, the filtered mass balance equation with the Favre's averaging can be written:

$$\frac{\partial}{\partial t} (\overline{\alpha_k \rho_k}) + \rho_k (\overline{\alpha_k} \tilde{\mathbf{u}}_k) = 0 \tag{16.19}$$

- The filtered momentum balance equation:

$$\begin{aligned}
 \frac{\partial}{\partial t} (\rho_k \overline{\alpha_k} \tilde{\mathbf{u}}_k) + \tilde{\tau}_{time} + \rho_k \nabla \cdot (\overline{\alpha_k} \tilde{\mathbf{u}}_k \otimes \tilde{\mathbf{u}}_k) + \tilde{\tau}_{conv} &= -\overline{\alpha_k} \nabla \overline{P} - \tilde{\tau}_{pressure} \\
 &\quad + \mu_k \nabla \cdot \left(\overline{\alpha_k} \underline{\underline{\tilde{S}}}_k \right) + \tilde{\tau}_{diff} \\
 &\quad + \overline{\alpha_k} \rho_k \mathbf{g} + \tilde{\mathbf{F}}_{drag,p \rightarrow k} + \tilde{\tau}_{drag} \\
 &\quad + \sigma \overline{\alpha_k} \hat{\kappa} \nabla \overline{\alpha_k} + \tilde{\tau}_{superf}
 \end{aligned} \tag{16.20}$$

with:

$$\begin{aligned}
 \tilde{\tau}_{time} &= \frac{\partial}{\partial t} (\overline{\alpha_k \rho_k \mathbf{u}_k}) - \frac{\partial}{\partial t} (\rho_k \overline{\alpha_k} \tilde{\mathbf{u}}_k) \\
 &= \frac{\partial}{\partial t} (\overline{\alpha_k \rho_k \mathbf{u}_k}) - \frac{\partial}{\partial t} \left(\rho_k \overline{\alpha_k} \frac{\overline{\alpha_k \mathbf{u}_k}}{\overline{\alpha_k}} \right) \\
 &= 0
 \end{aligned} \tag{16.21}$$

$$\tilde{\tau}_{conv} = \rho_k (\nabla \cdot (\overline{\alpha_k \mathbf{u}_k} \otimes \mathbf{u}_k) - \nabla \cdot (\overline{\alpha_k} \tilde{\mathbf{u}}_k \otimes \tilde{\mathbf{u}}_k)) \tag{16.22}$$

$$\begin{aligned}
 \tilde{\tau}_{diff} &= \mu_k \left(\nabla \cdot \left(\overline{\alpha_k} \underline{\underline{S}}_k \right) - \nabla \cdot \left(\overline{\alpha_k} \underline{\underline{\tilde{S}}}_k \right) \right) \\
 &= \mu_k \left(\nabla \cdot \left(\overline{\alpha_k} \underline{\underline{S}}_k \right) - \nabla \cdot \left(\overline{\alpha_k} \frac{\overline{\alpha_k} \underline{\underline{S}}_k}{\overline{\alpha_k}} \right) \right) \\
 &= 0
 \end{aligned} \tag{16.23}$$

$$\tilde{\tau}_{superf} = \sigma (\overline{\alpha_k \kappa} \nabla \alpha_k - \overline{\alpha_k} \hat{\kappa} \nabla \overline{\alpha_k}) = \bar{\tau}_{superf} \tag{16.24}$$

$$\tilde{\tau}_{pressure} = \overline{\alpha_k} \nabla \overline{P} - \overline{\alpha_k} \nabla \overline{P} = \bar{\tau}_{pressure} \tag{16.25}$$

$$\tilde{\tau}_{drag} = \overline{\mathbf{F}}_{drag} - \tilde{\mathbf{F}}_{drag} \tag{16.26}$$

with:

$$\begin{aligned}
 \overline{\alpha_{cg}} < 0.3 : \quad & \tilde{\mathbf{F}}_{bubble,cl \rightarrow cg} = \overline{\alpha_{cl}} \overline{\alpha_{cg}} \frac{18\mu_{cl}}{\overline{\alpha_{cl}} \hat{d}_p^2} (\tilde{\mathbf{u}}_{cl} - \tilde{\mathbf{u}}_{cg}) \\
 \overline{\alpha_{cg}} > 0.7 : \quad & \tilde{\mathbf{F}}_{droplet,cl \rightarrow cg} = \overline{\alpha_{cl}} \overline{\alpha_{cg}} \frac{18\mu_{cg}}{\overline{\alpha_{cg}} \hat{d}_p^2} (\tilde{\mathbf{u}}_{cl} - \tilde{\mathbf{u}}_{cg}) \\
 0.3 \leq \overline{\alpha_{cg}} \leq 0.7 : \quad & \tilde{\mathbf{F}}_{mix,cl \rightarrow cg} = \frac{0.7 - \overline{\alpha_{cg}}}{0.7 - 0.3} \tilde{\mathbf{F}}_{bubble} + \frac{\overline{\alpha_{cg}} - 0.3}{0.7 - 0.3} \tilde{\mathbf{F}}_{droplet}
 \end{aligned} \tag{16.27}$$

The filtered momentum balance equation can then be rewritten:

$$\begin{aligned}
 \frac{\partial}{\partial t} (\rho_k \overline{\alpha_k} \tilde{\mathbf{u}}_k) + \rho_k \nabla \cdot (\overline{\alpha_k} \tilde{\mathbf{u}}_k \otimes \tilde{\mathbf{u}}_k) + \tilde{\tau}_{conv} = & -\overline{\alpha_k} \nabla \overline{P} - \tilde{\tau}_{pressure} \\
 & + \mu_k \nabla \cdot \left(\overline{\alpha_k} \underline{\tilde{S}}_k \right) \\
 & + \overline{\alpha_k} \rho_k \mathbf{g} + \tilde{\mathbf{F}}_{drag,p \rightarrow k} + \tilde{\tau}_{drag} \\
 & + \sigma \overline{\alpha_k} \hat{\kappa} \nabla \overline{\alpha_k} + \tilde{\tau}_{superf}
 \end{aligned} \tag{16.28}$$

Subgrid terms	Simple filtering	Favre's averaging
τ_{time}	$\rho_k \left(\frac{\partial \overline{\alpha_k} \mathbf{u}_k}{\partial t} - \frac{\partial \overline{\alpha_k} \mathbf{u}_k}{\partial t} \right)$	-
τ_{conv}	$\rho_k (\nabla \cdot (\overline{\alpha_k} \mathbf{u}_k \otimes \mathbf{u}_k) - \nabla \cdot (\overline{\alpha_k} \tilde{\mathbf{u}}_k \otimes \tilde{\mathbf{u}}_k))$	$\rho_k (\nabla \cdot (\overline{\alpha_k} \mathbf{u}_k \otimes \mathbf{u}_k) - \nabla \cdot (\overline{\alpha_k} \tilde{\mathbf{u}}_k \otimes \tilde{\mathbf{u}}_k))$
τ_{diff}	$\mu_k \left(\nabla \cdot \left(\overline{\alpha_k} \underline{S}_k \right) - \nabla \cdot \left(\overline{\alpha_k} \underline{\tilde{S}}_k \right) \right)$	-
$\tau_{pressure}$	$\overline{\alpha_k} \nabla \overline{P} - \overline{\alpha_k} \nabla \overline{P}$	$\overline{\alpha_k} \nabla \overline{P} - \overline{\alpha_k} \nabla \overline{P}$
τ_{superf}	$\sigma (\overline{\alpha_k} \hat{\kappa} \nabla \overline{\alpha_k} - \overline{\alpha_k} \hat{\kappa} \nabla \overline{\alpha_k})$	$\sigma (\overline{\alpha_k} \hat{\kappa} \nabla \overline{\alpha_k} - \overline{\alpha_k} \hat{\kappa} \nabla \overline{\alpha_k})$
τ_{drag}	$\overline{\mathbf{F}}_{drag} - \hat{\mathbf{F}}_{drag}$	$\overline{\mathbf{F}}_{drag} - \tilde{\mathbf{F}}_{drag}$
τ_{interf}	$\rho_k (\nabla \cdot (\overline{\alpha_k} \mathbf{u}_k) - \nabla \cdot (\overline{\alpha_k} \tilde{\mathbf{u}}_k))$	-

Table 16.4: Summary of the subgrid terms appearing in the filtered two-fluid equations in the LBMo framework with the simple filtering $(\overline{\mathbf{u}}_k, \overline{P}, \overline{\alpha_k}, \hat{\kappa})$ and the Favre's averaging $(\tilde{\mathbf{u}}_k, \overline{P}, \overline{\alpha_k}, \hat{\kappa})$.

To summarize, all the subgrid terms obtained with the simple filtering and the Favre's averaging are displayed in Table 16.4. This table can be compared to Table 14.1, presenting the subgrid terms for the single-fluid formulation. With the two-fluid model, two new subgrid terms appear related to the pressure jump at the interface $\tau_{pressure}$ and the drag force τ_{drag} . Nevertheless, for the Favre's averaging, the diffusion, the temporal and the interfacial terms disappear. At this stage, the Favre's averaging presents the advantage of having less subgrid terms compared to the simple filtering. This means that we have three subgrid terms without modeling requirement. This is an important conclusion since the subgrid term modeling is always accompanied with an error. The reduction of the number of subgrid terms could improve the results by decreasing the quantity of errors adding by a higher number of modeled terms. Finally, one can note that the pressure and the surface tension subgrid terms keep the same expression with the two formulations: simple filtering and Favre's averaging.

16.4 Comparison of the order of magnitude of the different subgrid-scale terms

These subgrid terms are compared in terms of order of magnitude to find the predominant and negligible ones. For this purpose, a top hat filter is applied to the simulation results extracted at the peak of enstrophy for the three grids. Only the first neighborhood of each cell (filter size of 2) is considered to obtain the value of the subgrid terms. The subgrid term τ_{time} is not represented in this study since the analysis is proposed only for one time. Each subgrid term in the momentum balance equation is normalized by the convection resolved term. The interfacial subgrid term τ_{interf} appearing in the mass balance equation is normalized by its corresponding resolved part. In the single-fluid approach, the summation of the subgrid term and the convection (resp. interfacial) resolved term is made in the whole domain, as illustrated here with the convection subgrid term (simple filtering expression):

$$\bar{\tau}_{conv} = \frac{\sum_I^{ncel} |\bar{\tau}_{conv}^I|}{\sum_I^{ncel} |\rho_k \nabla \cdot (\bar{\alpha}_k^I \bar{\mathbf{u}}_k^I \otimes \bar{\mathbf{u}}_k^I)|} \quad (16.29)$$

Nevertheless, in the two-fluid formulation, to sum a subgrid term for the oil phase where there is no oil makes any sense. Thus, in this study, the subgrid terms of each phase are only considered when the volume fraction of this phase is larger than the computer error:

$$\bar{\tau}_{conv} = \frac{\sum_{\bar{\alpha}_k^I > 1.10^{-10}} |\bar{\tau}_{conv}^I|}{\sum_{\bar{\alpha}_k^I > 1.10^{-10}} |\rho_k \nabla \cdot (\bar{\alpha}_k^I \bar{\mathbf{u}}_k^I \otimes \bar{\mathbf{u}}_k^I)|} \quad (16.30)$$

16.4. COMPARISON OF THE ORDER OF MAGNITUDE OF THE DIFFERENT SUBGRID-SCALE TERMS

The results are presented in Figure 16.6. Table 16.5 proposes a classification of the subgrid terms according to the phase and the choice of the filtered quantities (Favre’s averaging or not) for the most refined grid. With the Favre’s averaging, the convection subgrid term is smaller compared to the simple LES filter. The subgrid terms τ_{superf} and $\tau_{pressure}$ are superposed in the two formulations since they have the same expressions in both cases and the convection resolved term has also the same value. The Favre’s averaging does not affect the classification of the subgrid terms for the two phases.

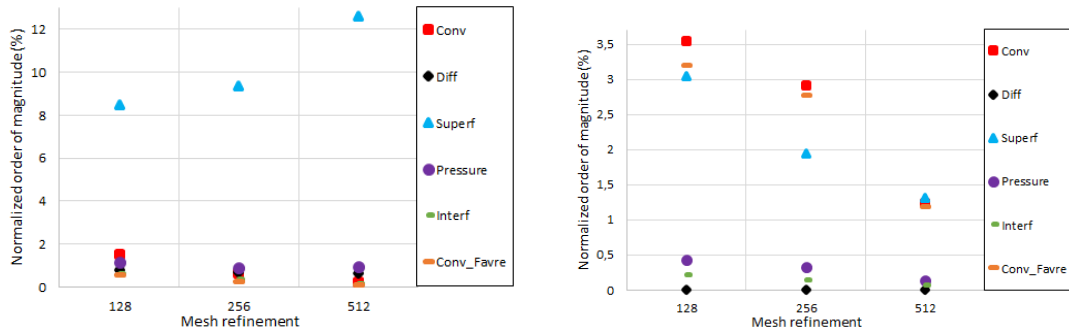


Figure 16.6: Order of magnitude of the normalized subgrid terms, left: for the oil phase, right: for the water phase, only the z component is displayed.

	Simple filtering		Favre’s averaging	
	Oil	Water	Oil	Water
1	τ_{superf}	τ_{superf}	τ_{superf}	τ_{superf}
2	$\tau_{pressure}$	τ_{conv}	$\tau_{pressure}$	τ_{conv}
3	τ_{diff}	$\tau_{pressure}$	τ_{conv}	$\tau_{pressure}$
4	τ_{conv}	τ_{interf}		
5	τ_{interf}	τ_{diff}		

Table 16.5: Classification of the subgrid terms according to their relative contribution for the 512^3 grid.

Moreover, as documented in [88, 96, 207], the subgrid term τ_{superf} is predominant for the two phases. For oil, the term is more than 10 times higher than the pressure subgrid term. Furthermore, a small contribution of the diffusion subgrid term τ_{diff} is observed for the two phases. Nevertheless, for the oil phase, contrary to the single-fluid formulation, this contribution is not negligible and very close to those of τ_{conv} and τ_{interf} . The results obtained with the single-fluid formulation seem to be closer to those obtained here for the water phase. One interesting comparison

could be to perform the one-fluid simulation with a higher quantity of oil compared to water to see if the diffusion subgrid term is still negligible. Indeed, one drawback of the summation of the terms in the whole domain (as done in Equation (16.29)) is that the contribution of each phase is not equal. It depends on the quantity of each phase in the flow. Thus, in the one-fluid approach, the weight of each subgrid term depends on the phase that is predominant in the computational domain.

As expected, the magnitude of each term decreases when the mesh is refined except τ_{superf} for the oil phase. This increase has been previously observed with single-fluid formulations. Nevertheless, the effect of the grid refinement on this subgrid term is mechanical in the two-fluid model. Indeed, the contribution of the term in the whole domain has the same order of magnitude for the two phases. Thus, the difference comes from the resolved convective term which does not have the same value for the two phases when the mesh refinement is fixed. This can be explained by two main specificities of the test case which both contribute to a higher resolved convection term in the water phase. First, the quantity of water in the test case is higher than the oil phase. Since the value of each term is considered in all the cells containing the phase, more contributions are added for the water phase. Thus, all the quantities obtained in the water phase before normalization are higher. Nevertheless, this effect vanishes as soon as the terms are normalized. This does not explain then the difference for the normalized surface tension subgrid term between the two phases. Therefore, the second effect that explains the increase of the resolved convection term is the physical properties of each phase. The oil phase has a higher viscosity. Thus, the velocities in the oil phase are smaller. The oil density is also smaller. So, whatever the grid refinement, the resolved convection term for the oil phase will be always smaller due to the combination of the oil quantity and physical properties. Now, if the mesh is refined, the velocities increase since the numerical viscosity decreases. Nevertheless, according to the viscosity of each phase, the variation of the velocities has not the same order of magnitude. The water phase has the smallest viscosity. Thus, this phase is more sensitive to a variation of the numerical viscosity. The velocities in the water phase increase more than in the oil phase. The resolved convection term increase then more in the water phase than in the oil phase. This effect is balanced by the increase of small inclusions when the mesh is refined, which induces an increase of the subgrid term. The evolution of the term contribution depends then on which effect is predominant. For the oil phase, it seems that the increase of small inclusions drive the evolution of the subgrid term, whereas for the water phase, the decrease of the numerical viscosity is predominant.

Finally, the contribution of the drag subgrid term τ_{drag} is not mentioned in Figure 16.6 for the sake of clarity. Its order of magnitude is largely higher than the contribution of the other subgrid terms.

16.5 Comparison of the turbulence models

16.5.1 Modeling errors for all the subgrid terms

In this section, a comparison of different turbulence models is proposed: Smagorinsky's model with $C_S = 0.1$ in the whole domain (see section 14.3.1.1), WALE model with $C_W = 0.5$ (section 14.3.1.2), Bardina's model (section 14.3.2.1), mixed Smagorinsky-Bardina's model (section 14.3.3) and ADM (section 14.3.2.2) with an order of 6. It has to be noted that only the Smagorinsky's and the WALE models can be applied to Favre's averaging. Indeed, by definition: $\tilde{\mathbf{u}}_k = \tilde{\mathbf{u}}_k$. As a reminder also, the functional models are applied to the two subgrid terms τ_{conv} and τ_{interf} (see section 14.3.1). The relative error of each model is evaluated using the L2 norm:

$$\epsilon_{conv}^{LES} = \sqrt{\frac{\sum_{\bar{\alpha}_k^I > 1.10^{-10}} (\bar{\tau}_{conv}^{DNS} - \bar{\tau}_{conv}^{LES})^2}{\sum_{\bar{\alpha}_k^I > 1.10^{-10}} (\bar{\tau}_{conv}^{DNS})^2}} \quad (16.31)$$

Figures 16.8 and 16.9 present these relative errors for each model and each subgrid term. This figures highlight that ADM is the most appropriate model for all the subgrid terms whatever the grid and the phase. Figure 16.7 displays the dispersion and the slope obtained between each model and the DNS results for the convective subgrid term. ADM is the only model to present a slope close to 1 with a limited dispersion. However, for the water phase, the error level of ADM applied to the pressure subgrid term remains high. This has a limited effect since the pressure term is not predominant, as shown in the previous section. Moreover, for all the turbulence models, the error is stable when the mesh is refined.

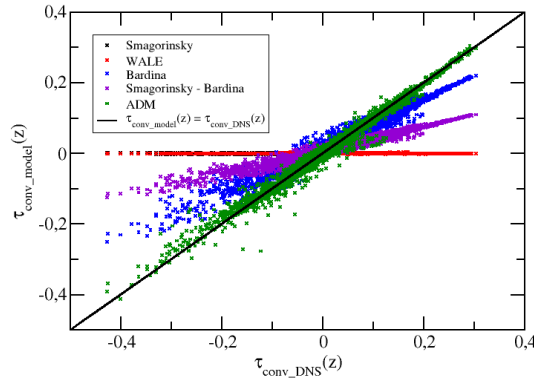


Figure 16.7: Correlation between the turbulence models and the convective subgrid terms evaluated by DNS, only the component in the z direction is considered, mesh with 128^3 cells, oil phase.

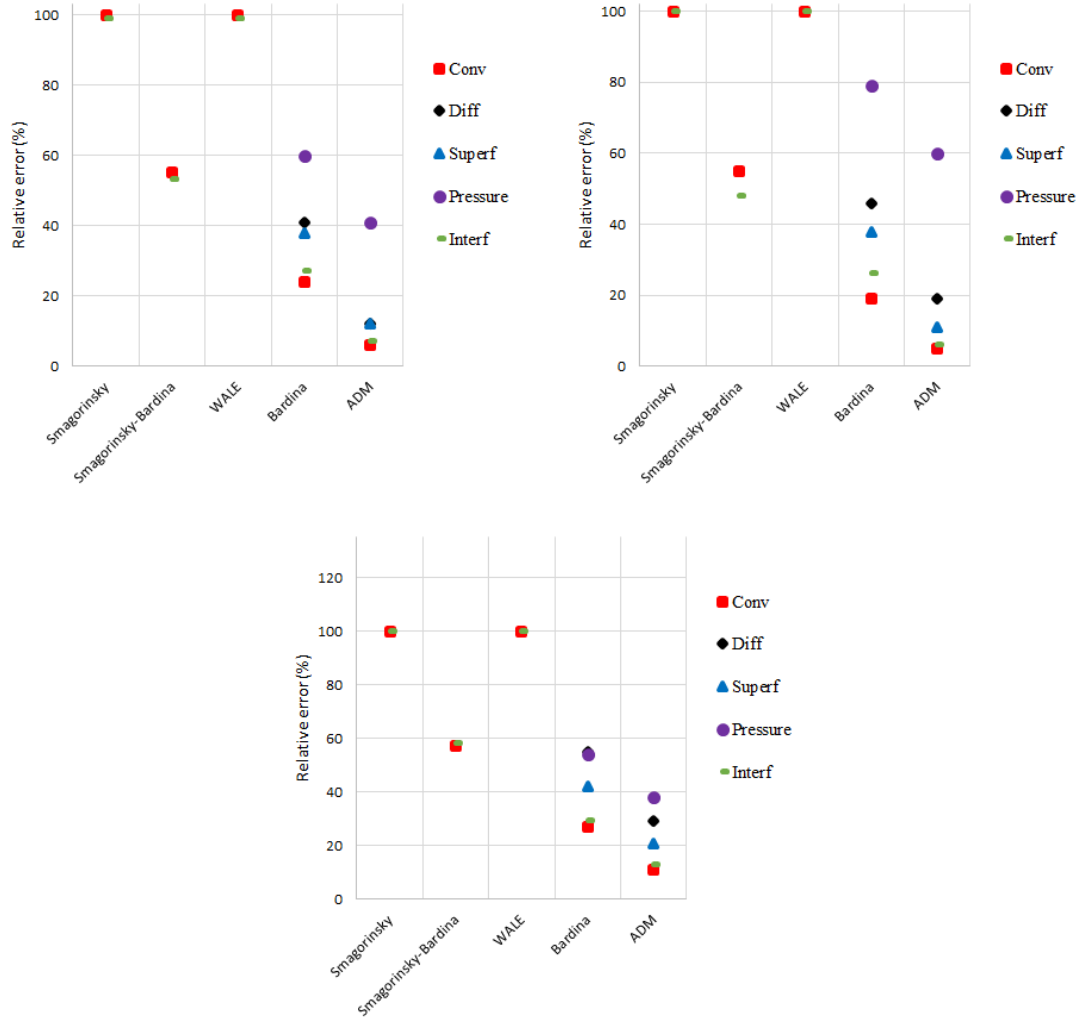


Figure 16.8: Relative error obtained by comparison between the modeled subgrid term and the terms obtained by DNS for the oil phase, the Smagorinsky's and WALE models applied to the Favre's average subgrid terms give the same results (relative error of 100 %), left to right: mesh with 128^3 cells, 256^3 cells and 512^3 cells, only the z component is displayed.

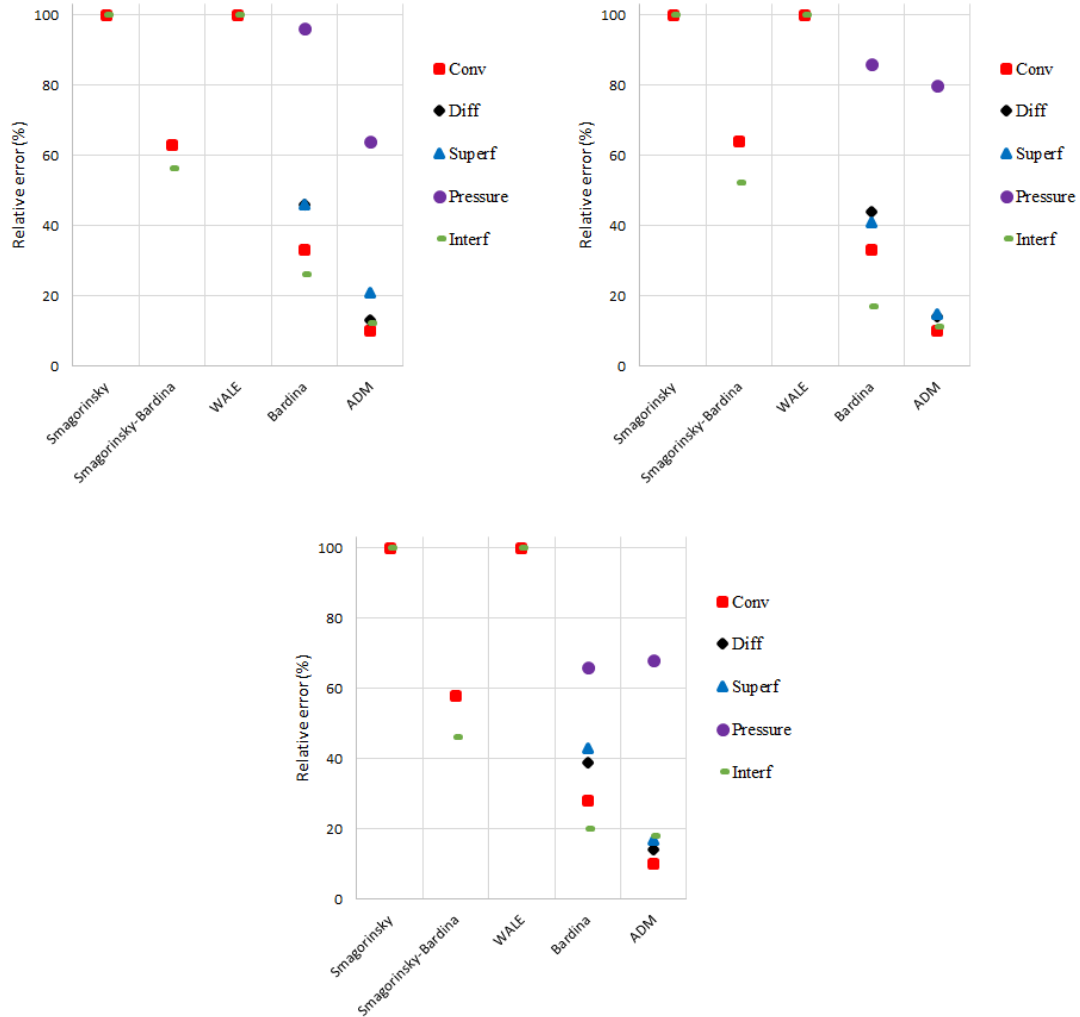


Figure 16.9: Relative error obtained by comparison between the modeled subgrid term and the terms obtained by DNS for the water phase, the error for the pressure subgrid term is always higher than 100 %, left to right: mesh with 128³ cells, 256³ cells and 512³ cells, only the z component is displayed.

16.5.2 Turbulent viscosity predicted by the turbulence models

Then, the ability of each turbulence model to reproduce the effective viscosity predicted by DNS is studied. For this purpose, the equivalent viscosity, whose expression is given in Equation (16.32), is compared with the turbulent viscosity of each model defined in Equation (16.33). The results for the Smagorinsky's model and ADM are displayed in Figure 16.10 for the most refined mesh (512³ cells). The equivalent viscosity can be negative especially close to interfaces. This observation has been previously made by Labourasse *et al.* [88]. The Smagorinsky's model is totally unable to reproduce these negative contributions but also the other variations

observed along the box height. On the contrary, a good agreement is obtained with ADM.

$$\mu_{eq} = \alpha_1 \frac{\overline{\tau}_{conv1}^{DNS} : \nabla \overline{\mathbf{u}}_1}{\underline{\underline{S}}_1 : \nabla \overline{\mathbf{u}}_1} + \alpha_2 \frac{\overline{\tau}_{conv2}^{DNS} : \nabla \overline{\mathbf{u}}_2}{\underline{\underline{S}}_2 : \nabla \overline{\mathbf{u}}_2} \quad (16.32)$$

$$\mu_{ADM} = \alpha_1 \frac{\overline{\tau}_{conv1}^{ADM} : \nabla \overline{\mathbf{u}}_1}{\underline{\underline{S}}_1 : \nabla \overline{\mathbf{u}}_1} + \alpha_2 \frac{\overline{\tau}_{conv2}^{ADM} : \nabla \overline{\mathbf{u}}_2}{\underline{\underline{S}}_2 : \nabla \overline{\mathbf{u}}_2} \quad (16.33)$$

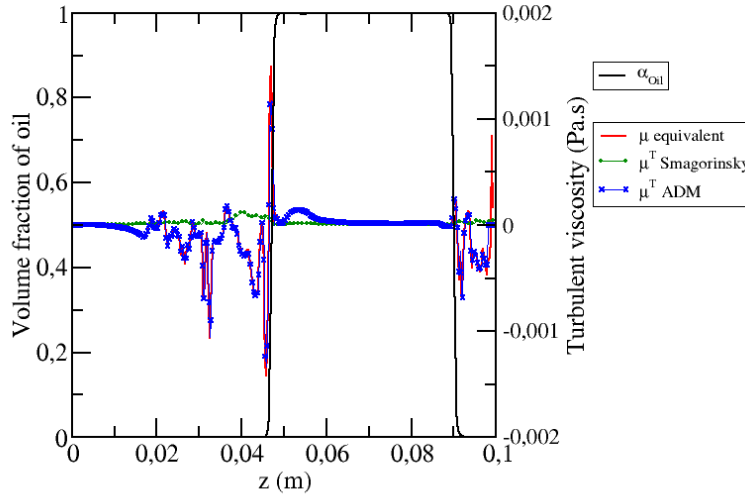


Figure 16.10: Comparison of the equivalent viscosity μ_{eq} predicted by DNS and the turbulent viscosity obtained with the Smagorinsky's model and ADM, the volume fraction of oil is also represents to locate interfaces, the viscosities are extracted from a slice of the domain at $x = y = 8$ cm, mesh with 512^3 cells.

16.5.3 Focus on the drag subgrid term τ_{drag}

No data have been given in Figures 16.8 and 16.9 for the drag subgrid term since the error is always higher than 100 %. As shown in Figure 16.11 left, this is probably due to the region splitting of the drag force expression, which induces a deviation of the modeled subgrid term at the boundaries [27, 166]. A solution to model this subgrid term could be to adapt the phase-conditioned filtering proposed by [200] for the velocity and stress tensor jump at interfaces to the regions defined in the drag force expression. To assess this assumption and to prepare the implementation of ADM in the code, a derivative expression of the drag force without region splitting is tested:

$$\mathbf{F}_{mix,1 \rightarrow 2} = \frac{1}{2} \alpha_1 \alpha_2 \left(\frac{18\mu_1}{\alpha_1 d_{pbubble}^2} + \frac{18\mu_2}{\alpha_2 d_{pdroplet}^2} \right) (\mathbf{u}_1 - \mathbf{u}_2) \quad (16.34)$$

with $d_{pbubble} = \sqrt{\frac{\mu_2}{\mu_1} \frac{\alpha_2}{\|\nabla \alpha_2\|}}$ and $d_{pdroplet} = \sqrt{\frac{\mu_2}{\mu_1} \frac{\alpha_1}{\|\nabla \alpha_1\|}}$.

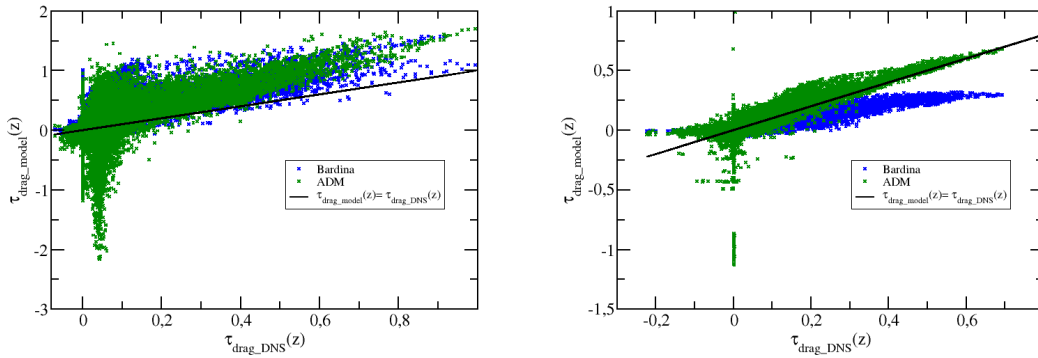


Figure 16.11: Correlation between the turbulence models and the drag subgrid term evaluated by DNS obtained, left: with a the original split version of the drag force expression in the intermediate region $0.3 \leq \alpha_2 \leq 0.7$, right: with the non splitting version defined in Equation (16.34), mesh with 128^3 cells, only the component in the z direction is considered.

This drag force is not suitable for the simulation of three fields but can be a first approximation in case of two continuous fields simulations. With this derivative expression, the error for ADM decreases from more than 100 % with the splitting version to less than 70 % with the non splitting one (see Figure 16.12). These errors are comparable to those obtained for the other subgrid terms. Finally, the dispersion and the slope of the two turbulence models (Bardina and ADM) with the non splitting version of the drag force are given in Figure 16.11. We do not see anymore the effect of the region splitting. However, some deviations are still observed close to the zero value. They seem to come from the definition of the volume fraction with ADM. Indeed, they disappear if the ADM volume fraction is replaced by the resolved volume fraction.

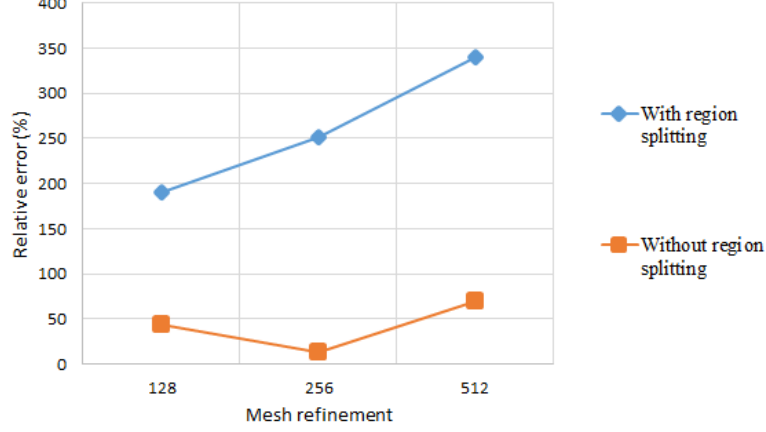


Figure 16.12: Relative error obtained for ADM with the split and non split expression of the drag force (Equation (16.34)) for the three grids, only the component in the z direction is considered.

16.5.4 Focus on the pressure subgrid term $\tau_{pressure}$

In section 2.4.2, we showed that the momentum balance equations (2.12) contained the following pressure term: $\nabla \cdot (\chi_k P_k \underline{I}_d) + P_k \underline{I}_d \cdot \mathbf{n}_k^{Int} \delta^{Int}$. This term was simplified in $\alpha_k \nabla P_k$ in the momentum balance equation (2.30). This simplification is obtained by developing $P_k \underline{I}_d \cdot \mathbf{n}_k^{Int} \delta^{Int}$ as follows:

$$\begin{aligned}
 \frac{1}{\Omega} \int_{S^{Int}} P_k \underline{I}_d \mathbf{n}_k^{Int} dS &= \langle P_k^{Int} \rangle \frac{1}{\Omega} \int_{S^{Int}} \mathbf{n}_k^{Int} dS \\
 &= - \langle P_k^{Int} \rangle \frac{1}{\Omega} \int_{\Omega} \nabla \chi_k d\Omega \\
 &= - \langle P_k^{Int} \rangle \nabla \alpha_k
 \end{aligned} \tag{16.35}$$

By taking $\langle P_k^{int} \rangle$ equal to P_k such as:

$$\begin{aligned}
 \nabla \cdot (\alpha_k P_k) - \langle P_k^{Int} \rangle \nabla \alpha_k &= \nabla \cdot (\alpha_k P_k) - P_k \nabla \alpha_k \\
 &= \alpha_k \nabla P_k
 \end{aligned} \tag{16.36}$$

which becomes $\alpha_k \nabla P$ with the assumption of a common pressure for all fields.

Other choices have been explored for $\langle P_k^{Int} \rangle$. Thus, as an example, Ndjinga *et al.* [141] proposed a different value for $\langle P_k^{Int} \rangle$, which ensures the hyperbolicity of the system, independently on the viscous terms. In these conditions, the pressure term becomes $\nabla \cdot (\alpha_k P)$. Thus, in this section, we study three different subgrid terms coming from the three possible formulations for the pressure term: $\alpha_k \nabla P$, $\nabla (\alpha_k P)$ and $\alpha_k \nabla P$:

$$\tau_{pressure}^1 = \overline{\alpha_k \nabla P} - \overline{\alpha_k} \nabla \overline{P} \tag{16.37}$$

$$\tau_{pressure}^2 = \nabla (\overline{\alpha_k P}) - \nabla (\overline{\alpha_k} \overline{P}) \quad (16.38)$$

$$\tau_{pressure}^3 = \overline{P \nabla \alpha_k} - \overline{P} \nabla \overline{\alpha_k} \quad (16.39)$$

For each subgrid term, the contribution in terms of order of magnitude and effect of the turbulence models (Bardina's model and ADM) is compared. Figure 16.13 shows that $\tau_{pressure}^1$ is smaller by a factor 10 for the coarse mesh. The two others are even higher than all the other subgrid terms of the two balance equations. Concerning the effect of the turbulence models, better results are obtained with $\tau_{pressure}^3$. Nevertheless, the error made for $\tau_{pressure}^1$ is only twice the error for the other pressure subgrid terms. In order to minimize the modeling error, it is thus better to use $\tau_{pressure}^1$ since the modeling error is only twice higher compared to the weight which is 10 times smaller in comparison with the other pressure subgrid terms. Nevertheless, when the mesh is refined, the gap between $\tau_{pressure}^1$ and the two other pressure subgrid terms tends to decrease in terms of contribution and modeling error. Thus, the choice of $\tau_{pressure}^1$ becomes less favorable for more refined grids. The same conclusions can be drawn with the Bardina's model.

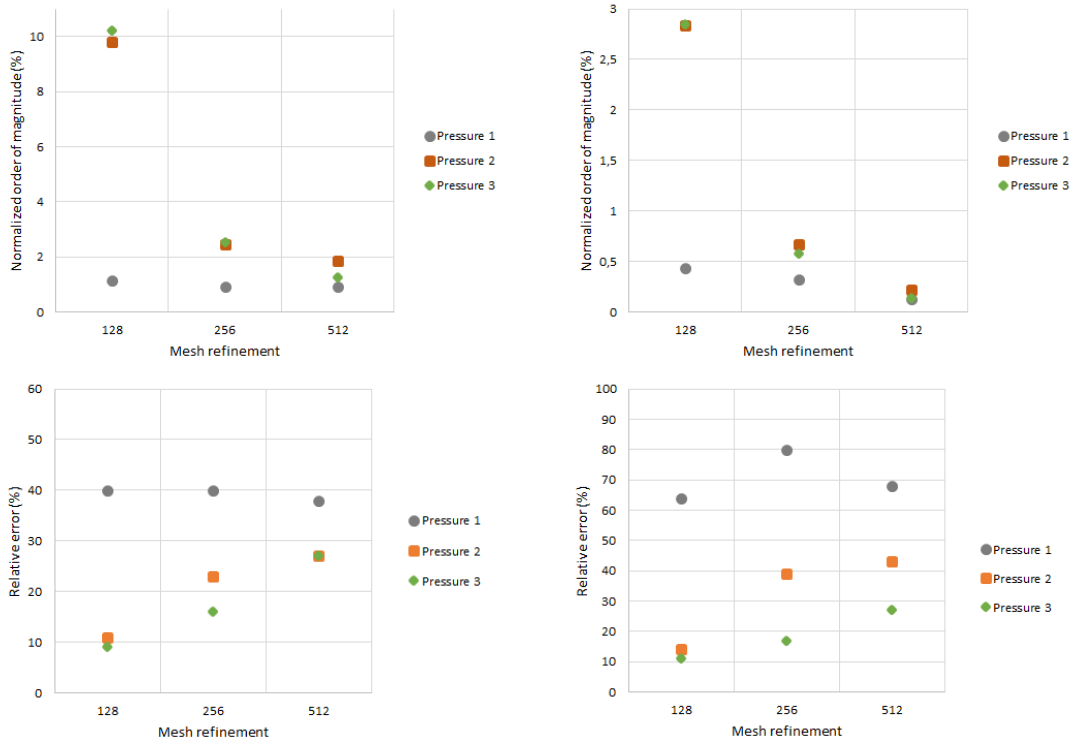


Figure 16.13: Study of the three possible subgrid terms, left column: oil phase, right column: water phase, top: relative contribution of each term, bottom: relative error of ADM, only the component in the z direction is considered.

16.5.5 Focus on the ADM order

In all these comparisons, ADM with an order of 6 has been used since it corresponds to the best results obtained with the *a priori* LES study of the test case using a single-fluid approach. However, in this section, a comparison of the relative error for the convection term and the deconvolution error on the velocity field is proposed according to the ADM order. The error for the convection term is evaluated using Equation (16.31) and the deconvolution error with:

$$\epsilon_{u_k}^{ADM} = \sqrt{\frac{\sum_{\alpha_k^I > 1.10^{-10}} (\overline{\mathbf{u}}_k^{DNS} - \overline{\mathbf{u}}_k^{ADM})^2}{\sum_{\alpha_k^I > 1.10^{-10}} (\overline{\mathbf{u}}_k^{DNS})^2}} \quad (16.40)$$

This error derives from the relaxation term $\Lambda_u (I_d - Q_N * G) * \overline{\mathbf{u}}$ with $\overline{\mathbf{u}}_k^{ADM} = Q_N * \overline{\mathbf{u}} = Q_N * G * \overline{\mathbf{u}}$. The estimation of this error gives an idea of the weight of the relaxation term without considering the coefficient Λ_u . The results are given in Figure 16.14 for the three grids. In the single-fluid formulation, when the order is increased, the accuracy increases until a plateau is reached for an order of 6. On the contrary, with the two-fluid model, if the order is increased, the accuracy is increased for small orders and decreased for larger orders. There is an optimal value. Under this value, the increase of the order improves the deconvolution of the velocity field and so the relative errors decrease. However, when the order is increased after this optimal value, the ADM approximation of the velocity includes values of the considered field in cells belonging to a far neighborhood. The flow in this neighborhood can be quite different from the cell of interest. This decorrelation has a negative effect and thus increases the deconvolution error. The optimal order is obtained when an equilibrium is reached between the positive effect of the order increase on the deconvolution approximation and the negative effect of the decorrelation of the cells in the far neighborhood. For the convection term, this optimal value is equal to 4. We can note that the conclusions are the same if we are considering another subgrid term. Concerning the deconvolution error, the best order is equal to 3 for the three grids. Finally, we see that the deconvolution error is very small compared to the ADM error of the subgrid terms (see Figure 16.8). This error decreases with the mesh refinement, which means that the more refined the mesh is, the better the velocity field is approximated by ADM whatever its order.

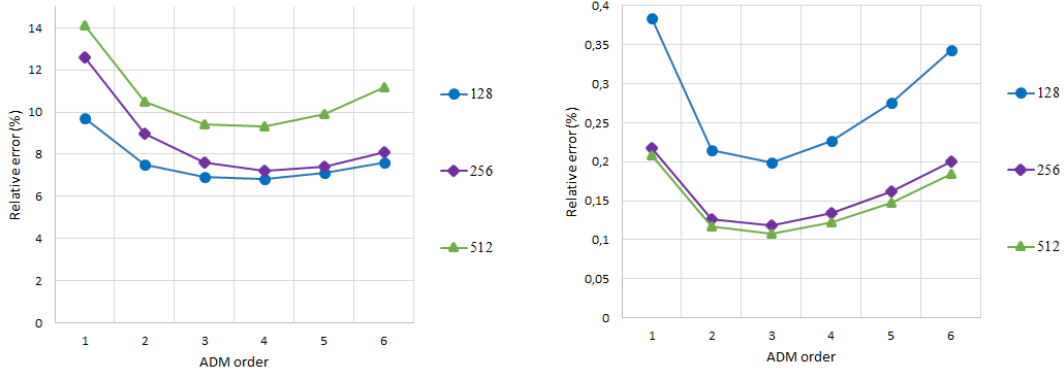


Figure 16.14: Relative error of the convection subgrid term (left) and the predicted velocity field (right) according to the ADM order for the three grids and the oil phase.

16.5.6 Effect of the filter

In this section, an analysis of the filter choice is proposed. The previous box filter is compared to a Gaussian filter. Figure 16.15 displays a comparison of the subgrid term weight according to the filter. Table 16.6 classifies the term according to their contribution with the Gaussian filter and has to be compared to Table 16.5. The weight of the subgrid terms τ_{superf} , τ_{conv} and τ_{diff} decreases with the Gaussian filter whereas it increases for τ_{interf} and $\tau_{pressure}$. The classification of the subgrid terms is affected by this evolution especially for the oil phase. However, with the Favre’s averaging, no changes are observed.

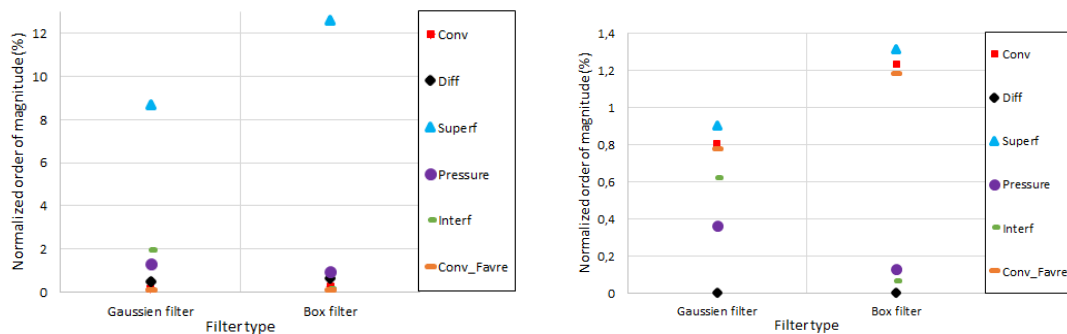


Figure 16.15: Order of magnitude of the normalized subgrid terms obtained with the box and the Gaussian filter, left: for the oil phase, right: for the water phase, only the z component is displayed, mesh with 512^3 cells.

	Simple filtering		Favre's averaging	
	Oil	Water	Oil	Water
1	τ_{superf}	τ_{superf}	τ_{superf}	τ_{superf}
2	τ_{interf}	τ_{conv}	$\tau_{pressure}$	τ_{conv}
3	$\tau_{pressure}$	τ_{interf}	τ_{conv}	$\tau_{pressure}$
4	τ_{diff}	$\tau_{pressure}$		
5	τ_{conv}	τ_{diff}		

Table 16.6: Classification of the subgrid terms according to their relative contribution for the 512^3 grid with the Gaussian filter.

Then, the turbulence models are compared with the two filters, see Figure 16.16 for the oil phase. The same results are obtained with the water phase. The filter has no effect on the Smagorinsky's and WALE models. These results were expected since these models are not strongly linked to the filter choice contrary to the Bardina's model and ADM. For these two models, the relative error decrease when the Gaussian filter is applied except for the pressure subgrid term. Once again, the results are in agreement with the expectations. Indeed, with the box filter, whatever the distance between the two cells, the same weight is given to all of them. However, with the Gaussian filter, the farther the cells are from the cell of interest, the smallest their contributions are. This approach seems better since the flow far from the cell of interest can be different enough to induce deconvolution errors and modeling inaccuracies.

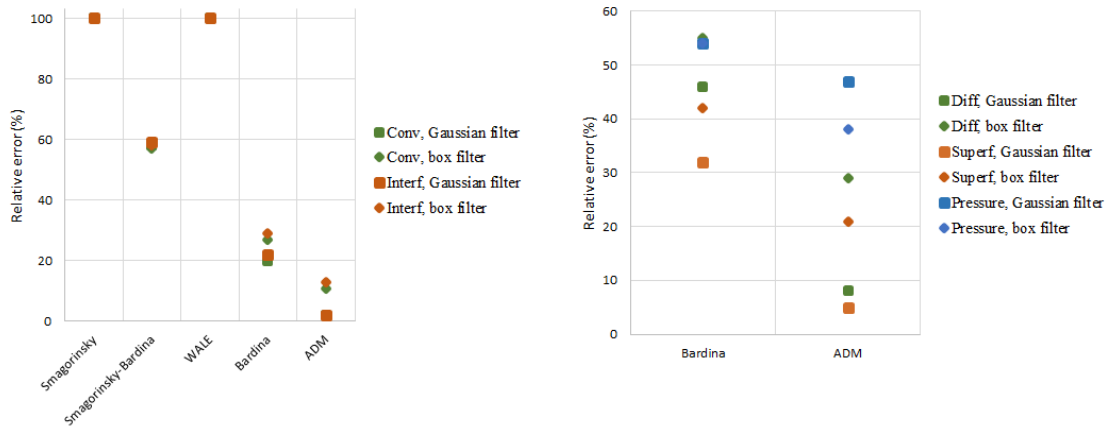


Figure 16.16: Relative error obtained by comparison between the modeled subgrid term and the terms obtained by DNS with the box and the Gaussian filters, for the oil phase with the 512^3 grid, only the z component is displayed.

16.6 Conclusion

The equations filtering highlighted new subgrid terms compared to the one-fluid model. These terms are specific to the simulation of large interfaces with the two-fluid model. Non negligible orders of magnitude have been obtained for these extra terms. The high subgrid contribution of the surface tension term has been confirmed with our approach. To finish, different turbulence models have been applied and compared. The best correlation with the DNS results has been obtained with ADM for all the subgrid terms. This result is very interesting since, contrary to functional models, ADM can theoretically be applied to all the subgrid terms.

In what follows, ADM will be assessed on different test cases. According to the results presented in this chapter, the order will be fixed at 3 and a Gaussian filter will be applied.

Chapter 17

True LES: implementation of the Approximate Deconvolution Model (ADM)

In the previous chapter, LES studies have been performed using filtered DNS. The results obtained with ADM were encouraging. Moreover, the standard models validated in Chapter 15 seemed not suitable for the simulation of the phase inversion benchmark. Thus, here, ADM is implemented and true LES with this model is presented. In the first section, the fully developed turbulent channel flow is simulated to validate the implementation of ADM. Then, preliminary LES are performed on two-phase flows with the METERO test case considering three fields. To finish, exploratory ADM simulations are performed on a two-phase two continuous fields flow. This chapter has been presented at the 7th International Symposium on Advances in Computational Heat Transfer (CHT-17, 28 May - 2 June 2017) [51].

The flows are all isothermal.

17.1 Résumé du chapitre

L'analyse *a priori* réalisée dans le chapitre précédent a permis de mettre en évidence que les modèles de type structuraux donnaient de meilleurs résultats que les modèles fonctionnels. Dans ce chapitre, le modèle ADM est donc implémenté. Une première validation est proposée en monophasique avec le cas de la turbulence pleinement développée en canal. Dans un second temps, la validation est étendue à une simulation diphasique en ne considérant que des champs continus. Une fois de plus, les écoulements sont isothermes.

17.2 Validation of the implementation on a single-phase flow

The fully developed turbulent channel flow is simulated (see chapter 15) to assess the implementation of ADM on a single-phase flow. Only the convective subgrid term is modeled since it is the only remaining subgrid term in the two-fluid model equations with only one phase. According to the results obtained in Chapter 16, its order is fixed at 3, the Gaussian filter is used and the ADM order is decreased close to walls. The ADM results are compared to the results obtained with the Smagorinsky’s model using the dynamic procedure. The simulations are performed with the more refined grid in the three directions, that is to say Grid 2 (see Table 15.1). The time step is constant, equal to 0.1 *ms*. Table 17.1 compares the bulk mean velocity and the wall shear velocity predicted by the three models. The bulk mean velocity is equal for the two models thanks to the dynamic procedure used to vary the mean pressure gradient. However, the wall shear velocity is less accurate with ADM.

	$u_{deb} (m.s^{-1})$	$u_{\tau} (m.s^{-1})$
Smagorinsky	19.65 (2.0 %)	0.89 (11 %)
ADM	19.65 (2.0 %)	0.83 (17 %)

Table 17.1: Computed bulk mean velocity and wall shear velocity for the two turbulence models, the relative error based on the experimental data are given in brackets, Grid 2.

Then, the profiles of $\langle u^r \rangle$, $\langle U'U' \rangle$, $\langle U'V' \rangle$ and $\langle V'V' \rangle$ are compared with the experimental data [144]. Figure 17.1 displays the profile of the average resolved velocity. In the left picture, the error made on the prediction of the wall shear velocity is visible. The Smagorinsky’s model is closer to the experimental data. Nevertheless, in the right picture, the curves are very similar since the bulk mean velocity predicted by the models are equal. Finally, Figure 17.2 presents the fluctuating velocities normalized by the computed bulk mean velocity. The same trends are observed for the two models. The profile of $\langle U'U' \rangle$ is overestimated and the profiles of $\langle U'V' \rangle$ and $\langle V'V' \rangle$ are underestimated. ADM predicts better $\langle U'U' \rangle$ but the peak is shifted to higher y^+ values. On the contrary, ADM is less accurate on the prediction of $\langle U'V' \rangle$ and $\langle V'V' \rangle$. Thus, the turbulent kinetic energy is better predicted by ADM. However, Gullbrand and Chow [62] achieved to obtain better results with ADM compared to the Smagorinsky’s model on the fully developed turbulent channel flows. Their time scheme was at least 2nd order and ADM at least 5th order. Moreover, the top hat filter was obtained by trapezoidal rule integration (see Equation (14.58) in section 14.5).

Finally, the average turbulent viscosity obtained with the two models is compared in Figure 17.3. The average is done over 100 *s* as previously done for the other quantities. For ADM, the turbulent viscosity is reconstructed using Equation

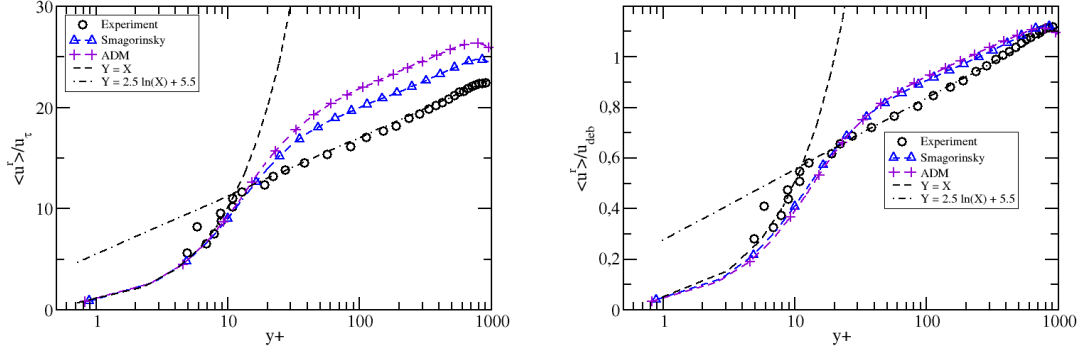


Figure 17.1: Comparison of the profiles of $\langle u^r \rangle$ with the experimental data [144] and two different LES models: Smagorinsky's model (blue curve with triangles) and ADM (purple curve with crosses), left: normalization by the computed wall shear velocity, right: by the computed bulk mean velocity, Grid 2.

(16.33). As also observed in the *a priori* LES study, the turbulent viscosity is higher with ADM and is negative in some regions. Concerning the turbulent viscosity levels for the Smagorinsky's model, similar results have been obtained in [135].

The implementation of ADM has been done at the end of the PhD according to the results obtained in the *a priori* LES study for a two-phase flow (see Chapter 16). The objective was to be able to perform LES for two-phase flows. Thus, the choice of the filter and ADM order has been done with respect to this criterion. The results obtained here on the fully developed turbulent channel flow should be improved by comparing different filters and ADM orders and increasing the time scheme order. Moreover, the modeling strategy for the relaxation term and the wall treatment has not been studied. Different modeling approaches have been considered in the literature (see section 14.3.2.2). However, the best combination obtained for the simulation of this test case (in terms of filter choice, ADM order, relaxation term modeling and wall treatment) could be not suitable for the simulation of two-phase flows. Since the thesis is focused on two-phase flows, the analysis has not been performed.

Nevertheless, this first analysis on a single-phase flow allows validating the implementation of ADM in the code NEPTUNE_CFD. In the next section, preliminary results are shown on two-phase flows.

CHAPTER 17. TRUE LES: IMPLEMENTATION OF THE APPROXIMATE DECONVOLUTION MODEL (ADM)

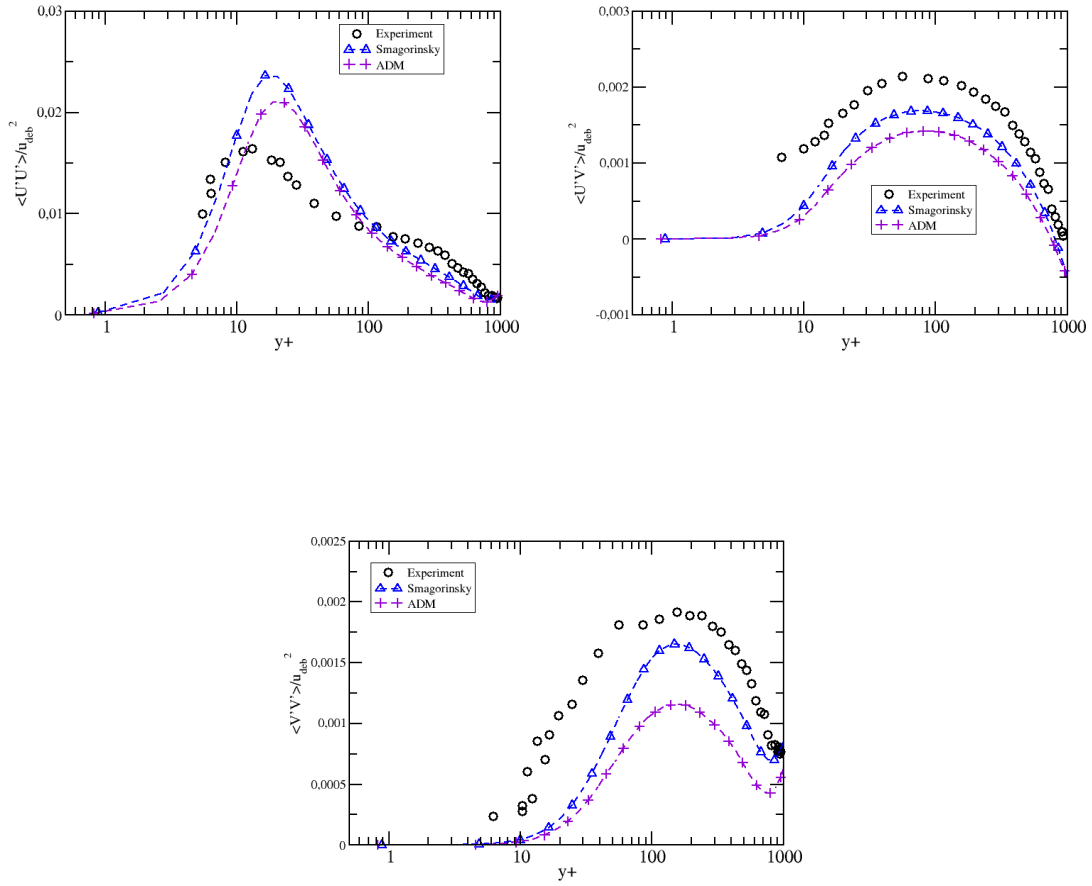


Figure 17.2: Comparison of the profiles of $\langle U'U' \rangle$, $\langle U'V' \rangle$ and $\langle V'V' \rangle$ with the experimental data [144] with two different LES models: Smagorinsky's model (blue curve with triangles) and ADM (purple curve with crosses), all the quantities are normalized by the computed bulk mean velocity, Grid 2.

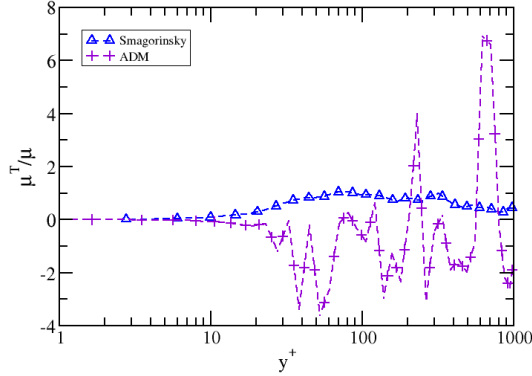


Figure 17.3: Instantaneous turbulent viscosity profile along the y direction obtained in the center of the domain (in x and z directions), Smagorinsky's model (blue curve with triangles) and ADM (purple curve with crosses), Grid 2.

17.3 To two-phase flow simulations with LES

In the previous studies, the METERO test cases have been simulated using RANS approaches. Here, the same simulations are performed using the WALE model with a wall law (see Equation (15.6) in section 15.2.2) on the intermediate grid. The use of a wall law is necessary since the first cell is located in the inertial layer (see section 15.2.2 for the definition of the inertial layer). Table 17.2 presents the value of the first cell position in wall coordinates and in the liquid phase obtained with the RANS simulations and the intermediate mesh.

Flow regimes	y^+
Dispersed bubble flow	234
Plug flow	146
Slug flow	167

Table 17.2: Position of the first cell of the intermediate mesh in wall coordinates in the liquid phase according to the flow regime, the maximum value along the tube is taken, METERO test case.

The air superficial velocity at the injection is fixed at 0.127 m.s^{-1} . Three liquid superficial velocities are simulated 4.42 m.s^{-1} , 2.65 m.s^{-1} and 1.59 m.s^{-1} corresponding respectively to a stratified bubble flow, plug flow and slug flow. The time steps are given in Table 17.3. For these three simulations, the multifield approach is used. Thus, the small spherical bubbles are treated using the dispersed model. It

has to be noted that the dispersion force is only available in RANS. Thus, it is only activated in the RANS simulations. The LBMo is activated for the large deformable bubbles. Three fields are defined: a continuous liquid field, a continuous gas field and a dispersed gas field. Isothermal transfer (breakup and coalescence) between the two gaseous fields are allowed. They are modeled using the initial isothermal mass transfer term (see section 3.6). Indeed, the term improvement proposed in Chapter 11 and based on the shape of the dispersed field cannot be used in LES since the model which calculates the inclusions diameter by solving an interfacial area equation is only available in RANS approaches. In LES, the dispersed bubble diameter is considered constant during the whole simulation. One can also note that the gravitational test case with $J_L = 5.31 \text{ m.s}^{-1}$ is not simulated with LES. Indeed, this test case is purely dispersed. No continuous gas field appears (see section 11.3). Thus, it is greatly affected by the deactivation of the dispersion force which is only available in RANS.

Flow regime	RANS	WALE
Dispersed bubble flow	0.5 ms	0.5 ms
Plug flow	0.25 ms	0.2 ms
Slug flow	0.12 ms	0.12 ms

Table 17.3: Time steps according to the flow regime and the turbulence model for the METERO test case with the intermediate grid.

In all the simulations (RANS and LES), turbulence models are only applied to the liquid field. Figure 17.4 proposes a quantitative comparison of the WALE model and the RANS approach. The prediction of the liquid velocity and the void fraction are improved by the use of a LES model. This result was expected since the RANS approach is based on an ensemble average description of turbulence effects. In flows containing only small spherical bubbles treated with a dispersed approach, this turbulence modeling is suitable. However, when large interfaces are resolved, the deterministic description intrinsically brought by LES is more appropriate.

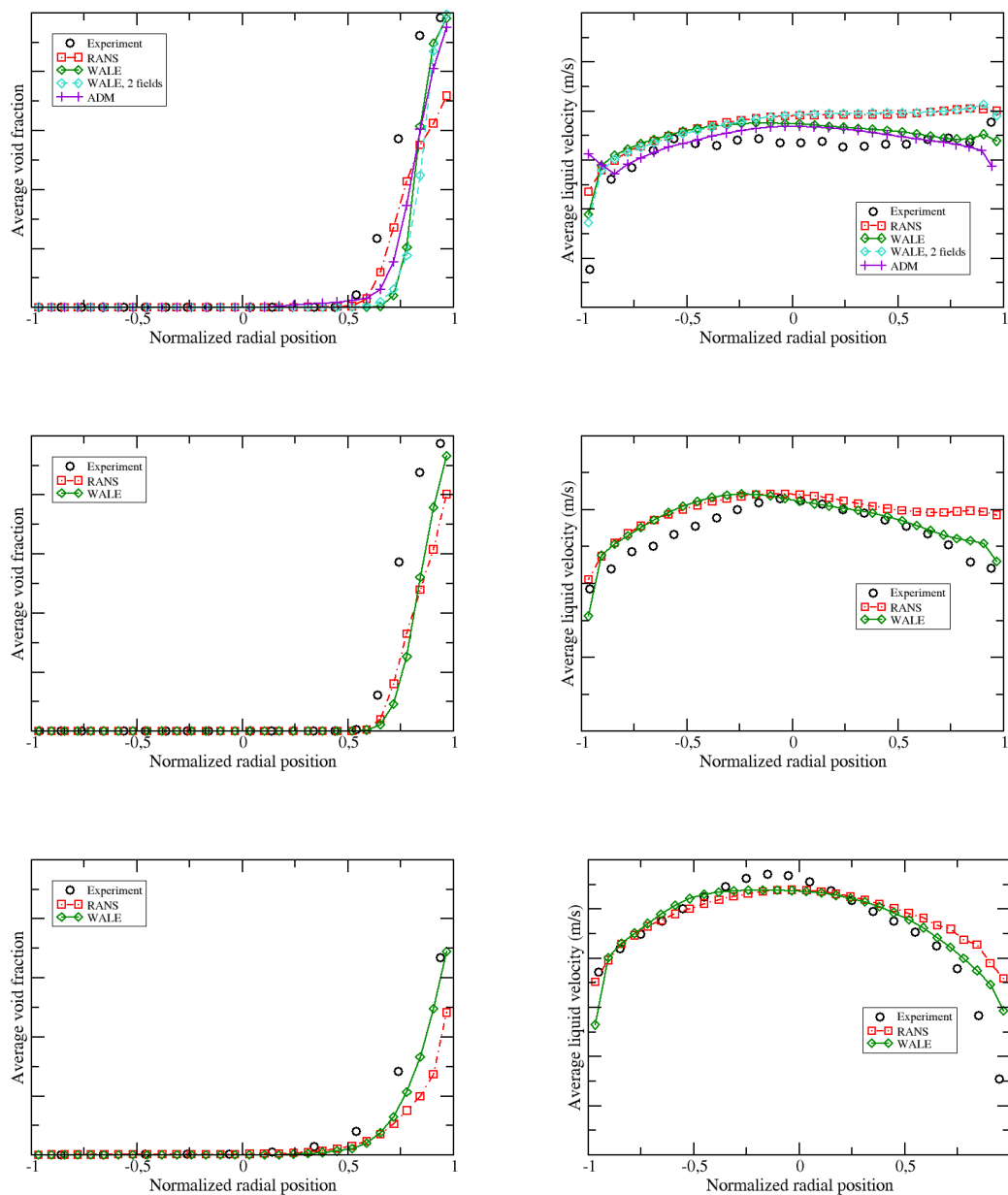


Figure 17.4: Average void fraction and average liquid velocity at $X = 40D$, top to bottom: slug flow ($J_L = 1.59 \text{ m.s}^{-1}$), plug flow ($J_L = 2.65 \text{ m.s}^{-1}$) and stratified bubble flow ($J_L = 4.42 \text{ m.s}^{-1}$), $J_G = 0.127 \text{ m.s}^{-1}$, intermediate grid.

17.4 ADM implementation for two-phase flows

Then, ADM is tested on the METERO test case. The implementation of ADM requires to make different choices which are specific or not to the two-fluid model. The choices have been made using the results obtained in the *a priori* LES study per-

formed in Chapter 16 and other works available in the literature. Before presenting the results of the simulation, the modeling choices are explained:

- **Filter choice:** Gaussian filters appear to give better results in the *a priori* LES study (see section 16.5.6). In the METERO test case, the grid cells are not perfectly cubic. Thus, a Gaussian filter is more suitable.
- **ADM order:** An order of 3 is chosen according to the results of the *a priori* LES study (see section 16.5.5).
- **Relaxation term:** Simulation with and without modeling of the relaxation term are performed and compared further. Only the Smagorinsky’s model with the dynamic procedure is chosen to model the relaxation term, in agreement with other works [31, 58, 62, 63, 81, 121]. Other models should be investigated (see section 14.3.2.2).
- **Wall treatment:** The ADM order is decreased close to walls. The use of a wall law is also investigated since the first cell of the mesh is located in the inertial region (see Table 17.2). These choices have also been made by Borggaard and Iliescu [18] and Chow *et al.* [31].

All these previous choices are necessary even for single-phase flows. However, the choices that follow are specific to two-phase flows with large interfaces treated with the two-fluid model and the LBMo.

- **Filtered velocity:** In the two-fluid model, the velocity of a field k is defined in the whole domain even if in one cell the field k is not present ($\alpha_k^I = 0$). In such cells, the value of the velocity of field k has no meaning and can be criticized. Thus, the following expression of the velocity is used for the filtering process:

$$\overline{\mathbf{u}}_k = \frac{\overline{\alpha}_k \overline{\mathbf{u}}_k}{\max(\overline{\alpha}_k, 1.10^{-4})} \quad (17.1)$$

With this expression, the smaller the volume fraction is, the smallest the velocity weight is in the filtering process. Other choices can be made, such as truncated filters. However, the filters must have specific properties especially over discontinuities [166].

- **Reconstructed volume fractions:** The ADM procedure does not ensure that α_k^{ADM} is between zero and one. However, $\sum_k \alpha_k^{ADM}$ is still equal to 1 in all the cells. This induces difficulties especially for the implementation of τ_{superf} . Thus, two ways are considered to fix this issue. In a first approach, α_k can be considered as a DNS quantity. In this case, it does not need to be reconstructed with the ADM procedure. The only remaining subgrid term is then the convective subgrid term. The second idea is to reconstruct α_k

and to correct the values such that the reconstructed volume fraction α_k^{ADM} is between 0 and 1. Once again, different methods can be chosen: conserving the ratio, clipping the value under 0 and larger than 1, etc... We have chosen to multiply by -1 the negative value of α_k . If α_1 is negative, its value is multiplied by -1 and α_2 is reajusted such that $\alpha_1 + \alpha_2 = 1$. This point is a major uncertainty in our implementation of ADM that would require further considerations.

- **Model for $\tau_{interface}$:** This subgrid term appears in the mass balance equation. The modeled subgrid term has to be consistent with mass conservation obtained with the resolved volume fractions. Nevertheless, this term corresponds to a transfer between the resolved volume fractions and the subgrid volume fractions. This transfer depends on the phase. Thus, mass conservation is not ensured since, by nature, $\tau_{interface}^1 + \tau_{interface}^2$ is not equal to 0. The volume fraction variation of phase 1 induced by the subgrid term is not necessarily compensated by the volume fraction variation of phase 2. The only possible way is to consider a mass conservation based on the deconvoluted volume fractions. However, due to the unavoidable deconvolution errors and the limited weight of this subgrid term (see section 16.4), this solution is not retained. The subgrid term is not computed and considered negligible.
- **Model for τ_{Drag} , $\tau_{pressure}$ and τ_{time} :** Trials were done to implement these terms. However, at some particular points, extreme values were obtained. Therefore, these terms are not computed for this work.

To validate this implementation, the slug flow test case ($J_L = 1.59 \text{ m.s}^{-1}$ and $J_G = 0.127 \text{ m.s}^{-1}$) is simulated. This test case is mainly composed by large interfaces. Thus, for the first two-phase flow simulations with ADM, only two continuous fields are considered. A first study is performed to evaluate the effect of considering two continuous fields and neglecting the dispersed gas field. The same simulation performed with the WALE model and the wall law in the previous section is done. However, only two continuous fields are defined: the continuous liquid field and the continuous gas field. The time step is equal to 0.25 ms . This simulation has to be compared to the same previously done with three fields. In Figure 17.4, we clearly observe a difference especially on the liquid velocity. To reduce this error, we should have used a stratified flow regime with a smaller liquid velocity (see Figure 11.2). However, no experimental data (void fraction and velocity profiles) were available with such speed injections.

After evaluating the error done by considering only continuous fields, ADM and different modeling choices are compared. ADM is activated only in the liquid phase, as previously done in RANS and WALE. The time step is equal to 0.05 ms . First, the simulation is performed by considering the volume fraction as a DNS value such that it is not reconstructed by the ADM process. Only the convective subgrid term remains. The relaxation term is not modeled and no wall law is used. The results, displayed in Figure 17.4 and repeated in Figure 17.5 are encouraging. Indeed, they are not so far from the experimental data.

Then, the Smagorinsky's model with a dynamic procedure is activated to model the relaxation term (see section 14.3.2.2). Two simulations are compared: with and without the Smagorinsky's model. In both cases, only the convective subgrid is modeled with ADM, the volume fraction being considered as a DNS quantity. Figure 17.5 highlights that the improvement is limited. Indeed, the liquid velocity profile seems better predicted whereas it is the opposite with the void fraction profile.

Now, the volume fraction is reconstructed. Seven subgrid terms have to be modeled. However, as previously explained, τ_{interf} , τ_{Drag} , $\tau_{pressure}$ and τ_{time} are not modeled in a first approach. Thus, only three subgrid terms remain: τ_{conv} , τ_{diff} and τ_{superf} . Preliminary results are obtained in Figure 17.5. This time, an improvement is observed if we compare with the simulation considering only the convective subgrid term. Thus, the modeling of the convective subgrid term seems not sufficient. This result was expected since the *a priori* LES study highlighted that the convective subgrid term was not the predominant term.

Finally, a wall law is added since the first cell of the mesh is located in the inertial region (see Table 17.2). Figure 17.5 shows that the addition of a wall law induces a deterioration of the results whatever the combinations.

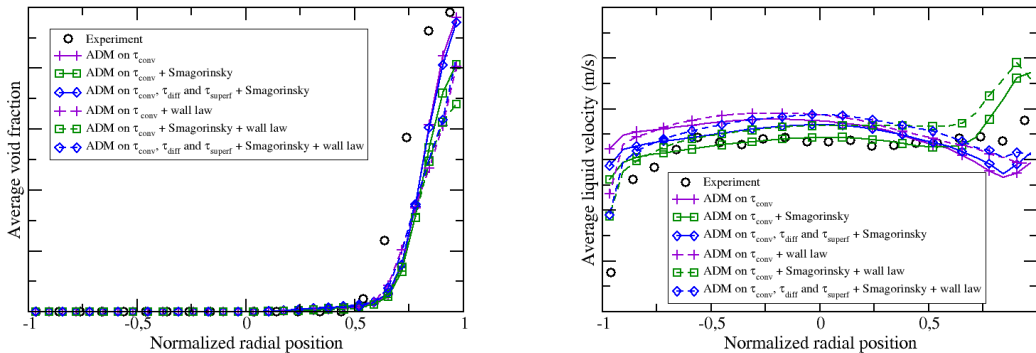


Figure 17.5: Average void fraction and average liquid velocity at $X = 40D$, slug flow ($J_L = 1.59 \text{ m.s}^{-1}$ and $J_G = 0.127 \text{ m.s}^{-1}$) computed with two continuous fields, intermediate grid.

17.5 Conclusion

This chapter showed preliminary results of LES simulations using ADM. The single-phase flow test case was used to have a first validation of the implementation. However, extensive studies should be performed to compare different filters and ADM orders and to assess the relaxation term modeling and the wall treatment. This could improve the results. Then, the METERO test case was simulated. LES using the WALE model gave encouraging results whatever the flow regime. Since ADM has never been implemented with two-fluid models, first simulations have been performed with the slug flow considering only two continuous fields. The results were encouraging and allow drawing some conclusions. As expected, it seemed better to

simulate all the subgrid models instead of considering only the convective subgrid term. We showed also that the results were improved by modeling the relaxation term. However, the use of a wall law affected badly the results. These simulations have to be considered as preliminary results since the study is not exhaustive according to all the choices that have been made. It gives some general trends that should be more investigated. As proposed for the single-phase flow test case, for each subgrid term, the ADM order should be assessed. Different filters should be compared. The wall treatment and the relaxation term modeling should be also studied. Finally, concerning the issues specific to the two-fluid model which are the filtered velocity and the volume fractions, only one combination has been tested. However, other solutions could be considered.

Chapter 18

Conclusion

After studying theoretically the properties of turbulent flows and presenting the different modeling strategies in the first two chapters, LES has been retained as the most suitable model for two-phase flow simulations using the multifield approach. Indeed, LES is based on a deterministic description of turbulent effects such as the large interface treatment in the LBMo. Since no LES models were available in the code NEPTUNE_CFD, the first step was the implementation of standard models and their validation on a single-phase flow test case. The simulations highlighted the ability of the code to perform LES. Reasonable agreements were obtained with the experimental data. The same level of accuracy have been reported in the literature for such turbulence models [112, 135]. Then, an *a priori* LES study has been proposed on a two-phase flow to have a first idea of the subgrid terms appearing in the two-fluid model equations with the LBMo and the best modeling strategy. This analysis showed that two extra subgrid terms appear in the equations and are specific to the LBMo, conducting to a total of seven subgrid terms. With the Favre's averaging, this number was decreased: only four terms remain. As also observed with one-fluid models, the weight of each term highlighted that the surface tension subgrid term was predominant. However, the diffusive subgrid term was not negligible. The comparison of turbulence models finally demonstrated that structural models and especially ADM were the most suitable models for all the subgrid terms appearing in the filtered equations. Nevertheless, these models cannot be applied to Favre's average quantities. Thus, all the terms have to be modeled. According to these results, preliminary simulations were performed with ADM on single and two-phase flows. Different modeling choices had to be done to implement ADM. They have been made using the results on the *a priori* LES study and works available in the literature. The results on the fully developed turbulent channel flows did not allow reaching the accuracy observed in the literature. Indeed, the filter and ADM order have been fixed by taking into account results obtained in the *a priori* LES study performed on a two-phase flow which does not have the same properties as single-phase flows. Thus, extensive studies should be performed to compare different filters and ADM orders and to assess the relaxation term modeling and the wall treatment, which has not been done in this chapter but should improve the results.

Then, the first two-phase flow simulations with ADM have been performed. Encouraging results were obtained that to our knowledge, are the first real LES brought with a multifield approach. However, if for the single-phase flow, different modeling choices are available, for two-phase flows especially with a two-fluid approach, the number of available possibilities is larger. Thus, different studies should be done. First, the main difficulties of the two-fluid model which are the velocity filtering and the ADM reconstruction of the volume fractions should be extensively studied. Then, for each subgrid term, the filter and ADM order should be assessed because there is no apparent reason that the same filter and ADM order are suitable for all the subgrid terms. After optimizing these two parameters, the wall treatment and the relaxation term modeling should be also explored.

Part IV

Industrial application

In the previous parts of this report, the different steps to perform simulations of turbulent non isothermal two-phase flows with a multifield approach based on a two-fluid model have been validated on various test cases, from elementary validations to experimental studies. However, few simulations have been performed in industrial configurations. Thus, the multifield approach has been applied to predict flow regimes in horizontal tubes, which is a crucial point to prevent tube breaking in steam generators and to improve their lifetime. Nevertheless, in these simulations, flows have been considered isothermal, which is not the case industrially. At this time in the thesis work, non isothermal simulations have not been performed with three fields including a dispersed one. Thus, in this part, the multifield approach is used to simulate more complex flows evolving in industrial geometries and characterized by multiple phenomena. All the flows considered in this part are then simulated with three fields: a continuous liquid field, a dispersed gas field and a continuous gas field. The LBMo strategy in its optimized version is used to simulate large interfaces. Mass transfers are considered between the two gas fields. Transfer for phase change developed in Chapter 9 are applied to the two continuous fields. The flows are incompressible, non isothermal and turbulent.

Chapter 19

ULPU-V experiment

The industrial application presented in this chapter corresponds to the ULPU experiment [39, 192]. The experiment has been performed at the University of California Santa Barbara. The objective is to assess coolability limits with an In-Vessel Retention (IVR) strategy. In case of severe accident, the IVR consists in flooding the reactor cavity with water to ensure an efficient cooling of the reactor vessel and then to prevent failures. The critical point is the understanding of heat removal at the vessel wall. The thermal loading has to remain under the local Critical Heat Flux (CHF) to ensure an efficient wall cooling. In the first section, the experiment is described. Then, the different steps required to perform a full multifield simulation are detailed.

19.1 Résumé du chapitre

Dans les précédentes parties de ce rapport, les différentes étapes pour simuler des écoulements anisothermes avec l'approche multi-champ et le modèle bi-fluide ont été validées avec un certain nombre de cas tests depuis les cas de vérification jusqu'aux études expérimentales. Cependant, très peu de simulations ont été réalisées dans des configurations industrielles. On peut citer l'exemple du cas METERO qui permet de valider la capacité du code à prédire des régimes d'écoulement dans un tube horizontal, ce qui constitue un point important pour anticiper la détérioration des tubes en U dans les générateurs de vapeur et donc d'améliorer leur durée de vie. Néanmoins, dans cette expérience, l'écoulement est anisotherme et donc peu représentatif de la réalité des écoulements dans les centrales nucléaires. Dans tout ce qui précède donc, aucune simulation anisotherme n'a été réalisée en considérant trois champs. L'objectif de ce chapitre est donc de simuler un écoulement turbulent anisotherme avec les termes de transferts implémentés et validés dans les précédentes parties en considérant trois champs: un champ continu liquide, un champ dispersé gaz et un champ continu gaz dans une géométrie industrielle. Pour ce faire, l'expérience ULPU est simulée. Cette expérience a pour objectif d'évaluer la capacité de refroidissement d'un réacteur nucléaire en cas d'accident grave.

19.2 Description of the experiment

A schematic view of the experimental setting is proposed in Figure 19.1. Different baffle configurations have been tested. In the simulation, only the third one with a diameter at the upper-most point equal to 152 mm and at the lowest point equal to 76 mm (see Figure 19.2) is considered. On the top of the baffle, a riser of glass with a diameter equal to 152 mm is used to simulate the full length of the reactor vessel, corresponding to the hot leg. In the cold leg, saturated water flows from the condenser into the downcomer.

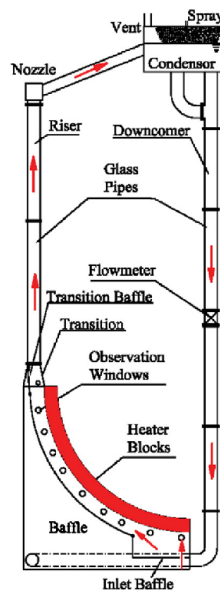


Figure 19.1: Schematic view of the ULPU-2400 facility [79].

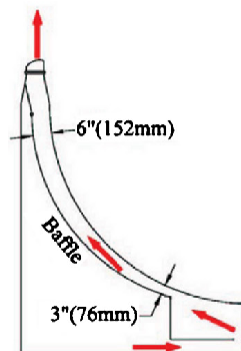


Figure 19.2: Schematic view of the baffle dimensions considered for the simulation of the ULPU experiment [79].

19.3 Simulation set up

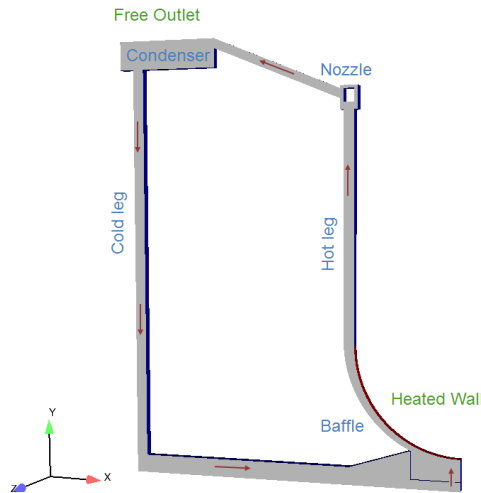


Figure 19.3: Schematic view of the computational domain with the main boundary conditions, the red arrows symbolize the flow direction.

The computational domain is presented in Figure 19.3. The whole domain is 6.23 m high (maximum height) and 5 m long (maximum length) and contains 97068 cells. The cold leg is located to the left and the hot leg to the right (reversed from the experiment). The grid is two-dimensional. Jamet *et al.* [79] studied the effect of this choice compared to a 3D grid. They showed that the results were qualitatively and quantitatively identical except a slight reduction of the velocity in the downcomer. The condenser is modeled by a free outlet at atmospheric pressure. In front of and behind, symmetrical boundary conditions are imposed. For the other boundary conditions, isothermal walls are considered (except the heated wall displayed in Figure 19.3). In a first approach, the reactor vessel is simulated using a heat flux profile along the heater block (see Figure 19.4). The angle θ is the angular position from the lower part of the baffle, meaning that the top of the heated wall is close to 90° . The maximum heat flux applied at the top of the baffle is equal to $1.61 \cdot 10^6\text{ W}\cdot\text{m}^{-2}$. The heat flux profile is established progressively until 1 s where the maximum heat flux is obtained at the top of the heated wall. The simulation is performed at atmospheric pressure. Gravity is considered. The loop contains water. The properties of the liquid water and steam are updated at each time step (see Figure 9.1 right) using the standard set of thermodynamic Equations Of State based on CATHARE functions [44]. An adaptative time step is applied with a maximum CFL number equal to 1.

Different phenomena appear in this flow configuration. First, nucleate boiling occurs at the heated wall. Dispersed bubbles are created in the baffle. In sub-saturated water, corresponding to high pressure regions, bubbles re-condensate. In

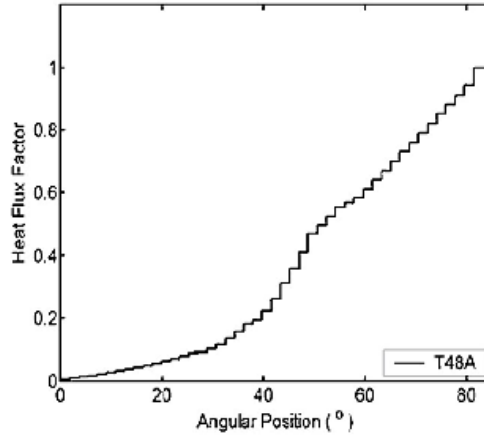


Figure 19.4: Heat flux profile used in the ULPU experiment [79].

low pressure part, flashing can also be observed with a spontaneous creation of steam.

All the simulations are performed with three fields: a continuous liquid field, a dispersed gas field and a continuous gas field. The dispersed gas field is treated using the dispersed approach presented in section 3.3. The dispersed bubble-size distribution is evaluated using an interfacial area transport equation [178]. The LBMo optimized in Part I is used for the simulation of large interfaces. The interface sharpening equation is implemented with the modification presented in Part II to deal with multifield simulations and non isothermal flows. Turbulence is modeled using a RANS approach in the continuous liquid field. This choice is motivated by the fact that the LES filtered two-fluid model equations have not been studied with a dispersed field and the interfacial area transport equation can not be activated with a LES approach.

19.4 First step: multifield simulation with standard phase change models

To achieve the multifield simulation and take into account all the phenomena occurring in the flow, different steps have been necessary since, in the previous simulations, multifield simulations have always been performed in isothermal flows. Thus, the first step that is proposed here is to activate nucleate boiling at the heated wall, to transfer the dispersed gas field in the continuous gas field according to the criteria presented in section 3.6 and to activate a flashing and a re-condensation model for the dispersed gas field. Details and validations on the nucleate boiling, re-condensation and flashing models can be found in [128, 129]. The mass transfers between the two continuous fields (treated with the new phase change model presented and validated in Chapter 9) are not considered in a first approach. Figure

19.5 displays the different mass transfers that are supposed to occur in the bulk. The red box highlights the transfers considered in the bulk. In this part, the ability of the code to deal with a three field simulation using the standard phase change models applied to the dispersed field is assessed.

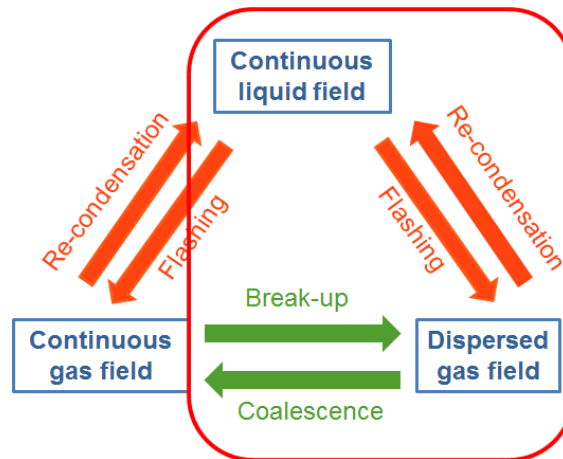


Figure 19.5: Schematic view of the bulk mass transfers occurring in the ULPU experiment simulated with the multifield approach, the red box highlights the transfer considered for the simulation.

The simulation results at different times are presented in Figures 19.6 and 19.7. First, we observe that dispersed bubbles are created at the wall by nucleate boiling. A part of these dispersed bubbles are transferred in the continuous gas field. However, before 0.6 s, they remain close to the heated wall. After this time, a steam slug begins to grow in the hot leg. Since the heat flux profile is established progressively before 1 s, at 0.6 s, the maximum heat flux is equal to $1.01 \cdot 10^6 \text{ W.m}^{-2}$. This first result highlights that the creation of a steam slug depends on the heat flux. Thus, in this configuration, the critical heat flux required to produce steam slugs is around equal to $1 \cdot 10^6 \text{ W.m}^{-2}$. Under this value, no slug appears in the flow. This is an important point since when a slug appears, the heated wall, representing the reactor vessel, is isolated from water which cannot cool the wall anymore. When the slug has appeared, it expands in all directions until 1 s, where it covers almost the whole baffle width. After 1 s, the steam slug condensates. The condensation process can be decomposed into two steps according to the mass transfer models applied to this simulation (see Figure 19.5). First, the continuous gas field is transferred in the dispersed gas field in the large bubble outskirts (see Figure 19.6). Then, this dispersed gas field re-condensate due to the re-condensation model. The steam slug is then located at different angles over time: 61° at 0.8 s, 56° at 1 s and 69° at 1.4 s. The criterion to obtain these values is that the cell at the wall has a volume fraction of continuous gas field larger than 0.9. These results are consistent with the observation made in the experiment since they found a CHF angle for the same baffle configuration and heat flux profile (run #10) equal to 67° [79]. The relative errors are then respectively equal to 9.0 % at 0.8 s, 16 % at 1 s and at 3.0 % at

1.4 s. At the top of the hot leg between the nozzle and the condenser, continuous gas field is visible at 0.8 s. This means that flashing occurred. Dispersed bubbles have been created and transferred into the continuous gas field. These large bubbles appear slightly after the creation of the steam slug in the baffle. After 1.4 s, the steam slug is supposed to disappear in the hot leg to reach a steady state. However, since the heat transfer model between the continuous liquid and gas fields is not activated, the simulation is stopped due to numerical errors.

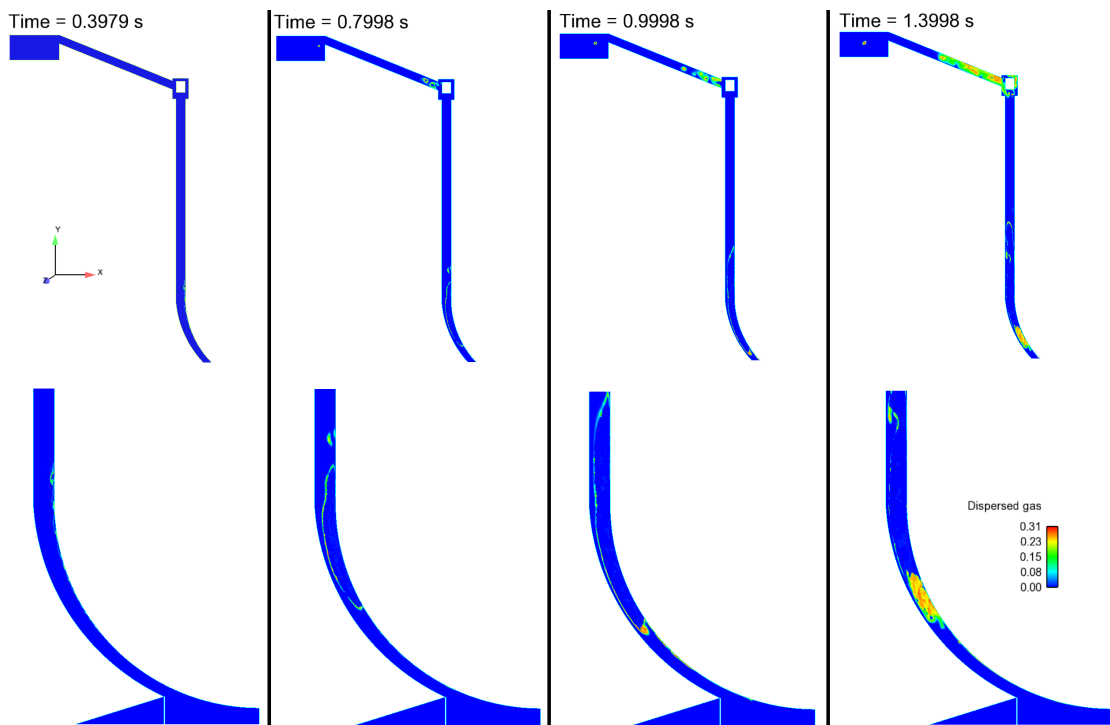


Figure 19.6: Dispersed gas field distribution over time, top: hot leg, bottom: zoom on the baffle region.

Figure 19.8 presents the liquid velocity distribution at 1.4 s. Comparable results have been obtained with two field simulations with the code NEPTUNE_CFD (see Figure 19.9). However, the liquid velocities between the nozzle and the condenser are smaller compared to the two field simulations. Nevertheless, it has to be noted that at 1.4 s a steady state has not been reached. In the inlet region, the hole induces flow acceleration at the bottom of the heated block and recirculation areas. The design of the inlet zone affects the flow at the bottom of the baffle. Moreover, the velocity observed in the downcomer at 1.4 s is equal to $0.6 \text{ m}\cdot\text{s}^{-1}$ which is in the order of magnitude of the expected velocity [79].

These results are comparable to two field simulations previously performed with the code NEPTUNE_CFD. Reasonable agreement with the experimental data have been observed. However, in two field simulations, the steam slug was considered dispersed. Thus, the interfacial area was largely overestimated. With the three field simulation, the steam slug is treated as a large interface between two continuous

19.4. FIRST STEP: MULTIFIELD SIMULATION WITH STANDARD PHASE CHANGE MODELS

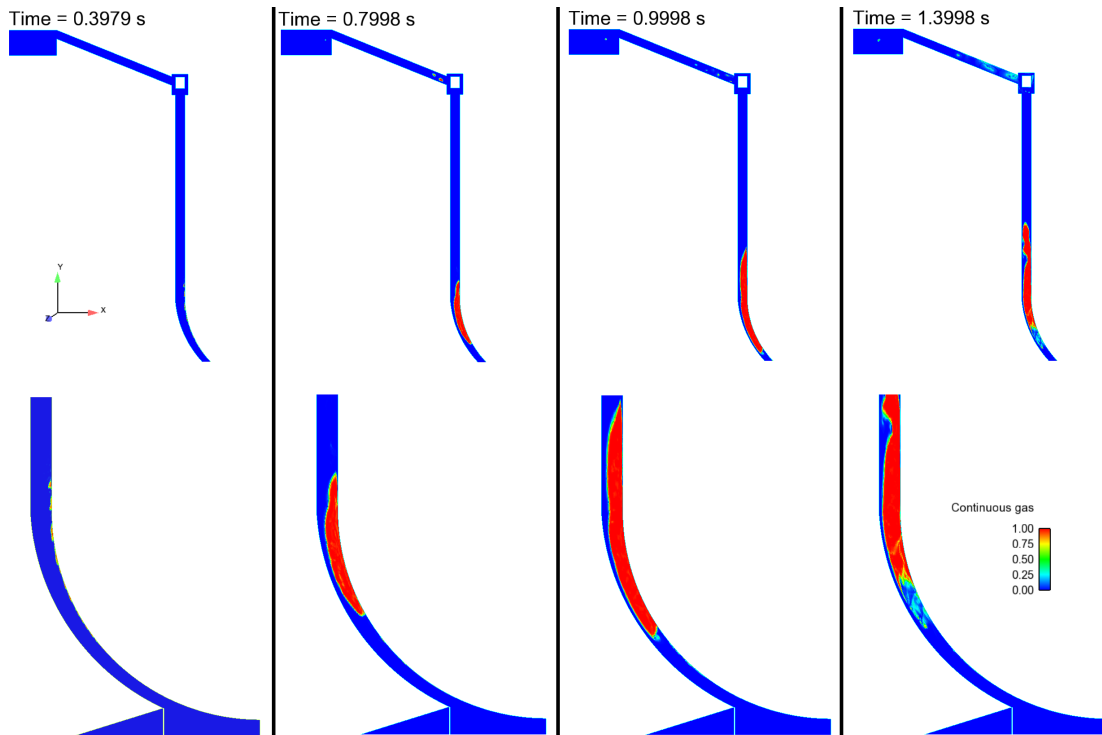


Figure 19.7: Continuous gas field distribution over time, top: hot leg, bottom: zoom on the baffle region.

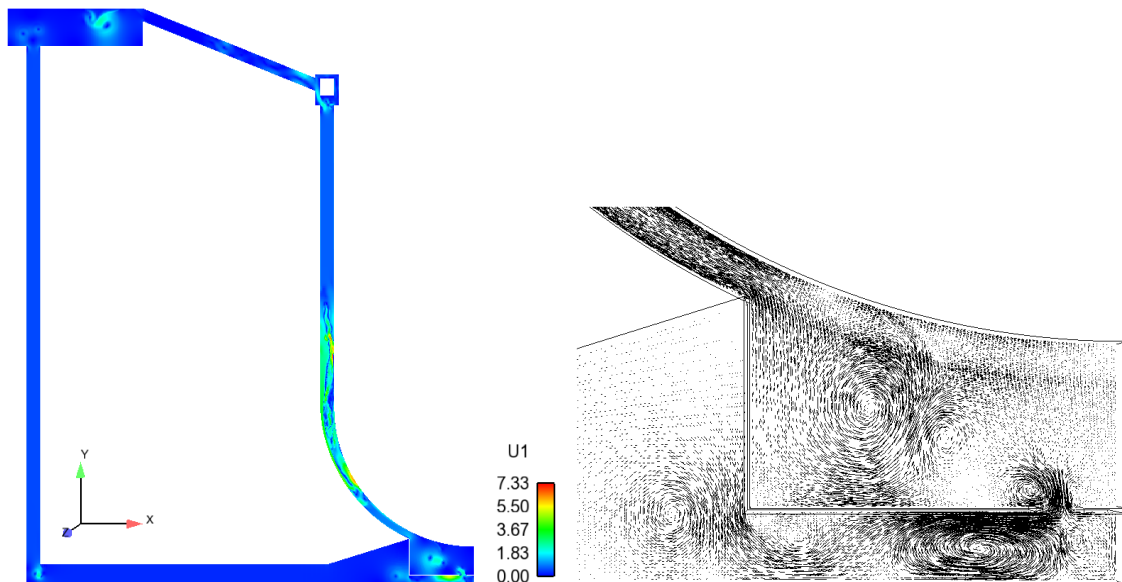


Figure 19.8: Liquid velocity distribution at 1.4 s in the whole domain (left) and zoom on the baffle region (right).

fields using the LBMo. Thus, the interfacial area is 100 times smaller (see Figure 10.10). Since several source terms are based on this quantity, the error is drastically

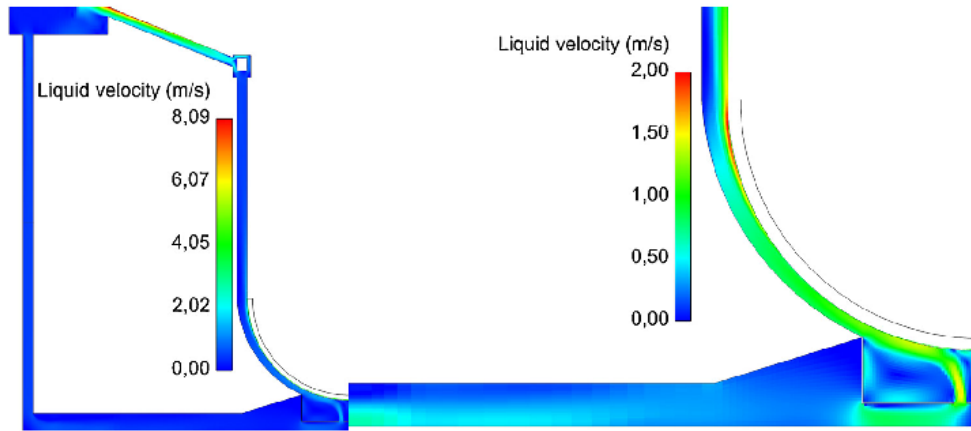


Figure 19.9: Variation of liquid velocity in the fluid domain obtained with two field simulations with the code `NEPTUNE_CFD` extracted from the publication of Jamet et al. [79], left: whole domain and right: focus on the inlet.

reduced by transferring the dispersed gas field in the continuous gas field.

However, the simulations performed in this section do not deal with mass transfers between the continuous liquid field and the continuous gas field. An error is made since phase change are supposed to occur at larges interfaces between the continuous gas field and the continuous liquid field.

19.5 Second step: multifield simulation with new phase change model for continuous fields

New phase change models have been developed in Chapter 9 to take into account non isothermal mass transfers between two continuous fields in large interfaces. Thus, in this section, we want to validate the ability to perform three field simulations with nucleate boiling at the wall using these new mass transfer terms in the bulk. After the nucleation of small spherical bubbles treated as a dispersed field at the wall, this dispersed field is entirely transferred in the continuous gas field. The new phase change models for large interfaces are then applied in the bulk. Figure 19.10 summarizes the different mass transfers that have to be taken into account in the bulk and in the red box those which are actually treated in this section. Thus, the large bubbles breakup, flashing and re-condensation between the continuous liquid field and the dispersed gas field are not considered. For the validation, a liquid at the saturation temperature is placed in a cubic box (side length equal to 2 cm) with a heated wall and outlets everywhere else. The grid contains 40^3 cells. A constant heat flux equal to 2.10^5 W.m^{-2} is applied at the heated wall. The liquid is at rest under atmospheric pressure. No gravity forces are considered. An adaptative time step is applied with a maximum CFL number equal to 1.

The results are displayed in Figure 19.11. In the first picture, the nucleation

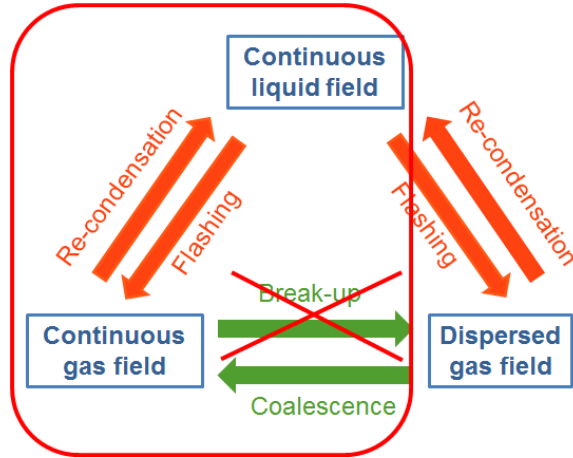


Figure 19.10: Schematic view of the bulk mass transfers occurring in the ULPU experiment simulated with the multifield approach, the red box highlights the transfer considered for the simulation.

of dispersed bubbles is observed at the heated wall. They are transferred in the continuous gas field. Thus, continuous gas field is created. Then, the isosurface of α_{cg} moves forward due to the phase change model.

19.6 Third step: Full multifield simulation

The objective of this section is to simulate the ULPU experiment with the multifield approach by treating all the mass transfers presented in Figure 19.12.

However, in the previous chapters and the previous sections, mass transfers related to phase change and occurring in the bulk have only been considered between two fields either the continuous liquid field and the dispersed gas field (section 19.4) or the continuous liquid field and the continuous gas field (section 19.5) (see Chapter 9). Indeed, the code has not been designed to deal with these four transfers at the same time.

Thus, to take into account these mass transfers, the new strategy developed consists in considering one type of transfer at even time steps and the other type at odd time steps. Figure 19.13 proposes a schematic view of this strategy. In the left column, the two different types of transfer are reported. They are available in case of two field simulations with continuous liquid and dispersed gas for the first one and continuous liquid / continuous gas for the second one. To perform three field simulations with the two types of transfer, each transfer has to be activated alternatively. In order to compensate the fact that each type of mass transfer is computed only half of the time, the computed terms are multiplied by a factor 2 for constant time steps and s for adaptive time steps. The evaluation of the s factor relies on the assumption that the mass transfer computed at time step $n - 1$ and n are equal to s times the mass transfer computed at time step n , which is equivalent

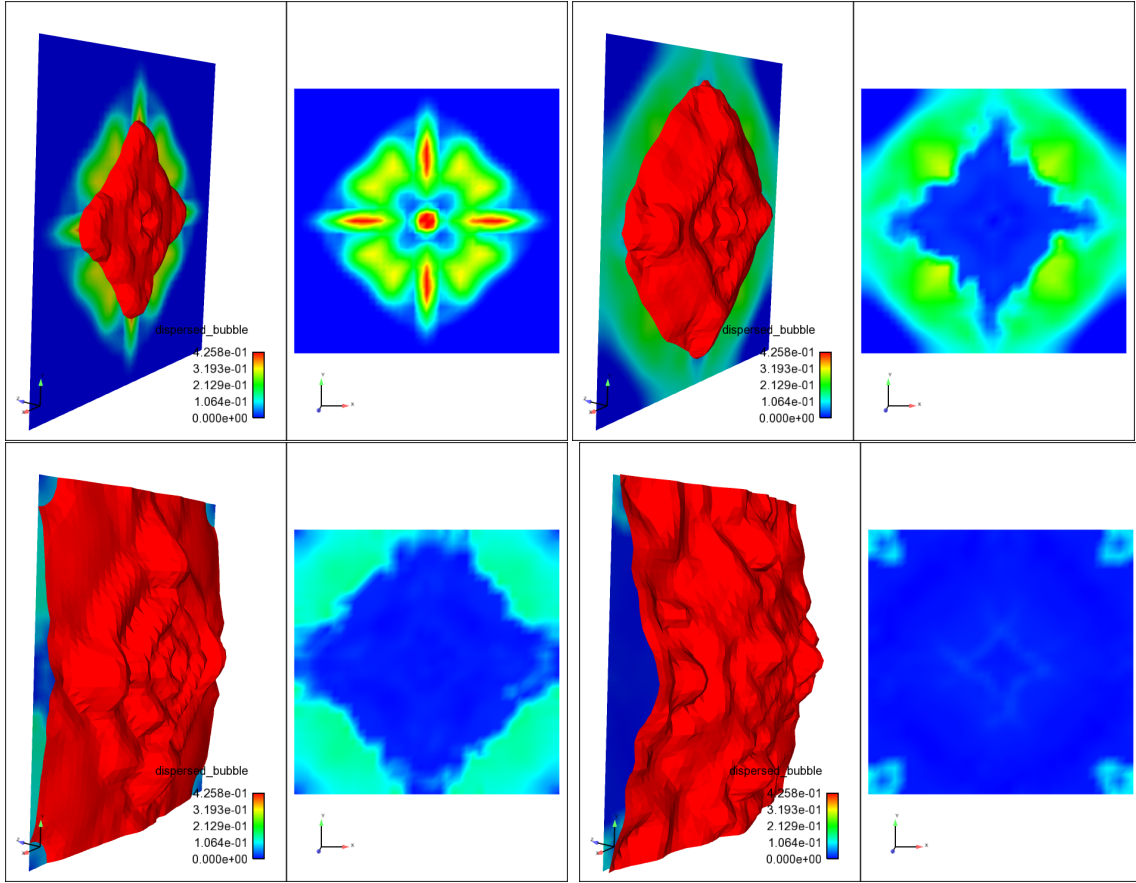


Figure 19.11: Evolution of the volume fractions of continuous and dispersed gas fields in a cubic box of saturated liquid with a heated wall, left: isosurface of the continuous gas field volume fraction $\alpha_{cg} = 0.5$ in red, right: volume fraction of the dispersed gas field at the heated wall.

to:

$$s\Gamma_k^n \simeq \Gamma_k^n + \Gamma_k^{n-1} \quad (19.1)$$

This assumption is reasonable while the characteristic time of the phenomenon is far greater than the simulation time step. This equation can be rewritten as:

$$\Gamma_k^{n-1} \simeq (s-1)\Gamma_k^n \quad (19.2)$$

A second assumption is made on the conservation of the instantaneous mass transfer between the time step $n-1$ and n :

$$\frac{\Gamma_k^n}{\Delta t_n} \simeq \frac{\Gamma_k^{n-1}}{\Delta t_{n-1}} \quad (19.3)$$

The combination of Equations (19.2) and (19.3) gives:

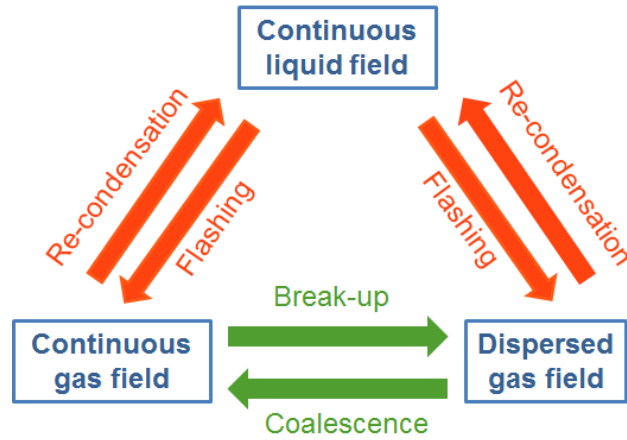


Figure 19.12: Schematic view of the bulk mass transfers occurring in the ULPU experiment simulated with the multifield approach.

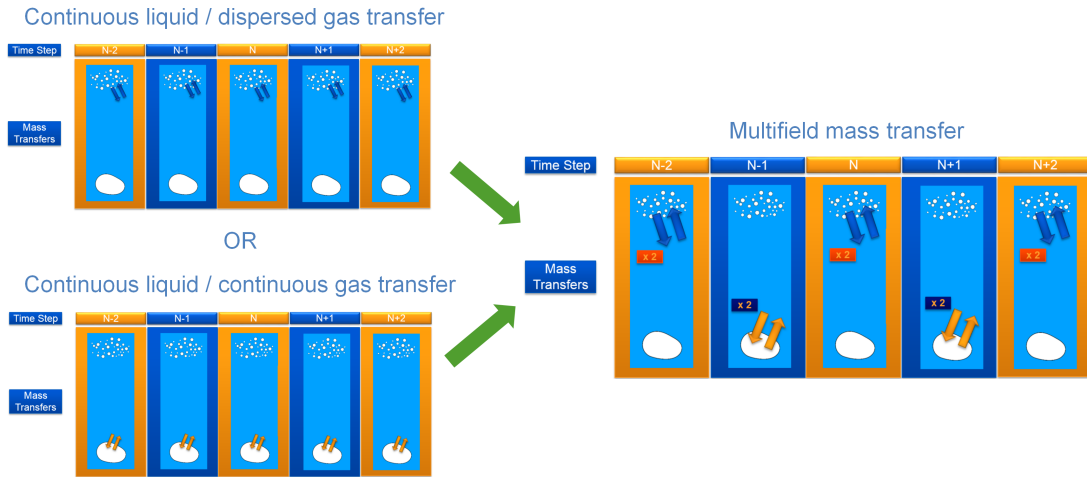


Figure 19.13: Schematic view of the strategy developed to take into account the different types of mass transfers appearing in a three field simulations of a non isothermal flow and occurring in the bulk, left column: the two types of mass transfers treated separately, right column: the two types of mass transfers treated simultaneously by considering one type of transfer at even time steps and the other type at odd time steps.

$$\frac{\Gamma_k^n}{\Delta t_n} \simeq \frac{(s-1)\Gamma_k^n}{\Delta t_{n-1}} \quad (19.4)$$

This gives the expression of s :

$$s = 1 + \frac{\Delta t_{n-1}}{\Delta t_n} \quad (19.5)$$

If $\Delta t_n = \Delta t_{n-1}$ that is to say a constant time step is used, then $s = 2$.

To evaluate the error made by considering mass transfer half of the time, two field simulations have been performed on the growing vapor bubble in several configurations. Encouraging results have been obtained [138].

The objective is to use this methodology to simulate the ULPU experiment by taking into account all the mass transfers. This work has not yet been done but is currently investigated.

19.7 Conclusion

This chapter highlighted the ability of the code to perform multifield simulations on non isothermal flows. Encouraging results have been obtained by considering only the mass transfer terms between the continuous liquid field and the dispersed gas field and modeling coalescence and breakup. However, work has still to be done to couple these mass transfers to the new phase change model developed in Chapter 9.

Part V
Conclusion

In this report, a first part have been dedicated to the different choices made for the simulation of complex laminar and isothermal two-phase flows within a multifield approach. This work is the basis for further applications to three field simulations with turbulence and heat and mass transfers. The multifield approach presented in this thesis is based on a two-fluid model and an Eulerian description of the small inclusions. These small spherical inclusions are modeled through a dispersed approach. Interfacial momentum transfers, such as drag, added mass, lift and turbulent dispersion forces are applied to the dispersed field. These closure laws have been validated in the code `NEPTUNE_CFD` on industrial test cases [40, 127, 132] and are currently at the state of the art. The main effort then concerned the large interfaces modeling. Within the multifield approach, these large interfacial inclusions are considered as boundaries between two continuous fields. This implies that in a water/steam flow with steam inclusions of different sizes, the small spherical ones are considered in the dispersed gas field whereas the larger ones are composed by a continuous gas field. For this two-phase flow, three fields are defined: a continuous liquid field, a dispersed gas field and a continuous gas field. The work done in this first part has thus been focused on the treatment of the continuous fields. For this purpose, a model, called the Large Bubble Model (LBMo), previously implemented by Denèfle [38] has been optimized. It consists in three main elements: an interface sharpening equation, a drag force law and a surface tension model. The first element is required to control the interface thickness. It has been shown that special care had to be taken in its implementation to ensure mass conservation and to limit the production of spurious velocities. Thus, different criteria have been developed in order to limit the resolution of the equation and to control the final interface thickness. Then, the spurious velocities induced by both the surface tension model and the interface sharpening equation have been assessed and allowed evaluating the order of magnitude of the critical Capillary number. Moreover, a new drag force expression has been implemented. This force is used to couple the velocity of the two continuous fields at the interface. The ability of the new formulation to simulate accurately two-phase flows containing large interfaces with a wide range of viscosities has been highlighted. This new formulation is also integrated in the multifield approach since it takes into account the possible existence of several fields for one phase. The model developed in this part has been finally compared to models dedicated to the simulation of large interfaces. Comparable results have been obtained for the same computational cost.

In a second part, two types of transfers have been explored: mass and heat transfers between two continuous fields due to phase change and mass transfers between the continuous and the dispersed fields of the same phase (without heat transfer). The first type of transfer concerns non isothermal flows, in which phase change is observed between two continuous fields of two different phases. A dedicated model for this transfer has been developed and implemented by transposing the methodology proposed by Brackbill *et al.* [21] to extend the surface tension model to interfaces with a non zero thickness. This new model allows obtaining reasonable agreements with theoretical results especially at higher pressure conditions which correlate with

the nuclear power plant situations. Concerning the isothermal transfers between the continuous and the dispersed fields of the same phase, a first study have been performed to show the ability of the code to handle these transfers. The multi-field approach was used to predict with a reasonable accuracy flow regimes. This last point was crucial in nuclear power plants where the knowledge of flow regimes should be improved in some components. However, the coalescence term was based on empirical considerations. Thus, a new model considering the dispersed bubble shape has been implemented and validated on various flow regimes.

In the third part, turbulence have been studied. Since large interfaces are resolved in the multifield approach, LES which is based on a deterministic description of turbulence was chosen as the most suitable model. Thus, properties of turbulent flows and LES have been first detailed. Then, standard LES models have been implemented and validated on a single-phase turbulent flow. This work showed the feasibility of LES with the code NEPTUNE_CFD. Then, an *a priori* LES study has been performed with the phase inversion benchmark which is a two-phase two continuous fields flow test case. Two-fluid model equations have been filtered to highlight the specific subgrid terms. Two specific subgrid terms appeared. Then, their order of magnitude has been assessed. This analysis showed that the subgrid term related to the surface tension model was predominant, in agreement with results obtained with one-fluid models. However, the diffusive subgrid term was not negligible. Finally, a comparison of different turbulence models has been performed to identify the most suitable model for all the subgrid terms. Structural models, especially the Approximate Deconvolution Model (ADM), allowed reaching encouraging error levels for all the subgrid terms. Thus, this model has been implemented. Preliminary results have been obtained with the fully developed turbulent channel flow (a single-phase flow). However, other authors reported better agreements with DNS or experimental data. An analysis of the different choices made for the implementation of the model highlighted that the ADM order should be increased and the effect of the filter, the relaxation term modeling and the wall treatment should be assessed. However, since the objective of the work was the simulation of two-phase flows, the study was not performed. Then, LES has been used to predict flow regimes. Better agreements with the experimental data were obtained compared to RANS approaches. Moreover, an encouraging true LES simulation with ADM was performed. Several modeling choices have been investigated but work has still to be done to improve the results.

Finally, a last part proposed to apply the developments presented in the previous parts to an industrial application. This application concerns a cooling strategy, called the In-Vessel Retention (IVR) strategy and is based on the ULPU experiment. The objective was the evaluation of the coolability limits of a reactor cavity flooding in case of severe accident. The two-phase flow involved in this study was turbulent and non isothermal and evolved in an industrial geometry. Different phenomena have been observed. First, nucleate boiling occurred at the heated wall. The dispersed gas field created at the wall could coalesce in the bulk to form large steam bubbles or re-condensate. Steam bubbles could also appear spontaneously by a flashing process

in low pressure regions. Preliminary simulations of the experiment have been able to reproduce all the phenomena.

Part VI
Perspectives

Different perspectives of this work can be expected not only on the three main parts of this report but also on more general phenomena not studied in this thesis.

First, concerning the first part of this report, the LBMo has not been tested on laminar and isothermal water/air interfacial test cases with high relative velocities at the interface which are particularly hard to compute. Thus, one perspective of this work should be to assess and improve the model roughness at least on such flows. Moreover, in the second part, phase change transfer terms in non isothermal flows allowed obtaining reasonable results for enough refined meshes. However, contrary to other methods, for coarse grids, the error level was larger. Results should then be improved since industrial studies are usually performed on such grids. Furthermore, as done for the surface tension model, spurious fluxes induced by the new phase change models should be assessed. This work has been done by Haroun *et al.* [65] who also proposed different methods to reduce these spurious fluxes. Concerning the isothermal transfers between two fields from the same phase (coalescence and breakup), a first perspective should be to extend the validation of the new coalescence term. Moreover, in the existing models, no information is transferred during the transition process. However, it could be interesting to know for example the local curvature of the large interface when it breaks up into small spherical bubbles to fix the diameter of these bubbles. This could improve the interfacial area conservation during the transfer. Finally, encouraging results have been obtained in the LES *a priori* study with ADM and then with true LES of turbulent two-phase flows. Nevertheless, the implementation of the model is not straightforward. Indeed, many elements inherent to the model are crucial: the ADM order, the filter choice, the treatment close to walls, the relaxation term modeling or specific to the two-fluid model: the filtering process close to interfaces and the filtered volume fraction. Moreover, some of the subgrid terms appearing in the filtered equations remain particularly difficult to compute. Many research group are currently working on them. This is for example the case of time and surface tension subgrid terms. For this second term, the issue is to be able to reproduce the effect of a mesh refinement on the geometrical shape of an interface [6, 70]. Better results are also expected by increasing the time order of the CMFD tool.

Moreover, in all this work, simulations with multiple phenomena have been performed. However, further work has still to be done to perform LES on complex turbulent non isothermal flows with the multifield approach. Indeed, LES has been restrained, in this thesis, to two continuous fields and isothermal flows. Different steps are necessary before reaching such level of complexity. First, the filtered two-fluid model equations for dispersed fields have to be studied. Lakehal [90] have already highlighted the subgrid terms appearing in these equations. However, turbulence models have to be assessed on these subgrid terms. Moreover, the model used to vary the dispersed bubble size (the Ruyer-Seiler model [178]) has to be coupled to LES. Then, to simulate non isothermal flows with LES, the energy balance equation has to be filtered and the subgrid terms modeling has to be investigated. Finally, validation test cases should be performed with non isothermal three field flows and LES to ensure that all the models work together. Furthermore, in the

specific case of two-phase flows with walls, such as the METERO test case, triple points with a wall, air and water can appear. In this work, the triple point modeling has not been explored. For wetting effects, the models based on VOF techniques [61, 100] could be adapted and validated for the LBMo in order to account for contact angles on solid surfaces. Finally, the multifield approach has been defined as a method able to simulate at the same time large and deformable inclusions and small and spherical ones without assumption on the type of phases inside and outside these structures. However, all the simulations presented in this thesis were limited to three fields with a continuous liquid field, a continuous gas field and a dispersed gas field. One important perspective is to apply the method with a continuous and a dispersed liquid field and then to extend it to four field simulations with both liquid inclusions in gas and gas inclusions in liquid.

Appendix A

To the need of the Large Bubble Model

This appendix aims at showing the need of the LBMo on the Bhaga and Weber's test case (see section 4.4.2 for the description of the test case). For this purpose, three simulations of case d have been performed. Each time one of the three elements of the LBMo (interface sharpening, surface tension and drag force law) are deactivated to highlight their effects.

A.1 Deactivation of the interface sharpening

In this section, the Bhaga and Weber's rising bubble test case is simulated with the surface tension model and the optimized expression of the drag force law but the interface sharpening equation is not solved. The obtained bubble is displayed in Figure A.1 (b) and has to be compared to (a). The interface is diffused and the bubble cannot be located with accuracy. The final velocity of the bubble is equal to 21.1 cm.s^{-1} corresponding to a relative error of 27 %. The diffusion of the interface slows down the bubble when it rises.

A.2 Deactivation of the surface tension model

After deactivating the interface sharpening, the surface tension model is not applied. The recompression equation is solved and the drag force law is activated. The results are presented in Figure A.1 (c). The bubble falls apart. The final bubble velocity is equal to 17.2 cm.s^{-1} but this value does not represent the reality of the bubble rising speed since the bubble lost its integrity.

One can note that the METERO test case in the plug flow configuration has also been simulated without surface tension (see section 11.2 for the description of the test case). The intermediate mesh has been used with a RANS model. The shape of the bubbles, the average void fraction and average liquid velocity profiles displayed in Figure A.2 are not affected by this deactivation. In the particular case

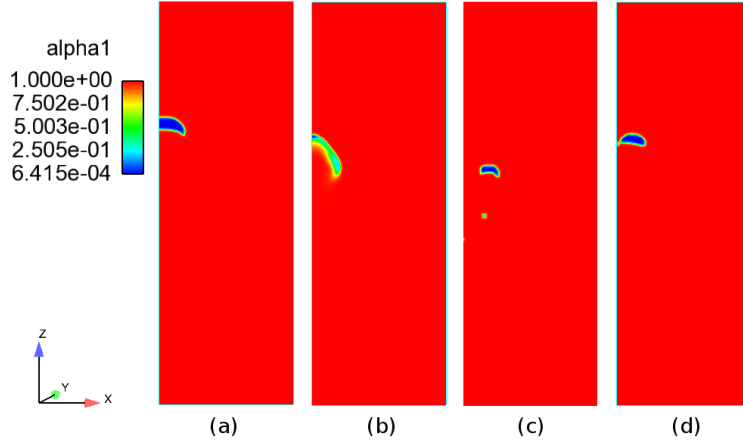


Figure A.1: Volume fraction of liquid in case d of the Bhaga and Weber's rising bubble test case obtained after 0.6 s, (a) complete LBMo simulation, (b) interface sharpening deactivated, (c) surface tension model deactivated and (d) drag force deactivated.

of purely convective flows, the surface tension model seems not necessary for an accurate simulation.

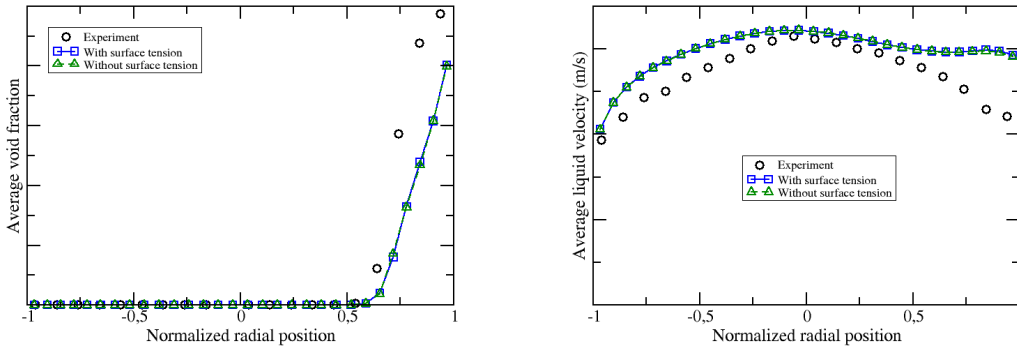


Figure A.2: Average void fraction and average liquid velocity profiles at $40D$ from the inlet, with and without the surface tension model, plug flow with $J_L = 2.65 \text{ m.s}^{-1}$ and $J_L = 0.127 \text{ m.s}^{-1}$, intermediate mesh, $\Delta t = 0.25 \text{ ms}$, RANS approach for turbulence modeling.

A.3 Deactivation of the drag force

Finally, the drag force law has been deactivated. The other elements of the LBMo remain activated. The results are show in Figure A.1 (d). The shape of the bubble is highly affected by the absence of coupling term between the continuous liquid and gas field especially at the center of the bubble. Nevertheless, the deactivation of the drag force law has a lower impact on the final velocity which is equal to 24.8 cm.s^{-1}

(relative error of 14 %).

A.4 Conclusion

In a rising bubble test case, the interface sharpening equation, the surface tension model and the drag force law are necessary for an accurate prediction of the shape and the velocity of the bubble.

Appendix B

Conservative implementation of the interface sharpening equation, further validations

This appendix proposes extra validations for the conservative implementation of the interface sharpening equation (see Chapter 4). The section is organised by test case. Some test cases have been used to validate different steps of the implementation.

B.1 Square bubble test case

To illustrate the effect of the conservative implementation combined with the choice of the drag force model, the test case of the square bubble is simulated.

This test case consists in the simulation of an air bubble with an initial square shape surrounded by liquid water. The initial bubble size is equal to 2 *cm*. The properties of the two fluids are given in Table B.1 with a surface tension coefficient equal to 0.08 *N.m*⁻¹. Gravity is applied but no surface tension is taken into account. The mesh is a square uniform Cartesian grid with 5 *cm* side length. Symmetry boundary planes are imposed everywhere.

	Density (<i>kg.m</i> ⁻³)	Viscosity (<i>Pa.s</i>)
Air bubble (subscript: <i>cg</i>)	1.29	1.10 ⁻⁵
Water (subscript: <i>cl</i>)	1000	1.10 ⁻³

Table B.1: Properties of water and air for the square bubble test case.

The three drag force laws used in Chapter 6 are compared for this simulation. In all this section, law 1 refers to the drag force law presented in Equation (6.1), law 2 to Equation (3.15) and law 3 to Equation (6.7). Three mesh refinements are used: 64 x 64 cells, 128 x 128 cells and 256 x 256 cells. The time steps are kept constant

APPENDIX B. CONSERVATIVE IMPLEMENTATION OF THE INTERFACE SHARPENING EQUATION, FURTHER VALIDATIONS

and given in Table B.2 for each simulation. The time steps are smaller for a given mesh refinement with the non conservative implementation associated to the first drag force law since the simulations have been done with a constant CFL number. Thus, as we can see in Figure B.1, the interface is more agitated so the velocities intensity is higher with the non conservative approach, which requires a reduction of the time steps to simulate the cases with the same CFL number.

Drag force law	Implementation of the interface sharpening equation	64 x 64 cells	128 x 128 cells	256 x 256 cells
Law 1	Conservative	0.1 <i>ms</i>	0.05 <i>ms</i>	0.025 <i>ms</i>
	Non conservative	0.05 <i>ms</i>	0.025 <i>ms</i>	0.0125 <i>ms</i>
Law 2	Conservative and non conservative	0.1 <i>ms</i>	0.05 <i>ms</i>	0.025 <i>ms</i>
Law 3	Conservative and non conservative	0.1 <i>ms</i>	0.05 <i>ms</i>	0.025 <i>ms</i>

Table B.2: Time steps according to the mesh refinement, the drag force model and the implementation of the interface sharpening equation for the square bubble test case.

The effect of the conservative implementation is compared with a non conservative method. The results with the intermediate mesh are presented in Figure B.1 for law 1, Figure B.2 for law 2 and Figure B.3 for law 3. The same conclusions can be drawn with the two other grids. For $t > 0.5$ s, the surface adopts a sloshing motion with the conservative version of the interface sharpening equation, as expected theoretically [207]. With the second and the third drag force law, this behavior is also observed with the non conservative implementation but the interface remains more agitated. Thus, the conservative property of the sharpening equation does not affect the physical results with these two drag force laws. On the contrary, with the first drag force law and the non conservative implementation, for $t > 0.5$ s, water is entrapped in a strong rotating motion inducing fragmentation and generation of droplets, which prevents the interface from stabilizing in a stratified medium. This effect remains whatever the mesh refinement. Therefore, the conservative implementation is crucial to predict the expected physical phenomena especially when the drag force law is not optimized. This test case does not allow discriminating the drag force laws 2 (Equation (3.15)) and 3 (Equation (6.7)) since the interface motion is very similar with the conservative version of the interface sharpening equation.

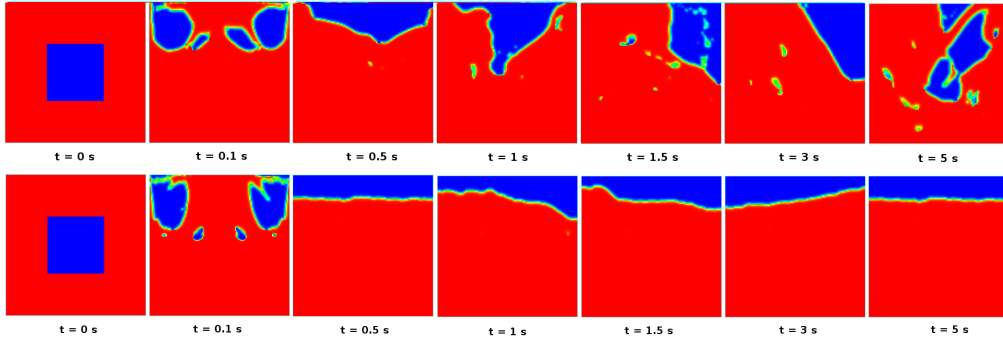


Figure B.1: Evolution of the square bubble in liquid water under gravity, mesh with 128×128 cells, drag force law 1 (Equation (6.1)), top: non conservative implementation of the interface sharpening equation (constant time step equal to 0.025 ms), bottom: conservative implementation (constant time step equal to 0.05 ms).

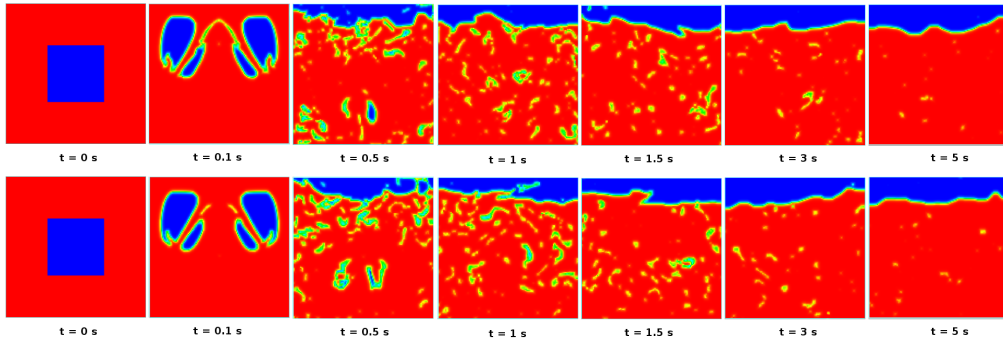


Figure B.2: Evolution of the square bubble in liquid water under gravity, mesh with 128×128 cells, drag force law 2 (Equation (3.15)), top: non conservative implementation of the interface sharpening equation, bottom: conservative implementation, constant time step equal to 0.05 ms.

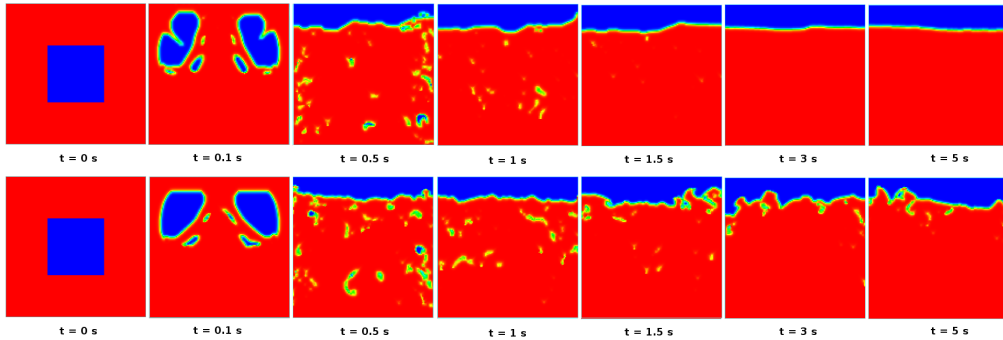


Figure B.3: Evolution of the square bubble in liquid water under gravity, mesh with 128×128 cells, drag force law 3 (Equation (6.7)), top: non conservative implementation of the interface sharpening equation, bottom: conservative implementation, constant time step equal to 0.05 ms.

B.2 Simulation of a stationary bubble

Simulations have also been performed with a stationary air bubble (see section 5.2) in still water to evaluate the spurious velocities induced by the resolution of the interface sharpening equation. This test case is particularly interesting for such studies since all the fluids are at rest. The bubble motion only depends on these spurious velocities which are not diluted in a flow velocity. Thus, they can be easily quantified.

B.2.1 Effect of a non conservative implementation

With the optimized threshold β , the benefit in terms of mass conservation of the conservative implementation compared to the addition of spurious velocities can be observed. For this comparison, the stationary bubble test case is simulated with a coarse mesh 64 x 64 cells. The time step is equal to 0.1 *ms*. The mass balance error obtained by time step in the whole domain and the maximum value of the air velocity (see Equation (2.1)) after 1 *s*, representing the spurious velocity, are presented in Table B.3 for the conservative and non conservative implementation of the interface sharpening equation. The spurious velocity intensity is increased by 13 % when the interface sharpening equation is implemented in a conservative way. Therefore, the gain in mass error is larger than the increase of spurious velocity intensity induced by a conservative implementation.

Implementation	Mass balance error	$Max(U_{cg}) (m.s^{-1})$
Conservative	10^{-17} %	0.17
Non conservative	10^{-10} %	0.14

Table B.3: Effect of the conservative and non conservative implementation of the interface sharpening equation on the mass balance error obtained by time step in the whole domain and the intensity of the spurious velocities after 1 *s* for the stationary bubble test case, grid with 64 x 64 cells, time step equal to 0.1 *ms*.

B.2.2 Optimization of the threshold value β

This test case is then used to optimize the threshold value β . The spurious velocities are evaluated for four different threshold values β : 1.10^{-4} , 5.10^{-4} , 1.10^{-3} and 1.10^{-2} and three different mesh refinements: 64 x 64 cells, 128 x 128 cells and 256 x 256 cells. The time step is equal to 0.1 *ms*, corresponding to a maximum CFL number of 0.9 for the most refined mesh. All the parameters studied in this test case (velocities and pressure) are evaluated at 1 *s*. Indeed, as shown in Figure B.6, at 0.3 *s*, the bubble has already reached its equilibrium.

For the analysis of the spurious velocities, two definitions of U_{cg} are considered. The first one refers to a single-fluid approach definition of the spurious velocities.

The velocity is considered in the air phase. It is evaluated where the phase is present, that is to say for $\alpha_{cg} > 1.10^{-3}$. The average velocity and the maximum value are defined as follows:

$$U_{cg} = \frac{\sum_{\alpha_{cg} > 1.10^{-3}} \alpha_{cg} \rho_{cg} u_{cg}}{\sum_{\alpha_{cg} > 1.10^{-3}} \alpha_{cg} \rho_{cg}} \quad \text{and} \quad U_{max} = \max_{\alpha_{cg} > 1.10^{-3}} (u_{cg}) \quad (2.1)$$

The second definition of U_{cg} is based on the velocity of the air phase evaluated only within the interface thickness. This analysis is more suitable to the two-fluid model since the spurious velocities are only considered where the interfacial source terms such as the drag force model are applied. The following expressions are used to calculate the average and maximum value of U_{cg}^{Int} :

$$U_{cg}^{Int} = \frac{\sum_{\alpha_{cl} \alpha_{cg} > 0.1} \alpha_{cg} \rho_{cg} u_{cg}}{\sum_{\alpha_{cl} \alpha_{cg} > 0.1} \alpha_{cg} \rho_{cg}} \quad \text{and} \quad U_{max}^{Int} = \max_{\alpha_{cl} \alpha_{cg} > 0.1} (u_{cg}) \quad (2.2)$$

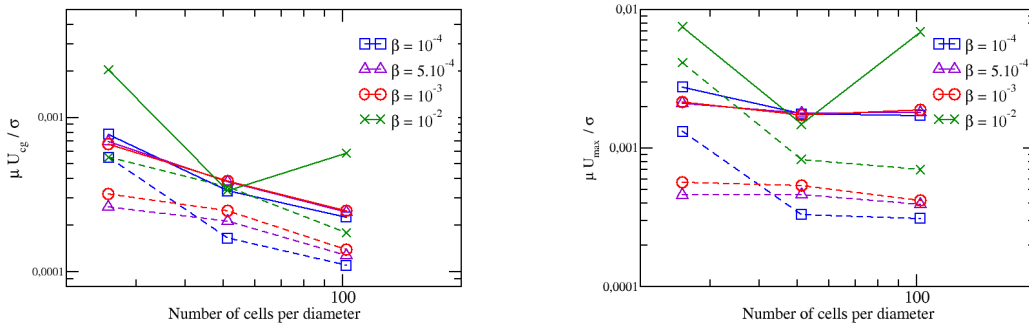


Figure B.4: Capillary number according to the mesh refinement and the threshold value β , left: average velocity, right: maximum velocity, the solid lines correspond to the velocities evaluated according to Equation (2.1) and the dashed lines to Equation (2.2).

In Figure B.4 (solid lines), the results are given by using Equation (2.1) for the definition of the spurious velocities U_{cg} , as done with single-fluid models in [152]. The X axis of the two graphs corresponds to the dimensionless quantity obtained by dividing the bubble diameter by the cell length. First, the decrease of the threshold value does not ensure an accurate prediction of the velocity field. Thus, only an optimization of this parameter can improve the quality of the results by limiting the spurious velocities. Indeed, on one hand, if the iteration number is low, the interface will require more compression at each time step and so induced more spurious velocities related to the sharpening step. As we can see in Table B.4, the iteration number with the threshold value $\beta = 1.10^{-2}$ is low for all the meshes and explains the absence of convergence. On the other hand, if the number of iterations is high, non zero mass fluxes continue to be added whereas the interface is enough

sharpened. Once again, spurious velocities are created. This last situation explains the higher Capillary number observed for the coarser mesh with $\beta = 1.10^{-4}$ (see Table B.4).

In Figure B.4 (dashed lines), the second point of view to evaluate the spurious velocities is proposed. The same behavior is observed when the mesh is refined or the threshold value is changed. The average and maximum values have the same order of magnitude at the interface and in the whole domain.

Finally, in Figure B.5, a comparison of our results (solid lines in Figure B.4 left) with other interface tracking methods is proposed. Thus, contrary to the VOF-PLIC method [104] and many other codes, the spurious velocities decrease with the mesh refinement. Moreover, for a given mesh refinement, the spurious velocities induced by our model are larger than in the Front-Tracking method of Popinet and Zaleski [153] but smaller than the two other methods which are the second gradient theory proposed by Jamet *et al.* [77] and the VOF-PLIC method [104].

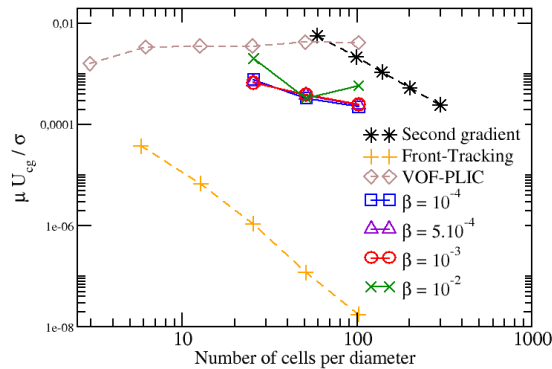


Figure B.5: Capillary number according to the mesh refinement obtained with three different methods: the second gradient theory proposed by Jamet *et al.* [77], the Front-Tracking method of Popinet and Zaleski [153], which includes a correction of the pressure gradient and the VOF-PLIC method [104].

In Figure B.6, the evolution of the spurious velocities over time is studied [78]. The simulations are performed with the intermediate mesh (128 x 128 cells). With $\beta = 1.10^{-3}$, $\beta = 5.10^{-4}$ and $\beta = 1.10^{-4}$, the Capillary number oscillates slightly until 0.25 s before stabilizing. The same observation can be done with $\beta = 1.10^{-2}$ but the variation range is higher. Indeed, since the interface sharpening equation is solved only once at each time step (see Table B.4), the compression mass fluxes are larger and so induced more spurious velocities. For $\beta \leq 1.10^{-3}$, the Capillary number variation is limited at the beginning of the simulation since the compression is enough efficient at each time step.

Finally, for all the simulations, the error made in the prediction of the Laplace equation is evaluated. The final radius of the bubble, the estimated bubble surface

B.2. SIMULATION OF A STATIONARY BUBBLE

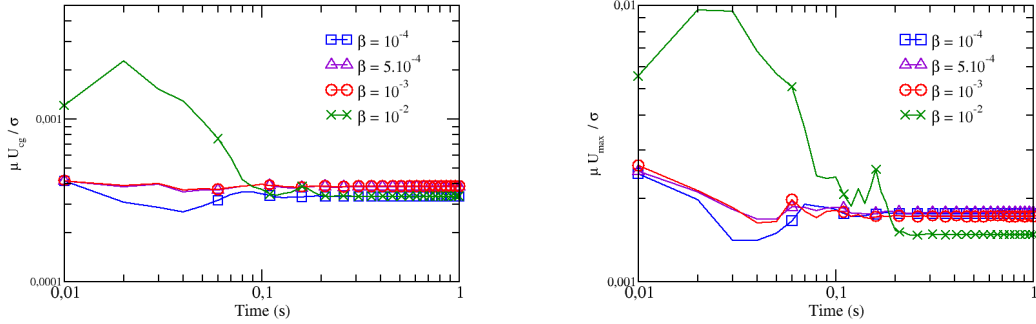


Figure B.6: Capillary number over time according to the threshold value β , mesh with 128×128 cells, left: average velocity, right: maximum velocity, the velocities are evaluated in the whole domain using Equation (2.1).

and the pressure fields in and out of the bubble are evaluated using the average expressions presented in section 5.2.2.

The results are displayed in Figure B.7. Convergence is obtained whatever the threshold value. Contrary to the velocity field, the results are very close for the four threshold values and do not allow discriminating the four values. To evaluate the order of convergence x of the pressure, the Richardson's extrapolation (Equation (5.9)) is used. With $\beta = 1.10^{-2}$, the order of convergence is equal to 1.6, with $\beta = 1.10^{-3}$ to 1.4, with $\beta = 5.10^{-4}$ and $\beta = 1.10^{-4}$ to 0.9. The order of convergence decreases slightly when the threshold value is decreased.

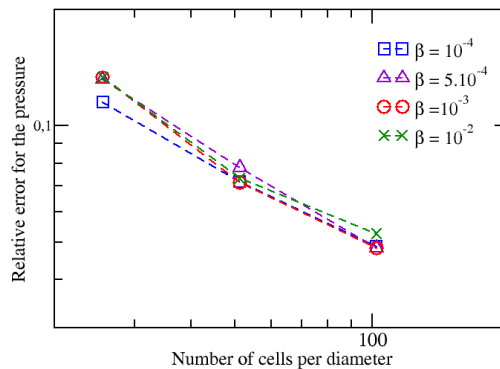


Figure B.7: Relative error for the pressure according to the mesh refinement and the threshold value β obtained with the simulation of a stationary bubble.

To conclude, the simulations of the stationary bubbles show that the threshold value must be carefully chosen to allow an efficient interface sharpening without adding too many spurious velocities. The mesh refinement study highlights that an

appropriate value can be chosen between 1.10^{-3} and 1.10^{-4} .

B.3 Simulation of an oscillating bubble

To optimize the threshold value β , an oscillating air bubble in liquid water has been simulated without gravity (see section 4.3.2). The bubble is initialized with an ellipsoidal shape with a deformation rate $\tilde{\epsilon} = 0.05$.

The study is performed with four different values for the threshold β : 1.10^{-4} , 5.10^{-4} , 1.10^{-3} and 1.10^{-2} . Three different mesh refinements are used: 64×64 cells, 128×128 cells and 256×256 cells. The time step is kept constant and is respectively equal to 0.05 ms , 0.025 ms and 0.0125 ms .

In Table B.4, the iteration number is displayed for each mesh and threshold value. The larger β is, the less the interface sharpening equation is iterated. This confirms that the criterion does its work to limit the equation iteration. Moreover, the iteration number decreases with the mesh refinement for a given threshold value. Indeed, the mesh refinement reduces the numerical diffusion and so the sharpening effort.

Mesh refinement	$\beta = 1.10^{-4}$	$\beta = 5.10^{-4}$	$\beta = 1.10^{-3}$	$\beta = 1.10^{-2}$
64×64 cells	25	4	2	1
128×128 cells	10	3	2	1
256×256 cells	7	2	1	1

Table B.4: Iteration number of the interface sharpening equation according to the mesh refinement and the choice of the threshold value β .

Then, in Table B.5, the oscillation frequency of the bubble is compared. It is important to note that the frequency is given with two significant figures due to the accuracy of the signal discretization. For $\beta = 1.10^{-4}$, the oscillation frequency is only given for the most refined mesh. Indeed, with the two other meshes, the bubble moves in the domain instead of oscillating regularly as expected. This phenomenon is caused by the high number of iterations of the interface sharpening equation, which induces the accumulation of spurious recompression mass fluxes since the interface required less iterations to be enough sharpened. These mass fluxes are injected in the momentum balance equation used to predict the velocity and induce spurious velocities. The mesh refinement reduces this iteration number and so decreases the spurious velocities, allowing the bubble oscillation. For $\beta = 1.10^{-2}$, $\beta = 1.10^{-3}$ and $\beta = 5.10^{-4}$, the oscillation frequency converges with the mesh refinement. For the intermediate and the refined mesh, the same frequency is obtained due to the accuracy of the method. For the coarser mesh, the oscillation frequency given here must be nuanced since some spurious oscillations and displacements of the bubble are observed. The results obtained with these three values of β are in good agreement

B.3. SIMULATION OF AN OSCILLATING BUBBLE

with the theory. However, with $\beta = 1.10^{-2}$, the lack of interface recompression results in a numerical fragmentation of the bubble interface, as shown in Figure B.8. To conclude, the values $\beta = 1.10^{-3}$ and $\beta = 5.10^{-4}$ are two potential candidates to define an optimized recompression threshold.

Mesh refinement	$\beta = 1.10^{-4}$	$\beta = 5.10^{-4}$	$\beta = 1.10^{-3}$	$\beta = 1.10^{-2}$
64 x 64 cells	-	5.1 s ⁻¹ (11 %)	5.1 s ⁻¹ (11 %)	5.2 s ⁻¹ (8.8 %)
128 x 128 cells	-	5.6 s ⁻¹ (1.8 %)	5.6 s ⁻¹ (1.8 %)	5.5 s ⁻¹ (3.5 %)
256 x 256 cells	5.6 s ⁻¹ (1.8 %)			

Table B.5: Bubble oscillation frequency according to the mesh refinement and the choice of the threshold value β , the relative errors are given in brackets.

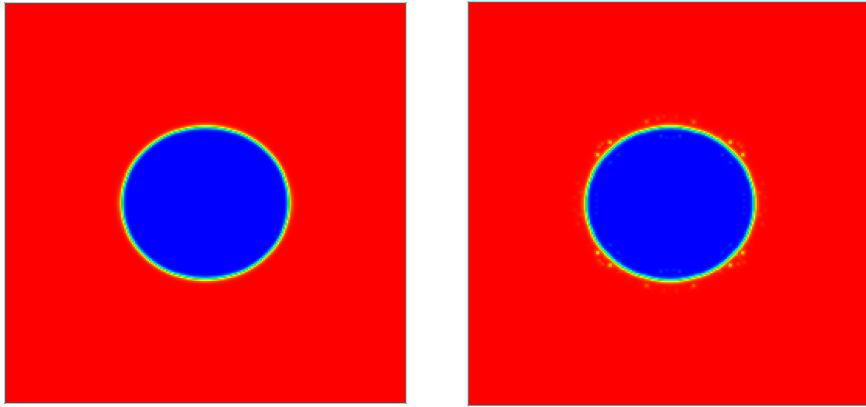


Figure B.8: Oscillating air bubble in liquid water at $t = 0.01$ s, left: $\beta = 1.10^{-3}$, right: $\beta = 1.10^{-2}$, mesh with 256 x 256 cells.

In a second study, the effect of the time step choice for one mesh refinement (128 x 128 cells) and one threshold value $\beta = 1.10^{-3}$ is observed. Three time steps are simulated : 0.025 ms, 0.0125 ms and 0.01 ms. The results are given in Table B.6. A good convergence of the oscillation frequency is obtained when the time step is decreased. Moreover, with a time step equal to 0.0125 ms, the interface sharpening equation is iterated only once like in the previous study with the same mesh but $\beta = 1.10^{-2}$ and a time step of 0.025 ms. Nevertheless, in this particular case, the prediction of the oscillation frequency is more accurate. Indeed, since the time step is reduced, the numerical diffusion at each time step is smaller. Thus, the interface needs less recompression iterations to be sharpened. Therefore, the interface is more efficiently sharpened at each time step, which conducts to a more

accurate prediction of the bubble motion. On the contrary, with the larger time step, the interface will be slightly thicker after one iteration of the interface sharpening equation. After a given duration of the simulation, this effect will be amplified, resulting in a less accurate interface location compared to a smaller time step. This effect can be seen in Figure 4.1. For a given iteration number (at the beginning of the recompression process), the final interface thickness is proportional to its initial width. Thus, the interfaces which are initially more diffused, that is to say in our context which have been obtained with a larger time step, are less sharpened after a given iteration number (equal to one here) of the recompression equation. One can note that in Figure 4.1, this phenomenon is amplified since we are studying much thicker interfaces than in this test case. No differences are observed with 0.0125 *ms* and 0.01 *ms* due to the precision of the method used to determine the oscillation frequency.

Time step	Iteration number	Oscillation frequency
0.025 <i>ms</i>	2	5.6 <i>s</i> ⁻¹ (1.8 %)
0.0125 <i>ms</i>	1	5.7 <i>s</i> ⁻¹ (0.2 %)
0.01 <i>ms</i>	1	5.7 <i>s</i> ⁻¹ (0.2 %)

Table B.6: Iteration number and bubble oscillation frequency according to the time step, $\beta = 1.10^{-3}$, the relative errors are given in brackets, mesh with the 128 x 128 cells.

This test case allow understanding more precisely the different phenomena appearing when the interface sharpening equation is iterated. The threshold value comparison highlighted that $\beta = 5.10^{-4}$ and $\beta = 1.10^{-3}$ predict the bubble oscillation frequency with the same accuracy.

B.4 Simulation of Thorpe’s experiment

Further studies have also been performed with the Thorpe’s experiment test case to optimize the threshold value and also to highlight the effect on the interface smearing criterion with other drag force laws.

B.4.1 Optimization of the threshold value β

With the Bhaga and Weber’s rising bubble test case, we showed that $\beta = 5.10^{-4}$ gave the best results in terms of final bubble velocity and bubble shape. However, the results obtained with $\beta = 1.10^{-3}$ were also quite close to the experimental data. The stationary and the oscillating bubble test cases did not allow discriminating these two values. Therefore, to validate the choice of $\beta = 5.10^{-4}$, the two values are compared with the Thorpe’s experiment test case. This new comparison allows a validation on a different flow type since the Thorpe’s experiment is an interfacial

liquid/liquid test case. The critical wavenumber, the time of the instability onset and the wave velocity are extracted from the interface motion, as detailed in section 4.5.2. The results are displayed in Table B.7. The time of the instability onset and the critical wavenumber are close for the two threshold values. Nevertheless, the simulation with $\beta = 1.10^{-3}$ predicts a smaller wave speed. Therefore, the threshold value $\beta = 5.10^{-4}$ seems appropriate for the simulation of different flow types.

Results	k_c (m^{-1})	t_{onset} (s)	u_{waves} ($cm.s^{-1}$)
$\beta = 5.10^{-4}$	219	2.1	3.1
$\beta = 1.10^{-3}$	200	2.1	1.9
Theory	232	1.5 – 1.7	2.38
Experiments	197 ± 58	1.88 ± 0.007	2.6
Bartosiewicz <i>et al.</i> [13]	143	1.9	2.5
Štrubelj [188]	157	2.0	3.0

Table B.7: Comparison of the critical wavenumber k_c , the time of the instability onset t_{onset} and the wave speed u_{waves} with two different threshold values β , the theoretical and experimental data and the simulations of Bartosiewicz *et al.* [13] and Štrubelj [188].

Finally, one can note the effect of the conservative implementation of the sharpening equation. Indeed, the mass balance error by time step in the whole domain decreases by 10^{-10} % with a non conservative implementation to 10^{-17} %.

B.4.2 Activation of the interface smearing criterion

A simulation with the drag force law 2 (see Equation (3.15)) is also performed to see a specific effect of the criterion on the interface smearing, which disappears with the drag force law 3 (Equation (6.7)). Figure B.9 proposes a comparison in terms of interface velocity between a simulation with systematic interface sharpening and another with the criterion proposed in section 4.5.1, which limits the recompression to diffused interfaces. The interface velocity is not well predicted if the interface sharpening equation is always applied. The implementation of the criterion is sufficient to correct this effect. Indeed, without the criterion, as soon as the simulation begins, the compression equation is solved. At this time, the interface is not diffused and looks like the first picture in Figure 4.8. Therefore, in all cells, the convective term $\nabla \cdot (\alpha_k (1 - \alpha_k) \mathbf{n})$ is equal to zero. Only the diffusive term $\epsilon \Delta \alpha_k$, is non zero in the cells on each side of the interface. Thus, the activation of the sharpening equation induces a non physical smearing of the interface. Nevertheless, in this case, the equation is solved only once thanks to the recompression threshold defined in section 4.4. Indeed, in the whole domain, no cells satisfy the condition $\alpha_{cl} \alpha_{cg} > 0.02$.

Therefore, the two terms $\sum_I^{ncel} \delta\alpha_k^I (1 - 2\alpha_k^I) \Omega^I$ and $\sum_I^{ncel} \alpha_{cl}^I \alpha_{cg}^I \Omega^I$ are taken equal to zero, which stops the interface compression after the first iteration. However, the spurious interface diffusion caused by this iteration induces after a few time steps the activation of the condition $\alpha_{cl}\alpha_{cg} > 0.02$. Then, the situation gets worse since the sharpening equation is iterated until the maximum number of iterations (fixed at 10 in our case) is reached. Indeed, due to the poor diffusion of the interface, the term $\sum_I^{ncel} \alpha_{cl}^I \alpha_{cg}^I \Omega^I$ is small. Moreover, the convective and diffusive terms of the sharpening equation predict also small modifications of the interface volume. Thus, the second term of the criterion $\sum_I^{ncel} \delta\alpha_k^I (1 - 2\alpha_k^I) \Omega^I$ is also very small. The ratio of these two terms is then easily higher than the threshold β . Therefore, the resolution of the compression equation cannot be stopped. Thus, non physical mass fluxes are taken into account for the estimation of the velocity field. With the new criterion, during all these time steps, the interface sharpening equation is deactivated and so do not introduce a spurious interface diffusion.

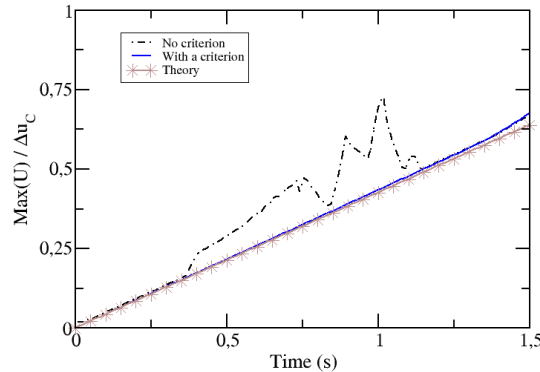


Figure B.9: Average interface velocity U normalized by the critical velocity over time with and without the interface smearing criterion, U is defined in Equation (4.21), the theory is given by Equation (4.20), drag force law 2 (see Equation (3.15)).

This effect is not visible with the drag force law 3 which compensates the effect of the non conservative implementation.

B.5 Conclusion

The results presented in this appendix confirms the conclusions of Chapter 4. A conservative implementation is important to ensure mass conservation and to predict well the different physical phenomena induced by the presence of large interfaces in a flow. Nevertheless, to limit spurious velocities, criteria are required to activate

the interface sharpening equation only if the interfaces are diffused and to stop the recompression process when the final interface thickness is reached. Details are given on how these two criteria work in different situations (non diffused interfaces, small time steps, etc). Finally, this appendix proposes to study the combined effects of the interface sharpening equation and the drag force model which are two predominant parameters for modeling interfacial interactions.

Appendix C

Validation of the Large Bubble Model on unstructured grids

In Part II, all the simulations have been performed on structured uniform Cartesian grid. Nevertheless, the industrial studies rarely uses such grids because domain geometries are often complex and some regions need to be more refined than others. Therefore, in this appendix, a short description and validation of the code behavior is proposed on unstructured grids. For this purpose, the first section is devoted to the presentation of the reconstruction process conducting to the addition of corrected terms. Then, the efficiency of the interface sharpening equation on unstructured grids is validated and the order of magnitude of spurious velocities induced by the Large Bubble Model on such grids is evaluated. All the meshes considered here are square grids with 5 cm side-length, obtained by Delaunay triangulation. Figure C.1 presents one of this grid composed by 9986 cells.

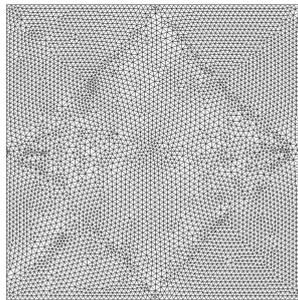


Figure C.1: Grid with 9986 cells obtained by Delaunay triangulation.

One can note that grids obtained with the Delaunay triangulation are not highly unstructured. Nevertheless, in industrial context, as far as possible, efforts are made to use grids with regular cells (cubic, rectangular and eventually triangular).

C.1 Reconstruction

Grids are considered unstructured when the neighbor number varies according to the considered vertex. In terms of cell center position, the straight line IJ formed by the centers I and J of two neighboring cells is not orthogonal to the face separating the two cells or does not cross the center of the cells face, as illustrated in Figure C.2. Thus, to reconstruct the value of a given variable X on I' knowing it on I, a correction at first order is used:

$$X_{I'} = X_I + \mathbf{II}' \cdot (\nabla X)_I \quad (3.1)$$

The same can be done at the cell face to obtain the projection of a variable in F, knowing it in O:

$$X_F = X_O + \mathbf{OF} \cdot \frac{1}{2} (\nabla X_I + \nabla X_J) \quad (3.2)$$

This last expression is used in particular to evaluate the curvature for the surface tension force and the mass fluxes in the interface sharpening equation. The curvature is obtained as follows (using the Gauss' theorem):

$$\kappa = - \int \nabla \cdot (\mathbf{n}) \Omega = \sum_{ij} \left(\mathbf{n}_{IJ} + \mathbf{OF} \cdot \frac{1}{2} (\nabla \mathbf{n}_I + \nabla \mathbf{n}_J) \right) \cdot S_{IJ} \quad (3.3)$$

with \sum_{IJ} the sum over the cell faces, \mathbf{n}_{IJ} the normal vector of the interface in O and S_{IJ} the surface vector of the cell face S_{ij} .

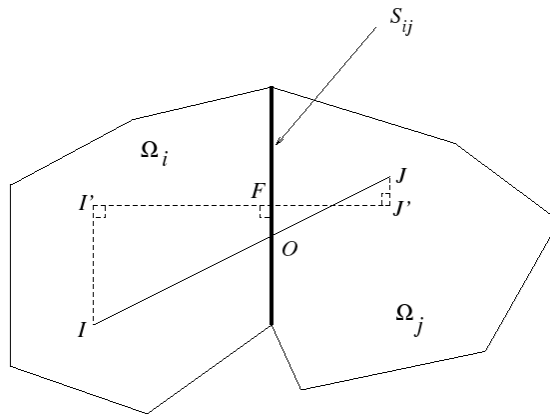


Figure C.2: Introduction of the notation for the correction terms applied to unstructured grids, I and J corresponds to the cell centers respectively of the cells Ω_i and Ω_j , I' and J' are their projection on the straight line orthogonal to the cell face S_{ij} and crossing it in F, O is the intersection between the line (IJ) and the cell face S_{ij} [38].

C.2 Efficiency of the interface sharpening equation

As described in section 4.4, the recompression threshold used to stop the interface sharpening equation when the interface has reached its final thickness is adapted to simulations involving unstructured grids. One main interrogation on this implementation is the efficiency of the sharpening step on such grids. To study this point, a stationary air bubble is simulated in still water (section 5.2) with an unstructured and two structured grids. The unstructured grid has been obtained by Delaunay triangulation (see Figure C.1) with 39734 cells and the two structured ones contain respectively 181 x 181 cells and 256 x 256 cells. The coarser structured mesh have a bit less cells than the unstructured grid and the refined structured grid approximately twice the cell number of the unstructured grid. The air bubble is initially diffused with a linear variation of the volume fraction between two circles of radii 1.1 *cm* and 0.9 *cm*. The interface sharpening is solved to sharpen the interface until the recompression threshold is reached. At the end of the recompression step, the positions of the isosurface of the air volume fractions ($\alpha_{cg} = 0.5$) are compared at 0.1, 0.5 and 0.9. Figure C.3 shows that the three obtained bubbles are superposed.

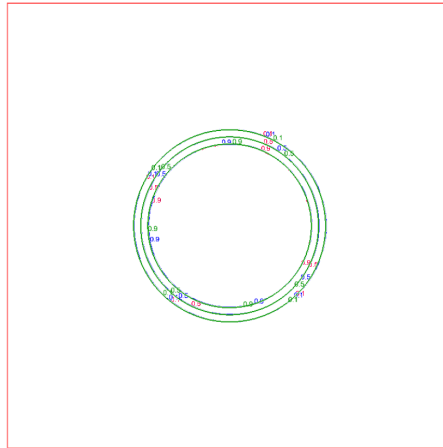


Figure C.3: Isosurface of the air volume fractions ($\alpha_{cg} = 0.5$) at 0.1, 0.5 and 0.9 obtained on an unstructured grid with 39734 cells (red) and two structured grid with respectively 181 x 181 cells (blue) and 256 x 256 cells (green), stationary bubble test case.

Therefore, this study shows that the interface sharpening equation is able to sharpen interfaces on unstructured grids. Moreover, the modified recompression threshold allows obtaining a regular interface thickness.

C.3 Evaluation of the spurious velocities

In this second section, the intensity of the spurious velocities obtained by using unstructured grids are evaluated. Thus, the stationary air bubble in still water is

simulated with three different unstructured grids obtained by Delaunay triangulation with respectively 2456, 9986 cells and 39734 cells. The time step is constant and respectively equal to $2 \cdot 10^{-4}$ s, $8 \cdot 10^{-5}$ s and $2 \cdot 10^{-5}$ s. The small time steps used for these simulations did not allow using more refined meshes. Nevertheless, the results on these three unstructured grids allow comparing the error levels with the structured grids. The comparison is presented in Figure C.4. The definitions for the evaluation of the relative errors and the capillary number can be found in section 5.2.2. The error levels are higher for all the quantities with the unstructured grids. These results were expected since no specific treatments, except the reconstruction presented in section C.1, have been applied to the surface tension model for unstructured meshes. The spurious velocities are concentrated in the interface region since their intensity is higher than in the whole domain. This study allows fixing the critical Capillary number for simulations on unstructured meshes, which is equal to 0.01. This value is ten times higher than for structured grids and corresponds to the value available in the literature [89, 148]. No mesh convergence is observed for the circularity. These results are due to the post-processing tool, which is not able to evaluate precisely the bubble perimeter L , required to evaluate the bubble circularity (see Equation 5.1). Indeed, if we look at the bubble shape in Figure C.3, it seems to have the same circularity with the three grids (structured and unstructured). It is superposed to the expected bubble contrary to the results presented in [38].

In Figure C.5, the distribution of the spurious velocities obtained with an unstructured grid is compared to a structured grid. As also observed in [38], with the unstructured grids, the recirculation regions are not organized along the diagonal directions but are more isotropically distributed.

Finally, the pressure profile is compared with the two grids (structured and unstructured) in Figure C.6. The unstructured mesh induces discrepancies of the pressure close to interfaces.

This study highlights that the spurious velocity level is higher on unstructured grids. Thus, to simulate flows with such meshes, the evaluation of the Capillary number will be a crucial step to ensure that the physical results are not affected by these velocities.

C.4 Conclusion

The studies proposed here highlight that the interface sharpening equation is valid also on unstructured grids. However, as expected, the spurious velocities are higher than on structured grids. It is important to note that a mesh convergence is still observed. The critical Capillary number is higher on such grids and has to be checked more carefully before performing simulations on unstructured meshes.

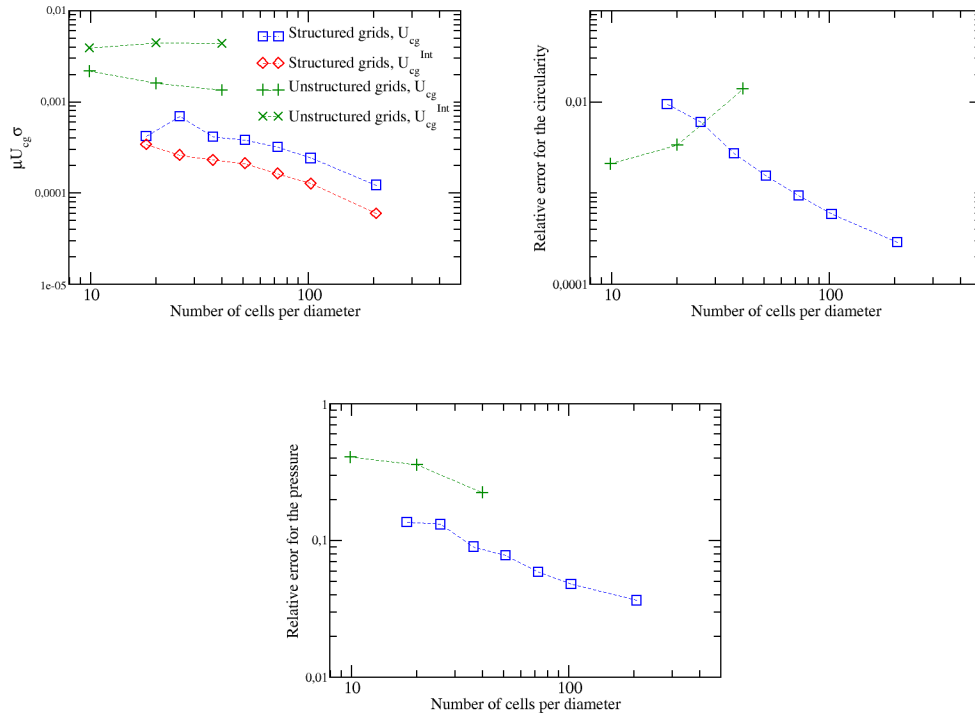


Figure C.4: Capillary number and relative error for the circularity and for the pressure obtained with the stationary bubble test case with structured and unstructured grids, logarithmic axes.

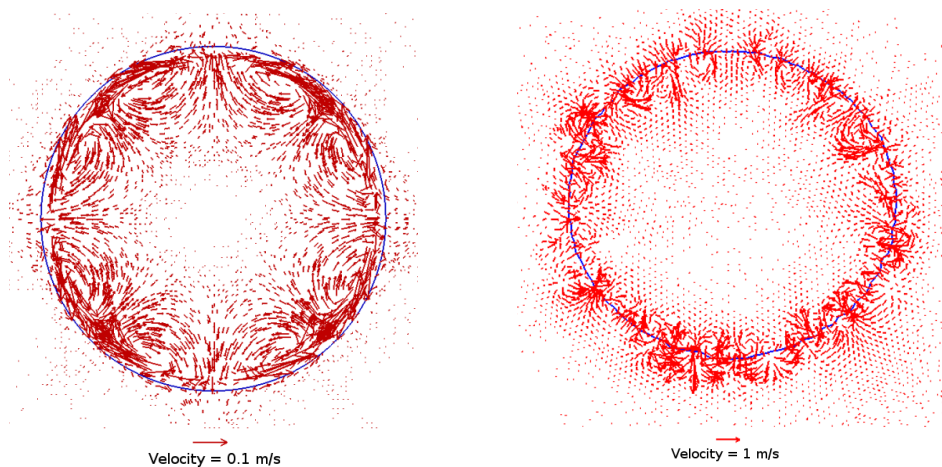


Figure C.5: Spurious velocities represented by the red arrows, the isosurface of the gas volume fraction ($\alpha_{cg} = 0.5$) appears in blue, left: structured grid with 181 x 181 cells and right: unstructured grid with 39734 cells.

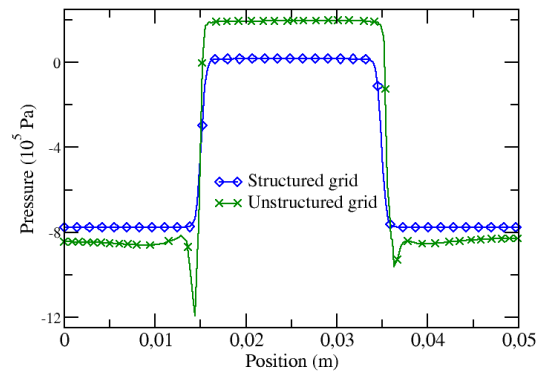


Figure C.6: Pressure profile obtained along one domain direction with a structured grid containing 181 x 181 cells (blue diamonds) and unstructured grid with 39734 cells (green crosses).

Appendix D

Calculation of convergence orders using the Richardson's extrapolation

The method to evaluate orders of convergence is based on the following Richardson's extrapolation [160]:

$$f_{th} = f_{m_1} + Cm_1^x + \mathcal{O}(m_1^x) \quad (4.1)$$

with f_{th} the theoretical value of the quantity f , x the convergence order, m_1 a mesh refinement and f_{m_1} the value of the parameter f obtained with the mesh refinement m_1 .

We can write the same expression for two other mesh refinements m_2 and m_3 :

$$f_{th} = f_{m_2} + Cm_2^x + \mathcal{O}(m_2^x) \quad (4.2)$$

$$f_{th} = f_{m_3} + Cm_3^x + \mathcal{O}(m_3^x) \quad (4.3)$$

By subtracting Equations (4.2) and (4.1), we obtain:

$$f_{m_2} - f_{m_1} = C(m_1^x - m_2^x) + \mathcal{O}(m_1^x - m_2^x) \quad (4.4)$$

The same subtraction is applied to Equations (4.3) and (4.2). Then, we express the ratio of these two equations to remove the unknown parameter C :

$$\frac{f_{m_3} - f_{m_2}}{f_{m_2} - f_{m_1}} = \frac{m_2^x - m_3^x}{m_1^x - m_2^x} + \mathcal{O}\left(\frac{m_2^x - m_3^x}{m_1^x - m_2^x}\right) \quad (4.5)$$

The specific situation where m_2 is twice more refined than m_1 and m_3 four times more refined is considered. Therefore, Equation (4.5) becomes:

$$\frac{f_{m_3} - f_{m_2}}{f_{m_2} - f_{m_1}} = \frac{\frac{1}{2^x} - \frac{1}{4^x}}{1 - \frac{1}{2^x}} + \mathcal{O}\left(\frac{m_2^x - m_3^x}{m_1^x - m_2^x}\right) \quad (4.6)$$

Then, the following simplification is applied:

$$\frac{\frac{1}{2^x} - \frac{1}{4^x}}{1 - \frac{1}{2^x}} = \frac{\frac{1}{2^x} \left(1 - \frac{1}{2^x}\right)}{1 - \frac{1}{2^x}} = \frac{1}{2^x} \quad (4.7)$$

Thus, Equation (4.6) can be written:

$$\frac{f_{m_3} - f_{m_2}}{f_{m_2} - f_{m_1}} = \frac{1}{2^x} + \mathcal{O}\left(\frac{m_2^x - m_3^x}{m_1^x - m_2^x}\right) \quad (4.8)$$

By taking the logarithmic formulation of Equation (4.8), we obtain the order of convergence x :

$$x = \frac{\ln(f_{m_2} - f_{m_1}) - \ln(f_{m_3} - f_{m_2})}{\ln(2)} \quad (4.9)$$

Appendix E

Further validations of the new drag force expression for the LBMo

This appendix proposes extra validations for the new drag force expression (6.7) developed in Chapter 6. Two test cases are considered: an interfacial liquid/liquid test case, the Rayleigh-Taylor instability in the Štrubelj's set of data [188] (see section 7.3) and a bubble test case, the oscillating bubble test case (see section 4.3.2).

E.1 Interfacial liquid/liquid test case: Rayleigh-Taylor instability

In Chapter 6, the simulation of the Kelvin-Helmholtz instability in the Thorpe's experimental configuration did not allow discriminating the new drag force (6.7) from the standard expression (6.1). The same comparison is thus proposed with the Rayleigh-Taylor instability in the Štrubelj's set of data [188] (see section 7.3). The new drag force expression (6.7) is compared to the standard expression (6.1) and the previous drag force expression (3.15) with $\tau = 1.10^{-7}$ s.

Figure E.1 displays the evolution of the interface position compared with the analytical expression (7.1). The evolution of the interface position is close to the theoretical curve for the three drag forces. The difference observed at the very beginning is due to the interface initialization. Moreover, the three drag forces predict the same interface position over time.

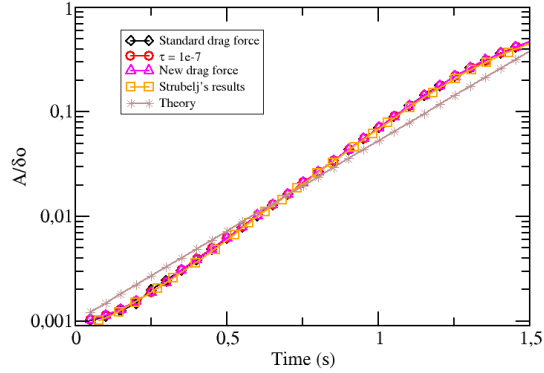


Figure E.1: Comparison between the three different drag forces and Štrubelj's simulation results [188], the curves are superimposed.

The same comment can be done for the evolution of the interface shape. Thus, only the results obtained with the LBMO coupled with the new drag force expression are presented in Figure E.2.

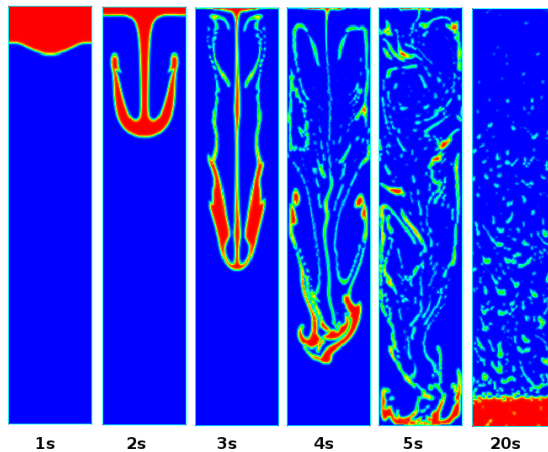


Figure E.2: Evolution of the Rayleigh Taylor instability obtained with the LBMO coupled with the new drag force (6.7).

The Rayleigh-Taylor instability in the Štrubelj's set of data [188] does not allow discriminating the drag force models. The standard drag force seems to be suitable for the simulation of interfacial liquid/liquid test cases.

E.2 Bubble test case: Oscillating bubble

To finish the validation of the new drag force expression, a last comparison is proposed between the new drag force model (6.7) and the previous drag force (3.15) with $\tau = 1.10^{-7}$ s. Indeed, with the Bhaga and Weber’s rising bubble test case, it was difficult to know which drag force allowed obtaining the best bubble shape and final velocity since the results were very comparable. Therefore, the oscillating bubble is simulated. The simulation parameters are given in section 4.3.2. For this study, the deformation rate is fixed at 0.05 and the mesh with 512 x 512 cells is used. The time step is equal to 0.0125 ms. The results are presented in Table E.1 and Figure E.3. The new drag force model (6.7) predicts better the frequency and the characteristic time of decay of the bubble oscillations.

Drag force model	f_0 (s^{-1})	τ_0 (s)
Previous drag force with $\tau = 1.10^{-7}$ s	5.56 (2.6 %)	2.35 (46 %)
New drag force	5.67 (0.7 %)	3.16 (28 %)

Table E.1: Frequency and characteristic time of decay of the bubble oscillations according to the drag force model, initial deformation rate equal to 0.05, mesh with 512 x 512 cells.

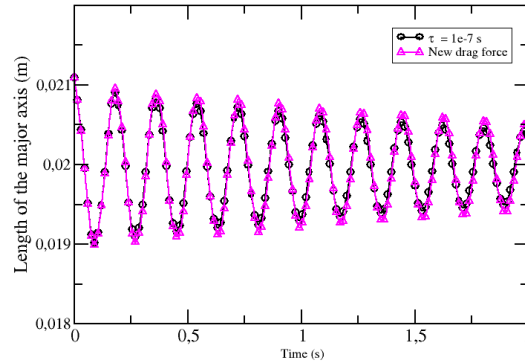


Figure E.3: Comparison between the two different drag forces in terms of bubble oscillation, initial deformation rate equal to 0.05, mesh with 512 x 512 cells.

E.3 Conclusion

These two extra simulations highlighted that the standard drag force (6.1) was able to simulate interfacial liquid/liquid test cases with the same accuracy than the

new drag force expression (6.7). Such test cases did not allow discriminating the two laws. Then, the oscillating bubble test case showed the improvement brought by the new drag force expression (6.7) compared to the previous expression (3.15) with $\tau = 1.10^{-7}$ s, which was not clear with Bhaga and Weber's rising bubble test case.

Appendix F

Few words about the Large Interface Model (LIM)

This appendix is devoted to the Large Interface Model (LIM) available in the code NEPTUNE_CFD for the simulation of large interfaces within the two-fluid model. In the first section, the tracking method is described. Then, the interfacial momentum source terms are presented. Finally, the treatment of mass transfer for interfaces with phase change is detailed.

F.1 Interface tracking method

The LIM, like the LBMo, has been developed to locate large interfaces in the computational domain at each time step of the calculation in order to apply specific models to them. The LIM can be split into two steps. The first step is the large interface recognition and the second the application of models [34].

To track the interface, the LIM is based on the LI3C method (Large Interface represented with 3 Cells thick layers). The goal of this method is to define three cells to describe the interface: one stratified cell containing the interface with a mixture of the two continuous fields ($\alpha_{cl}\alpha_{cg} \neq 0$) and one cell on each side of the first one with only one field in it, as shown in Figure F.1. The stratified cell is first detected thanks to the evaluation of the volume fraction gradient [34]. This cell is then used to detect the two others.

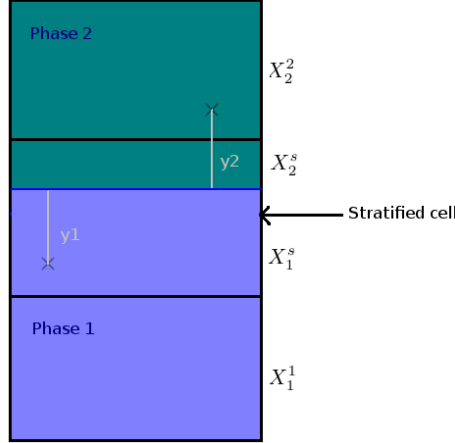


Figure F.1: Schematic view of the three cells in the LI3C method and notations for the heat flux, phase 1 corresponds to the liquid phase and phase 2 the vapor phase.

F.2 Interfacial momentum source terms

The second part of the LIM is dedicated to the models. These models have been developed over the last decades to simulate large interfaces with two-field codes. For laminar and isothermal flows, only the drag force and the friction models are applied. The drag force model corresponds to the standard expression (6.1). Within the three-cells stencil, this drag force is only applied in the interface normal direction and the friction model is added in the tangent direction to take into account the friction along the interface [34]. With this model, a velocity sliding is allowed at large interfaces since they have a finite thickness due to the cell size and cannot be considered resolved in the model. The friction force has the following expression:

$$\mathbf{F}_{Frict,cl \rightarrow cg} = \rho_{cg} (\mathbf{u}_{cg}^*)^2 \frac{(\mathbf{u}_{cl} - \mathbf{u}_{cg})}{\|\mathbf{u}_{cl} - \mathbf{u}_{cg}\|} A^{Int} \quad (6.1)$$

with \mathbf{u}_{cg}^* the gas friction velocity and A^{Int} the interface area.

In this thesis, all the simulations performed with LIM use the interface sharpening equation developed for the LBMo. Details about the implementation of the recompression equation can be found in Chapter 4.

Finally, since the LIM have been developed for horizontal flows, no surface tension model has been implemented. Therefore, for the comparison, the CSF model (see section 3.4.2) is used.

F.3 Phase change model with the LIM

In the framework of the LI3C, presented in section F.1, heat fluxes with smooth interfaces and without turbulence are implemented as follows for the liquid phase:

$$q_l^S = h_l (T_{sat} - T_l) \quad (6.2)$$

with h_l the exchange coefficient : $h_l = \frac{\lambda_l}{y_l}$. T_{sat} , T_l and y_l evaluated thanks to the volume fraction of the liquid phase in the stratified cell : α_s . One can note that the vapor heat flux can be obtained by replacing the subscript l by v . Therefore, T_l and y_l (replaced by X_l in the following expression) and T_{sat} are obtained using:

$$X_l = \alpha_s X_l^s + (1 - \alpha_s) X_l^1 \quad (6.3)$$

and

$$T_{sat} = (1 - \alpha_s) T_{sat}^s + \alpha_s T_{sat}^2 \quad (6.4)$$

The notations and the configuration of the three cells in the LI3C method are given in figure F.1.

To obtain the volume expression of the heat fluxes, the following relation is used, as done in [171]:

$$q_k^V = \frac{S^{Int}}{\Omega} q_k^S \quad (6.5)$$

With S^{Int} the interface surface in the cell containing the interface and Ω the cell volume.

For the liquid phase, the source term is evaluated in the stratified cell and then extrapolated in the two others cells.

All the mass and heat transfer terms are implicitly calculated.

Appendix G

Further comparisons between the LBMo and dedicated large interface tracking methods

In this appendix, further comparisons of the LBMo with dedicated approaches for the simulation of large interfaces are proposed (see Chapter 7). The first section is devoted to comparisons with one-fluid models (Front-Tracking and Level-Set). The next section is an extra comparison of the LBMo with the LIM with a bubble and an interfacial liquid/liquid test cases.

G.1 Comparison between the LBMo and one-fluid models

G.1.1 Rayleigh-Taylor instability

The simulation is performed with the Popinet and Zaleski's set of data [153]. For this test case, no surface tension is applied. Gravity is equal to 9.81 m.s^{-2} . The properties of the two fluids are given in Table G.1. The Atwood number is equal to 0.76.

	Density (kg.m^{-3})	Viscosity (Pa.s)
Liquid 1	1.225	$3.13.10^{-3}$
Liquid 2	0.1694	$3.13.10^{-3}$

Table G.1: Properties of the two liquid phases for the simulation of the Rayleigh-Taylor instability with Popinet and Zaleski's set of data [153].

The closed box has the following dimensions: $H = 4 \text{ m}$ and $L = 1 \text{ m}$. The interface is initialized in the middle of the box at 2 m with an initial amplitude of

the perturbation equal to $0.05 m$. The same boundary conditions are used as in section 7.3. The mesh contains 128×512 cells. The time step is constant, equal to $1 ms$.

In this configuration, the interface motion is quicker due to the higher Atwood number. Moreover, the amplitude of the initial interface deformation is higher. Therefore, with the parameters defined in Chapter 4 for the interface sharpening equation, the interface is not smooth but has a step shape. Thus, the 5 cells thickness induces, in this configuration, instabilities, visible in Figure G.1, which then are developed during the simulation and conduct to a non-physical result.

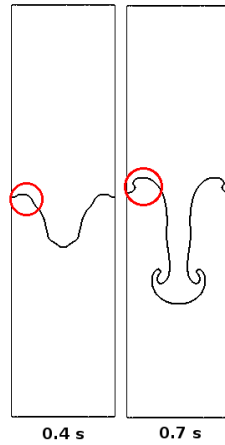


Figure G.1: Rayleigh-Taylor instability in the Popinet and Zaleski's configuration [153] with the parameters defined in Chapter 4 for the interface sharpening equation, instabilities (red circles for example) are developed at the interface at the beginning of the simulation and induces non-physical deformations.

To prevent the apparition of these instabilities, the solution is to increase the interface thickness only at the beginning of the simulation to be able to reproduce the detachment of the two particles at the end. Two simulations have been performed, called S1 and S2. In the first one (S1), the parameter ε is taken equal to $2\Delta x$ until $0.3 s$, which corresponds approximately to a thickness of 16 cells. Then, a linear function is used to reduce progressively ε until $0.5 s$, where the parameter reaches its original value of $\frac{\Delta x}{2}$. In the second simulation (S2), the transition is quicker in order to limit the use of a larger interface. Thus, ε is equal to $2\Delta x$ until $0.2 s$ and is reduced to $\frac{\Delta x}{2}$ at $0.3 s$. The results of these two simulations are proposed in Figure G.2. The evolution of the interface position and shape is in good agreement with the results of Popinet and Zaleski [153]. The simulation S2 is sensitively ahead of simulation S1, and so closer to the expected results. Finally, in our simulations, a detachment of two particles is observed at the end of the simulation, which is not the case in the Popinet and Zaleski's simulation [153]. Indeed, the two authors used a Front-Tracking method, which, contrary to our method, does not allow interface breakup.

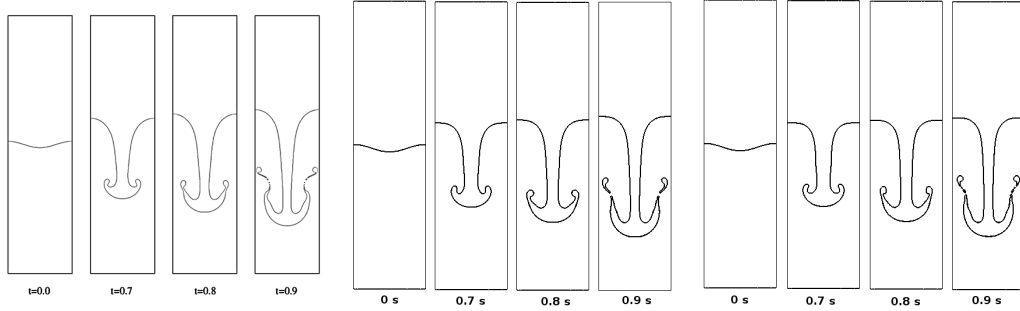


Figure G.2: Rayleigh-Taylor instability in the Popinet and Zaleski's configuration [153] with a variable parameter ε controlling the interface thickness fixed by the interface sharpening equation (see Chapter 4), left to right: simulation of Popinet and Zaleski [153], simulation S1 and simulation S2.

G.1.2 Kelvin-Helmholtz instability

To complete the validation, two other Kelvin-Helmholtz instability test cases have been simulated. These cases refer to experiments performed by Duponcheel and Bartosiewicz [43]. For these cases, experimental data and other simulation results obtained with a Level-Set code are available in the literature. This section corresponds to a paper published in Computers & Fluids [12].

G.1.2.1 Presentation of the two cases

The simulations are performed with the same parameters described in section 4.5.2. The theory is still valid. The only difference is the properties of the two fluids which are presented in Table G.2.

		Density ($kg.m^{-3}$)	Viscosity ($Pa.s$)	Surface tension ($N.m^{-1}$)
Case 2	Kerosene	783	0.0015	0.029
	Water	1000	0.001	
Case 3	n-Hexane	659	0.0003	0.035
	Water	1000	0.001	

Table G.2: Properties of the two liquid phases for the simulation of the Kelvin-Helmholtz instability in the experimental configuration of Duponcheel and Bartosiewicz [43].

The simulation is performed with a constant time step equal to $0.3 ms$ for case 2 and to $0.25 ms$ for case 3, which ensures that the CFL number stays under 0.9. Simulations in 3D have also been performed. The extra dimension is equal to $10 cm$. The mesh contains $80 \times 3660 \times 100$ cells. The time step is constant and equal to $0.5 ms$ for the two cases.

G.1.2.2 Presentation of the Level-Set code

These cases have been also simulated with a Level-Set code [56, 176]. This code solves the single-fluid Navier-Stokes' equations in velocity-pressure formulation. The Poisson equation for the pressure is solved using the multigrid HYPRE library. A Level-Set function is used to track the interface and is periodically re-initialized by solving a Hamilton-Jacobi equation to reset the Level-Set as a distance function. The momentum balance equation is discretized using second order finite differences while the transport of the Level-Set is computed using the WENO5 discretization [180]. The equations are integrated in time using a Runge-Kutta 3 scheme [181]. The simulations with this code have been performed in 2D on two different grids: a coarser 64 x 3904 grid and a finer 80 x 4880 grid. The time steps are adaptive with a Fourier limiter equal to 0.1 and a maximum CFL of 0.3.

G.1.2.3 Simulation of case 2

First, the side and top views of the Kelvin-Helmholtz instability are compared with the different simulations and the experiment. For the kerosene, the 3D top views are presented in Figure G.3. The experiment and the 3D simulations both predict an essentially 2D instability. Figure G.4 displays the side views obtained experimentally and with the Level-Set code, the LBMo simulation in 2D and 3D. The pictures are very similar. Nevertheless, the wavenumber seems to be smaller in the simulations than in the experiment. Moreover, the two codes in 2D predict some roll-up of the waves which have not been observed experimentally. Thus, the instability breakdown in the 3D simulations is in better agreement with the experiments.

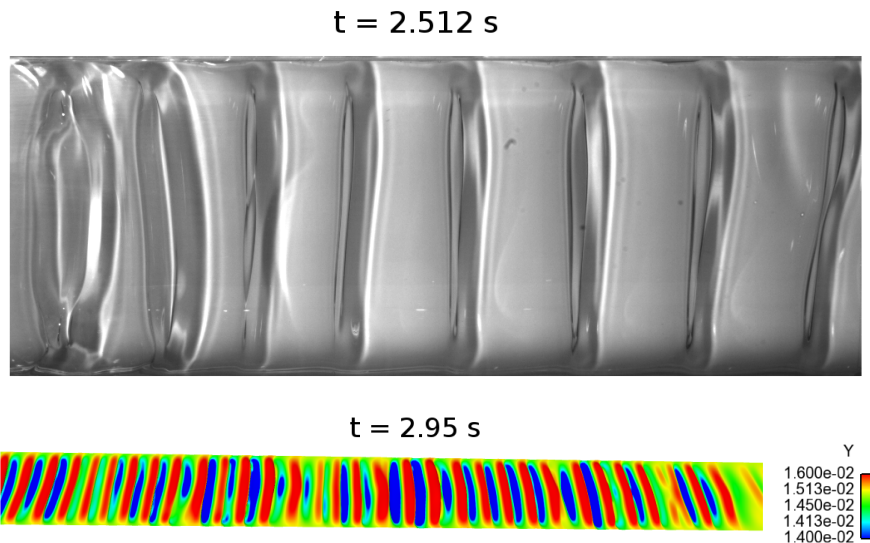


Figure G.3: Top views of case 2, top: experimental results at 2.512 s, bottom: NEPTUNE_CFD 3D at 2.95 s (mesh with 80 x 3660 x 100 cells, time step equal to 0.5 ms).

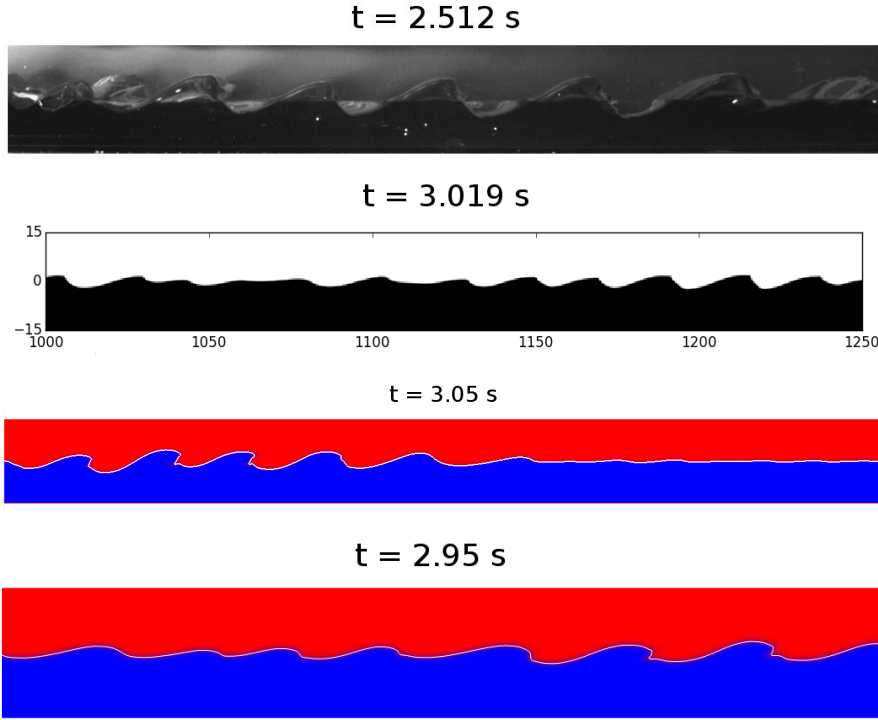


Figure G.4: Side views of case 2, top to bottom: experimental results at 2.512 s, Level-Set simulation at 3.019 s (mesh with 80 x 4880 cells), NEPTUNE_CFD 2D at 3.055 s (mesh with 80 x 4880 cells, time step equal to 0.3 ms) and NEPTUNE_CFD 3D at 2.95 s (mesh with 80 x 3660 x 100 cells, time step equal to 0.5 ms).

Results	k_c (m^{-1})		t_{onset} (s)	
	Case 2	Case 3	Case 2	Case 3
2D simulation	244	462	1.9	0.8
3D simulation	261	411	1.9	0.8
Level-Set, coarse grid	286	309	2.7	1.75
Level-Set, fine grid	322	405	2.7	1.65
Theory	270	309	1.1	0.81
Experiment	196	322	2.1	1.18

Table G.3: Comparison between our simulations, the simulations of Duponcheel and Bartosiewicz [43], the theoretical and experimental data, the 2D simulation with the LBMO corresponds to a grid with 80 x 4880 cells and a time step of 0.3 ms, the 3D simulation to a grid with 80 x 3660 x 100 cells and a time step of 0.5 ms, the Level-Set coarse grid to a 64 x 3904 cells grid and the Level-Set fine grid to a 80 x 4880 cells grid.

Then, if we characterize quantitatively the instability (Table G.3), the simulations predict larger critical wavenumbers than in the experiment and in theory. Nevertheless, the 3D simulation with the LBMo is closer to the experiment in terms of wavenumber. Concerning the second quantity, one can note that different methods have been used to determine the time of the instability onset. Thus, for the experiment and the Level-Set simulations, t_{onset} has been evaluated from the side views, when the deformation becomes visible whereas in the simulations performed with NEPTUNE_CFD, the standard deviation growth of the interface height in a log diagram has been used (see Figure G.5). This second method is more precise and can explain that the results are in better agreement with the theory and the experiment.

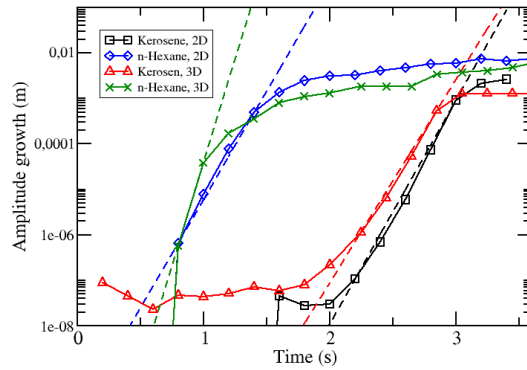


Figure G.5: Amplitude growth obtained by evaluating the standard deviation of the interface over time for cases 2 and 3, only the middle 0.6 meters long section of the channel is used for this analysis, the dashed line corresponds to the asymptotic amplitude growth used to determine the time of the instability onset.

G.1.2.4 Simulation of case 3

The same study is proposed for the n-hexane (case 3). Figure G.6 displays the side views. Compared to case 2, the maximum amplitude of the waves is smaller. Moreover, the waves predicted by the 3D simulations are less regular. Indeed, if we look at the top views in Figure G.7, we see that the predicted instability is not two-dimensional at all. The experimental results highlight a “V“-shape wave front structure, which is not clearly visible on the 3D simulation top view. However, if we compare the amplitude growth obtained with the LBMo in 2D and in 3D, the linear region of the growth disappear in the 3D simulation (see Figure G.5). Indeed, because of the non linear secondary instabilities, the linear theory is not valid anymore in 3D. This loss of the linear region is not observed on case 2 where no 3D structures have been highlighted in the experiments. Finally, in the 3D

simulations, the late evolution of the flow is interesting as larger 2D waves tend to appear later in superposition of the irregular wave pattern.

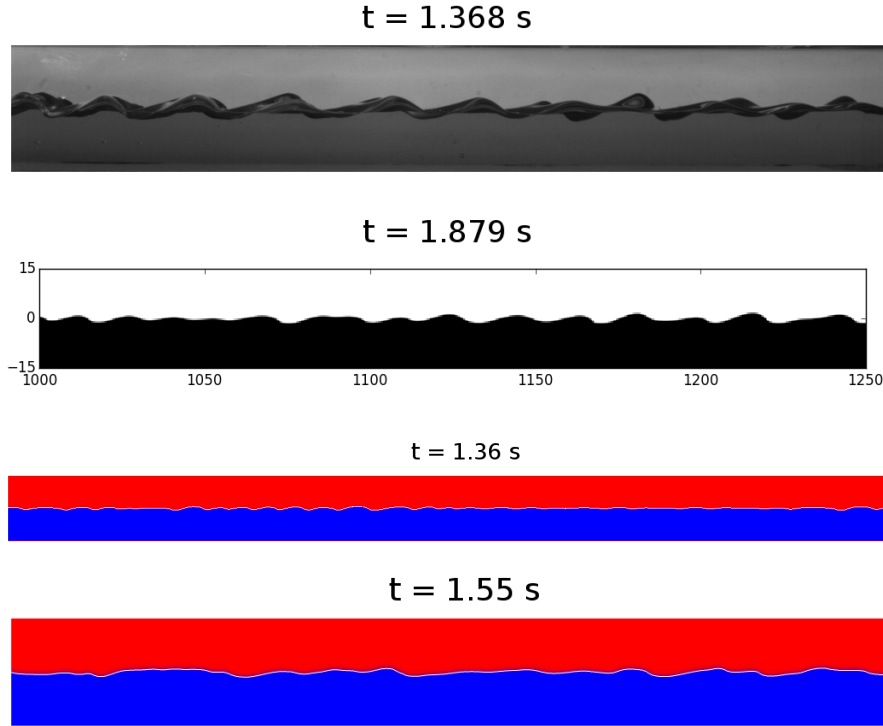


Figure G.6: Side views of case 3, top to bottom: experimental results at 1.368 s, Level-Set simulation at 1.879 s (mesh with 80×4880 cells), NEPTUNE_CFD 2D at 1.36 s (mesh with 80×4880 cells, time step equal to 0.25 ms) and NEPTUNE_CFD 3D at 1.55 s (mesh with $80 \times 3660 \times 100$ cells, time step equal to 0.5 ms).

As previously observed, the simulations predict a larger wavenumber. However, the LBMo predict quite well the time of the instability onset compared to the Level-Set. The effect of the grid is more important with the n-hexane than the kerosene. Indeed, the sensibility difference of the wavenumber to the mesh is likely due to the difference of viscosity between the kerosene and the n-hexane [43] (Table G.3). Finally, the experiments show that the instability growth is faster for the n-hexane. This is also observed in the 2D simulation with the LBMo when the evolution of the standard deviation growth is plotted in Figure G.5. The curve slope is larger for the n-hexane in the amplitude growth region (dashed lines).

To conclude on these two cases, the LBMo is able to simulate with a good accuracy the two Kelvin-Helmholtz instability test cases. The results are in good agreement with the experimental and theoretical data. For some parameters, a better prediction has been obtained with the LBMo than with the Level-Set method.

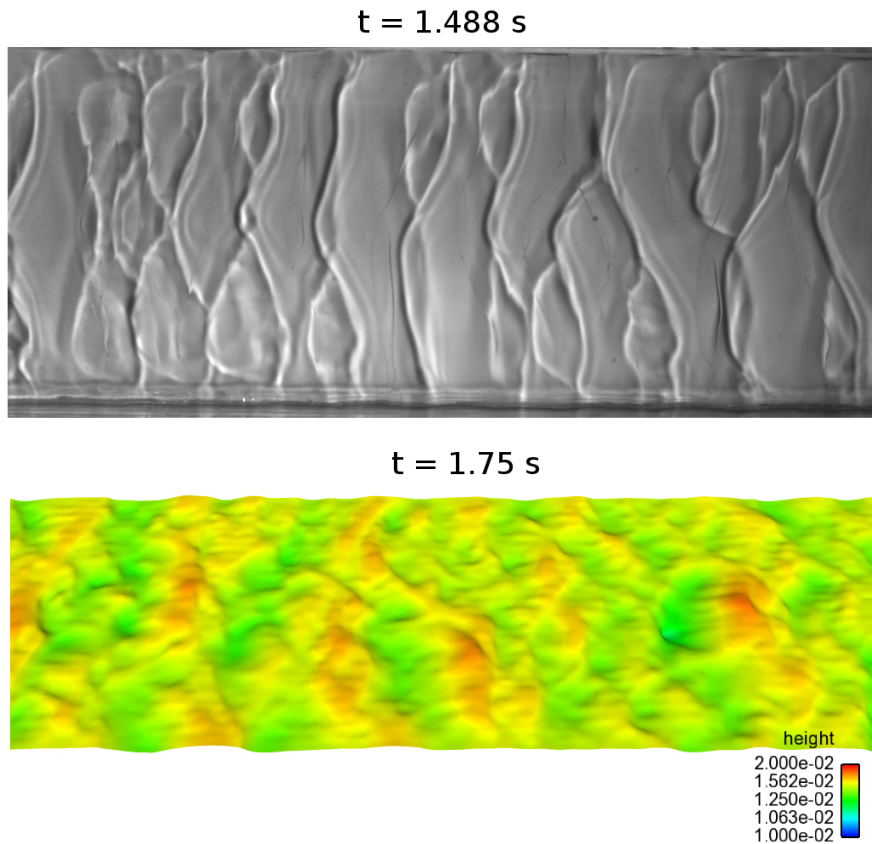


Figure G.7: Top views of case 3, top: experimental results at 1.488 s, bottom: NEPTUNE_CFD 3D at 1.75 s (mesh with 80 x 3660 x 100 cells, time step equal to 0.5 ms).

G.2 Comparison between the LBMo and the LIM

Two extra comparisons are presented in this section: one with the Bhaga and Weber's rising bubble test case (see section 4.4.2) and the other with the Rayleigh-Taylor instability in the Štrubelj's set of data (see section 7.3). LIM simulations are performed with the interface sharpening equation detailed in Chapter 4.

G.2.1 Bhaga and Weber's rising bubble test case

The two approaches are compared with the simulation of the Bhaga and Weber's bubbles in case d (see section 4.4.2 for details) in terms of final bubble shape and final velocity prediction. Figure G.8 displays the final bubble shape obtained with the LBMo and with the LIM. The two approaches overpredict the width of the bubble. Nevertheless, the effect is higher with the LIM.

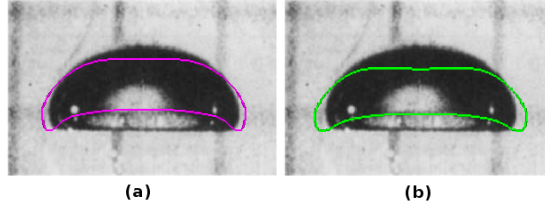


Figure G.8: Comparison between the LBMo (a) and the LIM (b), the predicted isosurfaces of α_{cg} ($\alpha_{cg} = 0.5$) at 0.6 s are superposed to the Bhaga and Weber's experimental data [16] in case d.

Then, the final bubble velocity is compared in Table G.4. The LIM slightly underevaluates the velocity.

Simulation	Final bubble velocity ($cm.s^{-1}$)
LBMo	28.9 (0.3 %)
LIM	27.7 (4.5 %)

Table G.4: Final bubble velocity obtained for case d with the LBMo and the LIM, the relative errors are given in brackets.

Finally, the two simulations have been performed on 24 cores for a duration of 30 minutes with the same grid and time step. The LBMo simulates the rising bubble test case with a better accuracy than the LIM without increasing the computational cost.

G.2.2 Rayleigh-Taylor instability

A last comparison is proposed with the simulation of the Rayleigh-Taylor instability in the Štrubelj's set of data (see section 7.3). The evolution of the interface position is displayed in Figure G.9 for the two approaches at short times, where the linear approximation is valid. The results are superposed. No differences are observed between the two models.

The interface shape evolves in the same way for the two approaches (see Figure E.2).

G.3 Conclusion

The results presented in this appendix confirms that the LBMo is able to simulate large interfaces with the same efficiency than dedicated methods using one-fluid or two-fluid models. The computational cost is not increased compared to the LIM.

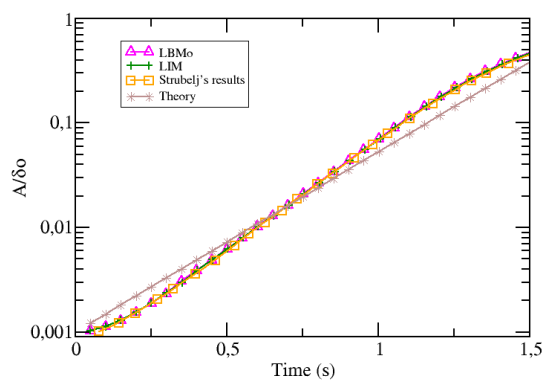


Figure G.9: Comparison between the LBMO, the LIM and Štrubelj's simulation results [188], the curves are superimposed.

Appendix H

Theory of the sucking problem

In this appendix, the expressions of the temperature profile and the evolution of interface position are demonstrated.

H.1 Notations

For this demonstration, a new spatial coordinate is defined to locate the steam/water interface at 0:

$$\xi = x - \int_0^t v_s(t') dt' \quad (8.1)$$

with v_s the interface velocity.

Then, the parameter η is introduced:

$$\eta = \frac{\xi}{\sqrt{2\chi_l t}} \quad (8.2)$$

Finally, different constants are used:

$$B = \frac{\chi_l \rho_l}{C \rho_v}, \quad C = \frac{\lambda_l}{L \rho_v} \quad \text{and} \quad \beta = \frac{\rho_v}{\rho_l} \quad (8.3)$$

H.2 Energy balance equations and other relations

The energy balance equation in the liquid phase with the new spatial coordinate has the following expression:

$$\frac{\partial T}{\partial t} + (v - v_s) \frac{\partial T}{\partial \xi} = \chi_l \frac{\partial^2 T}{\partial \xi^2} \quad (8.4)$$

By using the energy and mass jump conditions:

$$\begin{aligned} \rho_l (v_l - v_s) L &= -\lambda_l \left. \frac{\partial T}{\partial \xi} \right|_{\xi=0} \\ -\rho_g v_s &= \rho_l (v_s - v_l) \end{aligned} \quad (8.5)$$

We can rewrite Equation (8.4):

$$\frac{\partial T}{\partial t} - \beta v_s \frac{\partial T}{\partial \xi} = \chi_l \frac{\partial^2 T}{\partial \xi^2} \quad (8.6)$$

The interface velocity has the following expression:

$$v_s = C \left. \frac{\partial T}{\partial \xi} \right|_{\xi=0} \quad (8.7)$$

with T the liquid temperature.

H.3 Temperature profile

Let us consider the following expression for the liquid temperature:

$$T(x, t) = B\phi(\eta) \quad (8.8)$$

Using this expression in Equation (8.6), the differential equation for ϕ is obtained:

$$\phi'' + (\eta + \phi'(0))\phi' = 0 \quad (8.9)$$

Therefore, we have:

$$\frac{\phi''}{\phi'} = -(\eta + \phi'(0)) \quad (8.10)$$

After a first integration, we obtain:

$$\ln(\phi') = -\left(\frac{\eta^2}{2} + \phi'(0)\eta\right) + a \quad (8.11)$$

with $a = \ln(\phi'(0))$.

Then,

$$\phi' = \phi'(0) \exp\left(-\left(\frac{\eta^2}{2} + \phi'(0)\eta\right)\right) \quad (8.12)$$

This expression is integrated:

$$\phi = \int_0^\eta \phi'(0) \exp\left(-\left(\frac{\eta'^2}{2} + \phi'(0)\eta'\right)\right) d\eta' + b \quad (8.13)$$

To find a primitive of the exponential function, a binomial expansion is used:

$$\phi = \int_0^\eta \phi'(0) \exp\left(-\left(\frac{\eta'}{\sqrt{2}} + \frac{\phi'(0)}{\sqrt{2}}\right)^2 + \frac{\phi'(0)^2}{2}\right) d\eta' + b \quad (8.14)$$

Then, the following quantities are introduced:

$$x = \frac{\eta + \phi'(0)}{\sqrt{2}} \quad \text{and} \quad x_0 = \frac{\phi'(0)}{\sqrt{2}} \quad (8.15)$$

Therefore, we obtain:

$$\phi = \phi'(0) \exp(x_0^2) \int_{x_0}^x \sqrt{2} \exp(-x^2) dx + b \quad (8.16)$$

If the definition of the error function is used, $\text{erf}(x_0, x) = \frac{2}{\sqrt{\pi}} \int_{x_0}^x \exp(-t^2) dt$:

$$\phi = \phi'(0) \exp(x_0^2) \sqrt{\frac{\pi}{2}} \text{erf}(x_0, x) + b \quad (8.17)$$

To find b, the limit when η tends to 0 ($\lim_{x \rightarrow x_0} \text{erf}(x_0, x) = 0$) is taken:

$$\phi(\eta \rightarrow 0) = \frac{T_{sat}}{B} = b \quad (8.18)$$

Thus, we have the temperature profile:

$$T = T_{sat} + B\phi'(0) \exp(x_0^2) \sqrt{\frac{\pi}{2}} \text{erf}(x_0, x) \quad (8.19)$$

To determine the value of $\phi'(0)$, the value of the liquid temperature when η tends to $+\infty$ is used:

$$\begin{aligned} \lim_{x \rightarrow +\infty} \text{erf}(x_0, x) &= 1 \\ \lim_{\eta \rightarrow +\infty} \phi'(\eta) &= \frac{T_{max}}{B} \end{aligned} \quad (8.20)$$

Thus,

$$\phi'(0) \exp\left(\frac{\phi'(0)^2}{2}\right) = \sqrt{\frac{2}{\pi}} \frac{T_{max} - T_{sat}}{B} \quad (8.21)$$

H.4 Interface position

We have:

$$T(x, t) = B\phi(\eta) \quad \text{and} \quad \phi'(0) = \left. \frac{\partial \phi}{\partial \eta} \right|_{\eta=0} = \sqrt{2\chi_l t} \left. \frac{\partial \phi}{\partial \xi} \right|_{\xi=0} \quad (8.22)$$

Therefore,

$$\phi'(0) = \frac{\sqrt{2\chi_l t}}{B} \left. \frac{\partial T}{\partial \xi} \right|_{\xi=0} \quad (8.23)$$

Now, we know that:

$$\left. \frac{\partial T}{\partial \xi} \right|_{\xi=0} = \frac{v_s}{C} \quad \text{and} \quad BC = \frac{\chi_l \rho_l}{\rho_v} \quad (8.24)$$

Then,

$$\phi' (0) = \frac{\rho_v \sqrt{2t}}{\rho_l \sqrt{\chi_l}} v_s \quad (8.25)$$

Thus,

$$v_s = \phi' (0) \frac{\rho_l \sqrt{\chi_l}}{\rho_v \sqrt{2t'}} \quad (8.26)$$

With the interface velocity, we can deduce the interface position by using:

$$X (t) = \int_0^t v_s (t') dt' \quad (8.27)$$

with $X (t)$, the interface position.

Thus,

$$X (t) = \int_0^t \phi' (0) \frac{\rho_l \sqrt{\chi_l}}{\rho_v \sqrt{2t'}} dt' = \phi' (0) \frac{\rho_l \sqrt{2\chi_l t}}{\rho_v} \quad (8.28)$$

which gives:

$$X (t) = \frac{\phi' (0)}{\beta} \sqrt{2\chi_l t} \quad (8.29)$$

Appendix I

Further validations of the mass transfer term for large interfaces with phase change

In this appendix, further validations of the heat and mass transfer model developed for the simulation of large and deformable interfaces with phase change using the LBMo are presented. The results are compared with analytical solutions and the LIM (see Appendix F).

I.1 Sucking problem at $1.013.10^7 Pa$

In this section, the sucking problem is studied at a higher pressure: $1.013.10^7 Pa$, closer to pressure occurring in a reactor vessel or a steam generator of a nuclear power plant. No experimental data are available at such pressure. Thus, it is quite difficult to find test cases that allow assessing CMFD tools in such conditions.

	Density ($kg.m^{-3}$)	Viscosity ($Pa.s$)	Heat capacity ($J.kg^{-1}.K^{-1}$)	Thermal conductivity ($W.m^{-1}.K^{-1}$)
Steam	56.4	$2.2.10^{-5}$	$1.5.10^4$	$6.36.10^{-2}$
Liquid water	670	$8.5.10^{-5}$	$6.5.10^3$	0.520

Table I.1: Properties of the two fluids for the simulation of the sucking problem with a pressure of $1.013.10^7 Pa$.

The physical properties of steam and liquid water with this pressure condition are given in Table I.1. They are updated at each time step (see Figure 9.1 right) using the standard set of thermodynamic Equations Of State based on CATHARE functions [44]. The saturation temperature is equal to $584.15 K$ and the latent

APPENDIX I. FURTHER VALIDATIONS OF THE MASS TRANSFER TERM FOR LARGE INTERFACES WITH PHASE CHANGE

heat to $1.32 \cdot 10^6 \text{ J.kg}^{-1}$. The bulk liquid temperature is taken equal to $T_{max} = T_{sat} + 10 \text{ K} = 594.15 \text{ K}$. The temperature difference is higher than the first study since, at this high pressure, the interface motion is slower. Thus, the temperature gradient is increased to accelerate a bit the motion.

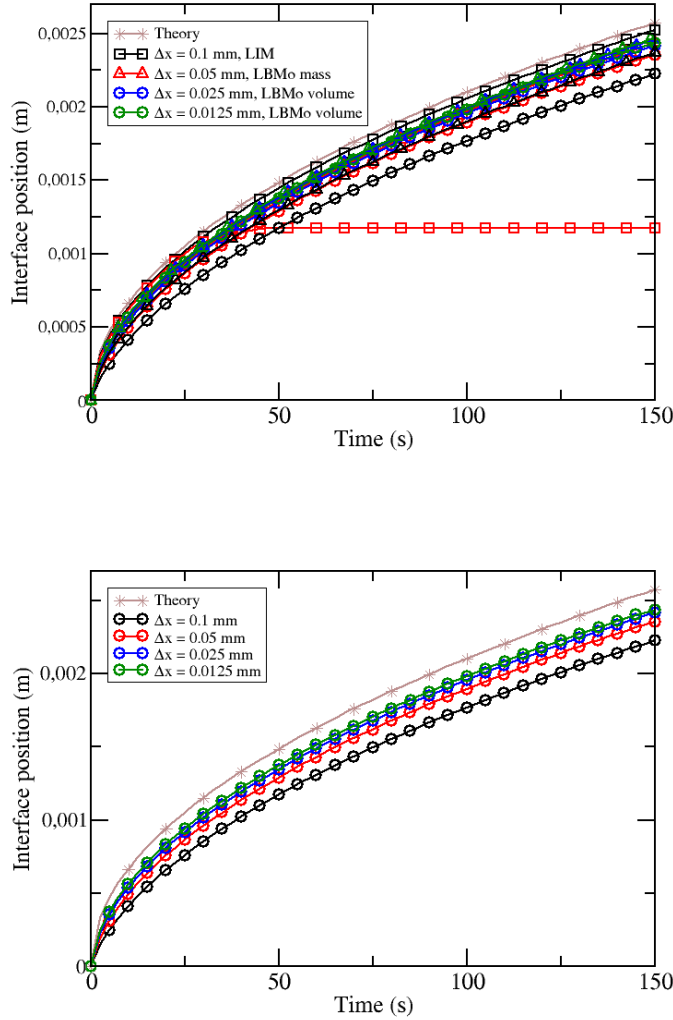


Figure I.1: Evolution of the interface position obtained with different heat transfer models and mesh refinements, sucking problem at a higher pressure equal to $1.013 \cdot 10^7 \text{ Pa}$, all the notations and colors are not given in the top picture for sake of clarity, squares: LIM, triangles: LBMo with a mass formulation, circles: LBMo with a volume formulation, black curves: $\Delta x = 1 \cdot 10^{-4} \text{ m}$, red curves: $\Delta x = 5 \cdot 10^{-5} \text{ m}$, blue curves: $\Delta x = 2.5 \cdot 10^{-5} \text{ m}$ and green curves: $\Delta x = 1.25 \cdot 10^{-5} \text{ m}$, bottom picture: results obtained with the LBMo and a volume formulation only.

The LBMo with the mass and volume formulations are compared with the LIM. The time steps are respectively equal to $2 \cdot 10^{-2} \text{ s}$, $5 \cdot 10^{-3} \text{ s}$, $1.25 \cdot 10^{-3} \text{ s}$ and $3 \cdot 10^{-4} \text{ s}$

in all cases. The time onset is evaluated with the same method presented in section 9.5.1.2. The results are presented in Figure I.1. This time, the results are more comparable with the three models. As previously observed with the Stefan problem, the expected interface motion is slower. It is then easier to compute and does not allow discriminating efficiently the approaches. Nevertheless, with the LIM and all the meshes except the coarse one, instabilities appear. With the LBMo, mesh convergence is always observed. The mass formulation is closer to the analytical results for the coarsest grids. Nevertheless, with the most refined mesh, the two formulations predict the same evolution. Finally, Figure I.2 displays the average relative error of the interface position for the first 150 s. The error induces by the LBMo with the mass formulation is smaller than with the volume formulation. The order of convergence of the methods are equal to 1.4 for the mass formulation and 1.1 for the volume one.

This study highlights that the heat and mass transfer model implemented for the LBMo is able to simulate interfaces with phase change with reasonable errors even in pressure conditions occurring in a reactor vessel or a steam generator of a nuclear power plant. The mass formulation seems to induce smaller errors. However, the simulation of the same problem at an atmospheric pressure showed that this formulation was not suitable. Therefore, the volume formulation is kept for all the other simulations of interfaces with phase change.

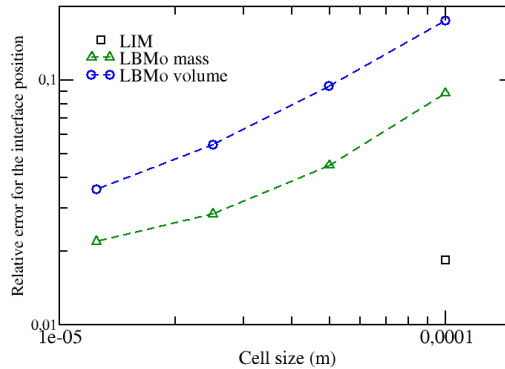


Figure I.2: Relative error for the interface position compared to the theoretical results at 150 s, sucking problem at a higher pressure equal to $1.013 \cdot 10^7$ Pa, squares: LIM, triangles: LBMo with a mass formulation and circles: LBMo with a volume formulation.

I.2 Growing steam bubble

In this section, the validation of the heat transfer model with the LBMo, is extended to a 3D simulation of the sucking problem. In this case, a growing vapor bubble is simulated in superheated water under zero gravity. This test case has been

analytically solved by Scriven [177] and used as a validation test case by different research groups [3, 87, 171, 184].

I.2.0.1 Theory

The evolution of the bubble radius over time obeys the following expression :

$$R(t) = 2\beta_v \sqrt{\chi_l t} \quad (9.1)$$

with β_v the growth constant, solution of the equation:

$$2\beta_v^2 \int_0^1 \exp\left(-\beta_v^2 \left((1-\zeta)^{-2} - 2\left(1 - \frac{\rho_v}{\rho_l}\right)\zeta - 1\right)\right) d\zeta = \frac{\rho_l C_{pl} \Delta T}{\rho_v (L + (C_{pl} - C_{pv}) \Delta T)} \quad (9.2)$$

with $\Delta T = T_{max} - T_{sat}$, T_{max} being the liquid temperature in the bulk. Scriven [177] proposes an approximation for the growth constant and the bubble radius when $\rho_v \ll \rho_l$:

$$\beta = \sqrt{\frac{3}{\pi}} \left(\frac{\Delta T}{\frac{\rho_v}{\rho_l} \left(\frac{L}{C_{pl}} + \frac{C_{pl} - C_{pv}}{C_{pl}} \Delta T \right)} \right) \quad (9.3)$$

$$R(t) = 2\sqrt{\frac{3}{\pi}} \left(\frac{\Delta T \sqrt{\rho_l C_{pl} \lambda_l t}}{\rho_v (L + (C_{pl} - C_{pv}) \Delta T)} \right) \quad (9.4)$$

I.2.0.2 Simulation

The simulation is performed in the first configuration of the sucking problem, that is to say with an atmospheric pressure $1.013 \cdot 10^5 Pa$ and a bulk liquid temperature equal to $378.15 K$. The physical properties of liquid water and steam are given in Table 9.1. They are updated at each time step (see Figure 9.1 right) using the standard set of thermodynamic Equations Of State based on CATHARE functions [44].

To limit the CPU consumption, the simulations are performed on a cubic uniform Cartesian mesh, corresponding to $\frac{1}{8}$ of the total computational domain (see Figure I.3). The bubble is initialized at a corner of the grid. Symmetry planes are defined on the corresponding faces. For the rest of the faces, outlet boundary conditions are chosen. Three mesh refinements are used: 80^3 cells, 160^3 cells and 320^3 cells. The time step is constant and respectively equal to $1 \cdot 10^{-4} s$, $5 \cdot 10^{-5} s$ and $2.5 \cdot 10^{-5} s$. The initial bubble radius is fixed at around $8 mm$, which corresponds to a time of $0.44 s$ according to Equation (9.4).

Contrary to the previous case, the surface tension force is activated since the simulation is now performed in 3D. Before beginning the simulation, it is therefore necessary to check the value of the Capillary number to ensure that the results will not be affected by the spurious velocities. The surface tension coefficient in this

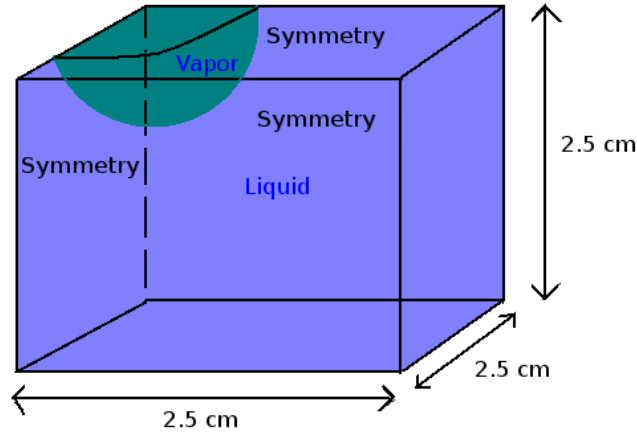


Figure I.3: Schematic view of the computational domain illustrating the position of the vapor bubble and the boundary conditions for the simulation of the growing steam bubble in superheated liquid water.

test case (see section I.3) is equal to $5.7 \cdot 10^{-2} \text{ N.m}^{-1}$ and the liquid viscosity to $2.7 \cdot 10^{-4} \text{ Pa.s}$. The theoretical interface velocity is equal to $3.8 \cdot 10^{-3} \text{ m.s}^{-1}$ at 2.5 s. The Capillary number is then equal to $1.8 \cdot 10^{-5}$ which is smaller than the critical capillary number obtained in section 5.3 and equal to 0.001. Therefore, without changes of the liquid viscosity or the surface tension coefficient, the simulations will be driven by spurious velocities. Moreover, the interface motion in this test case depends only on the heat transfer at the interface and is not affected by the value of the liquid viscosity and the surface tension coefficient. Thus, for this simulation, the liquid viscosity is modified to be equal to $2.7 \cdot 10^{-2} \text{ Pa.s}$ and the surface tension coefficient to $2.85 \cdot 10^{-2} \text{ N.m}^{-1}$.

Figure I.4 presents the results of the comparison. The discrepancies observed on the curves obtained with the LIM are due to the overprediction of the bubble growth. The bubble reaches the outlets of the domain before the end of the simulation. For the coarse grid, the LBMo is farther from the theoretical results than the LIM. However, when the mesh is refined, the LIM is not closer to the analytical results. Figure I.5 presents the corresponding average relative error for the interface position. The average is made over 2 s for the LBMo. For the LIM, the average process is stopped when the bubble reaches the domain boundaries. No convergence is observed with the LIM. The order of convergence is not calculated here since the grids are not refined enough.

This simulation confirms also the ability of the new heat and mass transfer model to predict interface motion based only on phase change effects in 3D.

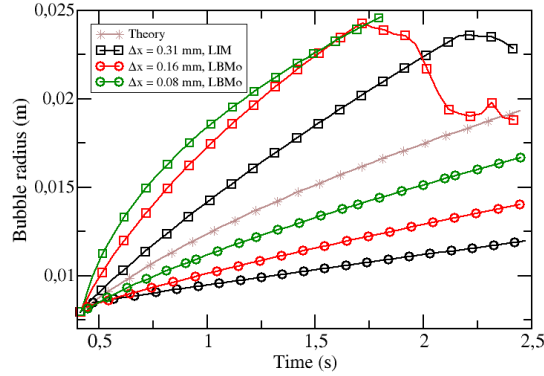


Figure I.4: Evolution of the steam bubble radius obtained with the heat transfer model of the LBMo and the LIM, all the notations and colors are not given in the picture for sake of clarity, squares: LIM, circles: LBMo with a volume formulation, black curves: mesh with 80^3 cells, red curves: 160^3 cells and green curves: 320^3 cells.

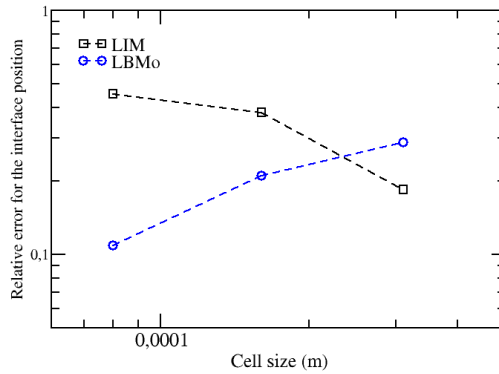


Figure I.5: Average relative error for the interface position compared to the theoretical results, growing steam bubble test case.

I.3 Inversed sucking problem

In all the previous simulations, only superheated fluids have been considered. However, the model is expected to work whatever the temperature of the fluids, under or over the saturation temperature. Thus, in this section, the inversed sucking problem is simulated. The liquid is under the saturation temperature at T_{min} and the wall temperature is fixed at $T_{wall} = T_{sat}$ so that steam is at the saturation

temperature (see Figure I.6). The simulation is performed at atmospheric pressure. Only the LBMo with the volume formulation is used since the goal is to show the ability of the new model to deal with condensation.

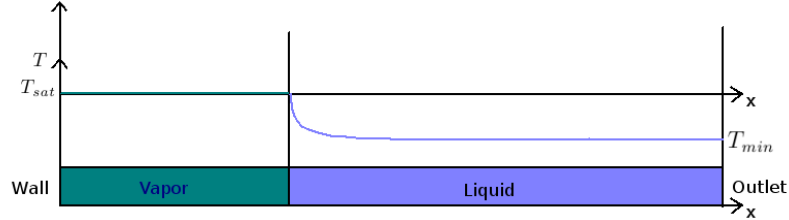


Figure I.6: Conditions of simulation at a given time for the inversed sucking problem, the vapor condensates and the interface moves to the left side.

The same theory can be applied to the inversed sucking problem [212]. The only difference is the direction of the interface motion. In the inversed test case, the interface goes from the right to the left due to vapor condensation whereas it went from the left to the right in the sucking problem due to liquid evaporation.

The physical properties of steam and water are given in Table 9.1. They are updated at each time step (see Figure 9.1 right) using the standard set of thermodynamic Equations Of State based on CATHARE functions [44]. The pressure of the system is equal to $1.013 \cdot 10^5 \text{ Pa}$ (the atmospheric pressure), the latent heat to $2.27 \cdot 10^6 \text{ J.kg}^{-1}$ and the liquid temperature in the bulk to $T_{min} = 368.15 \text{ K}$.

The same grids are used with the same boundary conditions. The time step is kept constant and respectively equal to $1.6 \cdot 10^{-3} \text{ s}$, $4 \cdot 10^{-4} \text{ s}$, $1 \cdot 10^{-4} \text{ s}$ and $2.5 \cdot 10^{-5} \text{ s}$. The liquid temperature is initialized using Equation (9.23) at $t = 0.1 \text{ s}$.

The results are given in Figure I.7. They are comparable to the sucking problem. The order of convergence obtained with this test case is equal to 1.0.

I.4 Conclusion

In this appendix, the first test case highlighted that the new heat and mass transfer model was suitable for the simulation of phase change under pressure conditions occurring in nuclear power plants. Then, the validation has been successfully extended to 3D and finally to a condensation test case.

APPENDIX I. FURTHER VALIDATIONS OF THE MASS TRANSFER TERM FOR
LARGE INTERFACES WITH PHASE CHANGE

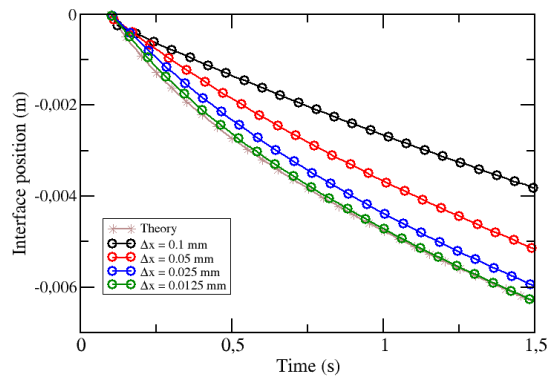


Figure I.7: Evolution of the interface position obtained with the LBMo and the volume formulation for 4 different mesh refinements, inversed sucking problem at an atmospheric pressure.

Appendix J

Effect of the turbulence modeling on the Hänsch's bubble column

In this appendix, we want to highlight the effect of the turbulence model on the transition between the two gas fields with the simulation of the Hänsch's column (see section [10.2](#)).

J.1 Simulation

The simulation is performed with the mesh containing $40 \times 100 \times 10$ cells, a constant time step equal to 0.4 ms and a characteristic time step of the transfer term of 0.1 ms . Three turbulence models are tested: MILES, WALE and RANS. The results in terms of volume occupied by each gas field is displayed in Figure [J.1](#). The curves are very similar even if the RANS solution differs from others for larger times.

J.2 Conclusion

Contrary to the METERO test case (see section [17.3](#)), in the Hänsch's bubble column test case, the turbulence model has a minor effect on the flow properties.

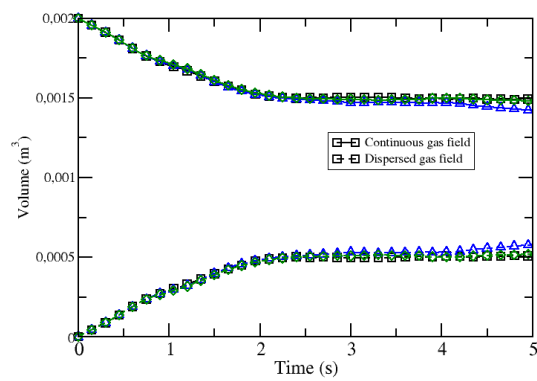


Figure J.1: Evolution of the volume occupied by the dispersed and the continuous gas fields over time, all the notations and colors are not given in the picture for sake of clarity, solid lines: volume occupied by the continuous gas field, dashed lines: volume occupied by the dispersed gas field, black squares: MILES, green diamonds: WALE and blue triangles: RANS, mesh with 40 x 100 x 10 cells, time step equal to 0.4 ms.

Appendix K

Castillejos' test case

In Chapter 10, the ability of the isothermal mass transfer terms presented in section 3.6 to model coalescence and breakup of bubbles is assessed with the Hänsch's bubble column. However, since no experimental data are available for this test case, in this appendix, a simulation of the Castillejos' experiment is proposed to have a quantitative comparison of the results. This simulation is also particularly challenging since, contrary to the other test case, the mesh is non uniform.

K.1 Test case description

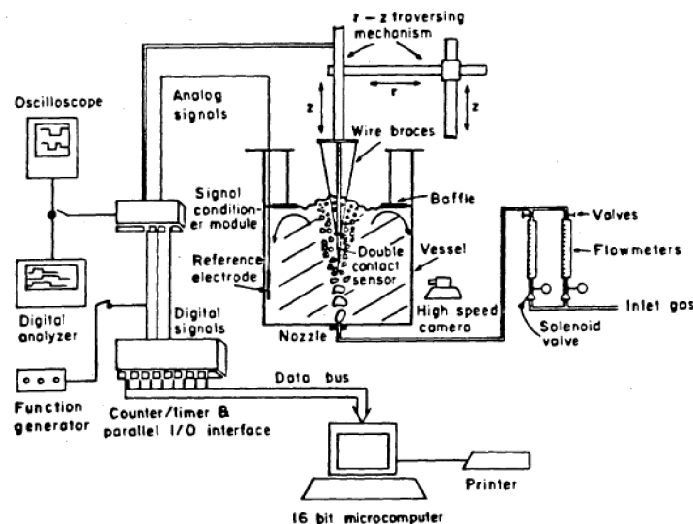


Figure K.1: Schematic view of the Castillejos' experiment [28].

In this test case, air is injected at the bottom of a cylindrical bubble column at a constant mass flow rate equal to $876 \text{ cm}^3 \cdot \text{s}^{-1}$ [28] (see Figure K.1). The diameter and the height of the column are equal to 0.5 m . The injector diameter is equal to 6.35 mm and the water height to 0.4 m . The air injected is considered as a

continuous gas field. The bubbles are considered resolved. Before reaching the free surface, the injected bubbles break up and form smaller inclusions treated as a dispersed field, such that the flow contains bubbles with sizes from about 6 μm to smaller than 1 mm (see Figure K.2).

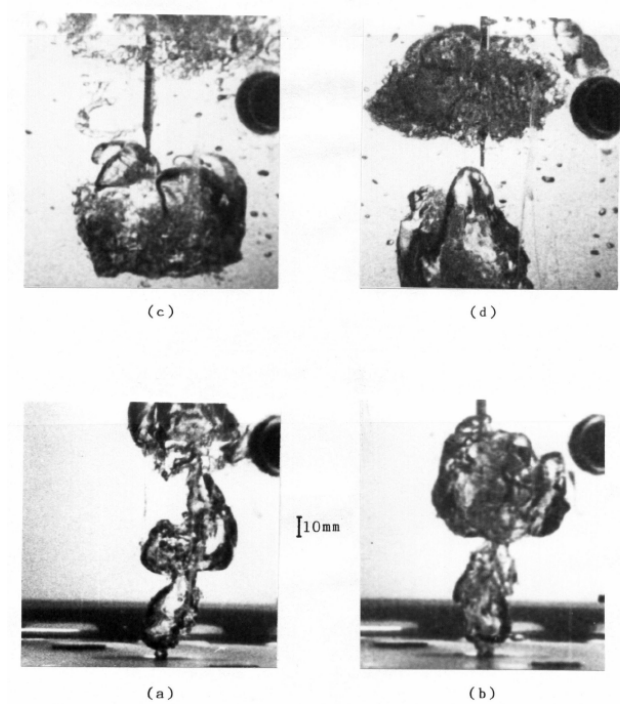


Figure 5.9 Large bubbles occurring at different positions in the plume. ($Q = 876 \text{ Ncm}^3/\text{s}$, $h = 400 \text{ mm}$, $d = 6.35 \text{ mm}$, probe at centreline $z = 110 \text{ mm}$ for (a) and (b), $z = 200 \text{ mm}$ for (c) and (d) photographs).

Figure K.2: Pictures of the flow in the Castillejos' experiment [28].

A non uniform grid is used with smaller cells at the center of the domain to describe better the bubble interfaces close to the inlet, as shown in Figure K.3. The grid contains 259904 cells. The time step is constant, equal to 5.10^{-5} s .

K.2 Simulation results

The results have been obtained with the RANS approach. The simulation is performed in the same conditions as apply to the Hänsch's bubble column, that is to say the optimized version of the LBMo detailed in Part I, the mass transfer terms presented in section 3.6 and the modification of the interface sharpening equation in section 10.3. The flow is also isothermal.

Figure K.4 proposes a picture of the bubble plume at 1 s which shows the existence of small spherical bubbles in red considered as a dispersed field. Figure K.5 compares at different heights the void fraction profiles. The simulation predicts

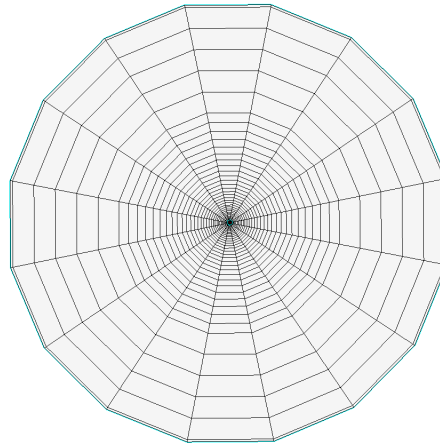


Figure K.3: Slice of the mesh used for the simulation of the Castillejos' test case [28].

quite well the profile close to the injection but overestimates the void fractions far from it. Indeed, some authors [150] have reported the use of a plate located at the water/air free surface with a hole in the middle which is not considered in this simulation. This could affect the void fraction profiles and explain the discrepancies observed particularly close to the water/air free surface. Due to these uncertainties, it has been decided not to investigate more this test case.

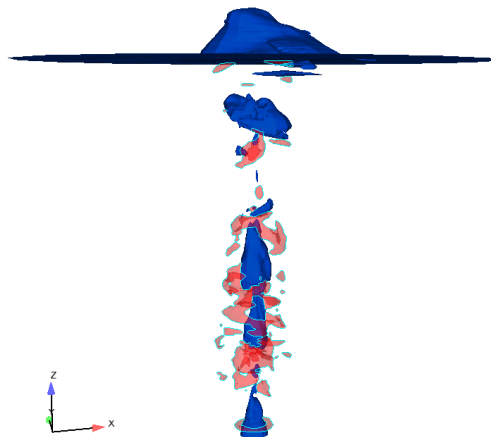


Figure K.4: Gas plume at 1 s after the beginning of the injection, the blue color represents the isosurface of the volume fraction of the continuous air field ($\alpha_{cg} = 0.5$) and the red color the isosurface of the dispersed gas field volume fraction ($\alpha_{dg} = 0.15$), RANS approach.

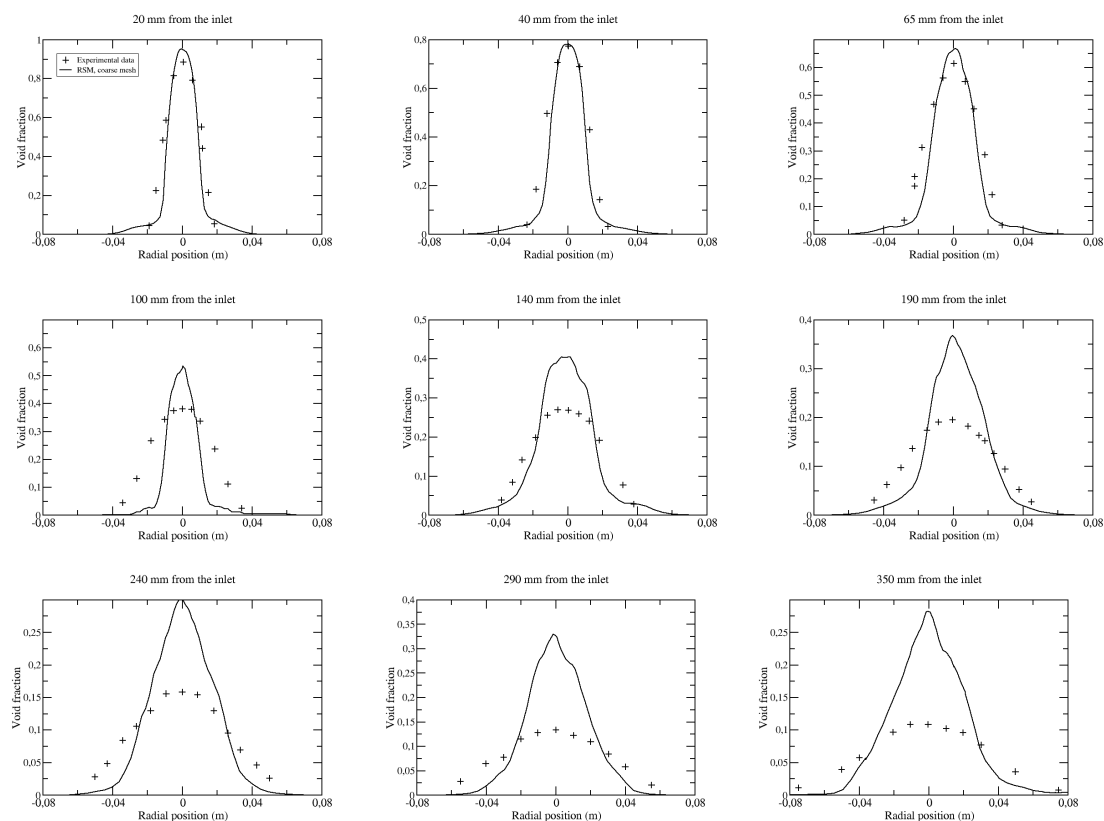


Figure K.5: Average void fractions profiles after 20 s of averaging obtained with the RANS model and compared to the experimental results.

K.3 Conclusion

The simulation of the Castillejos' test case is an extra validation of the isothermal mass transfer terms used in the multifield approach. Transfer are observed between the two gas fields. Dispersed gas field is created by the breakup of the large bubbles injected at the bottom of the domain. Then, this dispersed field coalesce to form large bubbles. Continuous gas field is created. Reasonable agreement with the experimental data close to the injection has been obtained.

Appendix L

Relations between LES results and experimental data

In this appendix, the link between the LES results and DNS or experimental data is detailed. The goal is to understand which quantities related to the fluid velocities can be compared to validate a model.

L.1 Notations

In this section, the notations are presented.

In experiments and DNS, the fluid velocity u^r can be decomposed into an average velocity \bar{U} and a fluctuating velocity U' :

$$u^r = \bar{U} + U' \quad (12.1)$$

This velocity u^r corresponds, for the LES results, to the sum of the resolved velocity \tilde{u} and the velocity of the subgrid scales u' :

$$u^r = \tilde{u} + u' \quad (12.2)$$

Thus, in experiments and DNS, the measured quantity is u^r whereas, in the LES results, u^r and u' are not directly available. Therefore, the two approaches cannot be linked directly. Nevertheless, we know that:

$$\bar{U} = \langle u^r \rangle = \langle \tilde{u} \rangle \quad (12.3)$$

and

$$\langle U' \rangle = \langle u' \rangle = 0 \quad (12.4)$$

$\langle . \rangle$ refers to a time average.

L.2 Average relations

To link the two approaches, the quantity u' is assumed to be negligible thanks to the LES model, which gives the following equation:

$$u^r = \tilde{u} \quad (12.5)$$

This equation can be rewritten:

$$U' = \tilde{u} - \bar{U} \quad (12.6)$$

Thus, let's consider the following quantity $\langle U'U' \rangle$:

$$\begin{aligned} \langle U'U' \rangle &= \langle (u^r - \bar{U})^2 \rangle \\ &= \langle (\tilde{u} - \bar{U})^2 \rangle \\ &= \langle \tilde{u}^2 + \bar{U}^2 - 2\tilde{u}\bar{U} \rangle \\ &= \langle \tilde{u}^2 \rangle + \bar{U}^2 - 2\bar{U} \langle \tilde{u} \rangle \end{aligned}$$

Using Equation (12.3), we obtain:

$$\begin{aligned} \langle U'U' \rangle &= \langle \tilde{u}^2 \rangle + \langle \tilde{u} \rangle^2 - 2 \langle \tilde{u} \rangle^2 \\ &= \langle \tilde{u}^2 \rangle - \langle \tilde{u} \rangle^2 \end{aligned}$$

The same method can be applied to link the crossed average, such as $\langle U'V' \rangle$:

$$\begin{aligned} \langle U'V' \rangle &= \langle (\tilde{u} - \bar{U})(\tilde{v} - \bar{V}) \rangle \\ &= \langle \tilde{u}\tilde{v} + \bar{U}\bar{V} - \tilde{u}\bar{V} - \tilde{v}\bar{U} \rangle \\ &= \langle \tilde{u}\tilde{v} \rangle + \bar{U}\bar{V} - \bar{V} \langle \tilde{u} \rangle - \bar{U} \langle \tilde{v} \rangle \\ &= \langle \tilde{u}\tilde{v} \rangle + \langle \tilde{u} \rangle \langle \tilde{v} \rangle - \langle \tilde{v} \rangle \langle \tilde{u} \rangle - \langle \tilde{u} \rangle \langle \tilde{v} \rangle \\ &= \langle \tilde{u}\tilde{v} \rangle - \langle \tilde{u} \rangle \langle \tilde{v} \rangle \end{aligned}$$

Appendix M

Extra validations of the standard LES models on a single-phase flow

For the sake of clarity, all the curves have not been presented in Chapter 15. This appendix details the results for all the three turbulence models studied in Chapter 15: MILES, WALE and Smagorinsky's model with the dynamic procedure corresponding to the studies performed in sections 15.4.3 and 15.4.4.

M.1 Sensibility to the mesh refinement in the span-wise direction

In this section, the effect of the mesh refinement in the x and z directions is studied for the three turbulence models. For this purpose, the fully developed turbulent channel flow is simulated with Grid 1 and 2. The properties of these two grids are presented in Table 15.1. Grid 2 is obtained by increasing the number of cells in the x and z directions and keeping the same space discretization along the y direction than Grid 1. The time step is equal to 0.2 *ms* with Grid 1 and 0.1 *ms* with Grid 2. Except the modification of the mesh and the time step, all the simulations parameters remain unchanged.

The results are given in Figures M.1 and M.2. The results are improved by the grid refinement in the span-wise direction, whatever the turbulence model.

APPENDIX M. EXTRA VALIDATIONS OF THE STANDARD LES MODELS ON A SINGLE-PHASE FLOW

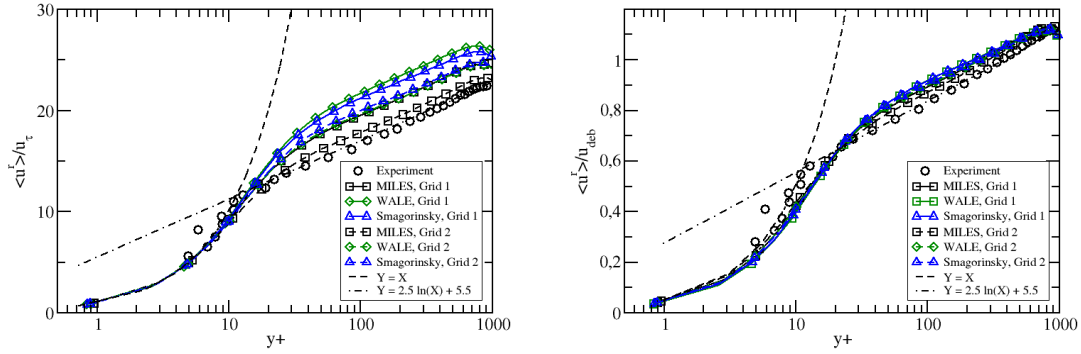


Figure M.1: Comparison of the profiles of $\langle u^r \rangle$ with the experimental data [144] and the three turbulence models for the two grids, left: normalization by the computed wall shear velocity, right: by the computed bulk mean velocity.

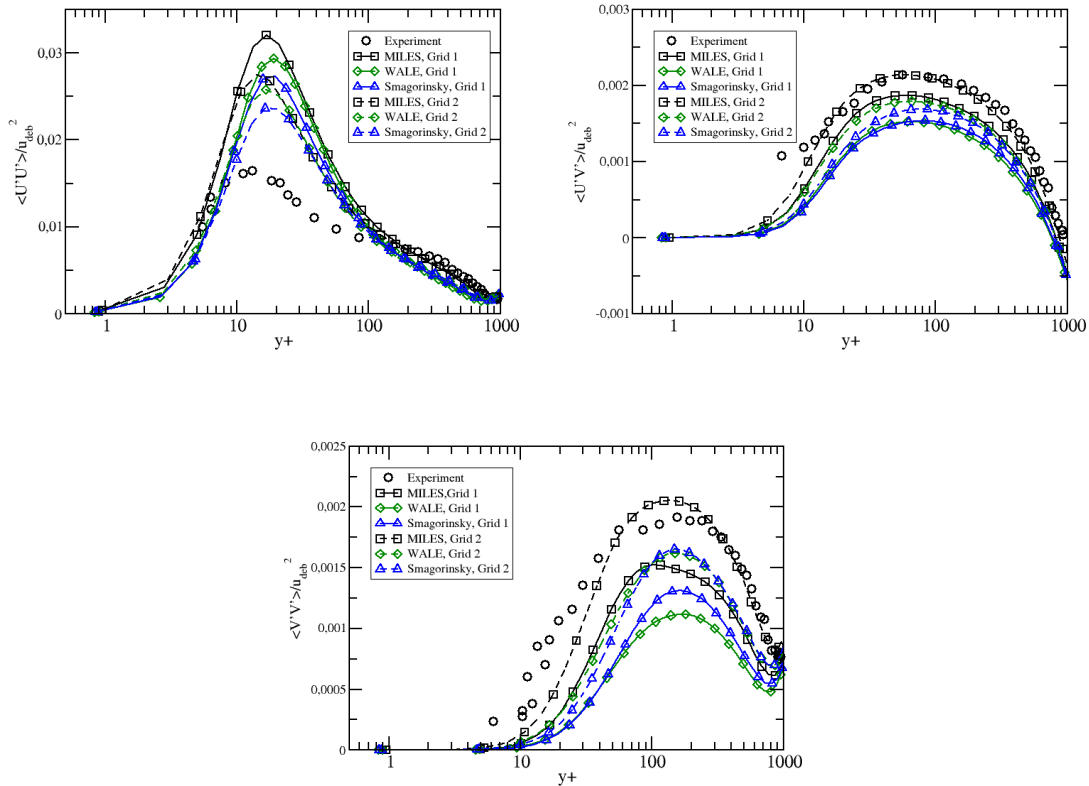


Figure M.2: Comparison of the profiles of $\langle U^r U^r \rangle$, $\langle U^r V^r \rangle$ and $\langle V^r V^r \rangle$ with the experimental data [144] and the three turbulence models for the two grids, all the quantities are normalized by the computed bulk mean velocity.

M.2 Sensibility to the mesh refinement in the stream-wise direction

Then, the effect of the grid coarsening in the y direction is studied. For this purpose, the simulations are performed with Grid 2, Grid 3 and Grid 4, corresponding to a first cell position respectively equal to $y^+ = 1$, $y^+ = 5$ and $y^+ = 10$. The time step is equal to 0.1 ms . Except the modification of the mesh, all the simulations parameters remain unchanged.

The profiles comparisons are presented for the three turbulence models in Figure M.3 for $\langle u^r \rangle$ and Figure M.4 for $\langle U'U' \rangle$, $\langle U'V' \rangle$ and $\langle V'V' \rangle$. Whatever the turbulence model, the effect of the mesh coarsening is limited for Grid 3. Discrepancies are mainly observed for Grid 4.

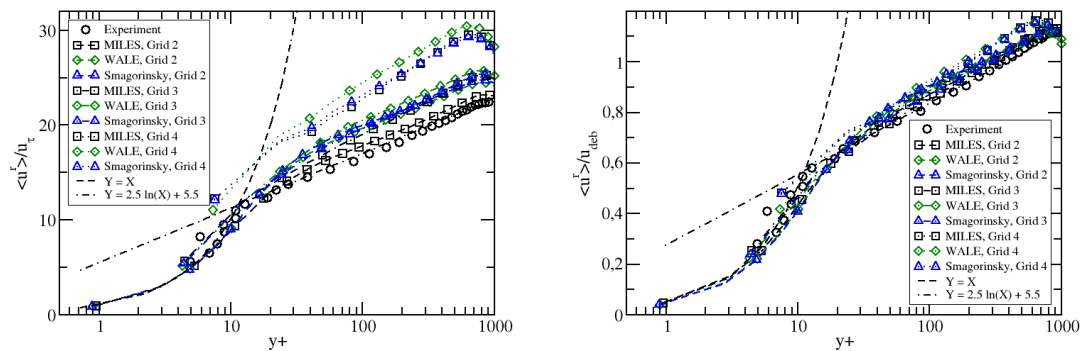


Figure M.3: Comparison of the profiles of $\langle u^r \rangle$ with the experimental data [144] and the three turbulence models for the three grids, left: normalization by the computed wall shear velocity, right: by the computed bulk mean velocity.

APPENDIX M. EXTRA VALIDATIONS OF THE STANDARD LES MODELS ON A SINGLE-PHASE FLOW

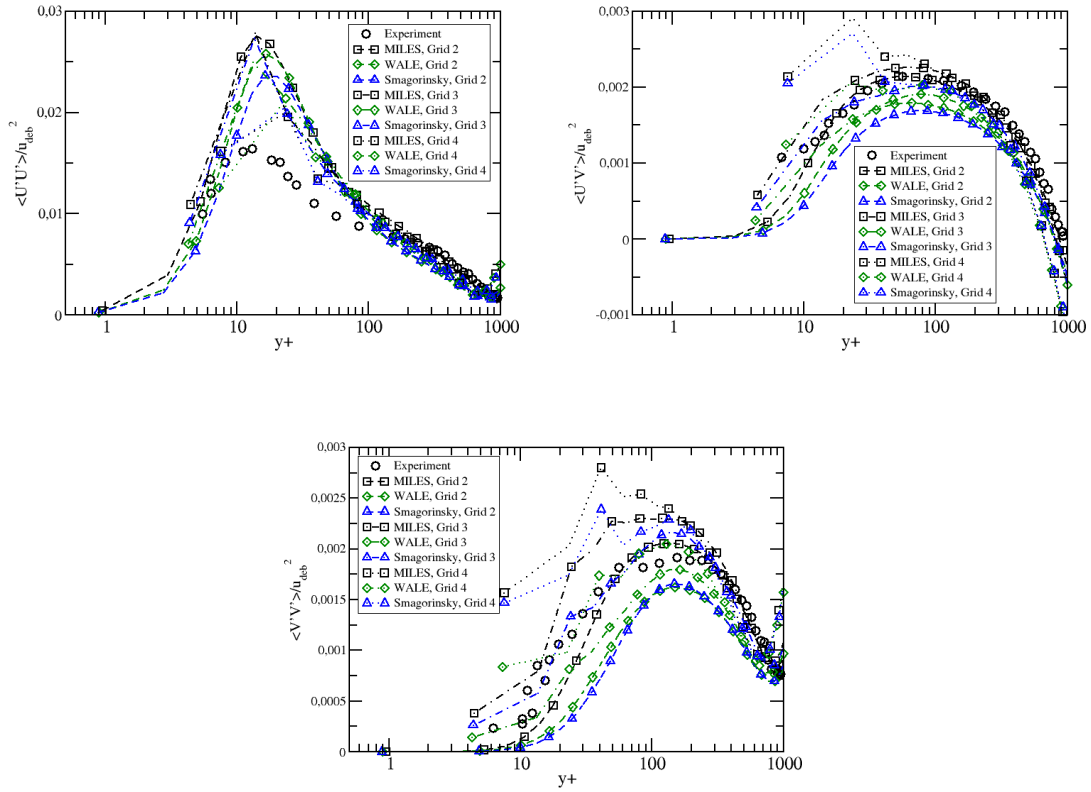


Figure M.4: Comparison of the profiles of $\langle U'U' \rangle$, $\langle U'V' \rangle$ and $\langle V'V' \rangle$ with the experimental data [144] and the three turbulence models for the three grids, all the quantities are normalized by the computed bulk mean velocity.

Appendix N

A priori LES study with the phase inversion benchmark, case 2

This appendix presents a complementary work for the *a priori* LES study performed on the phase inversion benchmark in Chapter 16. The same study is proposed on a second case of the benchmark [208] to validate the results on a slightly different flow configuration. Only continuous fields are considered. In all this appendix, case 1 refers to the case studied in Chapter 16 and case 2 to the case considered in this appendix.

This work has been accepted for publication in Computers & Fluids [209]. The paper proposes a comparison of the results presented in this appendix and the same study performed with a one-fluid model.

N.1 Presentation of the test case

This test case is very similar to the one presented in Chapter 16. The fluid properties remain the same (see Table 16.1). The only differences concern the surface tension coefficient and the domain size. The characteristic numbers corresponding to the two cases are presented in Table N.1. The second case has a largely higher Reynolds number, which means that the case will be more turbulent. Moreover, the increase of the Reynolds combined with the increase of the Weber number conduct to a larger scale separation and phase dispersion in the flow [96].

The test case is simulated with three different mesh refinements: 128^3 cells, 256^3 cells and 512^3 cells. The time steps are kept constant and are respectively equal to 2 ms, 1 ms and 0.5 ms such that the CFL number is constant and smaller than 0.9. The simulations have been performed with 144 cores for the first mesh and 1152 for the two others during respectively 11 hours, 38 hours and 1 month to reach 55 physical seconds.

	Surface tension coefficient ($N.m^{-1}$)	Cube size L (m)	Reynolds number	Weber number	Ohnesorge number
Case 1	0.045	0.1	7000	11	$4.7.10^{-4}$
Case 2	0.45	1	$2.46.10^5$	121	$4.7.10^{-5}$

Table N.1: Properties of the two simulated cases of the phase inversion benchmark, case 1 refers to the case in Chapter 16 and case 2 to the case considered in this appendix.

N.2 Validation of the macroscopic behavior

The picture of the flow close to the enstrophy peak (at around 3 in dimensionless time) is given in Figure N.1. As expected, the flow is more dispersed and composed by smaller inclusions compared to case 1. Nevertheless, the same trends are observed. As previously done with case 1, the evolution of the normalized kinetic energy, potential energy, enstrophy for each field and the volume ratio of oil in the top part of the box are compared for the three grids in Figure N.2. The normalized values used for this case are displayed in Table N.2. Some oscillations are present due to the sloshing motion. However, these oscillations are less regular due to the higher turbulent intensity in the water phase. Moreover, contrary to the first case, two peaks can be distinguished for the enstrophy, one for each phase. For the oil phase, it is located at $t^* \simeq 2.5$ and for the water phase, at $t^* \simeq 4$. Indeed, since the oil phase is more viscous, the development of vortical layers is quicker in this phase. For the two more refined meshes, it seems that, for the quantities based on large scale motion, convergence is reached.

	$E_{c,k}^n = \frac{1}{16}\rho_k U_g^2 L^3$	$E_{p,k}^n = \lim_{t \rightarrow +\infty} (E_{p,k})$	$E_{s,k}^n$ maximum of enstrophy for code DyJeAT with 1024^3 grid [208]
Oil	3.4063 J	1035 J	80.9 $m^3.s^{-2}$
Water	3.7847 J	3755 J	537.5 $m^3.s^{-2}$

Table N.2: Macroscopic quantities normalization for the case 2 of the phase inversion benchmark.

N.2. VALIDATION OF THE MACROSCOPIC BEHAVIOR

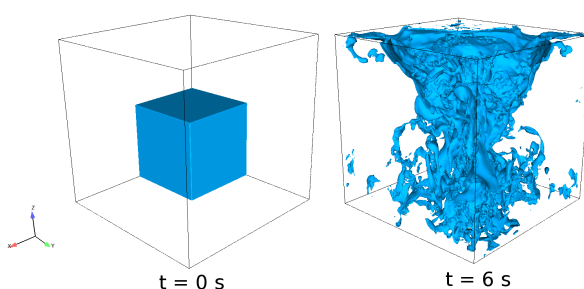


Figure N.1: Picture of the phase inversion benchmark in case 2, at the initialized state and close to the peak of enstrophy of the oil phase, case 2.

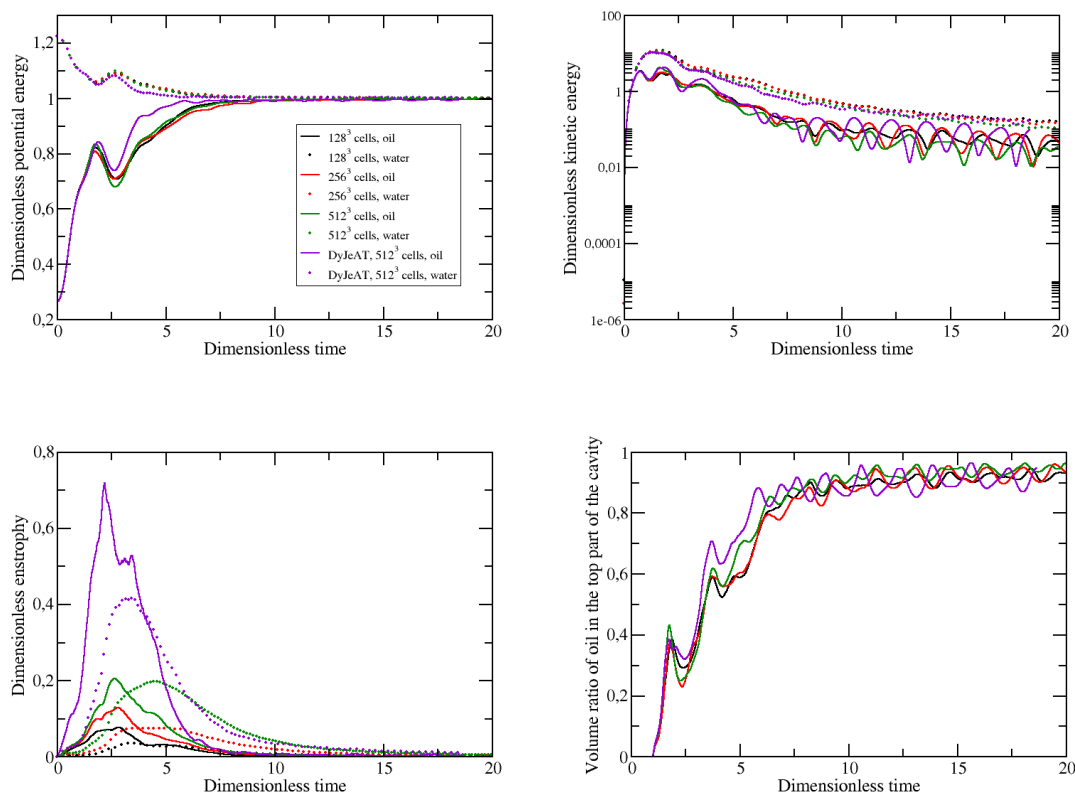


Figure N.2: Evolution of the dimensionless kinetic energy, potential energy, enstrophy and volume ratio of oil, the solid lines correspond to the oil phase, the dashed lines to water, the black curves refer to the coarser mesh: 128^3 cells, the red ones to the intermediate mesh: 256^3 cells, the green ones to the refined mesh: 512^3 cells and the purple curves to the code DyJeAT with the 512^3 grid, case 2.

To validate this simulation, the results are compared to the DNS results obtained with the code DyJeAT in Figure N.2. For potential and kinetic energies in the two phases, the two codes are in rather good agreement. They capture the same time

evolution with peak of energies being located at the same instants. For intermediate times, when droplet generation is maximum, some discrepancies are noticed. They are due to the different interface tracking techniques and also to single velocity field representation of the one-fluid model used in DyJeAT compared to two velocity description brought by the two-fluid model. Concerning enstrophy in the two phases, the code DyJeAT brings two to three times larger magnitudes than NEPTUNE_CFD. This difference of magnitude has also been reported in [208]. It was demonstrated that on a vorticity point of view, even the 2048^3 grid is not enough to perform a real DNS for the phase inversion benchmark whereas potential and kinetic energies can be assumed converged with the 512^3 mesh. Finally, the peak of enstrophy is located at the same dimensionless time for both codes.

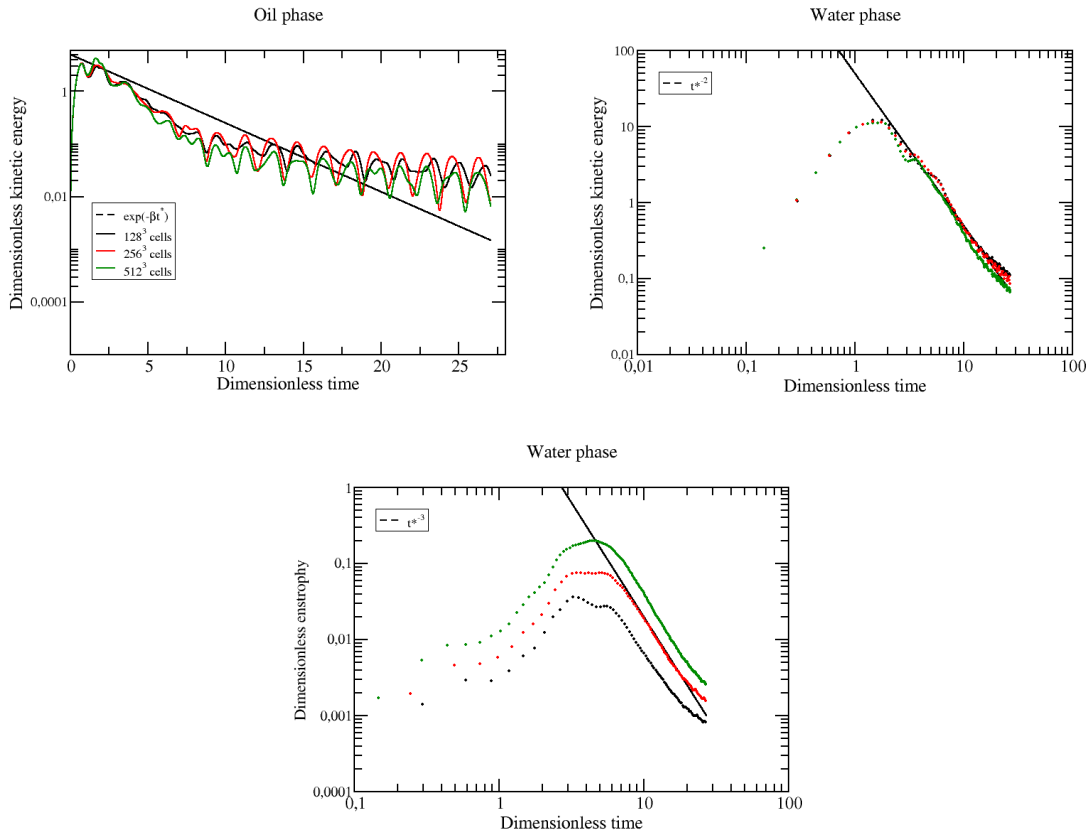


Figure N.3: Evolution of the dimensionless kinetic energy for the two phases and the dimensionless enstrophy for water, the black dashed lines correspond to different laws that fit the macroscopic quantities after the enstrophy peak, the solid lines correspond to the oil phase, the dashed lines to water, the black curves refer to the coarser mesh: 128^3 cells, the red ones to the intermediate mesh: 256^3 cells and the green ones to the refined mesh: 512^3 cells, case 2.

Then, the macroscopic quantities are fitted to the Stokes' law and the turbulent laws. The results are shown in Figure N.3. As observed with single-fluid approaches, the kinetic energy for the oil phase does not follow the Stokes' law anymore. Indeed,

the water phase is more turbulent in this case, which affects the oil phase inclusions which have a more complex motion. For the water phase, the evolution in t^{*-2} for the kinetic energy and in t^{*-3} for the enstrophy are conserved.

As previously done for case 1, for the rest of this study, the 512^3 grid will be considered enough refined to perform a DNS and to provide a representative simulation of the phase inversion benchmark.

N.3 Comparison of the order of magnitude of the different subgrid-scale terms

The simulation data are extracted for the three grids at the enstrophy peak of the oil phase. The same study with the same top hat filter is proposed (see section 16.4). The order of magnitude of the subgrid terms is studied in Figure N.4 and Table N.3. The Favre’s averaging affects the classification of the subgrid terms only for the oil phase where the pressure and convective subgrid terms are exchanged. This is due to the smaller contribution of the convection subgrid term with the Favre’s averaging. However, the two subgrid terms have a very similar weight. Compared to case 1, the classification of the terms is slightly different since the interfacial subgrid term has a higher contribution for the two phases. The surface tension subgrid term has also a similar weight compared to the other terms for the oil phase, whereas in case 1 it was at least four times higher. For the coarse mesh, its contribution is even smaller than the convective subgrid term. Nevertheless, it becomes predominant with the most refined grid, since, as also observed in case 1, the contribution of the convective subgrid term decreases when the mesh is refined and the surface tension subgrid term increases. For the water phase, this exchange occurs also but is due to the larger decrease of the convective term compared to the surface tension term. For the two phases, the diffusion term becomes the smallest subgrid term. Nevertheless, as previously noted with case 1, this term cannot be neglected for the oil phase. Finally, concerning the drag force subgrid term, its weight is smaller than in case 1. Indeed, since the inclusions are smaller, less large interfaces are present in the flow. The drag force term which is proportional to $\alpha_1\alpha_2$, is then smaller.

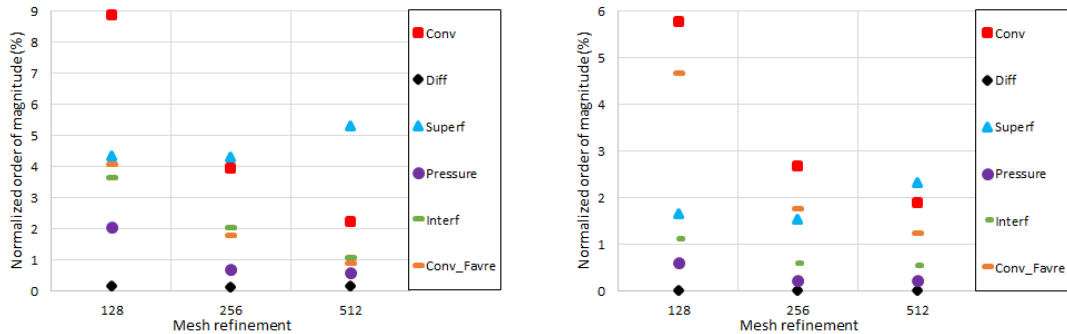


Figure N.4: Order of magnitude of the normalized subgrid terms, left: for the oil phase, right: for the water phase, only the z component is displayed, case 2.

	Simple filtering		Favre's averaging	
	Oil	Water	Oil	Water
1	τ_{superf}	τ_{superf}	τ_{superf}	τ_{superf}
2	τ_{conv}	τ_{conv}	$\tau_{pressure}$	τ_{conv}
3	τ_{interf}	τ_{interf}	τ_{conv}	$\tau_{pressure}$
4	$\tau_{pressure}$	$\tau_{pressure}$		
5	τ_{diff}	τ_{diff}		

Table N.3: Classification of the subgrid terms according to their relative contribution, fine grid with 512^3 cells, case 2.

N.4 Comparison of the turbulence models

Finally, the five turbulence models considered in section 16.5 are compared. Figures N.5 and N.6 display the relative error induced by each turbulence model for the two phases. The conclusions established with the first case remain valuable. The structural models especially ADM allow limiting the modeling error for all the subgrid terms. Nevertheless, the pressure term is better predicted by the models for the two phases than with case 1.

N.5 Conclusion

Case 2 is a more turbulent test case compared to case 1. The flow is thus more dispersed and composed of smaller inclusions. The interfacial subgrid terms have then a larger relative contribution compared to the other case. However, the efficiency of structural models is not affected by the flow properties. ADM remains the most suitable model for all the subgrid terms.

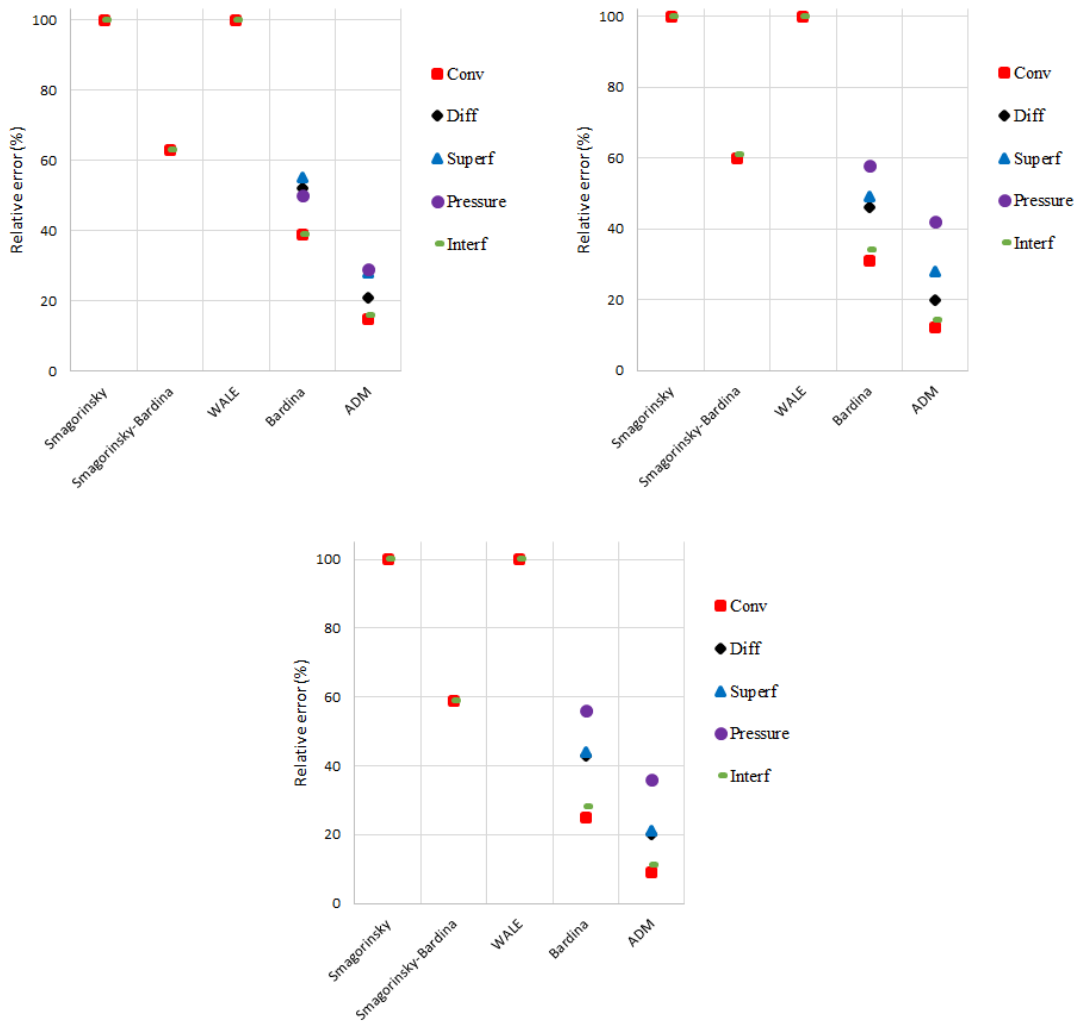


Figure N.5: Relative error obtained by comparison between the modeled subgrid term and the terms obtained by DNS for the oil phase, the Smagorinsky's and WALE models applied to the Favre's average subgrid terms give the same results (relative error of 100 %), left to right: mesh with 128^3 cells, 256^3 cells and 512^3 cells, case 2.

APPENDIX N. *A PRIORI* LES STUDY WITH THE PHASE INVERSION BENCHMARK, CASE 2

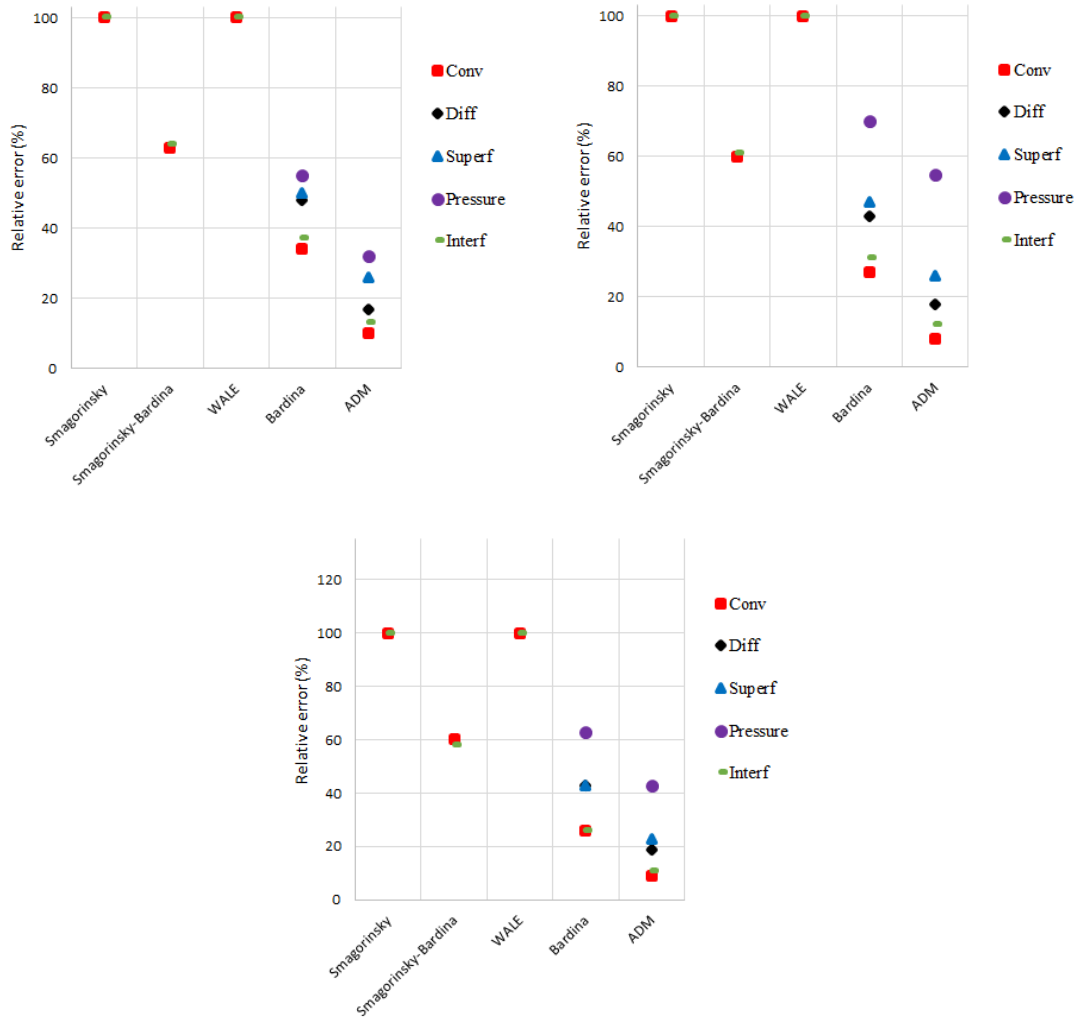


Figure N.6: Relative error obtained by comparison between the modeled subgrid term and the terms obtained by DNS for the water phase, left to right: mesh with 128^3 cells, 256^3 cells and 512^3 cells, case 2.

Bibliography

- [1] <http://www.aplusphysics.com/educators/activities/nucplant.html>.
- [2] ADAMS, N., AND STOLZ, S. A subgrid-scale deconvolution approach for shock capturing. *Journal of Computational Physics* 178, 2 (2002), 391–426.
- [3] AKHTAR, M., AND KLEIS, S. A Volume Of Fluid phase change model on adaptive octree grids. *Journal of ASTM International* 8, 3 (2011), 1–21.
- [4] ALIZADEHDAKHEL, A., RAHIMI, M., AND ALASAIRAFI, A. CFD modeling of flow and heat transfer in a thermosyphon. *International Communications in Heat and Mass Transfer* 37, 3 (2010), 312–318.
- [5] ANDERSON, T., AND JACKSON, R. Fluid mechanical description of fluidized beds. Equations of motion. *Industrial & Engineering Chemistry Fundamentals* 6, 4 (1967), 527–539.
- [6] ANISZEWSKI, W., BOGUSLAWSKI, A., M. MAREK, AND TYLISZCZAK, A. A new approach to sub-grid surface tension for LES of two-phase flows. *Journal of Computational Physics* 231 (2012), 7368–7397.
- [7] ARCHAMBEAU, F., MÉCHITOUA, N., AND SAKIZ, M. *Code_Saturne*: a finite volume code for the computation of turbulent incompressible flows - Industrial applications. *International Journal on Finite Volumes* 1 (2004).
- [8] ARIAS, F. Film boiling in magnetic field in liquid metals with particular reference to fusion reactor project. *Journal of Fusion Energy* 29, 2 (2010), 130–133.
- [9] BAILLY, C., AND COMTE-BELLOT, G. *Turbulence*. CNRS Edition, Paris, 2003.
- [10] BARDINA, J., FERZIGER, J., AND REYNOLDS, W. Improved subgrid scale models based on Large Eddy Simulation. *AIAA Paper 80-1357* (1980).
- [11] BARDINA, J., FERZIGER, J., AND REYNOLDS, W. Improved turbulence models based on Large Eddy Simulation of homogeneous, incompressible, turbulent flows. Tech. rep., Thermosciences Division, Department of Mechanical Engineering, Stanford University, 1983.

BIBLIOGRAPHY

- [12] BARTOSIEWICZ, Y., DUPONCHEEL, M., MIMOUNI, S., AND FLEAU, S. Experimental and numerical investigations of a two-phase wavy flow. *accepted in Computers & Fluids* (2016).
- [13] BARTOSIEWICZ, Y., LAVIÉVILLE, J., AND SEYNHAEVE, J.-M. A first assessment of the NEPTUNE_CFD code: Instabilities in a stratified flow comparison between the VOF method and a two-field approach. *International Journal of Heat and Fluid Flow* 29 (2008), 460–478.
- [14] BENHAMADOUCHE, S. *Large Eddy Simulation with the unstructured collocated arrangement*. PhD thesis, School of Mechanical, Aerospace and Civil Engineering, University of Manchester, 2006.
- [15] BESTION, D. Applicability of two-phase CFD to nuclear reactor thermal hydraulics and elaboration of Best Practice Guidelines. *Nuclear Engineering and Design* 253 (2012).
- [16] BHAGA, D., AND WEBER, M. E. Bubbles in viscous liquids: shape, wakes and velocities. *Journal of Fluid Mechanics* 105 (1981), 61–85.
- [17] BLANCHARD, G. *Modélisation et simulation multi-échelles de l'atomisation d'une nappe liquide cisailée*. PhD thesis, Institut Supérieur de l'Aéronautique et de l'Espace, Université de Toulouse, 2014.
- [18] BORGGAARD, J., AND ILIESCU, T. Approximate Deconvolution Boundary Conditions for Large Eddy Simulation. *Applied Mathematics Letters* 19, 8 (2006), 735–740.
- [19] BORIS, J. P., GRINSTEIN, F. F., ORAN, E. S., AND KOLBE, R. New insights into Large Eddy Simulation. *Fluid Dynamics Research* 10 (1992), 199–229.
- [20] BOTTIN, M., BERLANDIS, J., HERVIEU, E., LANCE, M., MARCHAND, M., ÖZTÜRK, O., AND SERRE, G. Experimental investigation of a developing two-phase bubbly flow in horizontal pipe. *International Journal of Multiphase Flow* 60 (2014), 161–179.
- [21] BRACKBILL, J. U., KOTHE, D. B., AND ZEMACH, C. A continuum method for modeling surface tension. *Journal of Computational Physics* 100 (1992), 335–354.
- [22] BRENNEN, C. E. *Fundamentals of Multiphase Flows*. Cambridge University Press, 2005.
- [23] BUNNER, A., AND TRYGGVASON, G. Effect of bubble deformation on the properties of bubbly flows. *Journal of Fluid Mechanics* 495 (2003), 77–118.
- [24] CALTAGIRONE, J.-P., VINCENT, S., AND CARUYER, C. A multiphase compressible model for the simulation of multiphase flows. *Computers & Fluids* 50 (2011), 24–34.

-
- [25] CAN, E., AND PROSPERETTI, A. A Level Set method for vapor bubble dynamics. *Journal of Computational Physics* 231 (2012), 1533–1552.
- [26] CAPECELATRO, J., PEPIOT, P., AND DESJARDINS, O. Eulerian-Lagrangian simulations of three-dimensional turbulent riser flows. In *Proceedings of the 63rd Annual Meeting of the APS Division of Fluid Dynamics* (Long Beach, California, 2010).
- [27] CARRARA, M. D., AND DESJARDIN, P. E. A filtered mass density function approach for modeling separated two-phase flows for LES II: Simulation of a droplet laden temporally developing mixing layer. *International Journal of Multiphase Flow* 34 (2008), 748–766.
- [28] CASTILLEJOS, A. H. *A study of the fluid-dynamic characteristics of turbulent gas-liquid bubble plumes*. PhD thesis, University of British Columbia, 1986.
- [29] CHASSAING, P. *Turbulence en mécanique des fluides : Analyse du phénomène en vue de sa modélisation à l’usage de l’ingénieur*. Collection Polytech, Toulouse, 2000.
- [30] CHESNEL, J., RÉVEILLON, J., DEMOULIN, F. X., AND MÉNARD, T. Sub-grid modeling of liquid atomization. In *Proceedings of the 6th International Conference on Multiphase Flow: ICMF 2007* (Leipzig, Germany, 2007).
- [31] CHOW, F., STREET, R., XUE, M., AND FERZIGER, J. Explicit Filtering and Reconstruction Turbulence Modeling for Large-Eddy Simulation of Neutral Boundary Layer Flow. *Journal of Atmospheric Sciences* 62 (2004), 2058–2077.
- [32] CLIFT, R., GRACE, J. R., AND WEBER, M. E. *Bubbles, drops, and particles*. Academic Press, New York, 1978.
- [33] COMTE-BELLOT, G. Ecoulement turbulent entre deux parois parallèles. *Publications Scientifiques et Techniques du Ministère de l’Air* 419 (1965).
- [34] COSTE, P. A Large Interface Model for two-phase CFD. *Nuclear Engineering and Design* 255 (2013), 38–50.
- [35] DEARDOFF, J. A numerical study of three-dimensional turbulent channel flow at large Reynolds number. *Journal of Fluid Mechanics* 41 (1970), 453–465.
- [36] DEEN, N. G., HJERTAGER, B. H., AND SOLBERG, T. Comparison of PIV and LDA Measurement Methods Applied to the Gas-Liquid Flow in a Bubble Column. In *Proceedings of the 10th International Symposium on Applications of Laser Techniques to Fluid Mechanics* (Lisbon, Portugal, 2000).
- [37] DELHAYE, J. Jump conditions and entropy sources in two-phase systems. Local instant formulation. *International Journal of Multiphase Flow* 1 (1974), 395–409.
-

BIBLIOGRAPHY

- [38] DENÈFLE, R. *Modélisation locale diphasique eau-vapeur des écoulements dans les générateurs de vapeur*. PhD thesis, Université Bordeaux 1, EDF R&D, 2013.
- [39] DINH, T., TU, J., SALMASSI, T., AND THEOFANOUS, T. Limits of coolability in the AP1000-related ULPU-2400 configuration V facility , CRSS technical report 0306. Tech. rep., University of California Santa Barbara, 2003.
- [40] DOUCE, A., MIMOUNI, S., GUINGO, M., MOREL, C., LAVIÉVILLE, J., AND BAUDRY, C. Validation of NEPTUNE_CFD 1.0.8 for adiabatic bubbly flow and boiling flow. In *Proceeding of Computational Fluid Dynamics for Nuclear Reactor Safety Applications: CFD4NRS-3* (Washington DC, USA, 2010).
- [41] DREW, D., AND LAHEY, R. Application of general constitutive principles to the derivation of multidimensional two-phase flow equations. *International Journal of Multiphase Flow* 5, 4 (1979), 243–264.
- [42] DRUI, F., LARAT, A., KOKH, S., AND MASSOT, M. A hierarchy of simple hyperbolic two-fluid models for bubbly flows. *HAL* (2016).
- [43] DUPONCHEEL, M., AND BARTOSIEWICZ, Y. Final report on the CFD-grade Thorpe experiment and its numerical simulation, Multiscale and multiphysics simulation of PTSM. Tech. rep., NURES SAFE, NUClear REactor SAFETY simulation platform, 2015.
- [44] EMONOT, P., SOUYRI, A., GANDRILLE, J., AND BARRE, F. CATHARE-3: a new system code for thermal-hydraulics in the context of the NEPTUNE project. *Nuclear Engineering and Design* 241 (2011), 4476–4481.
- [45] FAGHRI, A., AND ZHANG, Y. *Transport phenomena in multiphase systems*. Elsevier, 2006.
- [46] FANG, C., DAVID, M., ROGACS, A., AND GOOGSON, K. Volume Of Fluid simulation of boiling two-phase flow in a vapor-venting microchannel. *Frontiers in Heat and Mass Transfer* 1 (2010), 1–11.
- [47] FLEAU, S., MIMOUNI, S., MÉRIGOUX, N., AND VINCENT, S. Simulations of two-phase flows with a multifield approach. In *Proceedings of the 6th International Symposium on Advances in Computational Heat Transfer, CHT-15* (2015).
- [48] FLEAU, S., MIMOUNI, S., MÉRIGOUX, N., AND VINCENT, S. Validation of a multifield approach for the simulations of two-phase flows. *Computational Thermal Sciences* 7, 5-6 (2015), 441–457.
- [49] FLEAU, S., MIMOUNI, S., AND VINCENT, S. Study of an interface sharpening method for large interface tracking within a two-fluid model. In *Proceedings of 9th International Conference on Multiphase Flow: ICMF 2016* (Firenze, Italy, 2016).

- [50] FLEAU, S., VINCENT, S., AND MIMOUNI, S. LES modeling with a multifield approach. In *Proceedings of the 4th Conference on Turbulence and Interactions 2015: TI 2015* (2015).
- [51] FLEAU, S., VINCENT, S., AND MIMOUNI, S. LES simulations of turbulent two-phase flows within a multifield approach. In *Proceedings of the 7th International Symposium on Advances in Computational Heat Transfer* (2017).
- [52] FULGOSI, M., LAKEHAL, D., BANERJEE, S., AND ANGELIS, V. D. Direct Numerical Simulation of turbulence in a sheared air–water flow with a deformable interface. *Journal of Fluid Mechanics* 482 (2003), 319–345.
- [53] FUREBY, C., AND GRINSTEIN, F. Monotonically integrated Large Eddy Simulation of free shear flows. *AIAA Journal* 37 (1999), 544–556.
- [54] GANAPATHY, H., SHOOSHTARI, S., CHOO, K., DESSIATOUN, S., ALSHEHHI, M., AND OHADI, M. Volume Of Fluid-based numerical modeling of condensation heat transfer and fluid flow characteristics in microchannels. *International Journal of Heat and Mass Transfer* 65 (2013), 62–72.
- [55] GERMANO, M., PIOMELLI, U., MOIN, P., AND CABOT, W. A dynamic subgrid-scale eddy viscosity model. *Physics of Fluids* 3 (1991), 1760–1765.
- [56] GILLET, C. Développement d’un outil de calcul parallèle pour la simulation d’écoulements incompressibles diphasiques: application au cas d’un écoulement stratifié immiscible. Master’s thesis, Université catholique de Louvain, 2015.
- [57] GRIFFITH, P., AND WALLIS, G. Two-phase slug flow. *Journal of Heat Transfer* 83 (1961), 307–320.
- [58] GRIMAN, F., TERRACOL, M., AND SAGAUT, P. An explicit filtering method for Large Eddy Simulation on unstructured meshes. In *Proceedings of 40th Fluid Dynamics Conference and Exhibit* (2010).
- [59] GRINSTEIN, F., AND FUREBY, C. Recent Progress on MILES for High Reynolds Number Flows. *Journal of Fluids Engineering* 124 (2002), 848–861.
- [60] GUELFY, A., BESTION, D., BOUCKER, M., BOUDIER, P., FILLION, P., GRANDOTTO, M., HÉRARD, J.-M., HERVIEU, E., AND PÉTURAUD, P. NEPTUNE - A new software platform for advanced nuclear thermal hydraulics. *Nuclear Science and Engineering* 156 (2007), 281–324.
- [61] GUILLAUMENT, R., VINCENT, S., AND CALTAGIRONE, J.-P. An original algorithm for VOF based method to handle wetting effect in multiphase flow simulation. *Mechanics REsearch Communications* 63 (2015), 26–32.

BIBLIOGRAPHY

- [62] GULLBRAND, J., AND CHOW, F. The effect of numerical errors and turbulence models in Large-Eddy Simulations of channel flow, with and without explicit filtering. *Journal of Fluid Mechanics* 495 (2003), 323–341.
- [63] HABISREUTINGER, M., BOUFFANAIS, R., LERICHE, E., AND DEVILLE, M. A coupled approximate deconvolution and dynamic mixed scale model for Large-Eddy Simulation. *Journal of Computational Physics* 224, 1 (2007), 241–266.
- [64] HÄNSCH, S., LUCAS, D., KREPPER, E., AND HÖHNE, T. A multi-field two fluid concept for transitions between different scales of interfacial structures. *International Journal of Multiphase Flow* 47 (2012), 171–182.
- [65] HAROUN, Y., LEGENDRE, D., AND RAYNAL, L. Volume Of Fluid method for interfacial reactive mass transfer: Application to stable liquid film. *Chemical Engineering Science* 65 (2010), 2896–2909.
- [66] HÄRTEL, C., AND KLEISER, L. Analysis and modelling of subgrid-scale motions in near-wall turbulence. *Journal of Fluid Mechanics* 356 (1998), 327–352.
- [67] HARTEN, A. The artificial compression method for computation of shocks and contact discontinuities : III. Self adjusting hybrid schemes. *Mathematics of Computation* 32 (1978), 363–389.
- [68] HAYNES, P. *Contribution à la modélisation de la turbulence pour les écoulements à bulle : proposition d’un modèle multi-échelles diphasique*. PhD thesis, Institut National Polytechnique de Toulouse, France, 2004.
- [69] HERRMANN, M. A parallel Eulerian interface tracking/Lagrangian point particle multi-scale coupling procedure. *Journal of Computational Physics* 229 (2010), 745–759.
- [70] HERRMANN, M., AND GOROKHOVSKI, M. A Large Eddy Simulation sub-grid model for turbulent phase interface dynamics. In *Proceedings of the 11th Triennial International Annual Conference on Liquid Atomization and Spray Systems: ICLASS 2009* (2009).
- [71] HIRT, C. W., AND NICHOLS, B. D. Volume Of Fluid (VOF) method for the dynamics of free boundaries. *Journal of Computational Physics* 39 (1981), 201–225.
- [72] HOSOKAWA, S., AND TOMIYAMA, A. Bubble-induced pseudo turbulence in laminar pipe flows. *International Journal of Heat and Fluid Flow* 40 (2013), 97–105.
- [73] HUA, J., AND LOU, J. Numerical simulation of bubble rising in viscous liquid. *Journal of Computational Physics* 222 (2007), 769–795.

- [74] II, S., SUGIYAMA, K., TAKEUCHI, S., TAKAGI, S., MATSUMOTO, Y., AND XIAO, F. An interface capturing method with a continuous function: The THINC method with multi-dimensional reconstruction. *Journal of Computational Physics* 231 (2011), 2328–2358.
- [75] ISHII, M. *Thermo-fluid dynamic, theory of two-phase*. Eyrolles, University of Michigan, 1975.
- [76] ISHII, M., AND ZUBER, N. Drag coefficient and relative velocity in bubbly, droplet or particule flows. *American Institute of Chemical Engineers Journal* 25 (1979).
- [77] JAMET, D., LEBAGUE, O., COUTRIS, N., AND DELHAYE, J. Feasibility of using the second gradient theory for the simulation of liquid-vapor with phase change. *Journal of Computational Physics* 169 (2000), 624–651.
- [78] JAMET, D., TORRES, D., AND BRACKBILL, J. U. On the theory and computation of surface tension: the elimination of parasitic currents through energy conservation in the second gradient method. *Journal of Computational Physics* 182 (2002), 262–276.
- [79] JAMET, M., LAVIEVILLE, J., ATKHEN, K., AND MECHITOUA, N. Validation of NEPTUNE_CFD on ULPU-V experiments. *Nuclear Engineering and Design* 239 (2015), 468–475.
- [80] JARRIN, N., BENHAMADOUCHE, S., LAURENCE, D., AND PROSSERA, R. A synthetic-eddy-method for generating inflow conditions for Large-Eddy Simulations. *International Journal of Heat and Fluid Flow* 27, 4 (2006), 585–593. Special Issue of The Fourth International Symposium on Turbulence and Shear Flow Phenomena - 2005.
- [81] JEANMART, H., AND WINCHELMANS, G. Investigation of eddy-viscosity models modified using discrete filters: A simplified “regularized variational multiscale model” and an “enhanced field model”. *Physics of Fluids* 19, 5 (2007), 055110.
- [82] KADI, R., AISSANI, S., AND BOUAM, A. Numerical simulation of the direct contact condensation phenomena for PTS-related in single and combined-effect thermal hydraulic test facilities using TransAT CMFD code. *Nuclear Engineering and Design* 293 (2015), 346–356.
- [83] KATAOKA, I. Local instant formulation of two-phase flow. *International Journal of Multiphase Flows* 12, 5 (1986), 745–758.
- [84] KHAFIZOV, R., POPLAVSKY, V., RACHKOV, V., SOROKIN, A., ASHURKO, Y., VOLKOV, A., IVANOV, E., AND PRIVENZENTSEV, V. Experimental investigation of sodium boiling heat exchange in fuel subassembly mockup for

BIBLIOGRAPHY

- perspective fast reactor safety substantiation. *Nuclear Energy and Technology 1* (2015), 147–152.
- [85] KLINE, S. J., REYNOLDS, W., SCHRAUB, F. A., AND RUNSTADLER, P. W. The structure of turbulent boundary layers. *Journal of Fluid Mechanics* 30, 4 (1967), 741–773.
- [86] KUNKELMANN, C., IBRAHEM, K., SCHWEIZER, N., HERBERT, S., STEPHAN, P., AND GAMBARYAN-ROISMAN, T. The effect of three-phase contact line speed on local evaporative heat transfer: experimental and numerical investigations. *International Journal of Heat and Mass Transfer* 55 (2012), 1896–1904.
- [87] KUNKELMANN, C., AND STEPHAN, P. CFD simulation of boiling flows using the Volume-Of-Fluid method within OpenFoam. *Numerical Heat Transfer Part A* 56, 8 (2009), 631–646.
- [88] LABOURASSE, E., LACANETTE, D., TOUTANT, A., VINCENT, S., LUBIN, P., LEBAIGUE, O., CALTAGIRONE, J., AND SAGAUT, P. Towards Large Eddy Simulation of isothermal two-phase flows : governing equations and *a priori* tests. *Journal of Multiphase Flow*, 33 (2007), 1–39.
- [89] LAFAURIE, B., NARDONE, C., SCARDOVELLI, R., ZALESKI, S., AND ZANETTI, G. Modelling merging and fragmentation in multiphase flows with SURFER. *Journal of Computational Physics* 113 (1994), 134–147.
- [90] LAKEHAL, D. DNS and LES of turbulent multifluid flows. In *Proceedings of 3rd International Symposium on two-Phase Flow Modelling and Experimentation* (Pisa, Italy, 2004).
- [91] LAKEHAL, D., FULGOSI, M., YADIGAROGLU, G., AND BANERJEE, S. Direct Numerical Simulation of Turbulent Heat Transfer Across a Mobile, Sheared Gas-Liquid Interface. *Journal of Heat Transfer* 125 (2003), 1129–1139.
- [92] LAKEHAL, D., SMITH, B. L., AND MILELLI, M. Large-Eddy Simulation of bubbly turbulent shear flows. *Journal of Turbulence* 3, 25 (2002).
- [93] LAMB, H. *Hydrodynamics*. 6th Edition of Cambridge University Press, 1932.
- [94] LANCE, M., AND BATAILLE, J. Turbulence in the liquid phase of a uniform bubbly air-water flow. *Journal of Fluid Mechanics* 222 (1991), 95–118.
- [95] LAROCQUE, J. *Modélisation et simulation numérique d’écoulements incompressibles turbulents diphasiques à phases non miscibles : application à l’interaction d’un jet turbulent avec une surface libre dans une cavité*. PhD thesis, Université Bordeaux 1, 2008.

- [96] LAROCQUE, J., VINCENT, S., LACANETTE, D., LUBIN, P., AND CALTAGIRONE, J.-P. Parametric study of LES subgrid terms in a turbulent phase separation flow. *International Journal of Heat and Fluid Flow* 31 (2010), 536–544.
- [97] LAVIÉVILLE, J., MIMOUNI, S., GUINGO, M., AND MÉRIGOUX, N. A generalized turbulent dispersion model for bubbly flow numerical simulation in neptune_cfd. *Nuclear Engineering and Design* 312 (2017), 284–293.
- [98] LEBAS, R., MÉNARD, T., BEAU, P., BERLEMONT, A., AND DEMOULIN, F. Numerical simulation of primary break-up and atomization: DNS and modelling study. *International Journal of Multiphase Flow* 35, 3 (2009), 247–260.
- [99] LEE, W. A pressure iteration scheme for two-phase flow modeling. *Multiphase Transport Fundamentals, Reactor Safety, Applications, Hemisphere Publishing* (1980).
- [100] LEGENDRE, D., AND MAGLIO, M. Comparison between numerical models for the simulation of moving contact lines. *Computers & Fluids* 113 (2015), 2–13.
- [101] LELE, S. Compact finite difference schemes with spectral-like resolution. *Journal of Computational Physics* 103 (1992), 16–42.
- [102] LEONARD, A. Energy cascade in Large-Eddy Simulations of turbulent fluid flows. *Advances in Geophysics* 18 (1974), 237–248.
- [103] LESIEUR, M. *La turbulence*. Collection Grenoble Science, Grenoble, 1994.
- [104] LI, J. Calcul d’interface affine par morceaux (piecewise linear interface calculation). *Comptes Rendus de l’Académie des Sciences de Paris* 320, IIb (1995), 391–396.
- [105] LIAO, Y., LUCAS, D., KREPPER, E., AND SCHMIDTKE, M. Development of a generalized coalescence and break-up closure for the inhomogeneous MUSIG model. *Nuclear Engineering and Design* 241 (2011), 1024–1033.
- [106] LILLY, D. The representation of small-scale turbulence in numerical simulation experiments. In *Proceedings of IBM Scientific Computing Symposium on Environmental Sciences* (1967).
- [107] LILLY, D. A proposed modification of the Germano subgrid-scale closure method. *Physics of Fluids A: Fluid Dynamics* 4, 3 (1992), 633–635.
- [108] LING, Y., ZALESKI, S., AND SCARDOVELLI, R. Multiscale simulation of atomization with small droplets represented by a Lagrangian point-particle model. *International Journal of Multiphase Flow* 76 (2015), 122–143.

BIBLIOGRAPHY

- [109] LIOVIC, P., AND LAKEHAL, D. Interface-turbulence interactions in large scale bubbling processes. *International Journal of Heat and Fluid flow*, 28 (2006), 127–144.
- [110] LIOVIC, P., AND LAKEHAL, D. Multi-physics treatment in the vicinity of arbitrarily deformable gas–liquid interfaces. *Journal of Computational Physics* 222 (2007), 504–535.
- [111] LIU, S., MENEVEAU, C., AND KATZ, J. On the properties of similarity subgrid-scale models as deduced from measurements in a turbulent jet. *Journal of Fluid Mechanics* 275 (1994), 83–119.
- [112] LUBIN, P. *Simulation des grandes échelles du déferlement plongeant des vagues*. PhD thesis, Université Bordeaux 1, 2004.
- [113] LUND, T. The use of explicit filters in Large Eddy Simulation. *Computers and Mathematics with Applications* 46 (2003), 603–616.
- [114] MA, J., OBERAI, A., DREW, D., LAHEY, R., AND MORAGA, F. A quantitative sub-grid air entrainment model for bubbly flows – plunging jets. *Computers & Fluids* 39 (2010), 77–86.
- [115] MAEDA, A., SOU, A., AND TOMIYAMA, A. A hybrid method for simulating flows including fluid particles. In *Proceedings of FEDSM06: ASME Joint US - European Fluid Engineering Summer Meeting* (July 2006).
- [116] MAGNAUDET, J. Simulation d’écoulements en présence d’interfaces. In *Ecole de printemps de mécanique des fluides numérique* (1997), Ecole de Printemps de Mécanique des Fluides Numérique.
- [117] MAO, W. Numerical simulation of vapor-liquid phase change heat transfer and micromixing in microfluidic systems. Master’s thesis, Guangzhou Institute of Energy Conversion, Chinese Academy of Sciences, China, 2009.
- [118] MAREUGE, I., AND LANCE, M. Bubble-induced dispersion of a passive scalar in bubbly flows. In *Proceedings of 2nd International Conference on Multiphase Flow* (Kyoto, Japan, 1995).
- [119] MARTINEZ-MERCADO, J., GOMEZ, D., GILS, D., SUN, C., AND LOHSE, D. On bubble clustering and energy spectra in pseudo-turbulence. *Journal of Fluid Mechanics* 650 (2010), 287–306.
- [120] MARTINEZ-MERCADO, J., PALACIOS-MORALES, C., AND ZENIT, R. Measurement of pseudoturbulence intensity in monodispersed bubbly liquids for $10 < \text{Re} < 500$. *Physics of Fluids* 19, 10 (2007), 103302.
- [121] MATHEW, J., FOYSI, H., AND FRIEDRICH, R. A new approach to LES based on explicit filtering. *International Journal of Heat and Fluid Flow* 27 (2006), 594–602.

- [122] MAURY, B. Direct simulations of 2D fluid-particle flows in biperiodic domains. *Journal of Computational Physics* 156, 2 (1999), 325–351.
- [123] MÉCHITOUA, N., BOUCKER, M., LAVIÉVILLE, J., PIGNY, S., AND SERRE, G. An unstructured finite volume solver for two phase water/vapour flows based on an elliptic oriented fractional step method. In *Proceedings of 10th Int. Topl. Mtg. Nuclear Reactor Thermal Hydraulics (NURETH 10)* (Seoul, Republic of Korea, 2003).
- [124] MÉRIGOUX, N., LAVIÉVILLE, J., MIMOUNI, S., GUNGO, M., AND BAUDRY, C. A generalized large interface to dispersed bubbly flow approach to model two-phase flows in nuclear power plant. In *Proceedings of the Computational Fluid Dynamics in Nuclear Reactor Safety: CFD4NRS-6* (Cambridge, USA, 2016).
- [125] MEYERS, J., AND SAGAUT, P. On the model coefficients for the standard and the variational multi-scale smagorinsky model. *Journal of Fluid Mechanics* 569 (2006), 287–319.
- [126] MILELLI, M. *A numerical analysis of confined turbulent bubble plumes*. PhD thesis, Swiss Federal Institute of Technology Zurich, 2002.
- [127] MIMOUNI, S., ARCHAMBEAU, F., BOUCKER, M., LAVIÉVILLE, J., AND MOREL, C. A second order turbulence model based on a Reynolds stress approach for two-phase boiling flow and application to fuel assembly analysis. *Nuclear Engineering and Design* 240 (2010), 2225–2232.
- [128] MIMOUNI, S., ARCHAMBEAU, F., BOUCKER, M., LAVIÉVILLE, J., AND MOREL, C. A second order turbulence model based on a Reynolds stress approach for two-phase boiling flow. Part 1: Application to the ASU-annular channel case. *Nuclear Engineering and Design* 240 (2010), 2233–2243.
- [129] MIMOUNI, S., BOUCKER, M., LAVIÉVILLE, J., GUELFY, A., AND BESTION, D. Modelling and computation of cavitation and boiling bubbly flows with the neptune_cfd code. *Nuclear Engineering and Design* 238, 3 (2008), 680–692.
- [130] MIMOUNI, S., FLEAU, S., AND VINCENT, S. CFD calculations of flow pattern maps and LES of multiphase flows. *accepted in Nuclear Engineering and Design* (2016).
- [131] MIMOUNI, S., FLEAU, S., AND VINCENT, S. Towards a more general CFD modelling for all flow regimes. In *Proceedings of 9th International Conference on Multiphase Flow: ICMF 2016* (Firenze, Italy, 2016).
- [132] MIMOUNI, S., LAVIÉVILLE, J., SEILER, N., AND RUYER, P. Combined evaluation of second order turbulence model and polydispersion model for two-phase boiling flow and application to fuel assembly analysis. *Nuclear Engineering and Technology* 241, 11 (2011), 4523–4536.

BIBLIOGRAPHY

- [133] MOIN, P. *Fundamentals of Engineering Numerical Analysis*. Cambridge University Press, 2001.
- [134] MOIN, P., AND KIM, J. Numerical investigation of turbulent channel flow. *Journal of Fluid Mechanics* 118 (1982), 341–377.
- [135] MONTREUIL, E. *Simulation numérique pour l'aérothermique avec des modèles sous-maille*. PhD thesis, Université Pierre et Marie Curie, 2005.
- [136] MORAGA, F., CARRICA, P., DREW, D., AND LAHEY, R. A sub-grid air entrainment model for breaking bow waves and naval surface ships. *Computers & Fluids* 37 (2008), 281–298.
- [137] MOREL, C., RUYER, P., SEILER, N., AND LAVIEVILLE, J. Comparison of several models for multi-size bubbly flows on an adiabatic experiment. *International Journal of Multiphase Flow* 36, 1 (2010), 25–39.
- [138] MOTTIN, D. Development of a three-field mass transfer model for phase change in the code NEPTUNE_CFD. Master's thesis, Ecole Supérieure de Physique et de Chimie Industrielles de la Ville de Paris (ESPCI Paris) and EDF R&D, 2016.
- [139] MURZYN, F., AND CHANSON, H. Free surface fluctuations in hydraulic jumps: experimental observations. *Experimental Thermal and Fluid Science* 33 (2009), 1055–1064.
- [140] NAJJAR, F., AND TAFTI, D. Study of discrete test filters and finite difference approximations for the dynamic subgrid-scale stress model. *Physics of Fluids* 8 (1996), 1076–1088.
- [141] NDJINGA, M., KUMBARO, A., VUYST, F. D., AND LAURENT-GENGOUX, P. Influence of interfacial forces on the hyperbolicity of the two-fluid model. In *Proceedings of 5th International Symposium on Multiphase Flow, Heat Mass Transfer and Energy Conversion* (X'ian, China, 2005).
- [142] NICHITA, A., AND THOME, J. A Level Set method and a heat transfer model implementation into FLUENT for modeling of microscale two-phase flows. In *Proceedings of "AVT-178 Specialists" Meeting on System Level Thermal Management for Enhanced Platform Efficiency*. No. EPFL-CONF-151629 (2010).
- [143] NICOUD, F., AND DUCROS, F. Subgrid-scale stress modelling based on the square of the velocity gradient tensor. *Flow, Turbulence and Combustion* 62, 3 (1999), 183–200.
- [144] NIEDERSCHULTE, M., ADRIAN, R., AND HANRATTY, T. J. *PCH11: Fully Developed Turbulent Channel Flow Experiment*. Agard advisory report No345, 1998, ch. A Selection of Test Cases for the Validation of Large-Eddy Simulations of Turbulent Flows.

- [145] NONOMURA, T., KITAMURA, K., AND FUJIIA, K. A simple interface sharpening technique with a hyperbolic tangent function applied to compressible two-fluid modelling. *Journal of Computational Physics* 258 (2014), 95–117.
- [146] OLSSON, E., AND KREISS, G. A conservative Level Set method for two phase flow. *Journal of Computational Physics* 210 (2005), 225–246.
- [147] OLSSON, E., KREISS, G., AND ZAHEDI, S. A conservative Level Set method for two phase flow II. *Journal of Computational Physics* 225 (2007), 785–807.
- [148] PAN, Z., WEIBEL, J., AND GARIMELLA, S. Spurious Current Suppression in VOF-CSF Simulation of Slug Flow through Small Channels. *CTRC Research Publications* 243 (2015).
- [149] PATANKAR, S., AND SPALDING, D. A calculation procedure for heat, mass and momentum transfer in three-dimensional parabolic flows. *International Journal of Heat and Mass Transfer* 15, 10 (1972), 1787–1806.
- [150] PIGNY, S. Intermediate scales between simulation and modeling of two-phase flows. *Nuclear Engineering and Design* 241 (2011), 874–887.
- [151] POPE, S. *Turbulent flows*. Cambridge University Press, 2000.
- [152] POPINET, S. An accurate adaptive solver for surface-tension-driven interfacial flows. *Journal of Computational Physics* 228, 16 (2009), 5838–5866.
- [153] POPINET, S., AND ZALESKI, S. A Front-Tracking algorithm for accurate representation of surface tension. *International Journal for Numerical Methods in Fluid* 30 (1999), 775–793.
- [154] PRUETT, C., AND ADAMS, N. *A Priori* analyses of three subgrid-scale models for one-parameter families of filters. *Physics of Fluids* 12 (2000), 1133–1142.
- [155] RAYMOND, F., AND ROSANT, J.-M. A numerical and experimental study of the terminal velocity and shape of bubbles in viscous liquids. *Chemical Engineering Science* 55 (2000), 943–955.
- [156] REBOUX, S., SAGAUT, P., AND LAKEHAL, D. Large-Eddy Simulation of sheared interfacial flow. *Physics of Fluids* 18 (2006), 105105.
- [157] REYNOLDS, O. On the dynamical theory of incompressible viscous fluids and the determination of the criterion. *The Royal Society’s Philosophical Transactions A* 186 (1895), 123–164.
- [158] RIBOUX, G., RISSO, F., AND LEGENDRE, D. Experimental characterization of the agitation generated by bubbles rising at high Reynolds number. *Journal of Fluid Mechanics* 643 (2010), 503–539.

BIBLIOGRAPHY

- [159] RISSO, F., ROIG, V., AMOURA, Z., RIBOUX, G., AND BILLET, A. Wake attenuation in large Reynolds number dispersed two-phase flows. *Philosophical Transactions of the Royal Society of London A: Mathematical, Physical and Engineering Sciences* 366, 1873 (2008), 2177–2190.
- [160] ROACHE, P. *Verification and Validation in Computational Science and Engineering*. Hermosa Publishers, Albuquerque, New Mexico, 1998.
- [161] RODI, W., AND MANSOUR, N. N. Low Reynolds number $k - \epsilon$ modeling with the aid of direct simulation data. *Journal of Fluid Mechanics* 250, 509 (1993).
- [162] ROIG, V., AND DE TOURNEMINE, A. L. Measurement of interstitial velocity of homogeneous bubbly flows at low to moderate void fraction. *Journal of Fluid Mechanics* 572 (2007), 87–110.
- [163] SAGAUT, P. *Large Eddy Simulation for incompressible flows - An introduction*. Springer Verlag, 1998.
- [164] SAGAUT, P. *Large Eddy Simulation for Incompressible flows*. Springer-Verlag, 2004.
- [165] SAGAUT, P., DECK, S., AND TERRACOL, M. *Multiscale and Multiresolution Approaches in Turbulence: LES, DES and Hybrid RANS/LES Methods: Applications and Guidelines*. Imperial College Press, London, 2013.
- [166] SAGAUT, P., AND GERMANO, M. On the filtering paradigm for LES of flows with discontinuities. *Journal of Turbulence* 6, 23 (2005).
- [167] SALVETTI, M., AND BEUX, F. The effect of the numerical scheme on the subgrid scale term in Large-Eddy-Simulation. *Physics of Fluids* 10, 11 (1998), 3020–3022.
- [168] SAN, O., STAPLES, A., AND ILIESCU, T. *A posteriori* analysis of low-pass spatial filters for approximate deconvolution Large Eddy Simulations of homogeneous incompressible flows. *International Journal of Numerical Analysis and Modeling* 1, 1 (2014), 1–18.
- [169] SARGHINI, F., AND PIOMELLI, U. Scale-similar subgrid stress models for Large-Eddy Simulations. *AIAA Paper 98-0538* (1998).
- [170] SATO, Y., AND NICENO, B. A conservative local interface sharpening scheme for the constrained interpolation profile method. *International Journal for Numerical Methods in Fluids* 70 (2012), 441–467.
- [171] SATO, Y., AND NICENO, B. A sharp-interface phase change model for a mass-conservative interface tracking method. *Journal of Computational Physics* 249 (2013), 127–161.

- [172] SATO, Y., SADATOMI, I., AND SEKOGUSHI, I. Momentum and heat transfer in two-phase bubbly flow-I. *Journal of Multiphase Flow* 7 (1981).
- [173] SCARDOVELLI, R., AND ZALESKI, S. Direct Numerical Simulation of free-surface and interfacial flow. *Annual Review of Fluid Mechanics* 31 (1999), 567–603.
- [174] SCHEPPER, S. D., HEYNDERICHX, G., AND MARIN, G. Modeling the evaporation of a hydrocarbon feedstock in the convection section of a steam cracker. *Computers & Chemical Engineering* 33 (2009), 122–132.
- [175] SCHLATTER, P., STOLZ, S., AND KLEISER, L. LES of transitional flows using the approximate deconvolution model. *International Journal of Heat and Fluid Flow* 25, 3 (2004), 549–558.
- [176] SCHROOYEN, P., AND THIRY, S. Investigations expérimentales et numériques sur les instabilités de Kelvin-Helmholtz à l’interface entre deux fluides immiscibles. Master’s thesis, Université catholique de Louvain, 2010.
- [177] SCRIVEN, L. On the dynamics of phase growth. *Chemical Engineering Science* 10 (1959), 1–13.
- [178] SEILER, N., AND RUYER, P. Advanced model for polydispersion in size in boiling flows. In *Proceedings of 190^{eme} session du comité scientifique et technique de la Société Hydrotechnique de France: modélisation des écoulements diphasiques bouillants* (2008).
- [179] SERIZAWA, A., AND KATAOKA, I. Turbulence suppression in bubbly two-phase flow. *Nuclear Engineering and Design* 122 (1990), 1–16.
- [180] SHU, C. Essentially non-oscillatory and weighted essentially non-oscillatory schemes for hyperbolic conservation laws. Tech. rep., NASA (as NASA/CR-97-206253 report), 1997.
- [181] SHU, C., AND OSHER, S. Efficient implementation of essentially nonoscillatory shock-capturing schemes. *Journal of Computational Physics* 77 (1988), 439–471.
- [182] SMAGORINSKY, J. General circulation experiments with the primitive equations. *Monthly Weather Review* 91 (1963), 99–165.
- [183] SO, K., HU, X., AND ADAMS, N. Anti-diffusion method for interface steepening two-phase incompressible flow. *Journal of Computational Physics* 230 (2011), 5155–5177.
- [184] SON, G. A numerical method for bubble motion with phase change. *Numerical Heat Transfer Part B* 39, 5 (2001), 509–523.

BIBLIOGRAPHY

- [185] SPEZIALE, C. G. Turbulence modeling for time-dependant RANS and VLES: a review. In *Proceedings of CFD Conference 13th AIAA paper* (1997), pp. 1997–2051.
- [186] STEFANO, G. D., AND VASILYEV, O. Sharp cut-off vs. smooth filtering in LES. *Physics of Fluids 14*, 362 (2002).
- [187] STOLZ, S., ADAMS, N., AND KLEISER, L. An approximate deconvolution model for Large-Eddy Simulation with application to incompressible wall-bounded flows. *Physics of Fluids 13*, 4 (2001), 997–1015.
- [188] STRUBELJ, L. *Numerical simulations of stratified two-phase flows with two-fluid model and interface sharpening*. PhD thesis, University of Ljubljana, 2009.
- [189] SUN, D., XU, J., AND CHEN, Q. Modeling of the evaporation and condensation phase-change problems with FLUENT. *Numerical Heat Transfer Part B 66* (2014), 326–342.
- [190] SUSSMAN, M., SMEREKA, P., AND OSHER, S. A Level Set approach for computing solutions in incompressible two-phase flow. *Journal of Computational Physics 114* (1994), 146–159.
- [191] TAITEL, Y., BORNEA, D., AND DUKLER, A. E. Modelling flow pattern transition for steady upward gas-liquid flow in vertical tubes. *American Institute of Chemicals Engineers 26* (1980), 345–354.
- [192] THEOFANOUS, T., OH, S., AND SCOBEL, J. International nuclear energy research initiative, in-vessel retention technology development and use for advanced PWR designs in the USA and Korea. Tech. rep., University of California Santa Barbara, 2004.
- [193] THORPE, S. Experiments on the instability of stratified shear flows: immiscible fluids. *Journal of Fluid Mechanics 39* (1969), 25–48.
- [194] TIWARI, A., FREUND, J., AND PANTANO, C. A diffuse interface model with immiscibility preservation. *Journal of Computational Physics 252*, 290-309 (2013).
- [195] TOMAR, G., FUSTER, D., ZALESKI, S., AND POPINET, S. Multiscale simulations of primary atomization. *Computers & Fluids 39*, 10 (2010), 1864–1874.
- [196] TOMIYAMA, A., TAMAI, H., ZUN, I., AND HOSOKAWA, S. Transverse migration of single bubbles in simple shear flows. *Chemical Engineering Science 57* (2002), 1849–1858.

- [197] TOUTANT, A. *Modélisation physique des interactions entre interfaces et turbulence*. PhD thesis, Institut National Polytechnique de Toulouse, France, 2006.
- [198] TOUTANT, A., LABOURASSE, E., LEBAIGUE, O., AND SIMONIN, O. DNS of the interaction between a deformable buoyant bubble and a spatially decaying turbulence: *A priori* tests for LES two-phase flow modelling. *Computers & Fluids* 37 (2008), 877–886.
- [199] TRAN, M. L. *Modélisation Instationnaire de la Distribution Spatiale des Phases dans les écoulements Diphasiques en Régime à Bulles*. PhD thesis, Université Lyon 1, 1997.
- [200] TRONTIN, P., ESTIVALEZES, J., VINCENT, S., AND CALTAGIRONE, J.-P. A phase-conditioned filtering of incompressible interfacial multiphase flow equations: *A Priori* study for the modeling of LES subgrid scale terms. In *Proceedings of Turbulence and Interactions 2012* (La Saline-les-Bains, La Réunion, France, 2012).
- [201] TRONTIN, P., VINCENT, S., ESTIVALEZES, J., AND CALTAGIRONE, J. Detailed comparisons of front-capturing methods for turbulent two-phase flow simulations. *International Journal for Numerical Methods in Fluids* 59 (2008), 1543–1549.
- [202] TRONTIN, P., VINCENT, S., ESTIVALEZES, J., AND CALTAGIRONE, J. Direct Numerical Simulation of a freely decaying turbulent interfacial flow. *International Journal of Multiphase Flow* 38 (2010), 891–907.
- [203] UNVERDI, S. O., AND TRYGGVASON, G. A Front-Tracking method for viscous, incompressible, multi-fluid flows. *Journal of Computational Physics* 100 (1992), 25–37.
- [204] VALLET, A., AND BORGHI, R. Modélisation Eulérienne de l’atomisation d’un jet liquide. *Comptes Rendus de l’Académie des Sciences - Series IIB - Mechanics-Physics-Astronomy* 327, 10 (1999), 1015–1020.
- [205] VAN DRIEST, E. R. On turbulent flow near a wall. *Journal of Aeronautic Sciences* 23 (1956).
- [206] VINCENT, S. Modeling and simulation of multi-phase flows with fictitious domain approaches. In *Proceedings of Small Scale Modeling and Simulation of Turbulent Multi-phase Flows* (International Centre for Mechanical Sciences CISM, Udine, Italy, 2016).
- [207] VINCENT, S., LAROCQUE, J., LACANETTE, D., TOUTANT, A., LUBIN, P., AND SAGAUT, P. Numerical simulation of phase separation and *a priori* two-phase LES filtering. *Computers & Fluids* 37 (2008), 898–906.

BIBLIOGRAPHY

- [208] VINCENT, S., OSMAR, L., ESTIVALEZES, J.-L., ZALESKI, S., AUGUSTE, F., ANISZEWSKI, W., LING, Y., MÉNARD, T., PEDRONO, A., MAGNAUDET, J., CALTAGIRONE, J.-P., AND BERLEMONT, A. A phase inversion benchmark for multiscale multiphase flows. *under correction in Journal of Computational Physics* (2015).
- [209] VINCENT, S., TAVARES, M., FLEAU, S., MIMOUNI, S., OULD-ROUIS, M., AND ESTIVALEZES, J.-L. *A priori* filtering and LES modeling of turbulent two-phase flows Application to phase separation. *under correction in Computers & Fluids* (2016).
- [210] VREMAN, B., GEURTS, B., AND KUERTEN, H. On the formulation of the dynamic mixed subgrid-scale model. *Physics of Fluids* 6, 12 (1994), 4057–4059.
- [211] WEI, T., AND WILLMARTH, W. W. Reynolds-number effects on the structure of a turbulent channel flow. *Journal of Fluid Mechanics*, 204 (1989), 57–95.
- [212] WELCH, S., AND WILSON, J. A Volume Of Fluid based method for fluid flows with phase change. *Journal of Computational Physics* 160 (2000), 662–682.
- [213] WELLEK, R., AGRAWAL, A., AND SKELLAND, A. Shape of liquid drops moving in liquid media. *AIChE Journal* 12, 5 (1966), 854–862.
- [214] WRAY, A., AND HUNT, J. Algorithms for classification of turbulent structures. In *Topological Fluid Mechanics, Proceedings of the IUTAM Symposium* (1989), pp. 95–104.
- [215] WU, H., PENG, X., YE, P., AND GONG, Y. E. Simulation of refrigerant flow boilin in serpentine tubes. *International Journal of Heat and Mass Transfer* 50 (2007), 1186–1195.
- [216] XIAO, F., HONMA, Y., AND KONO, T. A simple algebraic interface capturing scheme using hyperbolic tangent function. *International Journal for Numerical Methods in Fluids* 48, 9 (2005), 1023–1040.
- [217] XIAO, F., II, S., AND CHEN, C. Revisit to the THINC scheme: A simple algebraic VOF algorithm. *Journal of Computational Physics* 230 (2011), 7086–7092.
- [218] YAKHOT, V., AND ORSZAG, S. Renormalization Group analysis of turbulence. *Physical review letters* 57, 14 (1986), 1722.
- [219] YANG, Z., PENG, X., AND YE, P. Numerical and experimental investigation of two-phase flow during boiling in a coiled tube. *International Journal of Heat and Mass Transfer* 51, 5 (2008), 1003–1016.
- [220] YOUNGS, D. *Time-dependent multi-material flow with large fluid distortion*. Academic Press, New York, 1982, p. 27.

- [221] ZARHAI, S., BARK, F., AND KARLSSON, R. On anisotropic subgrid modelling. *European journal of mechanics. B, Fluids* 14, 4 (1995), 459–486.
- [222] ZHANG, T. Numerical simulation of the dynamics of turbulent boundary layers: perspectives of a transition simulator. *Philosophical Transaction of The Royal Society of London* 336 (1991), 95–102.
- [223] ZHANG, Y., STREET, R., AND KOSEFF, J. A dynamic mixed subgrid-scale model and its application to turbulent recirculating flows. *Physics of Fluids A: Fluid Dynamics* 5 (1993), 3186–3196.
- [224] ZHANG, Y., AND VICQUELIN, R. Controlling bulk reynolds number and bulk temperature in channel flow simulations. *Journal of Computational Physics* 305 (2016), 208–216.
- [225] ZUBER, N. On the dispersed two-phases flow in the laminar flow regime. *Chemical Engineering Science* 19 (1964).
- [226] ZUZIO, D., AND ESTIVALEZES, J. An efficient block parallel AMR method for two phase interfacial flow simulations. *Computers & Fluids* 44, 1 (2011), 339–357.
- [227] ZUZIO, D., ESTIVALEZES, J.-L., VILLEDIEU, P., AND BLANCHARD, G. Numerical simulation of primary and secondary atomization. *Comptes Rendus Mécanique* 341, 1-2 (2013), 15–25.

Résumé

La compréhension des écoulements à bulles dans les centrales nucléaires demeure encore un élément limitant dans l'analyse des opérations et de la sûreté des installations. Pour ne citer qu'un exemple, l'amélioration de la durée de vie et de la performance des générateurs de vapeur nécessite d'appréhender les régimes d'écoulement au sein des tubes qui sont responsables de leur vibration. Cependant, pour simuler avec précision ces écoulements, les codes de simulation numérique doivent relever de nombreux défis parmi lesquels la capacité à simuler des inclusions ayant des tailles très variées. Dans cette thèse, une nouvelle approche, appelée approche multi-champ, est implémentée dans le code NEPTUNE_CFD, basé sur un modèle bi-fluide. Cette approche inclut une méthode de suivi d'interface pour les grandes structures déformables et prend en compte les effets liés à la turbulence et aux changements de phase.

Pour simuler de tels écoulements complexes en limitant le coût CPU, l'approche multi-champ considère séparément les petites inclusions sphériques des grandes inclusions déformables. Ainsi, les petites structures sphériques sont définies via un champ eulérien dispersé évoluant au sein d'un champ continu porteur, comme c'est habituellement le cas avec le modèle bi-fluide. Les grosses bulles déformables sont considérées comme des interfaces entre deux champs continus, un champ liquide et un champ gaz. Si on prend l'exemple d'un écoulement diphasique avec de l'eau et des bulles d'air de différentes tailles, trois champs sont alors définis pour cet écoulement: un champ continu liquide, un champ continu gaz et un champ dispersé gaz contenant les petites bulles sphériques. Cependant, simuler avec précision des interfaces entre deux champs continus avec le modèle bi-fluide nécessite le développement de traitements spécifiques afin de coupler les deux champs à l'interface et de limiter la diffusion de cette interface.

Après avoir amélioré la simulation des interfaces dans des écoulements laminaires, les effets liés à la turbulence sont étudiés. Une étude *a priori* de simulations aux grandes échelles est proposée pour identifier les termes sous-mailles et comparer différents modèles de turbulence disponibles dans la littérature. L'implémentation et la validation du modèle de turbulence retenu suite à l'étude sont détaillées. Les changements de phase sont ensuite explorés via le développement d'un modèle spécifique pour le terme de transfert de masse. Pour finir, des simulations trois champs sont présentées. De nouveaux critères sont définis pour modéliser la fragmentation des grandes inclusions déformables en petites bulles sphériques ainsi que la coalescence de ces dernières pour former de grandes bulles déformables.

A chaque étape de l'implémentation des différents modèles évoqués, des validations basées sur des données analytiques et issues d'expériences sont présentées afin de s'assurer que les phénomènes physiques sont bien prédits. Des cas tests dans des configurations industrielles sont également détaillés pour montrer la capacité de l'approche développée à simuler des écoulements complexes.

Mots clés: Ecoulements multi-phases, Modèle bi-fluide, Approche multi-champ, Couplage de modèles.

Abstract

Bubbly flows occurring in nuclear power plants remain a major limiting phenomenon for the analysis of operation and safety. As an example, the improvement of steam generator lifetime and performance relies on the comprehension of flow regimes inside the tubes responsible for tube vibrations. However, to ensure an accurate simulation of these flows, the Computational Multi-Fluid Dynamics (CMFD) codes have to take up many challenges, among others the ability of dealing with a variety of inclusion sizes. The classical two-fluid model allows simulating small spherical inclusions but is not able to compute large deformable inclusions. Thus, in this thesis, a new approach, called the multifield approach, is implemented in the CMFD code NEPTUNE_CFD, based on a two-fluid model. This approach includes an interface tracking method for large and deformable structures and takes into account turbulence and phase change effects.

To simulate such complex flows with reasonable computational costs, the multifield approach considers separately the small spherical inclusions and the large deformable ones. Thus, the small spherical structures are defined as a dispersed field evolving in a continuous carrier field, as usually done in the two-fluid model. The large deformable bubbles are considered as interfaces between two continuous phases treated as two different fields in the two-fluid model. In the example of a two-phase flow with water and air bubbles of different sizes, three fields are defined: a continuous liquid field, a continuous gas field and a dispersed gas field containing the small spherical bubbles. However, the accurate simulation of interfaces between the two continuous fields within the two-fluid model requires specific treatments to couple the two fields at the interface and to limit the interface smearing.

After improving the interface simulation in laminar flows, turbulence effects are investigated. An *a priori* Large Eddy Simulation (LES) study is performed to identify the predominant subgrid terms and to compare different available turbulence models. The implementation and validation of the most suitable model is proposed. Phase change interfaces are then explored with the development of a specific model for the mass transfer term. Finally, three field simulations are performed. New criteria are defined for the breakup of the large deformable inclusions into small spherical bubbles and for the coalescence of the latter forming large deformable bubbles.

Validation at each step of the models implementations are presented using analytical and experimental data to ensure that the physical phenomena are well predicted. Test cases in industrial configurations are finally performed to show the ability of the developed approach to deal with complex flows.

Keywords: Multiphase flows, Two-fluid model, Multifield approach, Model coupling.